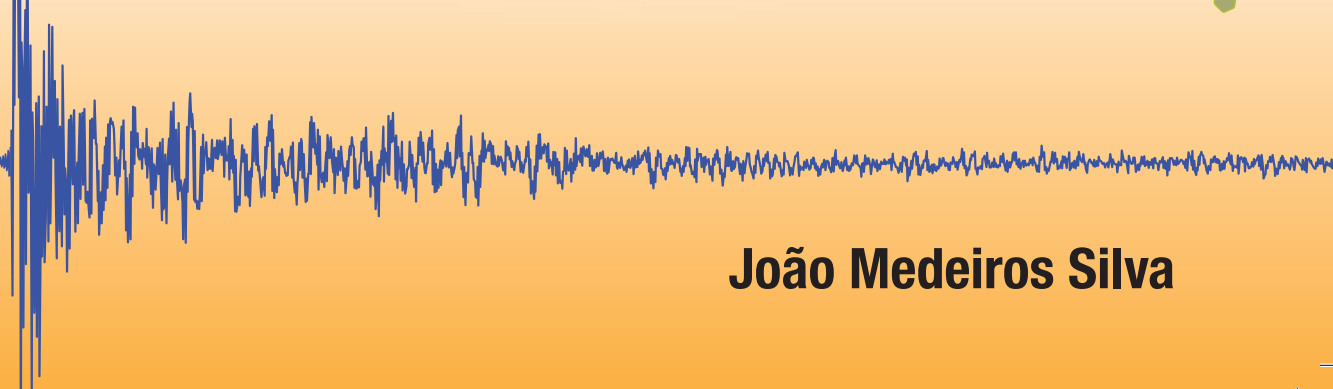
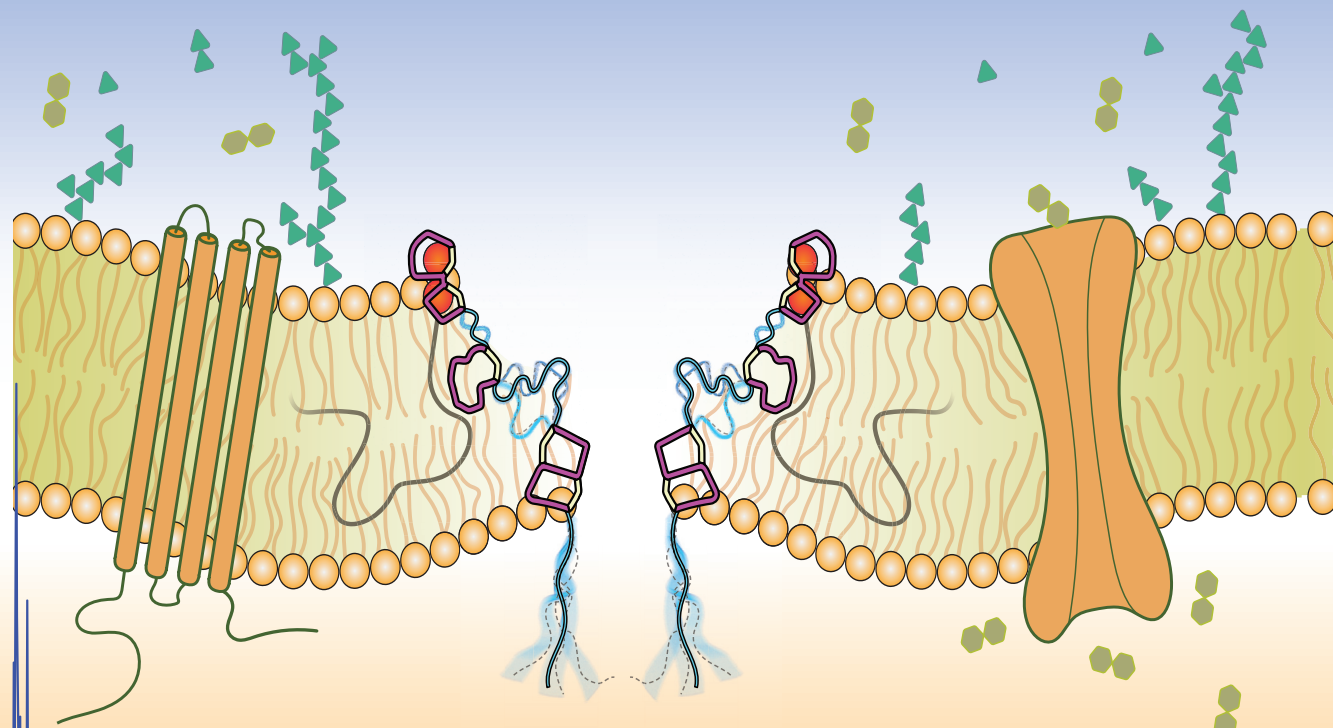


# Towards the physiologically relevant state with high-resolution solid state NMR

Towards the physiologically relevant state with high-resolution solid state NMR

João Medeiros Silva

2019



João Medeiros Silva

**Towards the physiologically relevant state  
with high-resolution solid state NMR**

**João Medeiros Silva**

ISBN 978-90-393-7219-7

Doctoral Thesis

Towards the physiologically relevant state with high-resolution solid state NMR

João Medeiros Silva

NMR Spectroscopy, Bijvoet Center for Biomolecular Research

Department of Chemistry, Faculty of Science, Utrecht University

Utrecht, The Netherlands

November 2019

Cover Art and Thesis Layout: João Medeiros Silva

Cover Layout: ProefchriftMaken

Printed in the Netherlands by ProefchriftMaken | [www.proefchriftmaken.nl](http://www.proefchriftmaken.nl)

Copyright © 2019 João Medeiros Silva

# **Towards the physiologically relevant state with high-resolution solid state NMR**

**Op weg naar de fysiologisch relevante toestand met hoge-  
resolutie vaste stof NMR**

(met een samenvatting in het Nederlands)

## **Proefschrift**

ter verkrijging van de graad van doctor aan de  
Universiteit Utrecht  
op gezag van de  
rector magnificus, prof.dr. H.R.B.M. Kummeling,  
ingevolge het besluit van het college voor promoties  
in het openbaar te verdedigen op

woensdag 13 november 2019 des middags te 2.30 uur

door

**João Medeiros Silva**

geboren op 23 juni 1991  
te São Miguel, Portugal

**Promotor:**

Prof. dr. M. Baldus

**Copromotor:**

Dr. M.H. Weingarth

-To my father, to my mother,  
who gave everything for  
their children's education.

-To my family.

-Ao meu pai, à minha mãe,  
que tudo fizeram pela  
educação dos seu filhos.

-À minha família.



## TABLE OF CONTENTS

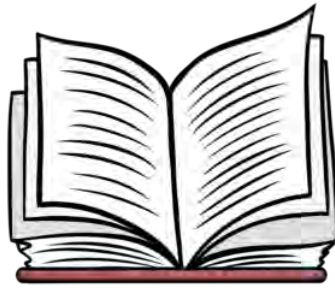
	List of abbreviations	8
<b>Chapter 1</b>	General Introduction	9
<b>Chapter 2</b>	<sup>1</sup> H detected solid-State NMR studies of water-inaccessible proteins <i>in vitro</i> and <i>in situ</i>	39
<b>Chapter 3</b>	Hydrogen bond strength in membrane proteins probed by time-resolved <sup>1</sup> H-detected solid state NMR and MD simulations	67
<b>Chapter 4</b>	Shifts in the selectivity filter dynamics cause modal gating in K <sup>+</sup> channels	81
<b>Chapter 5</b>	Supramolecular organization and functional implications of K <sup>+</sup> channel clusters in membranes	107
<b>Chapter 6</b>	High-resolution NMR Studies of antibiotics in cell membranes	125
<b>Chapter 7</b>	Progress on the Nisin-Lipid II pore structure	151
<b>Chapter 8</b>	Summary and outlook	163
	Acknowledgments	171
	List of publications	176
	About the author	177

## LIST OF ABBREVIATIONS

CSP	<u>C</u> hemical <u>S</u> hift <u>P</u> erturbations
CGMD	<u>C</u> oarse <u>G</u> raigned <u>M</u> olecular <u>D</u> ynamics
CP	<u>C</u> ross <u>P</u> olarization
DNP	<u>D</u> ynamic <u>N</u> uclear <u>P</u> olarization
ESI	<u>E</u> lectrospray <u>I</u> onization
FD	<u>F</u> ractional <u>D</u> euteration
FP	<u>F</u> ull <u>P</u> rotonation
GlcNAc	<u>N</u> - <u>A</u> cetyl- <u>D</u> - <u>g</u> lucosamine
HPLC	<u>H</u> igh- <u>P</u> erformance <u>L</u> iquid <u>C</u> hromatography
HSQC	<u>H</u> eteronuclear <u>S</u> ingle <u>Q</u> uantum <u>C</u> oherence
iFD	<u>i</u> nverse <u>F</u> ractional <u>D</u> euteration
ILV	<u>I</u> soleucine- <u>L</u> eucine- <u>V</u> aline methyl labelling
KcsA	Potassium ( <u>K</u> <sup>+</sup> ) <u>C</u> hannel from <i>Streptomyces lividans</i> <u>A</u>
LII	<u>L</u> ipid <u>I</u> I
MAS	<u>M</u> agic <u>A</u> ngle <u>S</u> pinning
MD	<u>M</u> olecular <u>D</u> ynamics
MISSISSIPI	<u>M</u> ultiple <u>I</u> ntense <u>S</u> olvent <u>S</u> uppression <u>I</u> ntended for <u>S</u> ensitive <u>S</u> pectroscopic Investigation of <u>P</u> rotonated <u>P</u> roteins
MLVs	<u>M</u> ulti- <u>l</u> aminar <u>V</u> esicles
MRSA	Methicillin-resistant Staphylococcus aureus
MurNAc	<u>N</u> - <u>A</u> cetyl <u>m</u> uramic acid
NMR	<u>N</u> uclear <u>M</u> agnetic <u>R</u> esonance
PARIS	<u>P</u> hase- <u>a</u> lternated <u>r</u> ecoupling <u>i</u> rradiation <u>s</u> cheme
PAIN	<u>P</u> roton <u>A</u> ssisted <u>I</u> nsensitive <u>N</u> uclei
PISSARRO	<u>P</u> hase- <u>I</u> nverted <u>S</u> upercycled <u>S</u> equence for <u>A</u> ttenuation of <u>R</u> otary <u>R</u> esonance
PD	<u>P</u> er <u>d</u> euteration
SDS PAGE	<u>S</u> odium <u>d</u> odecyl <u>s</u> ulfate- <u>p</u> olyacrylamide gel <u>e</u> lectrophoresis
ssNMR	<u>S</u> olid <u>S</u> tate <u>N</u> uclear <u>M</u> agnetic <u>R</u> esonance
SAIL	<u>S</u> tereo- <u>A</u> rray <u>I</u> sotope <u>L</u> abeling
T <sub>1</sub> / R <sub>1</sub>	Transverse relaxation <u>t</u> ime / <u>r</u> ate
TLC	<u>T</u> hin <u>L</u> ayer <u>C</u> hromatography
TM	<u>T</u> rans <u>m</u> embrane
WT	<u>W</u> ild- <u>T</u> ype

# CHAPTER 1

## General Introduction





## Introduction

Understanding how biomolecules work provides the basis to explain cellular processes that drive life. Structural biology addresses this tremendous challenge by characterizing the tridimensional structures of biomolecules using a range of different techniques. Especially X-ray Crystallography, solution state Nuclear Magnetic Resonance, and Cryo-Electron Microscopy have been major driving forces in the field, yet these techniques have their inherent disadvantages, in particular regarding heterogeneous and insoluble biological systems such as membrane-embedded proteins.

Structural studies on membrane proteins (MPs) usually require prior extraction from the cell's membrane using water-soluble detergents, followed by reconstitution in lipid bilayers. As it is reported in this thesis, and reviewed elsewhere,<sup>1</sup> the integrity and properties of MPs are strongly modulated by their lipid membrane environment. For this reason, it is necessary to study such systems in physiologically relevant media to avoid capturing non-natural molecular states. As a matter of fact, the same can be applied for all other types of biomolecules. Hence, special efforts have been employed to study these systems within a native and physiological environment.<sup>2-5</sup>

Solid state nuclear magnetic resonance (ssNMR) is a technique that is able to measure MPs directly in whole lipid membranes<sup>6</sup>. In this sense, ssNMR emerges as a powerful tool for investigating challenging heterogeneous systems, not only membrane proteins, but also prions,<sup>7,8</sup> amyloids fibrils,<sup>9-16</sup> cytoskeleton filaments,<sup>17</sup> viral capsids,<sup>18,19</sup> and many disordered species that lack a crystalline lattice. Moreover, with ssNMR it is possible to probe such molecules directly in whole cells at physiochemically native conditions. Another main advantage is the ability to study atom-resolved dynamics of molecules from picosecond to second time scales that can provide very important insights about molecular mechanisms, site-resolved interactions, thermodynamics and conformational states. The work described in this thesis seeks to efficiently study membrane-embedded systems in their native or native-like membranes. To this end, we developed solid-state NMR methodologies that enable studying entire membrane proteins, including the transmembrane domains that are often inaccessible, with atomic resolution and directly in their physiologically relevant environment.

The obtained results indicate that there are important biological features that can only be appreciated when these systems are studied *in situ*, this is, directly in the cellular membrane.

The following introductory sections provide some fundamental aspects of NMR spectroscopy and related methodologies. It also provides a biological context for two systems that were studied in this thesis, namely the potassium channel KcsA and the complex of the antibiotic Nisin with lipid II.

# Nuclear Magnetic Resonance

*NMR is a type of spectroscopy*

Nuclear Magnetic Resonance (NMR) is a spectroscopic technique that provides the spin-state transition energy of a given atomic nucleus, which is denoted by

$$\Delta E = \hbar\gamma B_0 \quad (1.1)$$

where  $B_0$  is the magnitude of the external magnetic field and  $\gamma$  is the gyromagnetic ratio of the nucleus, which is an intrinsic property just like mass or charge. This particular energy typically falls within the range of radiofrequencies, which comprise the lowest frequency energy range of the electromagnetic spectrum (Figure 1 A, B). Therefore, NMR spectroscopy does not compromise the chemical integrity of a given sample.

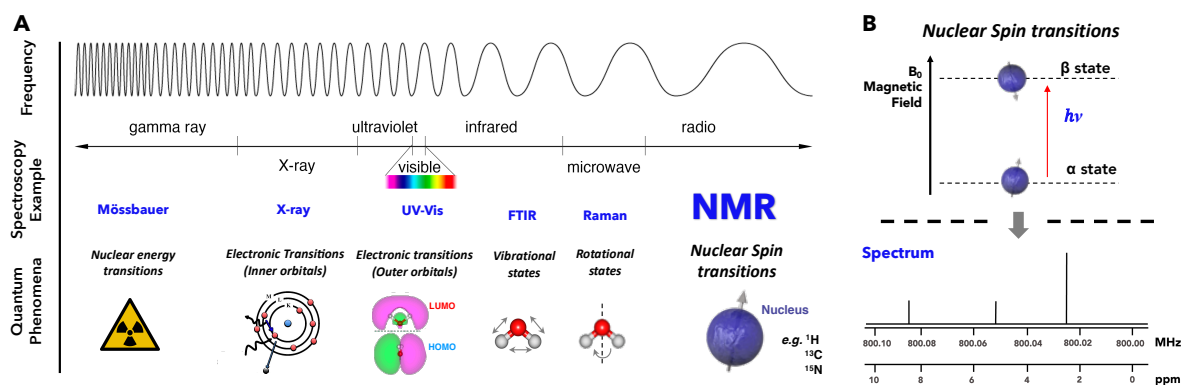


**Figure 1. A)** Electromagnetic spectrum and typical frequency range exploited by different spectroscopic techniques. The NMR phenomenon results from transitions between two nuclear spin states. Importantly, this phenomenon can only occur in nuclei that possess a spin, such as  $^1\text{H}$ ,  $^{13}\text{C}$  and  $^{15}\text{N}$ . **B)** Transitions between two spin states  $\alpha$  and  $\beta$  require the absorption of a photon in the radiofrequency range. When the system relaxes to the equilibrium state, this photon is emitted and detected to afford a typical NMR spectrum. In this case, three different nuclear spins correspond to three distinctive signals characterized by their chemical shift. Note the spectrum frequency scale is normalized to *ppm*, in order to compare spectra obtained at different magnetic fields  $B_0$ . Just like any other type of spectroscopy, an NMR spectrum (1D) is represented as a plot of wavelength/frequency range in the x-axis against the intensity of absorption/emission of a frequency in the y-axis. A 2D NMR spectrum comprises several 1D spectra that are modulated by a second frequency, and the same principle applies for other multi-dimensional spectra.

What makes NMR so useful is that the spin transition frequencies are extremely sensitive to the chemical environment. Thus, different nuclei in different chemical environments will display distinctive signals associated with a *chemical shift* (Figure 1 B). It is worth noting that the resonance frequency values depend on the magnetic field strength, whereas the relative chemical shift is independent of it. Therefore, the NMR spectra are typically normalized to *parts per million* (ppm) units (Figure 1 B) by using a reference value. This enables the comparison of results that were obtained in different NMR machines. A technical and quantum description of the NMR phenomena is beyond the scope of this introduction, and

the reader is referred to popular textbooks.<sup>20–22</sup>

### *NMR as structural technique*

NMR is a powerful tool that provides chemical and structural information at the atomic level. From a biological point of view, one of the biggest advantages of NMR is the possibility of studying proteins and other biological systems in physiological conditions. This is a key prerequisite to accurately understand the biological properties of biomolecules. It additionally allows studying very important protein dynamics and exchange processes in real time for each individual nucleus. Moreover, NMR does not require crystalline order, and it is applicable to flexible systems.

There are two types of NMR techniques for structural studies, solution state NMR and solid state NMR, that are applied depending on the system that is studied. Usually solution state NMR deals with small (< 20 kDa) soluble systems, whereas solid state NMR deals with bigger, insoluble systems. The limitations of solution state NMR are mostly due to fundamental aspects related with molecular correlation time and relaxation. To put it simply, small molecules typically result in much more resolved and sharp signals, whereas very large molecules (> 100 kDa) display signal linewidths that are broadened beyond detection. The challenges presented in this thesis deal with membrane proteins and liposomal systems that are far too large to be described using conventional solution state NMR techniques. For this reason, rather solid state NMR (ssNMR) is employed to study this type of systems, with the particular technical features introduced in the following section.

## Solid State Nuclear Magnetic Resonance

### Spin interactions in NMR

The Hamiltonian that defines the resonating energy of a nucleus is defined by the spin interaction with the external fields, i.e., the Zeeman interaction with  $B_0$ , represented in (1.1), and the excitation field  $B_1$  introduced by the r.f. coil, plus the total internal spin interactions (1.2).

$$\hat{H}_{total} = \hat{H}_{external} + \hat{H}_{internal} \quad (1.2)$$

The internal spin interactions depend on the nature of the sample and nuclei. Nuclei that possess a spin ( $I \neq 0$ ), such as  $^1\text{H}$ ,  $^{13}\text{C}$ , and  $^{15}\text{N}$ , are NMR active and behave like tiny magnets that can interact with each other. Fundamentally, these interactions can be classified in different types. The most relevant interactions for this thesis concern *chemical shift*, *J-coupling* and *dipolar coupling* that are described in Table 1.

**Table 1.** Hamiltonian descriptions for spin interactions of spins  $I$  and  $S$ .<sup>22</sup>

Spin Interaction	Hamiltonian
Chemical Shift	$\hat{H}_{cs} = \gamma_I \hat{\mathbf{I}} \cdot \boldsymbol{\sigma} \cdot \mathbf{B}_0$
Chemical Shift Anisotropy	$\hat{H}_{CSA} = \left( \omega_0 \sigma_{iso} + \frac{\omega_0 \Delta_\sigma}{2} \left[ (3 \cos^2 \theta_R - 1) - \eta_\sigma \sin^2 \theta_R \cos 2\phi \right] \right) \cdot \hat{\mathbf{I}}_z$
J-Coupling	$\hat{H}_j = J \cdot \hat{\mathbf{I}} \cdot \hat{\mathbf{S}}$
Homonuclear Dipole-Dipole Coupling	$\hat{H}_{DD} = -\frac{\mu_0 \gamma_I \gamma_S \hbar}{4\pi r_{I,S}^3} \left( \frac{1}{2} 3 \cos^2 \theta - 1 \right) (3 \hat{\mathbf{I}}_z \cdot \hat{\mathbf{S}}_z - \hat{\mathbf{I}} \cdot \hat{\mathbf{S}})$
Heteronuclear Dipole-Dipole Coupling	$\hat{H}_{DD} = -\frac{\mu_0 \gamma_I \gamma_S \hbar}{4\pi r_{I,S}^3} (3 \cos^2 \theta - 1) (2 \hat{\mathbf{I}}_z \cdot \hat{\mathbf{S}}_z)$

Definitions:  $\eta$  asymmetry parameter;  $\Delta$  anisotropy parameter;  $\omega_0$  Larmor frequency;  $\boldsymbol{\sigma}$  chemical shift tensor;  $\mu$  vacuum permeability;  $\hbar$  is the plank constant;  $J$  is the j-coupling constant;  $\theta_R$  is the angle between the tensor and  $B_0$ ;  $\theta$  is angle between the two nuclei and the magnetic field;  $r$  is the distance between the two nuclei.

Scalar coupling, also known as J-coupling, is an indirect interaction between two nuclei through the bonding electrons. This type of coupling is mediated across covalent bonds, the hyperfine interaction between the electron and the nucleus pair perturbs the energy levels of each other, typically leading to a splitting of the signal. Scalar couplings are isotropic, and present in liquids and solids. However, in ssNMR scalar couplings are often too small to be appreciated due to the large signal broadening effects from the anisotropic nature of other spin interactions.

The chemical shift, introduced in the previous section, results from the indirect interaction of the nucleus with  $B_0$  through its surrounding electrons (electron shielding). The chemical shift tensor is anisotropic and since molecules in solid state do not show overall tumbling, the anisotropy of the interaction dominates the spectrum. In the solid state, molecules adopt different orientations. Hence, each nucleus will display different resonating energies, resulting in the typical broadening of the signal (Figure 2 A,B). The resulting *powder pattern* is defined by the chemical shift anisotropy (CSA) tensor.

Two nuclei that possess magnetic moments can also interact with each other through space via their magnetic dipoles, which is known as dipolar coupling (DD). This interaction is also anisotropic and rapidly declines with the cube of the internuclear distance  $r$  ( $1/r^3$ ) (Figure 2 C). In solution, the rapid tumbling of molecules averages this interaction to zero, whereas in solids it causes major signal broadening effects due to the limited overall tumbling (Figure 2 C). Because of the strong distance dependence, dipolar couplings can be exploited as valuable interactions to determine distances between nuclei in ssNMR.

The dipolar Hamiltonian can also be expressed in polar coordinates using the respective raising and lowering operators,

$$\hat{H}_{DD} = -\frac{\mu_0 \gamma_I \gamma_S \hbar}{4\pi r_{IS}^3} (A+B+C+D+E+F) \quad (1.3)$$

where,

$$A = (3\cos^2\theta - 1) \hat{I}_z \cdot \hat{S}_z$$

$$B = \frac{1}{4} (3\cos^2\theta - 1) (\hat{I}^+ \cdot \hat{S}^- + \hat{I}^- \cdot \hat{S}^+)$$

$$C = \frac{3}{2} (\sin\theta \cos\theta e^{-i\phi}) (\hat{I}_z \cdot \hat{S}^+ + \hat{I}^+ \cdot \hat{S}_z)$$

$$D = \frac{3}{2} (\sin\theta \cos\theta e^{-i\phi}) (\hat{I}_z \cdot \hat{S}^- + \hat{I}^- \cdot \hat{S}_z)$$

$$E = \frac{3}{4} (\sin^2\theta e^{-2i\phi}) (\hat{I}^+ \cdot \hat{S}^+)$$

$$F = \frac{3}{4} (\sin^2\theta e^{-2i\phi}) (\hat{I}^- \cdot \hat{S}^-)$$

It is worth mentioning that only operator A survives the secular approximation for heteronuclear dipolar couplings. In the homonuclear case, the energy levels between nuclei are similar (i.e. degenerate), consequently the B operator must be considered in the secular approximation.

*Magic Angle Spinning – the faster the better*

The NMR spectra of static solids, or molecules that tumble very slowly, are dominated by the CSA and DD effects that dramatically broaden the signals. The CSA and DD Hamiltonians (Table 1) depend on the molecular orientations in the form of  $(3 \cos^2 \theta - 1)$ , where  $\theta$  is the angle between the orientation of the anisotropy tensor and  $B_0$  (Figure 2 A). Spectroscopists go around the resolution problem with a technique called *Magic Angle Spinning* (MAS). The *magic angle* term refers to the tilt angle of the sample container (i.e. rotor) relative to the magnetic field  $B_0$  at  $\theta_R = 54.74^\circ$ . The term *spinning* refers to the physical spinning of the rotor, meaning the angle  $\theta$  of the tensor (Figure 2 A) varies with time as the molecules rotate with the rotor. If the rotor is spun fast enough compared to the interaction anisotropy the angle  $\theta$  averages to  $\theta_R = 54.74^\circ$ , at which  $(3 \cos^2 54.74 - 1) = 0$ . As a result, CSA and DD can be averaged to their isotropic values, thereby increasing the resolution and sensitivity of the spectrum (Figure 2 B). In the homonuclear DD case, however, such as  $^1\text{H}$ - $^1\text{H}$  couplings, the energy states of the nuclei are degenerate due to the presence of the operator  $B$  (eq. 1.3) that relates to zero quantum transitions. Thus, the coupled spin states are constantly changing over time through zero quantum transitions at rates proportional to DD. The time-dependency of the spin systems leads to an inefficient averaging of the DD couplings with MAS. For  $^1\text{H}$ - $^1\text{H}$  couplings, spinning frequencies over hundreds of kHz would be necessary to efficiently average this type of interaction, but this is very difficult from a technical perspective. It is interesting to note that higher  $B_0$  fields reduce the degeneracy of homonuclear energy levels, therefore high magnetic fields are advantageous for removing  $^1\text{H}$ - $^1\text{H}$  dipolar couplings.

*The sensitivity/resolution issue and  $^1\text{H}$  detection*

One of the main challenges in this thesis focuses on measuring protein complexes in their native cellular conditions. This usually implies very low copy numbers of target molecules which are embedded in a complex and heterogeneous environment. Hence the sensitivity of the NMR measurements is absolutely crucial for the success of the study. We are thus compelled to gather all the means to maximize sensitivity, both from the sample preparation and NMR methodologies. In the present work we employed signal enhancement NMR techniques such as  $^1\text{H}$  detection and dynamic nuclear polarization, introduced as follows.

The intensity of a signal that is obtained by NMR depends on several factors. Fundamentally, the maximum signal detected is proportional to the external field ( $B_0$ ), temperature ( $T$ ) and gyromagnetic ratio ( $\gamma$ ), as given by the Boltzmann population difference between the ground energy state  $\alpha$  and the excited state  $\beta$ ,

$$\frac{n_\beta}{n_\alpha} = e^{\frac{-B_0\gamma\hbar}{T}} \quad (1.4)$$

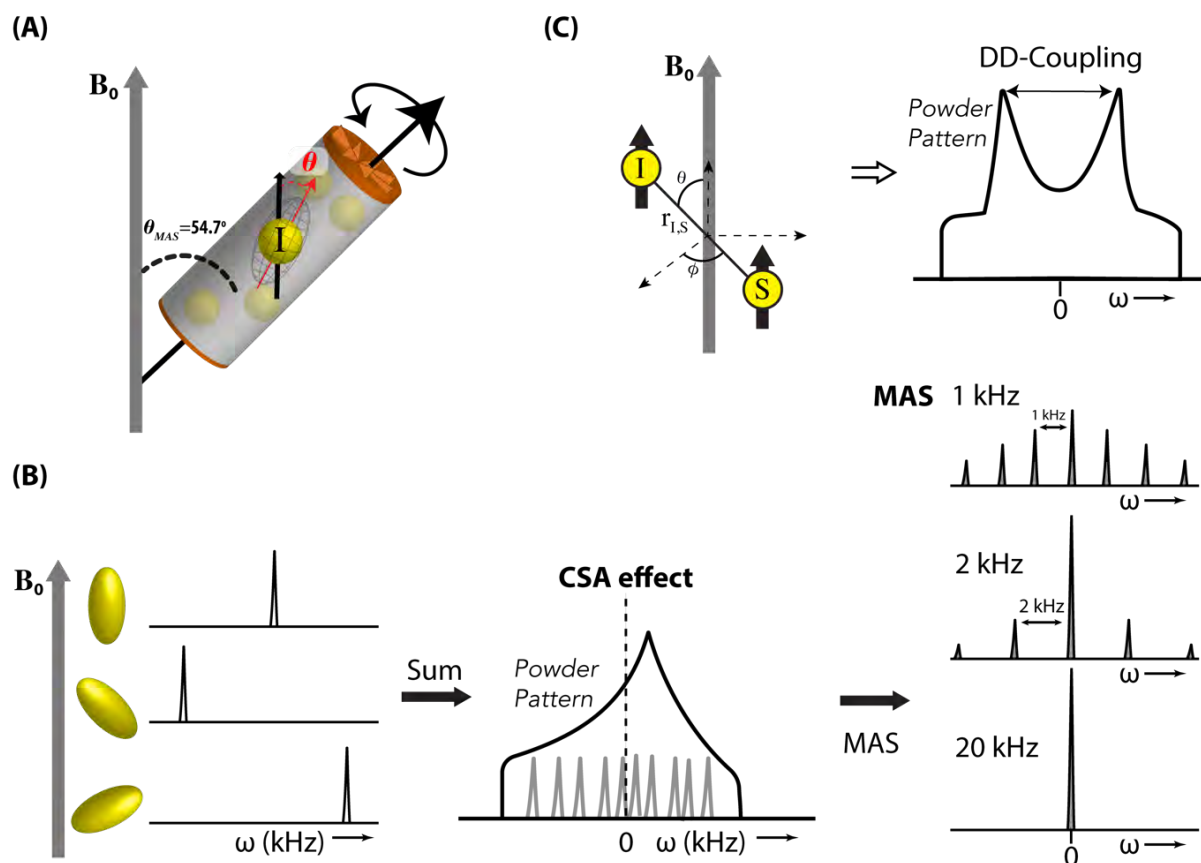


**Figure 2.** A) Schematic representation of magic-angle spinning. A rotor containing the sample rotates at high speed (several kHz) with a tilt angle of  $54.74^\circ$  with respect to the external  $B_0$  field. In solids, molecules adopt several orientations that define the second rank tensors (CSA and DD) at an angle  $\theta$  with respect to the  $B_0$ . This angle averages to the magic angle under high speeds. B) Illustration of the CSA effect and the effect of MAS on a spin  $\frac{1}{2}$  nucleus. When the MAS frequency is lower than the CSA interaction, the signal is split into sidebands separated by the MAS frequency, whereas the sidebands collapse under an isotropic peak when MAS greatly exceeds CSA. C) The strength of the dipolar coupling depends on the distance between two nuclei, in the form of  $1/r^3$ , and their orientation relative to the  $B_0$ . The resulting effects broadens the NMR signal to an extent proportional to the dipolar coupling magnitude, which is in the order of tens of kHz.

Accordingly, the signal intensity increases with higher magnetic fields and higher gyromagnetic ratios. Protons represent the nuclei with the highest  $\gamma$  for biological NMR, specifically  $\gamma(^1\text{H}) \approx 4 \times \gamma(^{13}\text{C}) \approx 10 \times \gamma(^{15}\text{N})$ . However, the  $^1\text{H}$  dimension displays very broad signals due to the strong homonuclear dipolar couplings, which are prominent nuclei in biological samples and render the direct detection of protons a challenge. This is why ssNMR predominantly used  $^{13}\text{C}$  and  $^{15}\text{N}$  detection in the past.

An alternative route to take advantage of the high  $\gamma(^1\text{H})$  uses a method named cross polarization (CP, Figure 3 A).<sup>23</sup> The CP method is a landmark in ssNMR. In simple words, it transfers the magnetization pool from  $^1\text{H}$  to a X nucleus ( $^{13}\text{C}/^{15}\text{N}$ ), via zero-quantum transitions, when both nucleus are irradiated at the same time at frequencies that fulfill the

Hartmann-Hahn condition<sup>24</sup>

$$\omega_X = \omega_{^1\text{H}} \pm n\omega_{\text{MAS}}, \text{ with } n=(1,2) \quad (1.5)$$

An additional advantage of CP is that the  $T_1$  relaxation time (i.e., how fast magnetization returns to equilibrium) also depends on protons, which have significantly shorter  $T_1$  than  $^{13}\text{C}$  or  $^{15}\text{N}$ , thus the experiments can be repeated more frequently improving the signal-to-noise ratio (S/N).

Following this perspective, one can even use the electron polarization to achieve much higher enhancements since the  $\gamma(e)$  is 658 times larger than  $\gamma(^1\text{H})$ . This principle is exploited by a technique called Dynamic Nuclear Polarization (DNP).<sup>25,26</sup> Briefly, it uses a gyrotron that generates microwaves which are used to irradiate the sample. The sample buffer contains small amounts of a tailored bi-radical molecule, e.g. AMUPol<sup>27</sup>, that acts as an antenna receiving the microwaves that polarize its unpaired electrons (Figure 3 B). The magnetization can be transferred from the electrons to the nuclei via the cross-effect<sup>28</sup> when,

$$\omega_{e1} \pm \omega_{e2} = \omega_{\text{Nucleus}} \quad (1.6)$$

The efficiency of this exchange mechanism is modulated by MAS. The resulting signal enhancement obtained by DNP is truly revolutionary, to a point where it enables studying proteins in intact cells; applications that were otherwise impossible.<sup>29–32</sup> However, DNP requires freezing the sample to cryogenic temperatures (<100 K), and freezing protein samples to this degree comes with a great cost in resolution as it generates large conformational heterogeneity and shortens transverse relaxations times, extensively broadening the NMR signals. Therefore, DNP represents a trade-off between resolution and sensitivity.

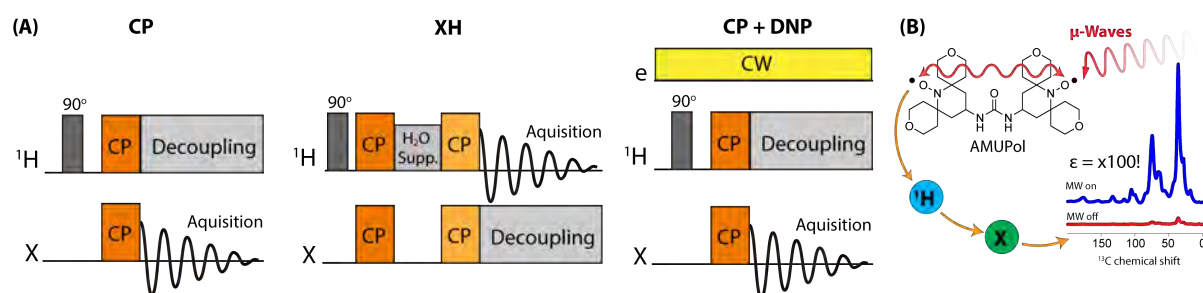


**Figure 3.** **A)** Representation of standard NMR pulse programs used in X-nucleus detected CP and  $^1\text{H}$ -detected CP. In DNP experiments, the sample is continuously irradiated with microwaves. **B)** Schematic representation of the DNP mechanism. Microwaves polarize the unpaired electrons of the radical (electron paramagnetic resonance), which was tailored with a specific spacing between radical groups. Cross-effect mechanisms transfer the magnetization to protons where spin diffusion spreads the magnetization in the sample. A CP step then transfers the magnetization from protons to carbons, resulting in a signal enhancement of up to two orders of magnitude.

With the advent of ultra-fast spinning MAS probes ( $> 60$  kHz),  $^1\text{H}$  detection also emerges as an effective technique to acquire signals with great sensitivity.<sup>33,34</sup> Assuming the sample and the physical conditions are equivalent, the comparison between sensitivity gains per unit of time of X and  $^1\text{H}$  detection can be represented as<sup>35,36</sup>

$$\frac{\text{S/N } (^1\text{H})}{\text{S/N (X)}} = \frac{f_{CP}}{\sqrt{2\kappa}} \sqrt{\left(\frac{\gamma_{^1\text{H}}}{\gamma_X}\right)^3} \sqrt{\frac{Lw_X}{Lw_{^1\text{H}}}} \sqrt{\frac{Q_{^1\text{H}}}{Q_X}} \quad (1.6)$$

where  $f$  is the CP polarization transfer efficiency,  $\kappa$  and  $Q$  are related to amplifier and probe quality specifications,  $Lw$  is the linewidth of the signal at half maximum and  $\gamma$  the gyromagnetic ratios. In a hand-waving approximation, provided that the signal linewidths and the other factors are comparable, the enhancement factor boils down to  $\left(\frac{\gamma_{^1\text{H}}}{\gamma_X}\right)^{\frac{3}{2}}$ , which is a factor 8 and 31 compared to  $^{13}\text{C}$  and  $^{15}\text{N}$  detected experiments, respectively. Moreover,  $^1\text{H}$  detection at fast MAS does not require high-power decoupling, which prevents sample heating and thereby enables recording experiments with more scans over time.

Other than sensitivity gain, protons are also very valuable and sensitive probes for chemical environment as they can account for different conformations, H-bonds, intermolecular interactions and topology (H/D exchange). Protons also aid the assignment of protein residues, structure calculation, and are important reporters of dynamics on the nanosecond to millisecond time scale.

Still, the  $^1\text{H}$  spectral resolution is quite problematic due to the severe effects of homonuclear couplings over the narrow chemical shift range in the  $^1\text{H}$  dimension. Many efforts have been employed to attenuate or remove the effect of the DD couplings, such as improved decoupling sequences,<sup>37,38</sup> ultra-fast MAS speeds<sup>39,40</sup> and deuteration schemes.

The most straightforward strategy to remove the DD coupling would be spinning the sample at much higher frequencies than the magnitude of anisotropy, but such speeds are extremely challenging due to physical and technical limitations. At the time of writing, MAS speeds of 111 kHz are now achievable with commercially available hardware,<sup>40</sup> but since higher speeds equals less sample, this feat might result in overall lower sensitivity due to the miniscule amount of sample measured (rotor volume of  $0.37 \mu\text{l}$ <sup>41</sup> for a 0.7 mm rotor, see general rotor properties in S1). For applications involving dilute samples, such as membrane proteins in liposomes or in their native milieu, the signal reduction may be impracticable.

For this reason, often the  $^1\text{H}$  dipolar couplings are rather attenuated via a chemical approach that replaces some of the protons by deuterium atoms. This strategy can confer a dramatic improvement in resolution, while further improving the sensitivity of the remaining  $^1\text{H}$ .

## Deuteration strategies

### Breaking $^1\text{H}$ - $^1\text{H}$ networks

Deuterium ( $^2\text{H}$ , or D) is an isotope of hydrogen with a quadrupolar spin ( $I=1$ ) and  $\gamma(^2\text{H}) \approx \gamma(^1\text{H})/6.5$ . Compared to  $^1\text{H}$ - $^1\text{H}$  dipolar couplings,  $^2\text{H}$ - $^1\text{H}$  couplings are much weaker (ca. 10-fold) and the DD interaction becomes time-dependent, therefore these couplings can be effectively averaged-out by MAS.

Biological systems, such as proteins, are very rich in  $^1\text{H}$  nuclei that inherently form extensive networks of dipolar-coupled protons, rendering  $^1\text{H}$  detection impractical due to the signal broadening effects. For this reason, several deuteration strategies have been developed, particularly for proteins, in order to replace some of the  $^1\text{H}$  nuclei by  $^2\text{H}$  and dilute the coupling networks, thereby increasing the resolution of the remaining protons (Figure 4).

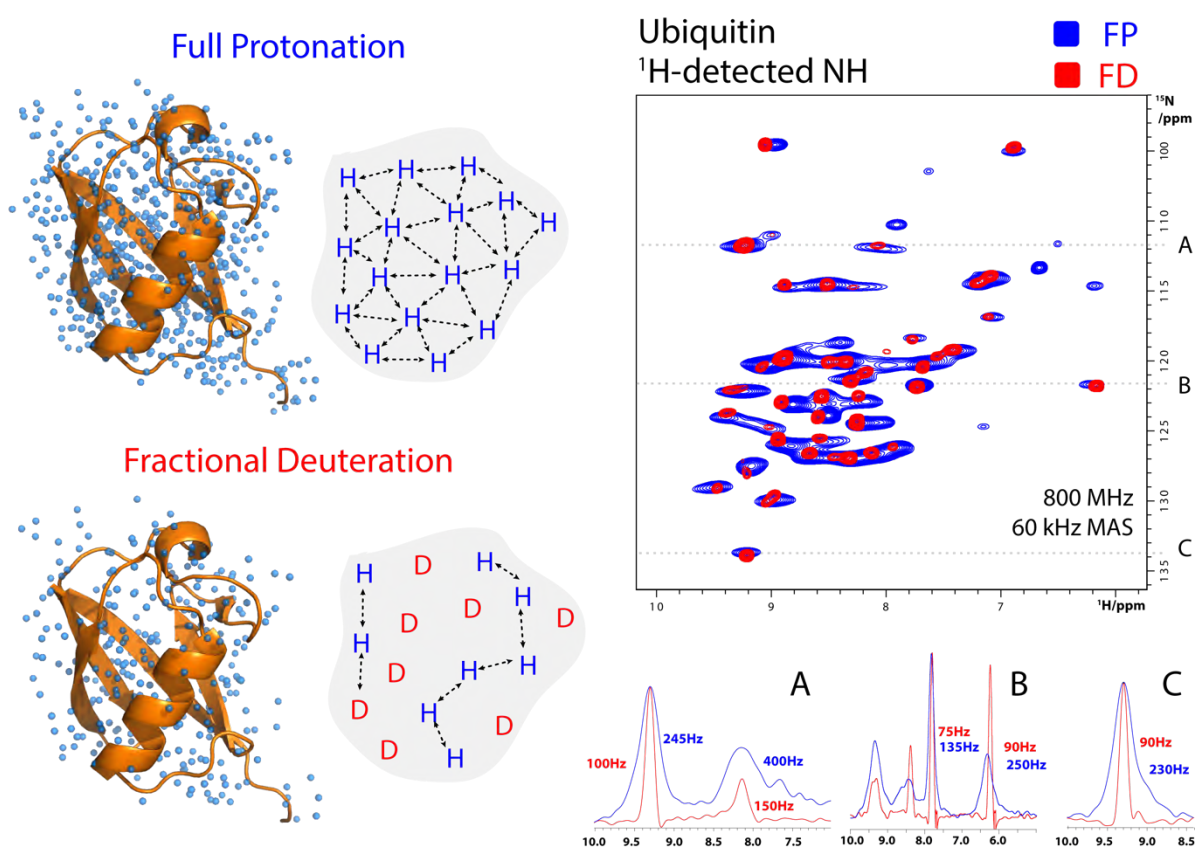


**Figure 3.** Illustration of the  $^1\text{H}$ -density (blue spheres) in fully protonated and fractionally deuterated ubiquitin. Deuteration dilutes the  $^1\text{H}$ - $^1\text{H}$  coupling networks, resulting in much better resolved signals with narrower linewidths.

Perdeuteration<sup>42</sup> is a classic deuteration strategy that requires complete deuteration of the protein and subsequently reintroduction of labile protons (i.e. NH), after  $^1\text{H}$  back-exchanging

with the solvent. The resulting  $^1\text{H}$  spectral resolution is very attractive, but there are many inherent drawbacks with this approach: first, it only provides insight into the amide  $\text{H}^{\text{N}}$  groups, hence critical structural information on aliphatic protons is absent; second, attaining the solvent-inaccessible  $\text{H}^{\text{N}}$  groups would require troublesome denaturation/refolding procedures, which are especially problematic for membrane proteins; third, the kinetic isotope effect of deuterium hampers the cell metabolism<sup>43–46</sup> resulting in slower or no growth, therefore this procedure is associated with very high costs for low sample yields. Furthermore, such levels of deuteration are not applicable to eukaryotic cells. Over the years, several alternative labelling schemes (Table 2) have been developed to better suit the requirements of a particular system, such as Fractional Deuteration<sup>47</sup>, Proton Clouds<sup>48</sup> and Reduced Adjoined Protonation<sup>49</sup>. Analogous to perdeuteration, these labelling schemes involve a compromise between sensitivity, resolution, and the type of protons probed. Therefore the best deuteration strategy will depend on the target protein, instrumentation and the purpose of the study.

**Table 2.** Comparison between labelling schemes for  $^1\text{H}$  detection studies.

Labelling Scheme	Full Protonation	Per-deuteration	Fractional Deuteration	Reduced Adjoined Protonation	ILV Methyl Labelling	Proton Clouds	SAIL*
<b>Carbon Source</b>	U[ $^{13}\text{C}$ , $^1\text{H}$ ] glucose	U[ $^{13}\text{C}$ , D] glucose	U[ $^{13}\text{C}$ , $^1\text{H}$ ] glucose	U[ $^{13}\text{C}$ , D] glucose	U[ $^{12}\text{C}$ , D] glucose/ [3- $^{13}\text{CH}_3$ , D <sub>n</sub> ]- - $\alpha$ -ketoisovalerate - $\alpha$ -ketobutyrate	U[ $^{12}\text{C}$ , D] glucose/ U[ $^{13}\text{C}$ , $^1\text{H}$ ] aminoacids	SAIL- aminoacids
<b>Medium</b>	100% $\text{H}_2\text{O}$	100% $\text{D}_2\text{O}$	100% $\text{D}_2\text{O}$	85-95% $\text{D}_2\text{O}$	100% $\text{D}_2\text{O}$	100% $\text{D}_2\text{O}$	0-100% $\text{D}_2\text{O}$
<b><math>\text{H}^{\text{N}}</math></b>	yes	$\text{H}_2\text{O}$ exposed	$\text{H}_2\text{O}$ exposed	random	$\text{H}_2\text{O}$ exposed	$\text{H}_2\text{O}$ exposed	specific
<b><math>\text{H}^{\alpha}</math></b>	yes	no	no	random	No	no	specific
<b><math>\text{H}^{\text{sidechain}}</math></b>	yes	no	partial	partial	I,L,V	specific	specific
<b>Reference</b>		[12,13,52]	[47]	[49]	[53]	[48]	[54,55]

\*SAIL – Stereo-Array Isotope Labelling, partially-deuterated aminoacids are included in the medium, the deuteration pattern will depend on the protein production method because it typically requires cell-free expression systems.

### What about solvent-inaccessible systems?

The resolution-enhancing labelling methods described in Table 2, except for SAIL, rely on protein expression in extensively or fully deuterated media with a subsequent solvent back-exchange step in order to detect NH groups. This approach inherently comes with two main disadvantages. The first disadvantage is the organism's incompatibility to deuterium due to the isotope kinetic effect, which reduces expression yields or even stops growth, especially for eukaryotic cell lines. The second disadvantage is that only solvent-exposed NH groups are accessible, while the solvent-inaccessible remain invisible. The latter is an issue for systems

that are less prone to H/D exchange such as amyloid fibrils and viral capsids<sup>56</sup> and is especially problematic for systems that cannot undergo refolding-folding procedures such as membrane proteins (Figure 4) and large globular proteins. These systems have thus to rely on full protonation that in the end might not provide enough resolution to characterize them. Chapter 2 tackles these issues with the development of a H<sub>2</sub>O-based deuteration method.

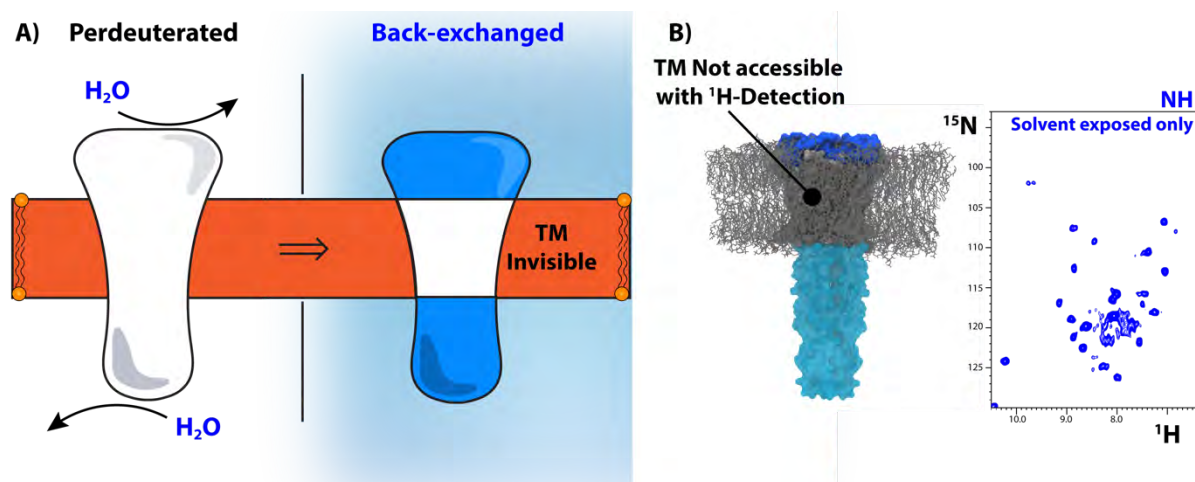


**Figure 4.** A) Available deuteration methods rely on back-exchange to reintroduce exchangeable protons into the systems, hence studies on transmembrane domains of membrane proteins become severely hampered. B) NH protons are important reporters of the state and conformation of the protein.

### *E. coli* aminoacid anabolism

The development of these meticulous labelling schemes requires an intimate understanding of the aminoacid metabolism from the host expression system, which corresponds to *E. coli* for the majority of cases. *E. coli*'s metabolic paths can be found in several comprehensive databases.<sup>57,58</sup> When glucose is the only carbon source available, the labelled aminoacid precursors are generated via three major metabolic pathways: glycolysis, tricarboxylic acid cycle (TCA) and pentose phosphate. Glycolysis directly provides the precursors for nearly half of all aminoacids, the pentose phosphate cycle provides precursors for the aromatic aminoacids, and the remaining aminoacids are derived from oxaloacetate and  $\alpha$ -ketoglutarate produced in the TCA cycle (Figure 5 A). It should be noted that all H $^{\alpha}$  groups are imported from the solvent during the transamination reaction (Figure 5 B). The protonation/deuteration patterns at the sidechain positions are however more complex to rationalise, in part due to the generation of oxaloacetate via two distinct routes that result in different degrees of deuteration (isotopomers) at the C3 position<sup>45</sup> (Figure S2). Nonetheless, in a general view, aminoacid precursors derived from glycolysis will retain higher levels of <sup>1</sup>H or D from the carbon source (glucose) at their sidechains, whereas TCA is prone to scramble the <sup>1</sup>H or D with the solvent.<sup>45</sup> For such cases, the aminoacid scrambling pathways and a detailed catabolism routes are discussed in recent reviews.<sup>41,59</sup>

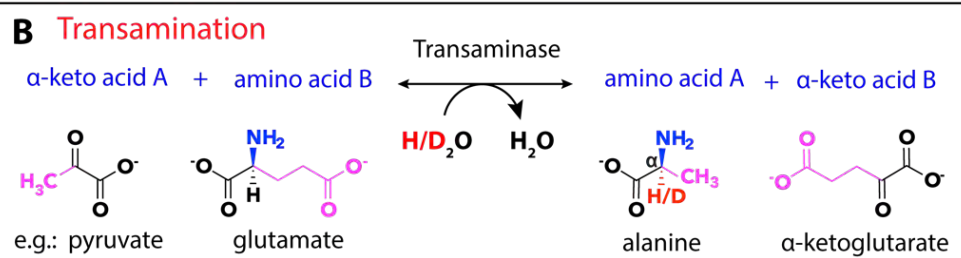
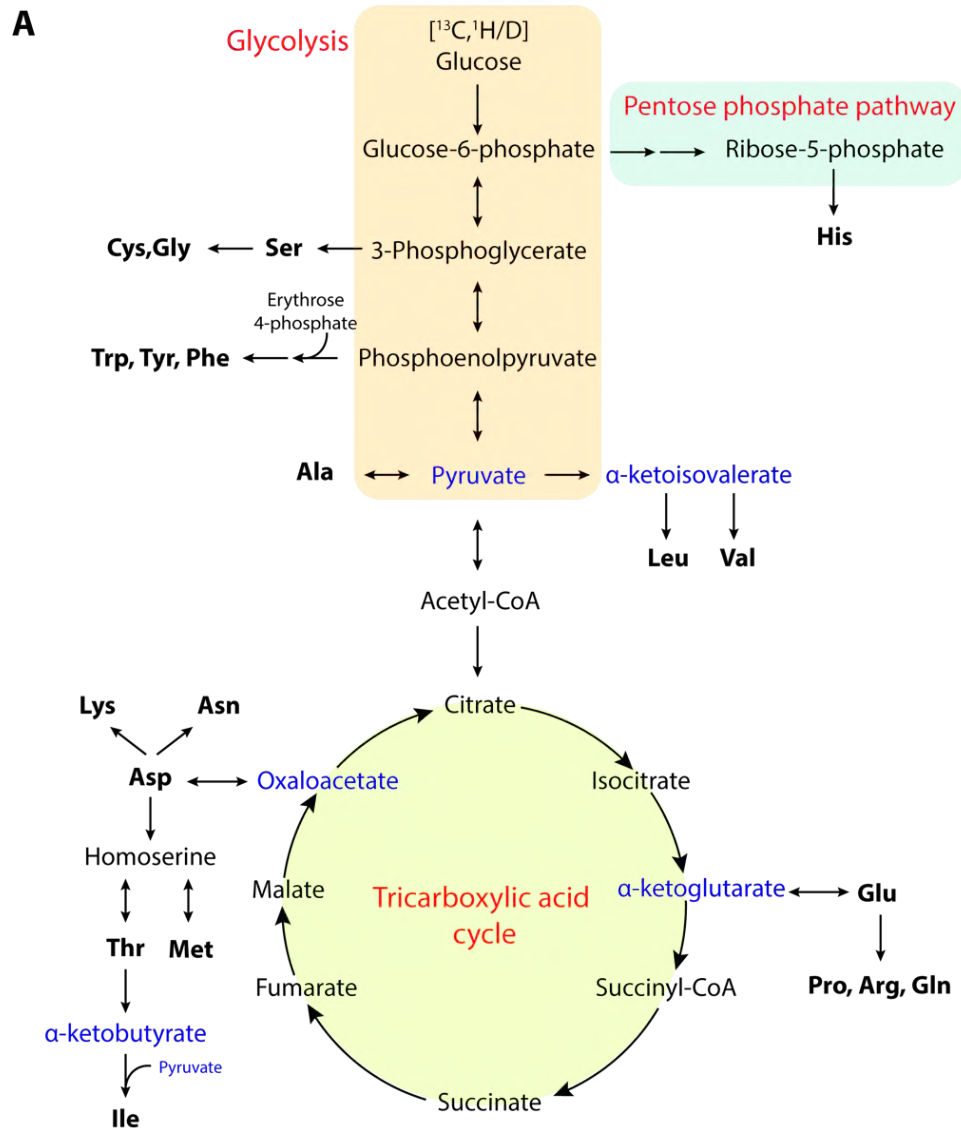


**Figure 5.** The simplified metabolic pathways for amino acid synthesis from glucose in *E. coli*.  $\alpha$ -keto acids are highlighted in blue. Adapted from reference.<sup>60</sup>

The second chapter of this thesis consists on the design of a new deuteration labelling scheme, called inverse Fractional Deuteration, which was applied to the potassium channel KcsA.

## The potassium channel KcsA

### *K<sup>+</sup> channels regulate the flow of potassium across membranes*

Potassium channels are membrane proteins that regulate the transport of potassium ions (K<sup>+</sup>) across the lipid membrane<sup>61,62</sup>. K<sup>+</sup> channels are present in almost all living organisms and play vital roles in essential cellular processes such as the regulation of cell homeostasis<sup>63</sup>, membrane potential<sup>64</sup> and electrical signalling<sup>65</sup>. In mammals, these proteins enable electrical conduction in excitable cells, i.e., neurons, muscle cells and endocrine cells<sup>63</sup>, thus malfunctions in K<sup>+</sup> channels are connected to a wide range of medical conditions (*channelopathies*<sup>66</sup>) such as low blood pressure, heart failure<sup>67</sup>, arrhythmia,<sup>68,69</sup> deafness,<sup>70</sup> epilepsy<sup>71</sup> and neurological<sup>72,73</sup> and mental<sup>74</sup> disorders. In order to carry their biological functions out, K<sup>+</sup> channels are able to retain both extreme ion specificity and throughput of ca. 10<sup>8</sup> ions/s, i.e. close to the aqueous diffusion rate limits<sup>63,75–77</sup>, while being tightly regulated with gating mechanisms. The fundamental features and medical relevance of K<sup>+</sup> channels prompted researchers to a multitude of structural and functional studies that resulted in one Nobel prize<sup>78</sup> and still carries on to this date. Most of these studies were carried out on KcsA<sup>79</sup> which is a representative, robust and very accessible potassium channel.

### *KcsA as a role model K<sup>+</sup> channel*

KcsA is a prokaryotic channel from *Streptomyces lividans*<sup>80</sup> and it is generally seen as a role-model for the function and structure of the pore-domain of K<sup>+</sup> channels (Figure 6 A,B).<sup>61</sup> KcsA forms a homo-tetrameric complex, each monomer includes two transmembrane helices (thus a 2TM type) that gate the channel via a pH sensor domain,<sup>81</sup> in contrast to more complex voltage-gated channels (6TM) found in humans such as KCNQ channels<sup>82</sup>. Although various K<sup>+</sup> channels display different structural features, the pore domain is remarkably well conserved in all known channels, namely the filter sequence TVGYG is tightly conserved across the three domains of life (Figure 6 C).<sup>83</sup> The filter architecture has then evolved to finely tune its chemical and structural properties in order to specifically favour the passage of potassium.<sup>63</sup> In detail: the backbone carbonyl groups of the filter adopt an arrangement that mimics the solvation configuration of K<sup>+</sup> in water, thus minimizing the energy barrier penalty<sup>77</sup>; water molecules in the channel water cavity promptly coordinate with K<sup>+</sup> once they exit from the filter; the diameter of the filter and spacing between carbonyl cages fit exactly the necessary diameters for K<sup>+</sup> without binding too tightly; and finally the negative dipole of the surrounding pore helices point directly to the centre of the cavity to help counterbalance the positive charge.<sup>84</sup> The transport of ions is however subject to complex regulating mechanisms described in the next section.

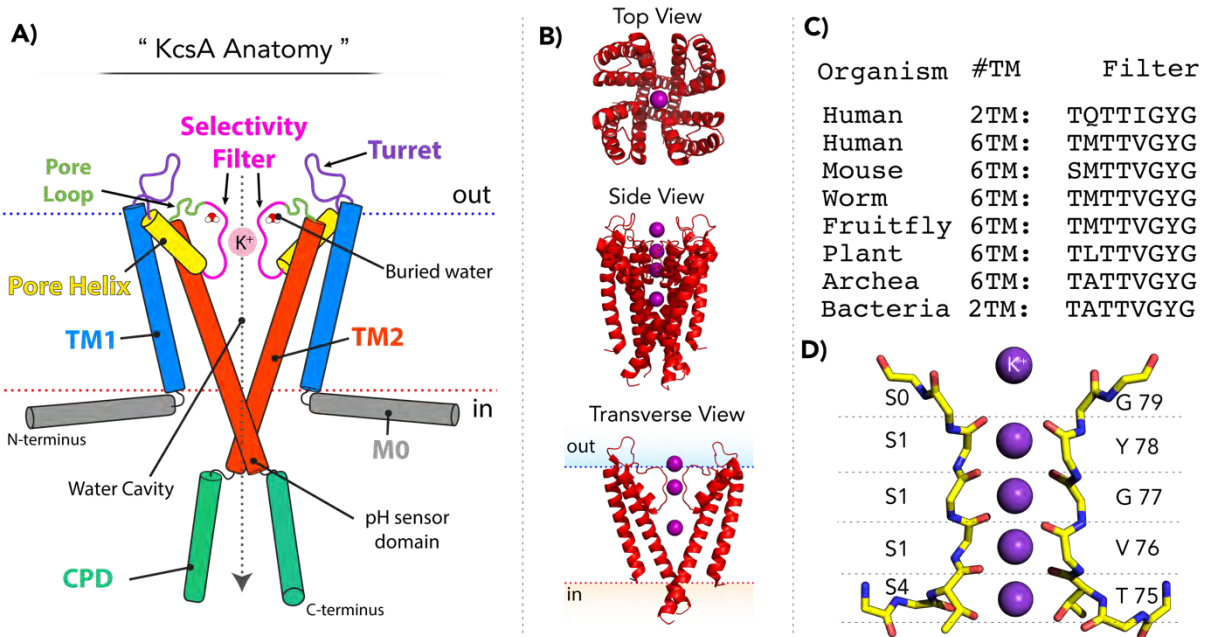


**Figure 6. A)** Nomenclature for the KcsA domains (closed state representation). The KcsA monomer is composed of two transmembrane  $\alpha$ -helices, outer helix TM1 and inner helix TM2, one turret loop in the extracellular region, one pore  $\alpha$ -helix and one filter domain. The filter and TM2 also control the flow of ions by a set of conformational changes, which represents gating. These changes can be regulated via the pore helix and the pH sensor domain of TM2.<sup>81,85</sup> The buried water behind the filter is also important for H-bond networks that regulate the filter conformation.<sup>86</sup> Note that the pore loop (shortened to P-loop) technically includes the selectivity filter of the channel, although often they are viewed as separate entities. The M0 helix is mainly responsible for membranar lipid interactions<sup>87</sup> and clustering of channels.<sup>88</sup> The cytoplasmatic domain (CPD) is quite flexible and is not deeply characterized, but appears to facilitate gate activation.<sup>85</sup> **B)** KcsA forms a tetramer. The upper panel is a top view, middle panel a side view and in the lower panel a transverse section of the complex. Obtained from PDB structure 1K4C,<sup>89</sup> closed conductive conformation. **C)** The filter signature sequence, 74-TTVGYG-79 in KcsA, is highly conserved among  $K^+$  channels, pointing to a very specific architecture. Alignment from reference.<sup>78</sup> **D)** The filter arrangement forms 4 polar oxygen cages that coordinate with potassium. Potassium ions sequentially translate from positions S0 to S4 separated by a water molecule, i.e.  $[K^+-w-K^+-w-K^+]$  or  $[w-K^+-w-K^+-w]$ .<sup>77,90</sup>

### Modal Gating at the filter

The  $K^+$  flux in KcsA is finely regulated by an interplay of sophisticated *gating* mechanisms. KcsA presents two gates that can be regulated independently, a lower gate that lies at the TM2 helix and is modulated by pH, and an upper gate that lies at the selectivity filter and is modulated by the pore domains (Figure 7 A, B). At neutral-basic pH values the lower gate is closed, impeding the flux of  $K^+$ , whereas at acidic pH values  $\approx 4$  the gate is opened allowing passage of ions (Figure 7 B).<sup>81</sup>

The upper gate regulates the kinetics of the passage of  $K^+$  through the channel in a time-depend manner. Typically, it conducts ions for a short period of time before reaching an inactive state that halts the flow; it then recovers to an active state and restarts the process in a cyclic fashion (Figure 7 A,C).<sup>91</sup> The inactivation process is termed C-type inactivation, and it is partially triggered by a reduction of  $K^+$  occupancy at the filter binding sites.<sup>92</sup> Remarkably,

it was observed that the bursts of  $K^+$  conductance are not kinetically equivalent. In fact, over time KcsA displays at least three different kinetic behaviors that are randomly manifested. The different burst patterns are termed *modal gating*, and can be classified according to the mean time of open/closed state:<sup>93</sup> modes with high open probability (high  $P_o$ ) where the mean open time is c.a. 100 ms, modes with low open probability (low  $P_o$ ) where the mean open time is c.a. 10 ms and a rapidly changing mode (flicker) with a mean open time of  $<1$  ms. Several other channels also display similar modal gating features that likely have specific implications for their physiological functions.<sup>94-96</sup>

Studying modal gating in ion channels is however very challenging, and the structural underpinning of modal gating is largely unknown. Nonetheless, it was discovered that point-mutations at residue E71 in the pore-helix result in discrete kinetic gating modes that correspond to those observed in wild-type KcsA. Hence, mutant E71A lock the channel in the high  $P_o$  state, mutant E71I represents the low  $P_o$  and mutant E71Q mimics the flickering state. Moreover, it was observed that these mutants either reduce or block C-type inactivation, and their kinetic behavior is not modulated by the lower gate.<sup>97</sup>

Although it is known the filter gating in KcsA is modulated by hydrogen bond networks behind the filter, the underlying molecular correlates responsible for the modal gating shifts were poorly understood. With the advancements in high-resolution ssNMR, and using the methods presented in Chapter 2, modal gating of KcsA was addressed in the Chapter 4 of this thesis.

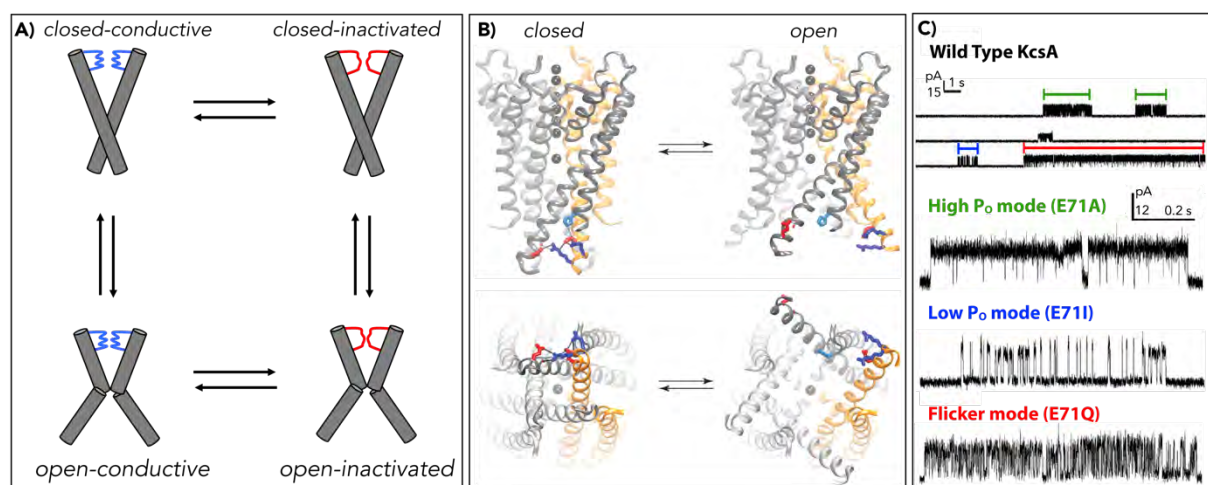


**Figure 7.** **A)** The gating cycle of KcsA. The lower gate can be in the open/closed conformation depending on the pH. The upper gate is formed by the filter (conductive/inactivated) and is regulated by the pore domains in a time-dependent manner. In WT KcsA, the inactivated state dominates over rather long periods of time (seconds) with bursts of activity in the conductive state (milliseconds) with variable kinetics. **B)** At  $pH > 5$  the TM helices bundle together blocking the passage of ions. At low  $pH \approx 4$ , charged residues E118 (red), E128 (red), H25 (cyan), R121 (blue) and R122 (blue) become protonated and the existing inter H-bond between TM1 and TM2 helices are broken, resulting in a kink of the TM2 helix that opens the channel. Image adapted from reference.<sup>81</sup> **C)** (Top) Representation of the modal gating behavior in KcsA with single channel currents under steady-state conditions,  $pH 3$  (lower gate open) and  $+150$  mV in  $200$  mM  $K^+$ . (Bellow) Dissection of each gating mode with the respective E71 mutant. Figure adapted from reference.<sup>97</sup>

## Lipid II binding antibiotics

### *An Urgent Need for New Antibiotics*

Antibiotics are the bedrock of modern medicine and the world is running out of these magic bullets at a dramatic pace. To date, antimicrobial resistance (AMR) has been observed against all clinically used antibiotics.<sup>98</sup> The rapid and global emergence of AMR, which is forecast to cause a staggering 10 million human deaths annually by the year 2050,<sup>99</sup> entails severe repercussions for public healthcare systems. At present, according to a recent extensive investigation, the healthcare burden of AMR in the European Economic Area (EEA) is already on a par with the combined effect of influenza, HIV, and tuberculosis, and about 33 000 people in the EEA die as a consequence of AMR every year.<sup>100</sup> Likewise, AMR is estimated to cause costs of billions of euros for the European economy.<sup>101</sup> To make things worse, the industry's drug-discovery pipeline for antibiotics is almost empty. It is hence of pressing need to develop new antibiotics that target unexploited pathways and that are robust to the development of resistance mechanisms. This has led to an increased interest in unconventional agents such as naturally occurring antimicrobial peptides (AMPs), against which bacteria have enormous difficulty in building up effective resistance mechanisms.

An especially interesting class of AMPs that target Lipid II, the precursor of the bacterial peptidoglycan (PGN) network,<sup>102,103</sup> are able to kill even the most refractory bacteria at nanomolecular concentrations. Especially AMPs that bind to the pyrophosphate motif of Lipid II are less prone to develop resistance mechanisms, since this motif is irreplaceable, hence Lipid II has been regarded as a hot target for development of new antibiotics.<sup>102,104</sup>

### *Lipid II – the Achilles' heel of bacteria*

Every bacterium is surrounded by a PGN network, a protective hull that is essential for its survival. To ensure cell viability, growth, and division, PGN biosynthesis must be tightly regulated. The PGN network is composed of strands of alternating N-acetylmuramic acid and N-acetylglucosamine (MurNAc–GlcNAc) disaccharides that are linked through *pentapeptide bridges*. The PGN building blocks are synthesized in the cytosol of the bacteria which are then imported to the periplasm region via the membrane-anchored lipid II that carries one complete PGN subunit linked through a pyrophosphate group to a C55 poly-isoprenoid moiety (Figure 8 A and S3). However, lipid II only exists in very low copy numbers, and it is constantly recycled through the so-called lipid II cycle to ensure efficient PGN synthesis. This implies that any drug that sequesters lipid II, and thereby stalls the PGN synthesis, is a potential antibiotic.<sup>102,104,105</sup> In the case of Gram-positive bacteria the plasma membrane is readily accessible from the outside, so certain peptides can exploit this weak spot and

specifically bind lipid II at its pyrophosphate group.<sup>106</sup> This is a unique mode of action that kills even highly resistant super-bugs such as methicillin-resistant *Staphylococcus aureus* (MRSA) at nanomolar concentrations, and against which resistance is difficult to acquire because the lipid II structure is highly conserved and the pyrophosphate group is irreplaceable.<sup>102</sup> In addition, since human cells do not produce lipid II, it is a target with low risk of unwanted toxicity. Peptides that bind lipid II could hence be promising templates for next-generation antibiotics. However, detailed structural information on their modes of action is critically required in order to develop these peptides into clinically applicable drugs. In this thesis, the ssNMR methods described in the previous section were employed to explore quantitative peptide – lipid II interactions, on the example of nisin, with high structural resolution in native-like and native cellular membranes.

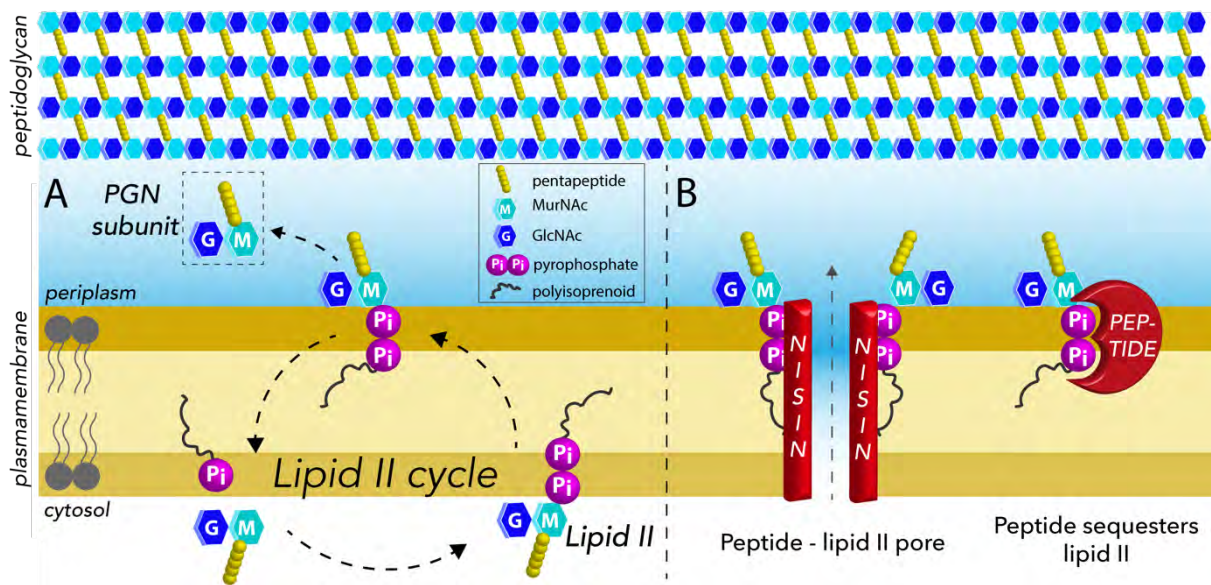


**Figure 8.** A) The cell envelope and the lipid II cycle. Lipid II is assembled in the cytosol and then transported across the plasma membrane to sustain PGN synthesis. B) Peptide antibiotics that bind lipid II kill bacteria through two known mechanisms, via targeted pore formation (left) and/or by blocking the lipid II cycle and, as result, the PGN synthesis(right).

## Nisin, the magic bullet

Lantibiotics are a series of post-translational modified AMPs that contain the aminoacids lanthionine and/or methyllanthionine (first discovered in wool, *lana* in Latin)<sup>107</sup>. The class A(I) lantibiotic nisin, produced by *Lactococcus lactis*, is the most widely studied lantibiotic that binds lipid II (Figure 9 A). Nisin was first identified in 1947<sup>108</sup>, it is globally used as a preservative in the food industry (E234) and has a recognized potential for clinical use,<sup>109</sup> including against drug-resistant bacterial strains and biofilms. Nisin kills bacteria at nanomolar concentrations through a unique mechanism called targeted pore formation,<sup>110</sup> for which eight nisin and four lipid II molecules are assumed to form a lethal hole that spans the plasma membrane (Figure 9 B).<sup>105</sup>

Although this mechanism was discovered > 15 years ago, the lipid II – nisin pore structure is still unknown. The only structural information derives from a solution NMR study in DMSO, which yielded the famous “pyrophosphate cage”, in which the amide back-bone protons of the thioether rings A and B coordinate to the lipid II pyrophosphate group in a 1:1 stoichiometry (Figure 9 B). However, the study was conducted in the absence of lipid bilayers where the pore complex is formed, thereby raising the question whether the calculated structure is physiologically representative. Hence, the nisin – lipid II pore complex was revisited in Chapters 6 and 7, this time on lipid bilayers and native bacterial membranes.

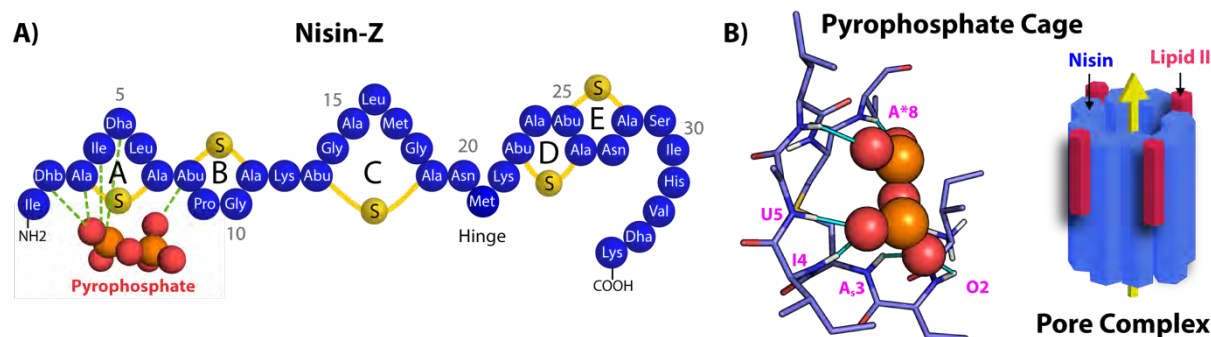


**Figure 9.** **A)** The lantibiotic nisin is composed of 34 residues, where the non-canonical Dhb, Dha, Ala-S and Abu are post-translational modified aminoacids. The lanthionine and methyllanthionine form 5 thioether rings; rings A and B are involved in lipid II binding and D and E rings are involved in pore formation, whereas the function of ring C is not clear. In this thesis, we employed the Nisin-Z variant (Z refers to the presence of an asparagine residue at position 27). **B)** Structure of the Pyrophosphate Cage motif discovered by Hsu *et al.*<sup>106</sup> In the pore complex, nisin is assumed to bind lipid II in a 2:1 stoichiometry, comprised by 8 nisin to 4 lipid II units in total.<sup>111</sup>

## Outline of the thesis

This introductory chapter laid a background for the work presented in the following chapters. Particularly, our motivation is to study membrane proteins with high resolution in physiological conditions, in order to discover underlying mechanisms that were not observable before. We did so by using state-of-art solid state NMR techniques.

In **Chapter 2** we develop a deuteration strategy that improves the  $^1\text{H}$ -signal resolution of solvent-inaccessible domains of proteins, granting access to the transmembrane domain of KcsA, including the entire filter. The improved resolution culminated with the measurement of this protein, for the first time ever, directly in native bacterial cell membranes. The developed methods paved the way for further studies on KcsA employed in Chapter 3 and Chapter 4. In **Chapter 3** we explore H/D exchange features in KcsA to investigate an unusually strong hydrogen bond network that is conserved in  $\text{K}^+$  channels. A closer structural analysis supported by MD simulations revealed that this hydrogen bond network might have functional relevance in gating mechanisms at the filter. In **Chapter 4** we investigate the molecular determinants of modal gating in  $\text{K}^+$  channels. We combined ssNMR with  $\mu$ -second long MD simulations to show that local changes in dynamics drive conformational changes at the selectivity filter, thereby triggering modal gating shifts in the channel.

In **Chapter 5**, we study the supramolecular arrangement of KcsA clusters in *E. coli* membranes by employing DNP-enhanced ssNMR, supported by MD simulations. We demonstrate that KcsA channels assemble into clusters in native-like lipid membranes, revealing an unexpected role of a membrane-associated helix for clustering and inter-channel communication.

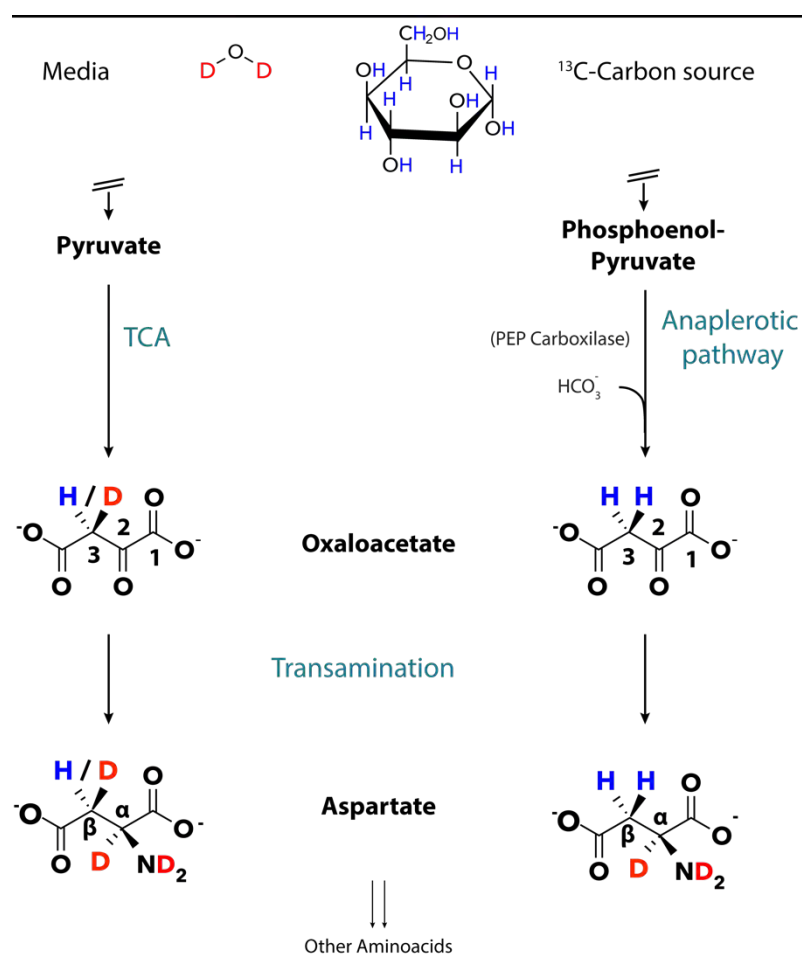
In **Chapter 6**, we study the nisin - lipid II complex in lipid bilayers using modern ssNMR techniques. Strikingly, our results show that nisin displays plastic features that adapt the antibiotic to the target cellular membrane where it is inserted. Interestingly these plastic components also correspond to hotspots for drug design. In **Chapter 7**, we continued structural studies of the nisin - lipid II pore. We made significant progress towards revealing the overall structure of the *magic bullet*. So far, we successfully describe the binding interface to Lipid II and solve the nisin monomer structure in the pore.

Finally, **Chapter 8** summarizes our findings about the importance of working in native-like conditions.

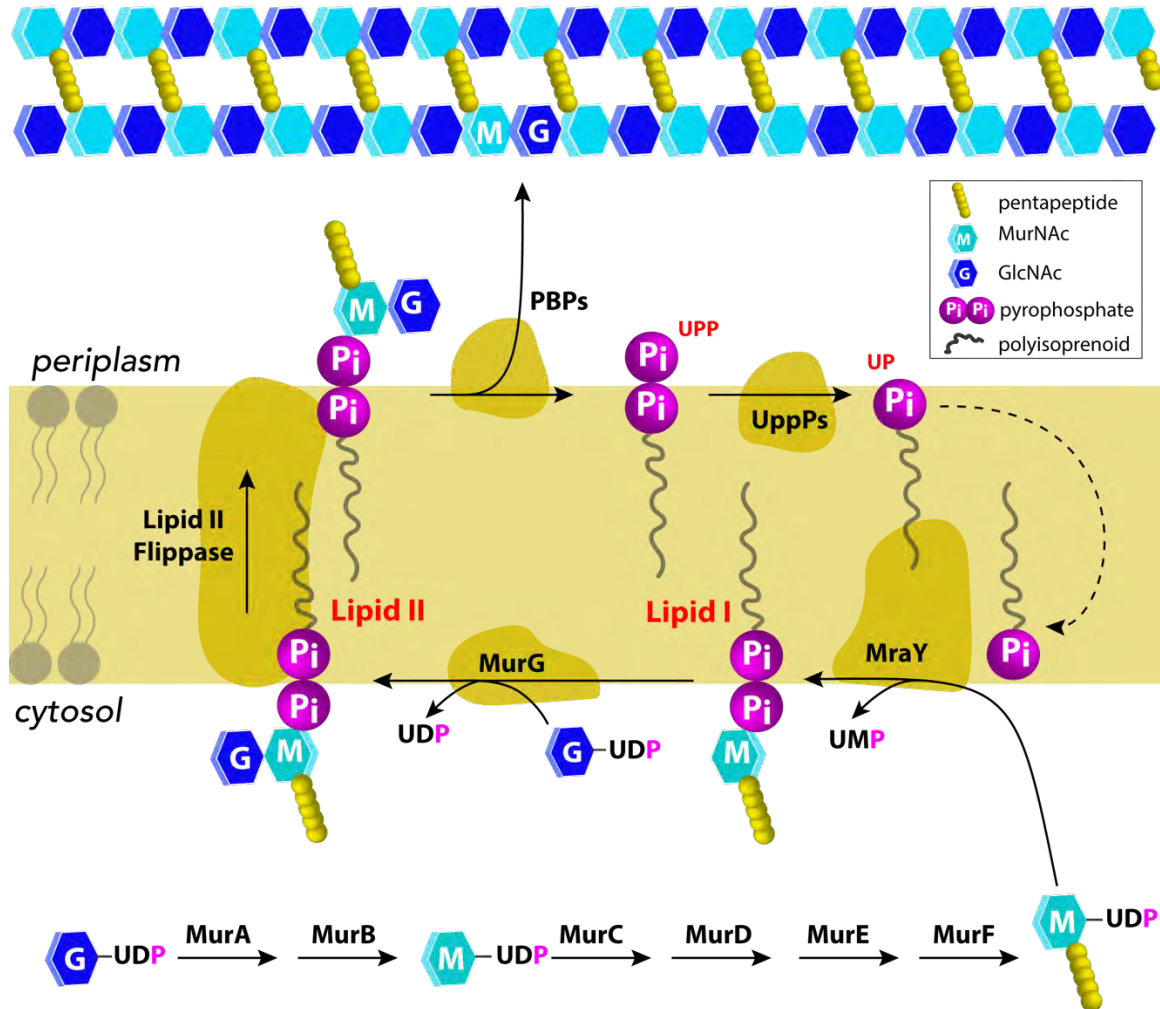
## Supplementary information

S1. Comparison of some properties of common MAS rotors. Adapted from Ref.<sup>112</sup>

Outer Diameter (mm)	7.0	4.0	3.2	2.5	1.9	1.3	0.7
Inner Diameter (mm)	5.6	3.0	2.2	1.7	1.5	0.9	0.5
Sample volume ( $\mu\text{L}$ )	246	70	30	14	10	1.7	0.37
Max. Spinning frequency (kHz)	7	15	24	35	42	65	111
Relative centrifugal force (RCF) at max. speed	0.55	1.36	2.55	4.19	5.33	7.65	12.4



S2. The diversity of deuteration at the aminoacid sidechains is partially explained by the formation of oxaloacetate by two different routes, the TCA and anaplerotic pathways, that result in differently labelled species. Oxaloacetate labeling at C3 mostly comes from the carbon source when it is generated through the anaplerotic pathway, whereas it mostly comes from the medium when generated through the TCA hence generating an isotopomer mixture. The oxaloacetate formation by these routes is further affected by the deuterium kinetic isotope effect, turning it difficult to control the extension of deuteration at the sidechains. Catabolism of the formed aminoacids further adds to the scrambling complexity of the deuteration. Adapted from reference.<sup>45</sup>



**S3.** General illustration for some of the main steps involved in PG synthesis. PG monomers are assembled in the cytoplasm. MraY catalyzes the formation of Lipid I, which is converted to Lipid II after addition of a GlcNAc unit catalyzed by MurG transferase. Lipid II is translocated to the outer leaflet of the bacterial membrane by a flippase, where various penicillin binding proteins (PBPs) cleave the PG headgroup to form the peptidoglycan layer, leaving behind the Lipid II carrier Undecaprenyl Pyrophosphate (UPP), which is then recycled by UPP phosphatases (UppPs) to afford undecaprenyl phosphate (UP).<sup>113</sup>

## References

- (1) Chipot, C.; Dehez, F.; Schnell, J. R.; Zitzmann, N.; Pebay-Peyroula, E.; Catoire, L. J.; Miroux, B.; Kunji, E. R. S.; Veglia, G.; Cross, T. A.; et al. Perturbations of Native Membrane Protein Structure in Alkyl Phosphocholine Detergents: A Critical Assessment of NMR and Biophysical Studies. *Chem. Rev.* **2018**, *118* (7), 3559–3607.
- (2) Luchinat, E.; Banci, L. In-Cell NMR in Human Cells: Direct Protein Expression Allows Structural Studies of Protein Folding and Maturation. *Acc. Chem. Res.* **2018**, *51* (6), 1550–1557.
- (3) Luchinat, E.; Banci, L. In-Cell NMR: A Topical Review. *IUCrJ* **2017**, *4* (2), 108–118.
- (4) Beck, M.; Baumeister, W. Cryo-Electron Tomography: Can It Reveal the Molecular Sociology of Cells in Atomic Detail? *Trends Cell Biol.* **2016**, *26* (11), 825–837.
- (5) Pfeffer, S.; Förster, F. *Structural Biology in Situ Using Cryo-Electron Subtomogram Analysis*; Springer, Cham, 2018; pp 237–259.
- (6) Renault, M.; Tommassen-van Boxtel, R.; Bos, M. P.; Post, J. A.; Tommassen, J.; Baldus, M. Cellular Solid-State Nuclear Magnetic Resonance Spectroscopy. *Proc. Natl. Acad. Sci.* **2012**, *109* (13), 4863–4868.
- (7) Gorkovskiy, A.; Thurber, K. R.; Tycko, R.; Wickner, R. B. Locating Folds of the In-Register Parallel -Sheet of the Sup35<sup>p</sup> Prion Domain Infectious Amyloid. *Proc. Natl. Acad. Sci.* **2014**, *111* (43), E4615–E4622.
- (8) Laws, D. D.; Bitter, H.-M. L.; Liu, K.; Ball, H. L.; Kaneko, K.; Wille, H.; Cohen, F. E.; Prusiner, S. B.; Pines, A.; Wemmer, D. E. Solid-State NMR Studies of the Secondary Structure of a Mutant Prion Protein Fragment of 55 Residues That Induces Neurodegeneration. *Proc. Natl. Acad. Sci.* **2001**, *98* (20), 11686–11690.
- (9) Wasmer, C.; Lange, A.; Van Melckebeke, H.; Siemer, A. B.; Riek, R.; Meier, B. H. Amyloid Fibrils of the HET-s(218-289) Prion Form a Solenoid with a Triangular Hydrophobic Core. *Science (80-. )*. **2008**, *319* (5869), 1523–1526.
- (10) Seuring, C.; Greenwald, J.; Wasmer, C.; Wepf, R.; Saupe, S. J.; Meier, B. H.; Riek, R. The Mechanism of Toxicity in HET-S/HET-s Prion Incompatibility. *PLoS Biol.* **2012**, *10* (12), e1001451.
- (11) Heise, H.; Celej, M. S.; Becker, S.; Riedel, D.; Pelah, A.; Kumar, A.; Jovin, T. M.; Baldus, M. Solid-State NMR Reveals Structural Differences between Fibrils of Wild-Type and Disease-Related A53T Mutant  $\alpha$ -Synuclein. *J. Mol. Biol.* **2008**, *380* (3), 444–450.
- (12) Antzutkin, O. N.; Leapman, R. D.; Balbach, J. J.; Tycko, R. Supramolecular Structural Constraints on Alzheimer's  $\beta$ -Amyloid Fibrils from Electron Microscopy and Solid-State Nuclear Magnetic Resonance †. *Biochemistry* **2002**, *41* (51), 15436–15450.
- (13) Balbach, J. J.; Ishii, Y.; Antzutkin, O. N.; Leapman, R. D.; Rizzo, N. W.; Dyda, F.; Reed, J.; Tycko, R. Amyloid Fibril Formation by A $\beta$  16-22 , a Seven-Residue Fragment of the Alzheimer's  $\beta$ -Amyloid Peptide, and Structural Characterization by Solid State NMR †. *Biochemistry* **2000**, *39* (45), 13748–13759.
- (14) Bertini, I.; Gonnelli, L.; Luchinat, C.; Mao, J.; Nesi, A. A New Structural Model of A $\beta$  40 Fibrils. *J. Am. Chem. Soc.* **2011**, *133* (40), 16013–16022.
- (15) Chimon, S.; Ishii, Y. Capturing Intermediate Structures of Alzheimer's  $\beta$ -Amyloid, A $\beta$ (1–40), by Solid-State NMR Spectroscopy. *J. Am. Chem. Soc.* **2005**, *127* (39), 13472–13473.
- (16) Colvin, M. T.; Silvers, R.; Ni, Q. Z.; Can, T. V.; Sergeev, I.; Rosay, M.; Donovan, K. J.; Michael, B.; Wall, J.; Linse, S.; et al. Atomic Resolution Structure of Monomorphic A $\beta$  42 Amyloid Fibrils. *J. Am. Chem. Soc.* **2016**, *138* (30), 9663–9674.
- (17) Yan, S.; Guo, C.; Hou, G.; Zhang, H.; Lu, X.; Williams, J. C.; Polenova, T. Atomic-Resolution Structure of the CAP-Gly Domain of Dynactin on Polymeric Microtubules Determined by Magic Angle Spinning NMR Spectroscopy. *Proc. Natl. Acad. Sci. U. S. A.* **2015**, *112* (47), 14611–14616.
- (18) Barbet-Massin, E.; Felletti, M.; Schneider, R.; Jehle, S.; Communie, G.; Martinez, N.; Jensen, M. R.; Ruigrok, R. W. H.; Emsley, L.; Lesage, A.; et al. Insights into the Structure and Dynamics of Measles Virus Nucleocapsids by 1H-Detected Solid-State NMR. *Biophys. J.* **2014**, *107* (4), 941–946.
- (19) Szymczyna, B. R.; Gan, L.; Johnson, J. E.; Williamson, J. R. Solution NMR Studies of the Maturation Intermediates of a 13 MDa Viral Capsid. *J. Am. Chem. Soc.* **2007**, *129* (25), 7867–7876.
- (20) Levitt, M. H. *Spin Dynamics : Basics of Nuclear Magnetic Resonance*.
- (21) Keeler, J. *Understanding NMR Spectroscopy*; John Wiley and Sons, 2010.
- (22) Duer, M. J. *Introduction to Solid-State NMR Spectroscopy*; Blackwell, 2004.
- (23) Pines, A.; Gibby, M. G.; Waugh, J. S. Proton-enhanced NMR of Dilute Spins in Solids. *J. Chem. Phys.* **1973**, *59* (2), 569–590.

- (24) Hartmann, S. R.; Hahn, E. L. Nuclear Double Resonance in the Rotating Frame. *Phys. Rev.* **1962**, *128* (5), 2042–2053.
- (25) Hall, D. A.; Maus, D. C.; Gerfen, G. J.; Inati, S. J.; Becerra, L. R.; Dahlquist, F. W.; Griffin, R. G. Polarization-Enhanced NMR Spectroscopy of Biomolecules in Frozen Solution. *Science* **1997**, *276* (5314), 930–932.
- (26) Carver, T. R.; Slichter, C. P. Polarization of Nuclear Spins in Metals. *Phys. Rev.* **1953**, *92* (1), 212–213.
- (27) Sauvée, C.; Rosay, M.; Casano, G.; Aussenac, F.; Weber, R. T.; Ouari, O.; Tordo, P. Highly Efficient, Water-Soluble Polarizing Agents for Dynamic Nuclear Polarization at High Frequency. *Angew. Chemie Int. Ed.* **2013**, *52* (41), 10858–10861.
- (28) Lilly Thankamony, A. S.; Wittmann, J. J.; Kaushik, M.; Corzilius, B. Dynamic Nuclear Polarization for Sensitivity Enhancement in Modern Solid-State NMR. *Prog. Nucl. Magn. Reson. Spectrosc.* **2017**, *102–103*, 120–195.
- (29) Kaplan, M.; Cukkemane, A.; van Zundert, G. C. P.; Narasimhan, S.; Daniëls, M.; Mance, D.; Waksman, G.; Bonvin, A. M. J. J.; Fronzes, R.; Folkers, G. E.; et al. Probing a Cell-Embedded Megadalton Protein Complex by DNP-Supported Solid-State NMR. *Nat. Methods* **2015**, *12* (7), 649–652.
- (30) Narasimhan, S.; Scherpe, S.; Lucini Paioni, A.; van der Zwan, J.; Folkers, G. E.; Ovaas, H.; Baldus, M. DNP Supported Solid-State NMR of Proteins inside Mammalian Cells. *Angew. Chemie Int. Ed.* **2019**.
- (31) Paioni, A. L.; Renault, M. A. M.; Baldus, M. DNP and Cellular Solid-State NMR. *eMagRes* **2018**, *7*, 51–62.
- (32) Takahashi, H.; Ayala, I.; Bardet, M.; De Paëpe, G.; Simorre, J.-P.; Hediger, S. Solid-State NMR on Bacterial Cells: Selective Cell Wall Signal Enhancement and Resolution Improvement Using Dynamic Nuclear Polarization. *J. Am. Chem. Soc.* **2013**, *135* (13), 5105–5110.
- (33) Chevelkov, V.; van Rossum, B. J.; Castellani, F.; Rehbein, K.; Diehl, A.; Hohwy, M.; Steuernagel, S.; Engelke, F.; Oschkinat, H.; Reif, B. <sup>1</sup>H Detection in MAS Solid-State NMR Spectroscopy of Biomacromolecules Employing Pulsed Field Gradients for Residual Solvent Suppression I. *J. Am. Chem. Soc.* **2003**, *125* (26), 7788–7789.
- (34) Reif, B.; Griffin, R. <sup>1</sup>H Detected <sup>1</sup>H,<sup>15</sup>N Correlation Spectroscopy in Rotating Solids. *J. Magn. Reson.* **2003**, *160* (1), 78–83.
- (35) Mishkovsky, M.; Frydman, L. Sensitivity Enhancement in 1D Heteronuclear NMR Spectroscopy via Single-Scan Inverse Experiments. *ChemPhysChem* **2004**, *5* (6), 779–786.
- (36) Ishii, Y.; Tycko, R. Sensitivity Enhancement in Solid State <sup>15</sup>N NMR by Indirect Detection with High-Speed Magic Angle Spinning. *J. Magn. Reson.* **2000**, *142* (1), 199–204.
- (37) Weingarth, M.; Bodenhausen, G.; Tekely, P. Low-Power Decoupling at High Spinning Frequencies in High Static Fields. *J. Magn. Reson.* **2009**, *199* (2), 238–241.
- (38) Madhu, P. K. High-Resolution Solid-State NMR Spectroscopy of Protons with Homonuclear Dipolar Decoupling Schemes under Magic-Angle Spinning. *Solid State Nucl. Magn. Reson.* **2009**, *35* (1), 2–11.
- (39) Andreas, L. B.; Le Marchand, T.; Jaudzems, K.; Pintacuda, G. High-Resolution Proton-Detected NMR of Proteins at Very Fast MAS. *J. Magn. Reson.* **2015**, *253*, 36–49.
- (40) Agarwal, V.; Penzel, S.; Szekely, K.; Cadalbert, R.; Testori, E.; Oss, A.; Past, J.; Samoson, A.; Ernst, M.; Böckmann, A.; et al. De Novo 3D Structure Determination from Sub-Milligram Protein Samples by Solid-State 100 KHz MAS NMR Spectroscopy. *Angew. Chemie Int. Ed.* **2014**, *53* (45), 12253–12256.
- (41) Demers, J.-P.; Fricke, P.; Shi, C.; Chevelkov, V.; Lange, A. Structure Determination of Supra-Molecular Assemblies by Solid-State NMR: Practical Considerations. *Prog. Nucl. Magn. Reson. Spectrosc.* **2018**, *109*, 51–78.
- (42) Crespi, H. L.; Rosenberg, R. M.; Katz, J. J. Proton Magnetic Resonance of Proteins Fully Deuterated except for <sup>1</sup>H-Leucine Side Chains. *Science* (80-.). **1968**, *161* (3843), 795–796.
- (43) Saur, W. K.; Crespi, H. L.; Halevi, E. A.; Katz, J. J. Deuterium Isotope Effects in the Fermentation of Hexoses to Ethanol by *Saccharomyces Cerevisiae*. I. Hydrogen Exchange in the Glycolytic Pathway. *Biochemistry* **1968**, *7* (10), 3529–3536.
- (44) Saur, W. K.; Peterson, D. T.; Halevi, E. A.; Crespi, H. L.; Katz, J. J. Deuterium Isotope Effects in the Fermentation of Hexoses to Ethanol by *Saccharomyces Cerevisiae*. II. A Steady-State Kinetic Analysis of the Methyl Group of Ethanol in an Isotopic Mirror Fermentation Experiment. *Biochemistry* **1968**, *7* (10), 3537–3546.
- (45) Hochuli, M.; Szyperski, T.; Wüthrich, K. Deuterium Isotope Effects on the Central Carbon Metabolism of *Escherichia Coli* Cells Grown on a D<sub>2</sub>O-Containing Minimal Medium. *J. Biomol. NMR* **2000**, *17* (1), 33–42.
- (46) Opitz, C.; Ahrné, E.; Goldie, K. N.; Schmidt, A.; Grzesiek, S. Deuterium Induces a Distinctive *Escherichia Coli* Proteome That Correlates with the Reduction in Growth Rate. *J. Biol. Chem.* **2019**, *294* (7), 2279–2292.

- (47) Mance, D.; Sinnige, T.; Kaplan, M.; Narasimhan, S.; Daniëls, M.; Houben, K.; Baldus, M.; Weingarth, M. An Efficient Labelling Approach to Harness Backbone and Side-Chain Protons in  $^1\text{H}$ -Detected Solid-State NMR Spectroscopy. *Angew. Chemie Int. Ed.* **2015**, *54* (52), 15799–15803.
- (48) Sinnige, T.; Daniëls, M.; Baldus, M.; Weingarth, M. Proton Clouds to Measure Long-Range Contacts between Nonexchangeable Side Chain Protons in Solid-State NMR. *J. Am. Chem. Soc.* **2014**, *136* (12), 4452–4455.
- (49) Asami, S.; Schmieder, P.; Reif, B. High Resolution  $^1\text{H}$ -Detected Solid-State NMR Spectroscopy of Protein Aliphatic Resonances: Access to Tertiary Structure Information. *J. Am. Chem. Soc.* **2010**, *132* (43), 15133–15135.
- (50) Reif, B.; Jaroniec, C. P.; Rienstra, C. M.; Hohwy, M.; Griffin, R. G.  $1\text{H}$ – $1\text{H}$  MAS Correlation Spectroscopy and Distance Measurements in a Deuterated Peptide. *J. Magn. Reson.* **2001**, *151* (2), 320–327.
- (51) Paulson, E. K.; Morcombe, C. R.; Gaponenko, V.; Dancheck, B.; Byrd, R. A.; Zilm, K. W. Sensitive High Resolution Inverse Detection NMR Spectroscopy of Proteins in the Solid State. *J. Am. Chem. Soc.* **2003**, *125* (51), 15831–15836.
- (52) Rosen, M. K.; Gardner, K. H.; Willis, R. C.; Parris, W. E.; Pawson, T.; Kay, L. E. Selective Methyl Group Protonation of Perdeuterated Proteins. *J. Mol. Biol.* **1996**, *263* (5), 627–636.
- (53) Huber, M.; Hiller, S.; Schanda, P.; Ernst, M.; Böckmann, A.; Verel, R.; Meier, B. H. A Proton-Detected 4D Solid-State NMR Experiment for Protein Structure Determination. *ChemPhysChem* **2011**, *12* (5), 915–918.
- (54) Wang, S.; Parthasarathy, S.; Xiao, Y.; Nishiyama, Y.; Long, F.; Matsuda, I.; Endo, Y.; Nemoto, T.; Yamauchi, K.; Asakura, T.; et al. Nano-Mole Scale Sequential Signal Assignment by  $^1\text{H}$ -Detected Protein Solid-State NMR. *Chem. Commun.* **2015**, *51* (81), 15055–15058.
- (55) Kainosho, M.; Torizawa, T.; Iwashita, Y.; Terauchi, T.; Mei Ono, A.; Güntert, P. Optimal Isotope Labelling for NMR Protein Structure Determinations. *Nature* **2006**, *440* (7080), 52–57.
- (56) Andreas, L. B.; Jaudzems, K.; Stanek, J.; Lalli, D.; Bertarello, A.; Le Marchand, T.; Cala-De Paepe, D.; Kotelovica, S.; Akopjana, I.; Knott, B.; et al. Structure of Fully Protonated Proteins by Proton-Detected Magic-Angle Spinning NMR. *Proc. Natl. Acad. Sci. U. S. A.* **2016**, *113* (33), 9187–9192.
- (57) Kanehisa, M.; Furumichi, M.; Tanabe, M.; Sato, Y.; Morishima, K. KEGG: New Perspectives on Genomes, Pathways, Diseases and Drugs. *Nucleic Acids Res.* **2017**, *45* (D1), D353–D361.
- (58) Keseler, I. M.; Mackie, A.; Santos-Zavaleta, A.; Billington, R.; Bonavides-Martínez, C.; Caspi, R.; Fulcher, C.; Gama-Castro, S.; Kothari, A.; Krummenacker, M.; et al. The EcoCyc Database: Reflecting New Knowledge about Escherichia Coli K-12. *Nucleic Acids Res.* **2017**, *45* (D1), D543–D550.
- (59) Lacabanne, D.; Meier, B. H.; Böckmann, A. Selective Labeling and Unlabeling Strategies in Protein Solid-State NMR Spectroscopy. *J. Biomol. NMR* **2018**, *71* (3), 141–150.
- (60) Movellan, K. T.; Eszter, ; Najbauer, E.; Supriya Pratihari, ; Salvi, M.; Giller, K.; Becker, S.; Andreas, L. B. Alpha Protons as NMR Probes in Deuterated Proteins. *J. Biomol. NMR* **2019**, *73*, 81–91.
- (61) LeMasurier, M.; Heginbotham, L.; Miller, C. Kcsa: It's a Potassium Channel. *J. Gen. Physiol.* **2001**, *118* (3), 303–314.
- (62) Hodgkin, A. L.; Huxley, A. F. A Quantitative Description of Membrane Current and Its Application to Conduction and Excitation in Nerve. *J. Physiol.* **1952**, *117* (4), 500–544.
- (63) Yellen, G. The Voltage-Gated Potassium Channels and Their Relatives. *Nature* **2002**, *419* (6902), 35–42.
- (64) Hoshi, T.; Armstrong, C. M. C-Type Inactivation of Voltage-Gated  $\text{K}^+$  Channels: Pore Constriction or Dilation? *J. Gen. Physiol.* **2013**, *141* (2), 151–160.
- (65) Prindle, A.; Liu, J.; Asally, M.; Ly, S.; Garcia-Ojalvo, J.; Süel, G. M. Ion Channels Enable Electrical Communication in Bacterial Communities. *Nature* **2015**, *527* (7576), 59–63.
- (66) Lehmann-Horn, F.; Jurkat-Rott, K. Voltage-Gated Ion Channels and Hereditary Disease. *Physiol. Rev.* **1999**, *79* (4), 1317–1372.
- (67) Schulze-Bahr, E.; Wedekind, H.; Haverkamp, W.; Borggreffe, M.; Assmann, G.; Breithardt, G.; Funke, H. The LQT Syndromes – Current Status of Molecular Mechanisms. *Z. Kardiol.* **1999**, *88* (4), 245–254.
- (68) Kirsch, G. E. Ion Channel Defects in Cardiac Arrhythmia. *J. Membr. Biol.* **1999**, *170* (3), 181–190.
- (69) Wang, Q.; Curran, M. E.; Splawski, I.; Burn, T. C.; Millholland, J. M.; VanRaay, T. J.; Shen, J.; Timothy, K. W.; Vincent, G. M.; de Jager, T.; et al. Positional Cloning of a Novel Potassium Channel Gene: KVLQT1 Mutations Cause Cardiac Arrhythmias. *Nat. Genet.* **1996**, *12* (1), 17–23.
- (70) Kubisch, C.; Schroeder, B. C.; Friedrich, T.; Lütjohann, B.; El-Amraoui, A.; Marlin, S.; Petit, C.; Jentsch, T. J. KCNQ4, a Novel Potassium Channel Expressed in Sensory Outer Hair Cells, Is Mutated in Dominant Deafness. *Cell* **1999**, *96* (3), 437–446.

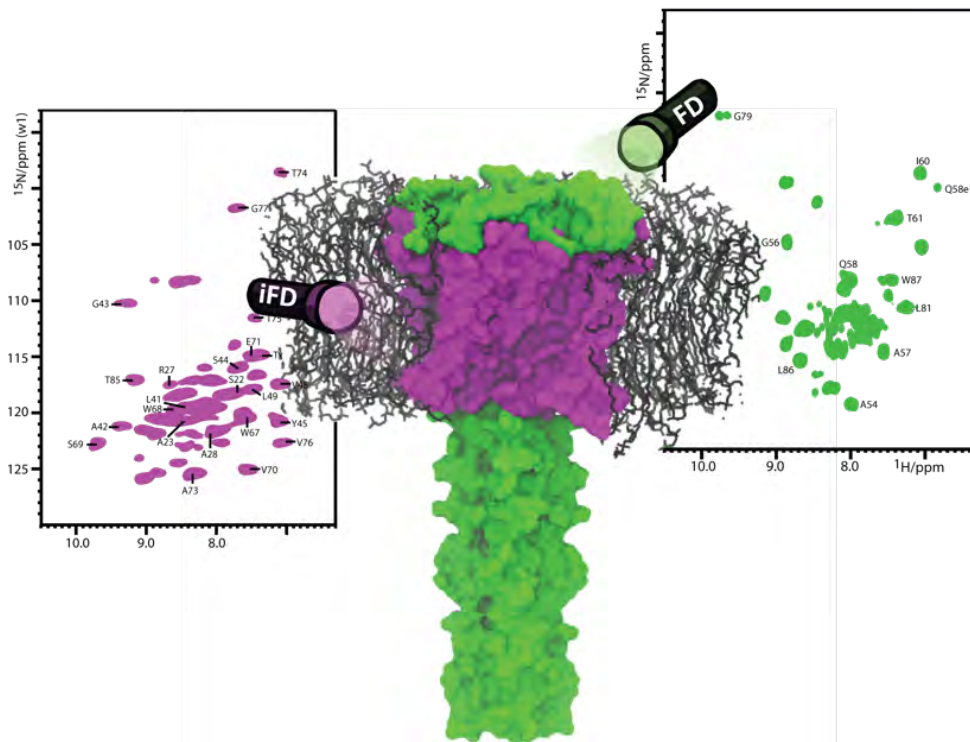
- (71) Charlier, C.; Singh, N. A.; Ryan, S. G.; Lewis, T. B.; Reus, B. E.; Leach, R. J.; Leppert, M. A Pore Mutation in a Novel KQT-like Potassium Channel Gene in an Idiopathic Epilepsy Family. *Nat. Genet.* **1998**, *18* (1), 53–55.
- (72) Shah, N. H.; Aizenman, E. Voltage-Gated Potassium Channels at the Crossroads of Neuronal Function, Ischemic Tolerance, and Neurodegeneration. *Transl. Stroke Res.* **2014**, *5* (1), 38–58.
- (73) Jentsch, T. J. Neuronal KCNQ Potassium Channels: Physiology and Role in Disease. *Nat. Rev. Neurosci.* **2000**, *1* (1), 21–30.
- (74) Parekh, P. K.; Sidor, M. M.; Gillman, A.; Becker-Krail, D.; Bettelini, L.; Arban, R.; Alvaro, G. S.; Zambello, E.; Mutinelli, C.; Huang, Y.; et al. Antimanic Efficacy of a Novel Kv3 Potassium Channel Modulator. *Neuropsychopharmacology* **2018**, *43* (2), 435–444.
- (75) Allen, T. W.; Bliznyuk, A.; Rendell, A. P.; Kuyucak, S.; Chung, S. H. The Potassium Channel: Structure, Selectivity and Diffusion. *J. Chem. Phys.* **2000**, *112* (18), 8191–8204.
- (76) Allen, T. W.; Kuyucak, S.; Chung, S.-H. Molecular Dynamics Estimates of Ion Diffusion in Model Hydrophobic and KcsA Potassium Channels. *Biophys. Chem.* **2000**, *86* (1), 1–14.
- (77) Morais-Cabral, J. H.; Zhou, Y.; MacKinnon, R. Energetic Optimization of Ion Conduction Rate by the K<sup>+</sup> Selectivity Filter. *Nature* **2001**, *414* (6859), 37–42.
- (78) MacKinnon, R. Potassium Channels and the Atomic Basis of Selective Ion Conduction. *Biosci. Rep.* **2004**, *24* (2), 75–100.
- (79) Xu, Y.; McDermott, A. E. Inactivation in the Potassium Channel KcsA. *J. Struct. Biol.* **2019**, 100009.
- (80) Schrempf, H.; Schmidt, O.; Kümmerlen, R.; Hinnah, S.; Müller, D.; Betzler, M.; Steinkamp, T.; Wagner, R. A Prokaryotic Potassium Ion Channel with Two Predicted Transmembrane Segments from *Streptomyces lividans*. *EMBO J.* **1995**, *14* (21), 5170–5178.
- (81) Thompson, A. N.; Posson, D. J.; Parsa, P. V.; Nimigeon, C. M. Molecular Mechanism of PH Sensing in KcsA Potassium Channels. *Proc. Natl. Acad. Sci.* **2008**, *105* (19), 6900–6905.
- (82) Robbins, J. KCNQ Potassium Channels: Physiology, Pathophysiology, and Pharmacology. *Pharmacol. Ther.* **2001**, *90* (1), 1–19.
- (83) Shealy, R. T.; Murphy, A. D.; Ramarathnam, R.; Jakobsson, E.; Subramaniam, S. Sequence-Function Analysis of the K<sup>+</sup>-Selective Family of Ion Channels Using a Comprehensive Alignment and the KcsA Channel Structure. *Biophys. J.* **2003**, *84* (5), 2929–2942.
- (84) Lockhart, D.; Kim, P.; MacKinnon, R.; Kuo, A.; Gulbis, J. M.; Cohen, S. L.; Chait, B. T.; MacKinnon, R. Internal Stark Effect Measurement of the Electric Field at the Amino Terminus of an Alpha Helix. *Science* (80-. ). **1992**, *257* (5072), 947–951.
- (85) Uysal, S.; Vásquez, V.; Tereshko, V.; Esaki, K.; Fellouse, F. A.; Sidhu, S. S.; Koide, S.; Perozo, E.; Kossiakoff, A. Crystal Structure of Full-Length KcsA in Its Closed Conformation. *Proc. Natl. Acad. Sci. U. S. A.* **2009**, *106* (16), 6644–6649.
- (86) Weingarth, M.; van der Cruysen, E. A. W.; Ostmeyer, J.; Lievestro, S.; Roux, B.; Baldus, M. Quantitative Analysis of the Water Occupancy around the Selectivity Filter of a K<sup>+</sup> Channel in Different Gating Modes. *J. Am. Chem. Soc.* **2014**, *136* (5), 2000–2007.
- (87) Iwamoto, M.; Oiki, S. Amphipathic Antenna of an Inward Rectifier K<sup>+</sup> Channel Responds to Changes in the Inner Membrane Leaflet. *Proc. Natl. Acad. Sci.* **2013**, *110* (2), 749–754.
- (88) Visscher, K. M.; Medeiros-Silva, J.; Mance, D.; Rodrigues, J. P. G. L. M.; Daniëls, M.; Bonvin, A. M. J. J.; Baldus, M.; Weingarth, M. Supramolecular Organization and Functional Implications of K<sup>+</sup> Channel Clusters in Membranes. **2017**.
- (89) Zhou, Y.; Morais-Cabral, J. H.; Kaufman, A.; MacKinnon, R. Chemistry of Ion Coordination and Hydration Revealed by a K<sup>+</sup> Channel–Fab Complex at 2.0 Å Resolution. *Nature* **2001**, *414* (6859), 43–48.
- (90) Sansom, M. S. P.; Shrivastava, I. H.; Bright, J. N.; Tate, J.; Capener, C. E.; Biggin, P. C. Potassium Channels: Structures, Models, Simulations. *Biochim. Biophys. Acta - Biomembr.* **2002**, *1565* (2), 294–307.
- (91) Cordero-Morales, J. F.; Cuello, L. G.; Zhao, Y.; Jogini, V.; Cortes, D. M.; Roux, B.; Perozo, E. Molecular Determinants of Gating at the Potassium-Channel Selectivity Filter. *Nat. Struct. Mol. Biol.* **2006**, *13* (4), 311–318.
- (92) Cuello, L. G.; Jogini, V.; Cortes, D. M.; Perozo, E. Structural Mechanism of C-Type Inactivation in K<sup>+</sup> Channels. *Nature* **2010**, *466* (7303), 203–208.
- (93) Chakrapani, S.; Cordero-Morales, J. F.; Perozo, E. A Quantitative Description of KcsA Gating II: Single-Channel Currents. *J. Gen. Physiol.* **2007**, *130* (5), 479–496.
- (94) Dreyer, I.; Michard, E.; Lacombe, B.; Thibaud, J.-B. A Plant Shaker-like K<sup>+</sup> Channel Switches between Two

- Distinct Gating Modes Resulting in Either Inward-Rectifying or 'Leak' Current. *FEBS Lett.* **2001**, 505 (2), 233–239.
- (95) Singer-Lahat, D.; Dascal, N.; Lotan, I. Modal Behavior of the Kv1.1 Channel Conferred by the Kv $\beta$ 1.1 Subunit and Its Regulation by Dephosphorylation of Kv1.1. *Pflügers Arch. - Eur. J. Physiol.* **1999**, 439 (1), 18–26.
- (96) Cooper, E.; Shrier, A. Inactivation of A Currents and A Channels on Rat Nodose Neurons in Culture. *J. Gen. Physiol.* **1989**, 94 (5), 881–910.
- (97) Chakrapani, S.; Cordero-Morales, J. F.; Jogini, V.; Pan, A. C.; Cortes, D. M.; Roux, B.; Perozo, E. On the Structural Basis of Modal Gating Behavior in K<sup>+</sup> Channels. *Nat. Struct. Mol. Biol.* **2011**, 18 (1), 67–74.
- (98) Ventola, C. L. The Antibiotic Resistance Crisis: Part 1: Causes and Threats. *PT* **2015**, 40 (4), 277–283.
- (99) *Tackling Drug-Resistant Infections Globally: Final Report and Recommendations the Review on Antimicrobial Resistance, Chaired by Jim O'Neill*; 2016.
- (100) Cassini, A.; Högberg, L. D.; Plachouras, D.; Quattrocchi, A.; Hoxha, A.; Simonsen, G. S.; Colomb-Cotinat, M.; Kretzschmar, M. E.; Devleeschauwer, B.; Cecchini, M.; et al. Attributable Deaths and Disability-Adjusted Life-Years Caused by Infections with Antibiotic-Resistant Bacteria in the EU and the European Economic Area in 2015: A Population-Level Modelling Analysis. *Lancet Infect. Dis.* **2019**, 19 (1), 56–66.
- (101) Gandra, S.; Barter, D. M.; Laxminarayan, R. Economic Burden of Antibiotic Resistance: How Much Do We Really Know? *Clin. Microbiol. Infect.* **2014**, 20 (10), 973–980.
- (102) Breukink, E.; de Kruijff, B. Lipid II as a Target for Antibiotics. *Nat. Rev. Drug Discov.* **2006**, 5 (4), 321–323.
- (103) Scheffers, D.-J.; Tol, M. B. LipidII: Just Another Brick in the Wall? *PLOS Pathog.* **2015**, 11 (12), e1005213.
- (104) Müller, A.; Klöckner, A.; Schneider, T. Targeting a Cell Wall Biosynthesis Hot Spot. *Nat. Prod. Rep.* **2017**, 34 (7), 909–932.
- (105) Oppedijk, S. F.; Martin, N. I.; Breukink, E. Hit 'em Where It Hurts: The Growing and Structurally Diverse Family of Peptides That Target Lipid-II. *Biochim. Biophys. Acta - Biomembr.* **2016**, 1858 (5), 947–957.
- (106) Hsu, S.-T. D.; Breukink, E.; Tischenko, E.; Lutters, M. A. G.; de Kruijff, B.; Kaptein, R.; Bonvin, A. M. J. J.; van Nuland, N. A. J. The Nisin-Lipid II Complex Reveals a Pyrophosphate Cage That Provides a Blueprint for Novel Antibiotics. *Nat. Struct. Mol. Biol.* **2004**, 11 (10), 963–967.
- (107) Bierbaum, G.; Sahl, H.-G. Lantibiotics: Mode of Action, Biosynthesis and Bioengineering. *Curr. Pharm. Biotechnol.* **2009**, 10 (1), 2–18.
- (108) Mattick, A. T. R.; Hirsch, A.; Berridge, N. J. Further Observations on an Inhibitory Substance (Nisin) from Lactic Streptococci. *Lancet* **1947**, 250 (6462), 5–8.
- (109) Shin, J. M.; Gwak, J. W.; Kamarajan, P.; Fenno, J. C.; Rickard, A. H.; Kapila, Y. L. Biomedical Applications of Nisin. *J. Appl. Microbiol.* **2016**, 120 (6), 1449–1465.
- (110) Breukink, E.; Wiedemann, I.; van Kraaij, C.; Kuipers, O. P.; Sahl, H. G.; de Kruijff, B. Use of the Cell Wall Precursor Lipid II by a Pore-Forming Peptide Antibiotic. *Science* **1999**, 286 (5448), 2361–2364.
- (111) Hasper, H. E.; de Kruijff, B.; Breukink, E. Assembly and Stability of Nisin-Lipid II Pores. *Biochemistry* **2004**, 43 (36), 11567–11575.
- (112) Demers, J.-P.; Chevelkov, V.; Lange, A. Progress in Correlation Spectroscopy at Ultra-Fast Magic-Angle Spinning: Basic Building Blocks and Complex Experiments for the Study of Protein Structure and Dynamics. *Solid State Nucl. Magn. Reson.* **2011**, 40 (3), 101–113.
- (113) Piepenbreier, H.; Diehl, A.; Fritz, G. Minimal Exposure of Lipid II Cycle Intermediates Triggers Cell Wall Antibiotic Resistance. *Nat. Commun.* **2019**, 10 (1), 2733.



# CHAPTER 2

## $^1\text{H}$ Detected Solid-State NMR Studies of Water-Inaccessible Proteins *In Vitro* and *In Situ*



## Abstract

$^1\text{H}$  detection can significantly improve solid-state NMR spectral sensitivity and thereby allows for the study of more complex proteins. However,  $^1\text{H}$ -detection commonly requires Perdeuteration of proteins, which severely limits its application to systems with restricted water-accessibility such as membrane proteins. In this chapter, we present an approach that enables high-resolution  $^1\text{H}$ -detected solid-state NMR studies of water-inaccessible protein. This approach, coined *Inverse Fractional Deuteration*, is shown to be even applicable in highly complex environments such as cellular surfaces.

We demonstrate the potential of our method with the ion channel KcsA both in liposomes and directly in the bacterial cell membrane. As result, our approach provided important new insights into the selectivity filter of KcsA, which is responsible for ion conduction and is highly conserved in  $\text{K}^+$  channels, and we show that the selectivity filter undergoes pronounced molecular motion on functionally relevant timescales. We expect this approach to open new avenues for biomolecular ssNMR.

*Based on the publication:*

João Medeiros-Silva, Deni Mance, Mark Daniëls, Shehrazade Jekhmane, Klaartje Houben, Marc Baldus and Markus Weingarth

$^1\text{H}$ -Detected Solid-State NMR Studies of Water-Inaccessible Proteins *In Vitro* and *In Situ*.

*Angewandte Chemie International Edition* **2016** 55(43): 13606–13610

## Introduction

Proton (<sup>1</sup>H) detection can greatly increase spectral sensitivity in solid-state NMR (ssNMR) spectroscopy and thereby enables the study of more complex proteins.<sup>1</sup> <sup>1</sup>H-detected ssNMR experiments usually require a stark dilution of the <sup>1</sup>H network to diminish line-broadening dipolar <sup>1</sup>H–<sup>1</sup>H couplings, which can be achieved by expressing proteins in deuterated solvents.<sup>2–8</sup>

Whereas such high degrees of deuteration can provide excellent <sup>1</sup>H signal resolution, these labelling techniques necessitate a proton/deuterium (H/D) back-exchange step to incorporate amino protons (H<sup>N</sup>). Consequently, water-inaccessible protein regions remain invisible for <sup>1</sup>H detection unless unfolding and refolding protocols are used, which are tedious, not broadly applicable, and limited to *in vitro* preparations. Moreover, deuterated solvents can reduce or prevent protein expression, especially in mammalian cells, and are generally associated with high costs for low-yield proteins.

A remedy to these problems would be the use of fully protonated proteins;<sup>9–13</sup> however, such systems often provide limited spectral resolution. Even at very fast magic angle spinning (MAS) frequencies (> 100 kHz),<sup>14,15</sup> the resolution in fully protonated samples is governed by residual <sup>1</sup>H–<sup>1</sup>H couplings. Moreover, the sensitivity loss that is due to the small sample volumes required for > 100 kHz MAS may not be compensated for in heterogeneous systems such as cellular samples. These issues have thus far critically limited the application of <sup>1</sup>H detection for the study of water-inaccessible protein regions, which is a major obstacle for ssNMR spectroscopy as binding pockets and active sites alike can be buried deep inside protein cores, far away from the bulk water. It is a particularly severe problem for the study of membrane proteins, whose transmembrane (TM) parts are critical for their function and do not undergo exchange in protonated buffers.<sup>6,11,16</sup> This prompted us to develop a two-step approach that is generally applicable *in vitro* and *in situ*, works at moderate MAS frequencies of 60 kHz and provides well-resolved <sup>1</sup>H-detected NMR spectra of water-inaccessible protein regions. In the first step, we enhance the <sup>1</sup>H resolution by employing a novel labeling scheme, dubbed inverse fractional deuteration (iFD), which is based on protonated solvents (100 % H<sub>2</sub>O) and fully deuterated [<sup>13</sup>C]glucose in the growth medium. In the second step, we wash the iFD-labeled protein with deuterated buffers (100 % D<sub>2</sub>O), which further markedly improves the spectral resolution. We first studied the iFD labeling approach on ubiquitin and then, in combination with the D<sub>2</sub>O wash, used it to assign the TM part of the ion channel KcsA in lipid bilayers. Based on our assignments, we present a site-resolved study of the dynamics of the TM part, which is crucial to fully understand ion channel gating. Remarkably, our approach even provides sufficient spectral quality for site-resolved analysis of a membrane protein *in situ*, i.e., directly in a bacterial cell membrane.

## Results and discussion

### *Inverse Fractional Deuteration on Ubiquitin*

iFD labeling is the first of two consecutive steps to improve the resolution of water-inaccessible protons, especially for  $H^N$  and  $H^\alpha$ , which are most important for backbone assignments. The efficacy of iFD labeling was first evaluated with ubiquitin as model-system. Figures 1A,B show the  $^1H$ -detected 2D NH and CH spectra of iFD-labeled [ $^{13}C$ ,  $^{15}N$ ] ubiquitin in aqueous (100 %  $H_2O$ ) buffers, acquired at 60 kHz MAS and 950 MHz  $^1H$  frequency using MISSISSIPI water suppression<sup>17</sup> and PISSARRO decoupling<sup>18</sup>.

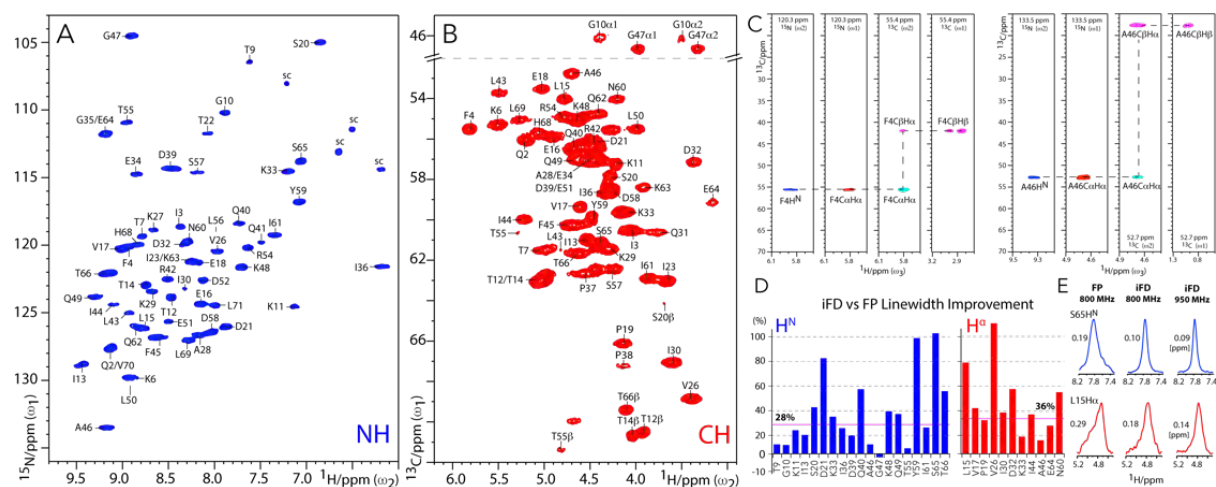


**Figure 1.** Dipolar  $^1H$ -detected ssNMR experiments in iFD ubiquitin measured at 950 MHz and 60 kHz MAS. **A)** 2D NH spectrum (blue). **B)**  $C\alpha H\alpha$  region of a 2D CH spectrum (red). **C)**  $^1H$ -detected side-chain assignments. Strip plots are shown for 3D  $C\alpha NH$  (blue), 3D  $NC\alpha H\alpha$  (red), and 3D CCH (cyan and magenta for negative and positive signals, respectively) experiments. DREAM<sup>19</sup>  $^{13}C$ - $^{13}C$  transfer was used for the 3D CCH experiment. **D)**  $^1H$ -linewidth improvement between fully protonated (FP) and inversely fractionally deuterated (iFD) ubiquitin signals. Only fully resolved signals were considered. **E)** Representative  $t_1$  cross-sections extracted from 2D NH (blue) and CH (red) spectra of FP and iFD ubiquitin.

The obtained spectra are well resolved and feature an average linewidth of 0.1–0.2 ppm for  $H^N$  and  $H^\alpha$  at 950 MHz, which is excellent considering the average high  $^1H$  density of 80 % in iFD proteins, and constitutes a substantial average linewidth improvement of about 30–35 % compared to fully protonated (FP) ubiquitin (Figures 1D and E; see also Supplementary information S1-S4 for a detailed  $^1H$  linewidth and population description). Moreover, as both  $H^\alpha$  and, obviously,  $H^N$  are recruited from the protonated solvent during protein expression, their  $^1H$  levels are close to 100 % in iFD ubiquitin (Figure 2A). We also observed a very good resolution of around 0.1 ppm for many side-chain  $^1H$  (Figure S2), although the resolution of certain methyl groups was compromised by isotopologue effects (Figure S4). Hence, owing to the high  $^1H$  density and resolution in iFD ubiquitin, the backbone and many side-chain

protons could be readily assigned (Figure 1 C). We first correlated backbone H<sup>N</sup> protons, that had been previously assigned,<sup>20</sup> to H $\alpha$  protons using 3D C $\alpha$ NH and NC $\alpha$ H $\alpha$  experiments. We then used a 3D CCH experiment to detect side-chain <sup>1</sup>H, which were connected to backbone H<sup>N</sup> via the H $\alpha$  protons. The experimental details are described in the Methods section.

Given that the sample preparation quality is equivalent (see Figure S3), the discrepancy in signal linewidth improvement between residues in iFD ubiquitin is related to different protonation levels at the respective side-chain (Figure 2A and Table S5). For example, the resolution of Gly-H<sup>N</sup> barely improves with iFD labelling because Gly has no sidechain and the <sup>1</sup>H-density around Gly-H<sup>N</sup> hence hardly changes. The resolution of residues such as Ser, Phe, or Tyr improves substantially, because the H $\beta$ -levels is considerably reduced for these residue types. Thus, what matters for the linewidth improvement, in general, is the reduction of the <sup>1</sup>H-density around a given <sup>1</sup>H, which depends on the aminoacid composition and 3D structure of a given protein (Figure 2B).

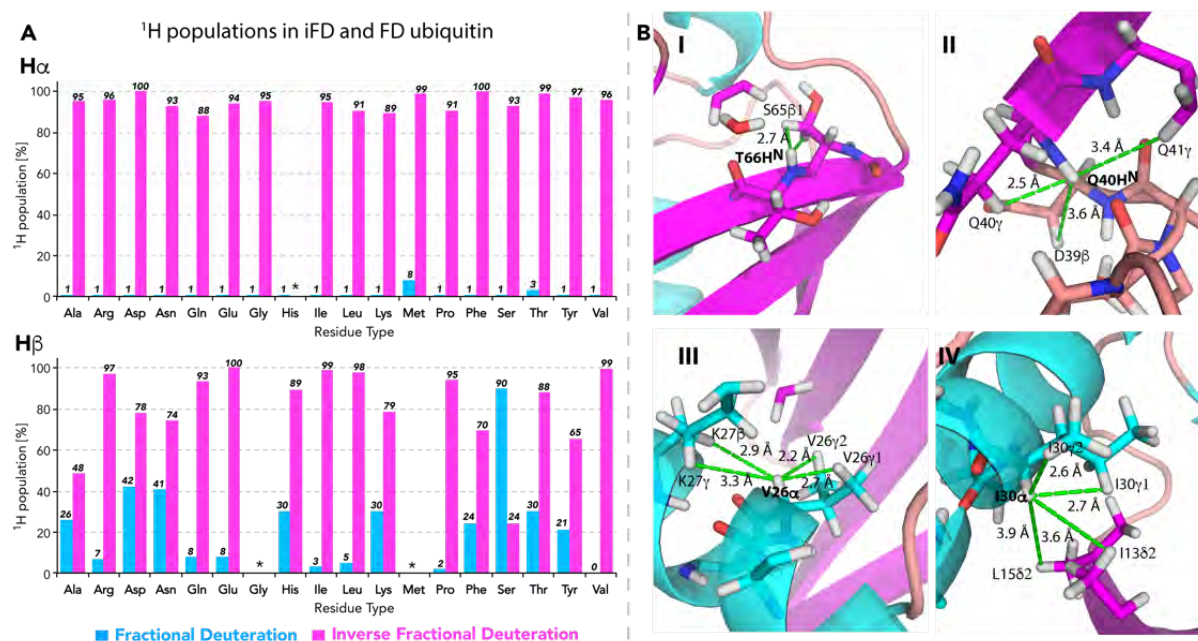


**Figure 2.** A) Protonation levels for H $\alpha$  and H $\beta$  protons in iFD vs FP ubiquitin. The very high protonation levels at the H $\alpha$  positions can be easily rationalized given that H $\alpha$  are essentially incorporated during protein expression from the solvent, which is proton-based (100 % H<sub>2</sub>O) in iFD labelling, while the H $\alpha$  levels are close to zero with D<sub>2</sub>O-based FD labelling. The H $\beta$  levels also correlate inversely with FD labelling. B) Panels I-IV show examples of H<sup>N</sup> and H $\alpha$  which show relatively stark linewidth gains in iFD ubiquitin because the <sup>1</sup>H density in proximity is considerably reduced with iFD labelling (25–75 %). **Panel I** (T66H<sup>N</sup>): The closest proton to T66H<sup>N</sup> is S65H $\beta$  which has only ~25% 1H-level with iFD labeling. **Panel II** (Q40H<sup>N</sup>): Three close-by sidechain <sup>1</sup>H (Q40 $\gamma$ /Q41 $\gamma$ /D39 $\beta$ ) are only populated to ~50 %. **Panel III** (V26H $\alpha$ ): Four near-by sidechain <sup>1</sup>H (K27 $\gamma$ /K27 $\beta$ /V26 $\gamma$ 1/V26 $\gamma$ 2) are only populated to ~50-75 %. **Panel IV** (I30H $\alpha$ ): Four close-by sidechain <sup>1</sup>H (I1382/L1582/I30 $\gamma$ 2/I30 $\gamma$ 1) are only populated to ~50-75 %.

*Inverse Fractional Deuteration in KcsA*

To improve the  $^1\text{H}$  resolution of water-inaccessible protein regions, we further combined iFD labeling with a  $\text{D}_2\text{O}$  wash step. This was demonstrated with the  $\text{K}^+$  channel KcsA, a well-accepted model for ion channel gating.<sup>21</sup> Figure 3B shows a 2D NH spectrum of iFD [ $^{13}\text{C}$ ,  $^{15}\text{N}$ ]-labeled KcsA, reconstituted in *E. coli* lipids and protonated buffers, acquired at 60 kHz MAS and 800 MHz. This spectrum, which shows the  $\text{H}^{\text{N}}$  signals of the entire channel, demonstrates improved resolution when compared to earlier results with fully protonated KcsA,<sup>11</sup> and readily allows identifying previously assigned water-exposed signals (annotated in red, which are also present in FD KcsA in Figure 3A).<sup>20</sup> To exclusively select the TM domain, we incubated iFD-labeled KcsA in  $\text{D}_2\text{O}$  and acquired a 2D NH spectrum, which featured a stark enhancement in spectral quality with well-resolved signals as narrow as 0.13 ppm (Figures 3C, E). The resolution improvement is partly due to the virtually complete disappearance of the water-exposed residues, which reduces spectral congestion (See Figure S6 for a spectral overlay). Remarkably, the removal of water protons (and other exchangeable  $^1\text{H}$ ) further narrows the linewidth of the TM  $\text{H}^{\text{N}}$  by 25 % on average compared to the spectrum shown in Figure 2A (Figure 2E and Table S7). The latter has not been observed before in ssNMR spectroscopy and implies that residual dipolar couplings to water protons in the solvent can contribute to the broadening of the  $^1\text{H}$  linewidth in highly protonated membrane proteins, even at 60 kHz MAS and a sample temperature of 35 °C. Such couplings are presumably substantial in KcsA owing to the presence of large internal water-filled cavities and buried water.<sup>11</sup> We could assign approximately half of the resonances in the spectrum in Figure 3C based on 3D  $\text{C}\alpha\text{NH}$ ,  $\text{C}\alpha(\text{CO})\text{NH}$ ,  $\text{CONH}$ , and  $\text{CO}(\text{C}\alpha)\text{NH}$  experiments (Figure 3D), supplemented with 3D  $\text{N}\text{C}\alpha\text{CX}$  and 2D  $\text{N}(\text{CO})\text{CX}$  spectra (Figure 3F) to identify residue types, and supported by available  $^{13}\text{C}$  and  $^{15}\text{N}$  chemical-shift data.<sup>22,23</sup> These assignments include a number of functionally essential structural elements that can be accessed here for the first time with  $^1\text{H}$  detection.

The selectivity filter, responsible for the stringent selection of  $\text{K}^+$  over  $\text{Na}^+$  ions, comprises the 75-TVGYG-79 signature sequence, which is common to all  $\text{K}^+$  channels.<sup>21</sup> Whereas only the exchangeable G79 residue was detectable in a former study,<sup>20</sup> here we could also assign residues T74–G77, providing access to almost the entire filter. Moreover, we assigned the pore helix L66–E71, a critical element for C-type inactivation,<sup>21</sup> as well as large stretches of the TM1 (transmembrane 1) helix including residues L41–L49, which precede the lipid-sensitive turret.<sup>22</sup> However, we could not unambiguously assign residues of the inner TM2 (transmembrane 2) helix, which was partly due to spectral overlap. Yet, while certain TM2 residues (such as V93–V95) were identified in the spectrum in Figure 3C, our data suggest that the TM2 helix partly exchanges with  $\text{D}_2\text{O}$ , especially C-terminal of the flexible hinge G104.<sup>21</sup>

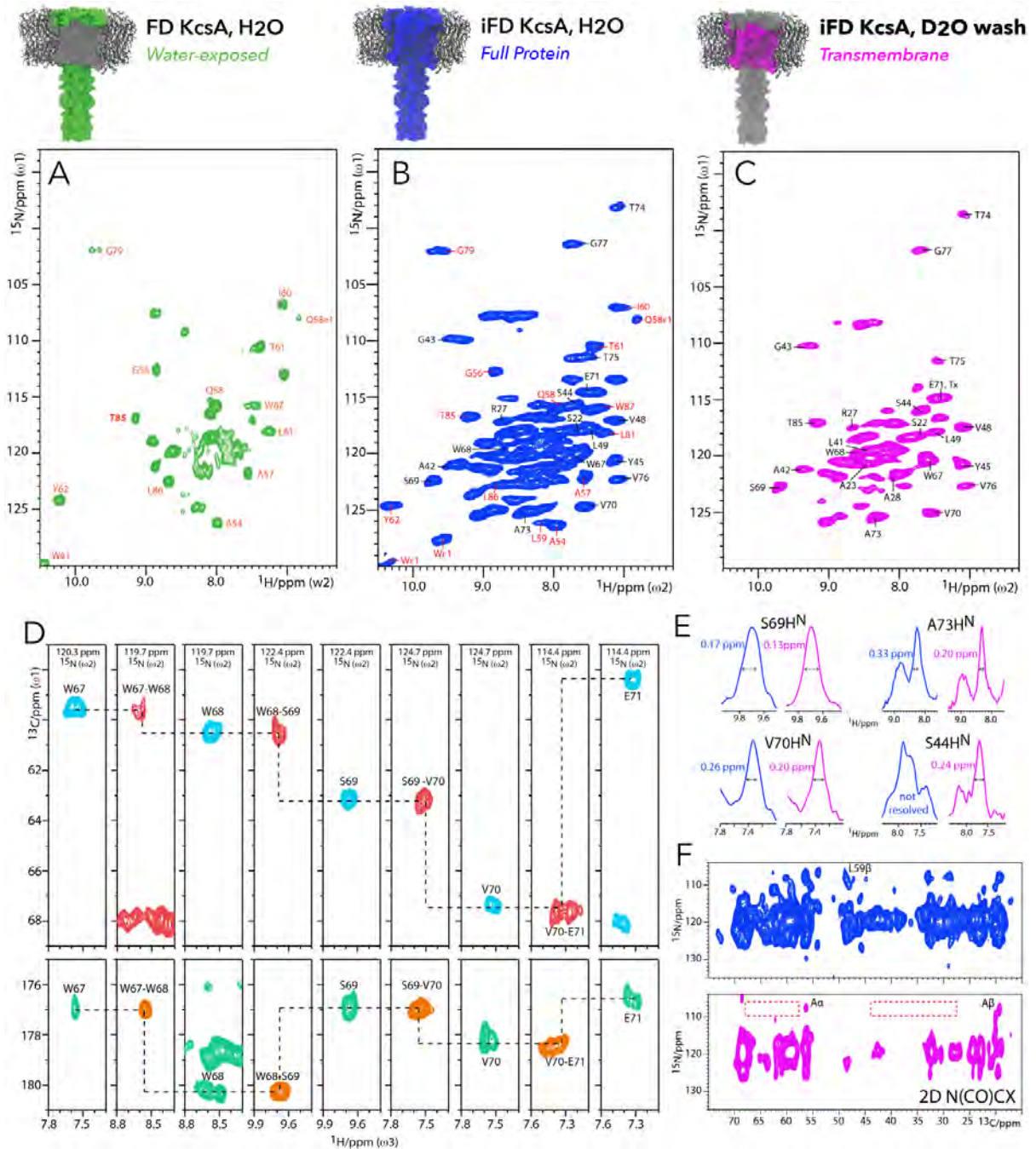


**Figure 3.**  $^1\text{H}$  detection of water-inaccessible regions in the ion channel KcsA. All  $^1\text{H}$ -detected data were recorded at 800 MHz and 60 kHz MAS. 2D NH spectra of reconstituted A) FD KcsA (green) B) iFD KcsA in  $\text{H}_2\text{O}$  (blue) and C) iFD KcsA after a  $\text{D}_2\text{O}$  wash (magenta). Assignments in red and black were obtained with FD KcsA<sup>20</sup> and iFD KcsA, respectively. Notice that all  $\text{H}^{\text{N}}$  are present in iFD KcsA in  $\text{H}_2\text{O}$ , whereas water-accessible  $^1\text{H}$  are exclusively present in FD KcsA and only the  $^1\text{H}$  of the TM remain after the  $\text{D}_2\text{O}$  wash in iFD. D)  $^1\text{H}$ -detected assignments of residues W67–E71 of the pore helix. Strip plots are shown for 3D  $\text{C}\alpha\text{NH}$  (cyan),  $\text{C}\alpha(\text{CO})\text{NH}$  (red),  $\text{CONH}$  (orange), and  $\text{CO}(\text{C}\alpha)\text{NH}$  (turquoise) experiments. E)  $t_1$  cross-sections extracted from 2D NH spectra of iFD KcsA before (blue) and after (magenta) a  $\text{D}_2\text{O}$  wash. F) Cut-out from a 2D  $\text{N}(\text{CO})\text{CX}$  spectra of (top)  $\text{H}_2\text{O}$ -incubated KcsA measured at 700 MHz and 14 kHz MAS and (bottom)  $\text{D}_2\text{O}$ -incubated KcsA, measured at 800 MHz and 17 kHz MAS. The  $^1\text{H}$ - $^{15}\text{N}$  CP contact time was kept short (250  $\mu\text{s}$ ) to select water-inaccessible residues with protonated HN, as described<sup>16</sup>. In the  $\text{D}_2\text{O}$ -exchanged spectrum, the signals arising from the

glycines (100-110  $^{15}\text{N}$  ppm) are transferred to alanine residues. This means that the flexible hinge residues G104 and G116 possibly exchanged since these would transfer the magnetization to F103 and V115 respectively, which would have appeared at the region delimited by the red boxes.

This hypothesis was corroborated by a 2D N(CO)CX experiment in  $\text{D}_2\text{O}$  with short initial  $^1\text{H}$ - $^{15}\text{N}$  CP times,<sup>16</sup> in which G104 and G116 could not be observed (Figure 3 F), and it is in line with studies in micelles.<sup>24</sup> It was also corroborated by the observation of only about 50 signals in the 3D C $\alpha$ NH spectrum although we should observe approximately 65 resonances if all TM H $^{\text{N}}$  were retained in  $\text{D}_2\text{O}$ . H/D exchange within the membrane is therefore a curse and a blessing – whereas it complicates assignments owing to missing sequential contacts, it can give insight into protein flexibility and membrane topology. In this regard, it should be noted that the FD and iFD- $\text{D}_2\text{O}$  labelling schemes are complementary to each other (Figure 3 A, C) and can be used as such to study the different domains of membrane protein.

### *An atomic insight into the native state*

The high spectral quality conferred by our iFD two-step approach even allows measuring the TM part of KcsA directly in a native cell membrane.<sup>25-28</sup> Cell membranes are much more complex than reconstituted liposomes in terms of lipid and protein composition, and this can influence membrane protein function. However, adequate spectral quality is a challenge in cellular ssNMR studies owing to the low concentration of the target protein. *In situ* iFD KcsA was expressed in the *E. coli* inner membrane using rifampicin to ensure selective  $^{13}\text{C}$ ,  $^{15}\text{N}$ -labeling of KcsA and reduce the endogenous spectral background.<sup>27</sup> The outer membrane was removed to increase the amount of KcsA in the sample, which was then incubated in deuterated solvents for three days prior to the ssNMR experiments. We obtained a surprisingly well-resolved *in situ* 2D NH spectrum (Figure 4 A), which exhibited the clear spectral fingerprint of closed-conductive KcsA<sup>22</sup> (Figure 4B) without any discernible background signal. This is remarkable as the KcsA concentration *in situ* was about seven times lower than *in vitro* (see methods). We could readily annotate the *in situ* spectrum based on our *in vitro* assignments. To the best of our knowledge, this was the first time that a few nanomoles of a membrane protein (that is, ca. 3 nanomoles of KcsA, corresponding to ca. 175 mg of protein) could be assigned *in situ* with  $^1\text{H}$ -detected ssNMR spectroscopy. Cellular KcsA showed only small chemical shift perturbations (CSPs) compared to reconstituted KcsA (Figure 4 C), implying that *E. coli* lipids are good membrane mimics. Yet, we observed a few marked differences *in situ*, which we discuss in the following section, together with the assignments and relaxation studies performed *in vitro*. In addition, many signals in the *in situ* spectrum are strongly broadened by up to 100 % (Figure 4 D), which arises from inhomogeneous line broadening owing to the cellular heterogeneity. This type of broadening is independent of the MAS frequency and likely impacts on sensitivity when using smaller (< 1.3 mm) rotor diameters.

*Dynamics are sensitive to the membrane composition*

We used our assignments to perform a detailed analysis of the motion in the TM part of KcsA. Understanding this motion is of high relevance for the ion channel function, which depends on dynamic changes of membrane-embedded structural elements.<sup>29,30</sup> It is also of particular interest to decipher the motion of the filter as its flexibility is assumed to be related to a ubiquitous ion channel regulatory mechanism known as modal gating.<sup>29</sup> NMR relaxation is a powerful method to study protein dynamics,<sup>31,32</sup> and many of our assigned <sup>1</sup>H<sup>N</sup> signals are well-resolved (Figure 3 C), which is a prerequisite for site-resolved analysis. It has previously been shown that <sup>15</sup>N transverse rotation frame relaxation ( $T_{1\rho}$ ), which is a sensitive reporter of motion on the nano- to micro- second timescale, can be quantitatively extracted in fully protonated samples at higher (> 50 kHz) MAS frequencies,<sup>33</sup> at which coherent contributions to the magnetization decay are largely suppressed. We first measured the bulk <sup>15</sup>N  $T_{1\rho}$  as a function of the spinlock amplitude (Figure S9). In agreement with measurements in GB1 and membrane protein ASR,<sup>33,34</sup> we found a relaxation plateau for spinlock fields from about 10 to 25 kHz, yielding a bulk <sup>15</sup>N  $T_{1\rho}$  of approximately 100 ms for the TM part of KcsA. The site-resolved <sup>15</sup>N  $T_{1\rho}$  relaxation rates ( $R_{1\rho}$ ) show a rather uniform dynamic regime for the lipid-confined TM part, which is in line with measurements in micelles<sup>35</sup> (Figures 5 A, B).

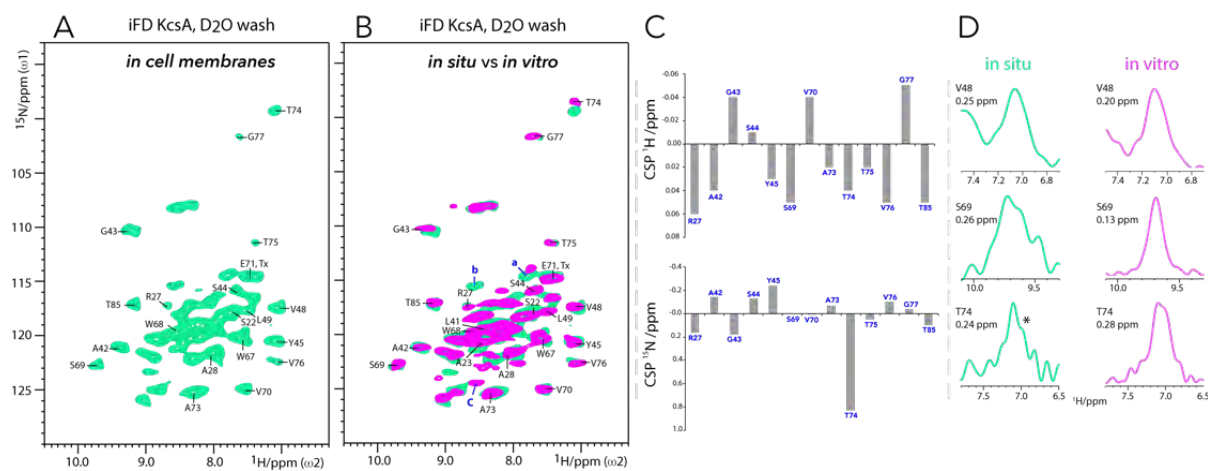


**Figure 4.** **A)** 2D NH spectrum of iFD/D<sub>2</sub>O KcsA measured directly in cell membranes of *E. coli*. The spectrum was recorded at 60 kHz MAS and 800 MHz. **B)** Spectral overlay of Figures 3 C and 4 A, i.e., *in vitro* (magenta) and *in situ* (green). The spectra superimpose very well, except for T74 and the unassigned signals a, b and c. Signal a is a threonine residue and shows a large CSP (+0.6 <sup>15</sup>N ppm). Signal b is present in *in vitro* KcsA, however much weaker than in native cell membranes, which suggests local topology differences between the two samples. Differences in the topology and water-accessibility are presumably also the reasons for the absence of signals c in cellular KcsA, since signal c became also weaker in the reconstituted KcsA sample over time. **C)** Chemical shift perturbations (CSP) of assigned and resolved peaks. CSP were derived as the chemical shift difference between signals in 2D NH spectra of *in situ* and *in vitro* D<sub>2</sub>O-washed iFD KcsA (i.e., CSP = *in situ* – *in vitro*). The CSPs are relatively small, especially for the protons. **D)** t<sub>1</sub> cross-sections from Figures 4A and 3C. See Table S5 for complementary linewidth analysis. \* S/N ratio of T74 was ~7.3 and potentially too low for a correct determination of the linewidth.

However, the entire filter stretch T74–G77 remarkably features modestly, but clearly enhanced  $^{15}\text{N}$   $R_{1\rho}$ , which is indicative of slow and presumably collective molecular motion. This motion very likely corresponds to slow nanosecond to microsecond dynamics as residues T74 and T75 did not show increased fast nanosecond motion in a previous  $^{15}\text{N}$   $T_1$  relaxation study.<sup>36</sup> Such slow motions have not been observed before in membrane-embedded KcsA and can be important for its function as the filter backbone is immediately involved in ion conductance. Interestingly, flicker transitions,<sup>29</sup> a form of modal gating represented by rapid channel opening and closure, also occur on the microsecond timescale, and flickering is indeed thought to be related to dynamic rearrangements around V76. Increased filter dynamics were also corroborated by reduced signal intensities in dipolar experiments (Figure 5 G). The conformational flexibility is also reflected in the  $\text{H}^{\text{N}}$  linewidth, which is consistently larger for the filter than for the pore helix (Table S7). The TM1 helix residues A42–L49 are least subjected to slow motion and feature slightly smaller  $R_{1\rho}$  rates than the pore helix. However, the G43 $\text{H}^{\text{N}}$  resonance, which is by far the broadest of all  $\text{H}^{\text{N}}$  (0.44 ppm), is split into two signals with different relaxation decays (Figures 5 C, D). As the G43 chemical shift is sensitive to the filter ion-binding mode,<sup>23</sup> this splitting may hence also be related to the conformational flexibility of the filter. Intriguingly, unlike almost all other resonances, the G43 $\text{H}^{\text{N}}$  resonance is much narrower (0.31 ppm) *in situ*, most likely because only one conformation is present (Figure 5 E). This finding suggests that the KcsA conformational dynamics are, at least locally, altered in native bacterial membranes compared to liposomes.

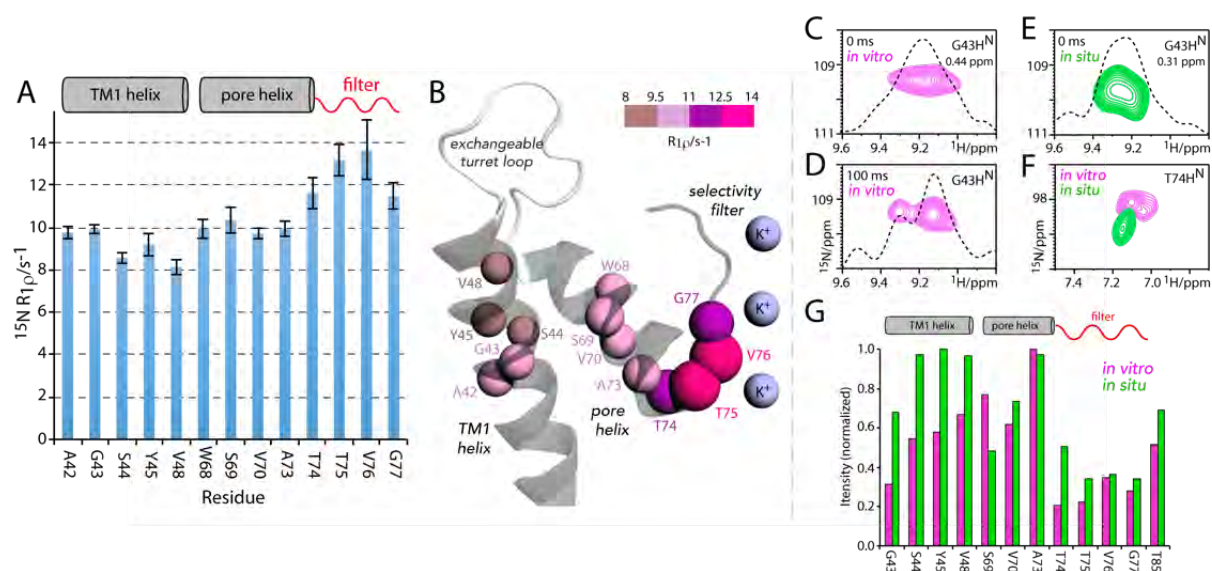


**Figure 5.** Dynamics recorded for the TM part of D<sub>2</sub>O-washed iFD KcsA. All data were acquired at 60 kHz MAS and 800 MHz using a  $^{15}\text{N}$  spinlock field of 20 kHz. **A**)  $^{15}\text{N}$   $R_{1\rho}$  relaxation rates. **B**) Illustration of the  $^{15}\text{N}$   $R_{1\rho}$  rates on the KcsA structure (PDB No. 1K4C). Analyzed residues are shown as color-coded spheres whose size is proportional to  $R_{1\rho}$ . **C**, **D**)  $^{15}\text{N}$   $T_{1\rho}$  experiments *in vitro* with a spinlock duration of 0 ms or **D**) 100 ms reveal two signals for G43 $\text{H}^{\text{N}}$ . **E**) G43 $\text{H}^{\text{N}}$  exhibits only one conformation *in situ*. **F**) T74 showed a  $^{15}\text{N}$  chemical shift perturbation of +0.8 ppm *in situ*. **G**) Signal-to-noise ratios of resolved residues *in vitro* (magenta) and *in situ* (green) D<sub>2</sub>O-washed KcsA.

While the spectral sensitivity inhibits site-resolved relaxation studies in cellular KcsA, an analysis of signal intensities in dipolar experiments showed the lowest intensities for residues T74–G77. This result strongly suggests that the enhanced filter dynamics are maintained in the native membrane (Figure 5G). In fact, the conformational flexibility of the filter seems to be further enhanced *in situ* as the filter signals are much reduced compared to those of the TM1 helix. Remarkably, also the relative intensities of the filter residues are changed, especially for T74, which displays the lowest intensity of all filter residues *in vitro* and by far the highest sensitivity *in situ*. This suggests that the dynamics of the filter are changed in cellular KcsA, which is further corroborated by a relatively strong <sup>15</sup>N CSP of +0.8 ppm for T74 *in situ* (Figures 4 C and 5 F). A potential reason for this apparently different behavior of the filter may be the altered lipid composition in the bacterial membrane, which is known to influence the filter,<sup>22</sup> or differential clustering of KcsA channels.<sup>37</sup> Against the backdrops presented here, it is therefore important to explore how exactly molecular motion modulates the channel function. Whereas this data clearly shows enhanced filter dynamics, further extensive measurements are necessary to fully understand the timescales and amplitudes of these dynamics.

## Conclusion

In conclusion, this chapter introduces an approach that enables the <sup>1</sup>H detection of water-inaccessible proteins with high sensitivity and resolution. We expect this method to be especially powerful for the study of membrane proteins and amyloid fibrils, which both exhibit domains that are unaffected by hydrogen/deuterium exchange. Moreover, this method allowed for the first time the use of <sup>1</sup>H detection for the detailed analysis of a membrane protein in native cell membranes. This constitutes an important advance in ssNMR spectroscopy as membrane protein function often critically depends on the native environment.

## Material and Methods

### *Sample Preparation*

#### Inverse Fractional Deuterated ubiquitin

Ubiquitin was expressed in *E.coli* BL21 cells on H<sub>2</sub>O-based M9 medium supplemented with 0.5 g/L <sup>15</sup>NH<sub>4</sub>Cl and 2 g/L D-glucose-<sup>13</sup>C<sub>6</sub>-d<sub>7</sub>. The purification procedure and further sample preparation was followed as described previously.<sup>20</sup> Briefly, cells were harvested and lysed by sonication after lysozyme treatment. Cell debris was removed and the clear supernatant was loaded into a HiTrap MonoS column (cation exchange). Sample was purified with a gradient (5 – 30 %) of NaCl using an ÄKTA system and elution was monitored by A<sub>280nm</sub> (Buffer A 20 mM NH<sub>4</sub>Ac pH 5.1, Buffer B 1 M NaCl 20mM NH<sub>4</sub>Ac pH 5.1). Fractions of interest were loaded into

a Sephadex G-75 (gel filtration) using 150 mM NaCl, 20mM NH<sub>4</sub>Ac pH 5.1 as running buffer to afford pure ubiquitin, as evaluated by SDS-PAGE (Figure 6). Samples were concentrated using a Amicon Centrifugal Filter with a 3.0 kDa filter cutoff and were ready for analysis. Obtained yield was ~16 mg/L.

Solution state NMR samples were buffer exchanged with 50 mM Tris buffer pH 7.5 prior to measurement. Microcrystalline ubiquitin for solid-state NMR was obtained by dissolving it in 20 mM citrate buffer pH 4 (final concentration) and 2-Methyl-2,4-pentanediol (60 % final). Crystals were collected by centrifugation at 100.000 ×g and filled into a 1.3 mm zirconia rotor.

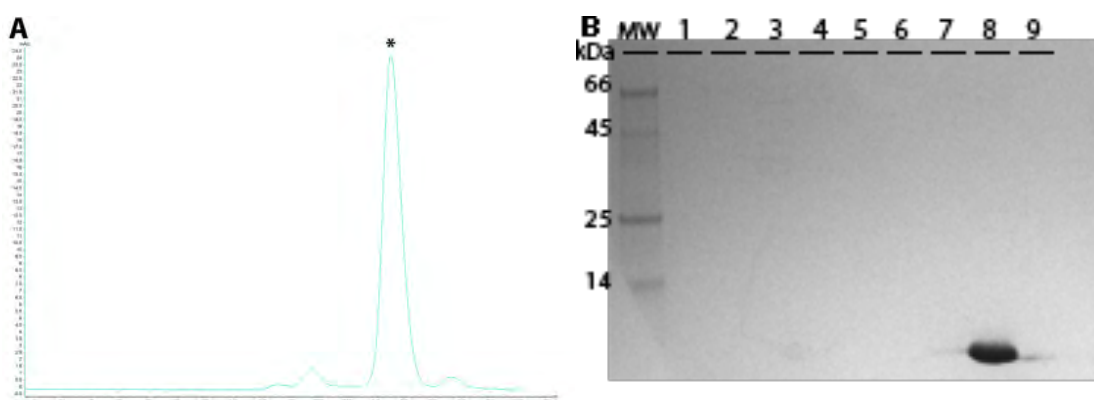


**Figure 6.** A) Elution profile of ubiquitin during gel filtration. B) SDS-Page. Well #8 contains the fraction annotated in A).

#### Fully Protonated ubiquitin

FP ubiquitin followed the same procedure as the previous iFD sample, except that fully protonated D-glucose-<sup>13</sup>C<sub>6</sub> was supplemented instead of deuterated glucose. The yield was ~20 mg/L.

#### Inverse Fractional Deuterated KcsA in vitro

KcsA was expressed in *E.coli* M15 cells using standard H<sub>2</sub>O-based M9 medium supplemented with 0.5 g/L <sup>15</sup>NH<sub>4</sub>Cl and 2 g/L D-glucose-<sup>13</sup>C<sub>6</sub>-d<sub>7</sub>. The protein was extracted and purified as described previously,<sup>22</sup> resulting in a final yield of 10 mg/L. Briefly, cells were harvested, treated with lysozyme and lysed by French press (12.5 psi). Cell debris was removed with a low spinning centrifugation (2.000 ×g) and membranes were collected with a high spinning centrifugation at 70.000 ×g. Membrane pellets were resuspended in phosphate buffer (50 mM, 150 mM KCl, pH 7.5) and DM detergent at 40 mM, until whole pellet was dissolved. Sample was incubated with NiNTA beads (Thermo Fischer) and KcsA was eluted with an imidazole gradient in the same buffer (pH adjusted to 7.8) at 4 mM DM. Imidazole was removed by buffer exchange using an a Amicon filter 50 kDa cutoff. Protein concentration was estimated by a detergent compatible Bradford assay (Thermo Fischer), using BSA as standard.

Liposome reconstitution was performed using *E.coli* polar lipids (Avanti) at 1:100 protein:lipid molar stoichiometry. Detergent was removed using polystyrene beads (Bio-Beads SM-2), as also previously described.<sup>22</sup> Prior to ssNMR measurements, reconstituted samples were suspended in fully protonated phosphate buffer. For D<sub>2</sub>O-washed KcsA, samples were washed twice in fully deuterated phosphate buffer (50 mM pH7, 50 mM NaCl and 50 mM KCl) and incubated in ~1 ml of deuterated buffer for three days prior to the measurements.

For the solid-state NMR measurements, liposomes were filled into a 1.3 mm zirconia rotors for <sup>1</sup>H-detection experiments and into 3.2 mm zirconia rotors for <sup>13</sup>C-detected experiments.

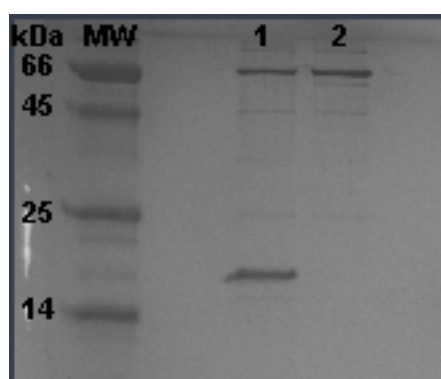


**Figure 7.** SDS Page of pure fractions collected after the NiTNA purification. Fraction #1 was boiled whereas #2 was not, which shows that the top band corresponds to KcsA tetramer (MW ~66 kDa) and the bottom band to the monomer (~16.5 kDa).

#### Inverse Fractional Deuterated KcsA in situ

KcsA was expressed in *E.coli* Lemo21 cells using the T7 inhibition system as described.<sup>27</sup> Cells were first grown in unlabeled M9 media until saturation. Prior to induction, the cells were harvested and re-suspended in an H<sub>2</sub>O-based M9 medium supplemented with 0.1 mg/mL rifampicin, 0.5 g/L <sup>15</sup>NH<sub>4</sub>Cl and 2 g/L D-glucose-<sup>13</sup>C<sub>6</sub>-d7. After expression, cells were washed, lysed and the cellular membranes were extracted. The membrane fractions were separated according to their density difference using a sucrose gradient (gradient (w/v) 36%, 45%, 51%, 55 %). The inner membrane fraction was collected, washed twice with phosphate buffer (pH 7) and incubated in ~1ml of deuterated phosphate buffer (pH7) for a total of three days before the ssNMR measurements. This procedure (except for the D<sub>2</sub>O-wash) is described with greater detail in Ref. (27).

#### Qualitative determination of KcsA in the native inner cell membrane

The KcsA concentration was estimated in a qualitative approach by comparing the signal-to-noise (S/N) ratios of the 2D NH spectra measured *in situ* and *in vitro* (Figures 3C and 4A). For comparison, the signals plotted in Figure 5G were employed. Signal intensities were used

rather than integrals, therefore we did not consider signals S69, A73, T75, and G77 for the S/N analysis, because these signals are substantially broader *in situ* than *in vitro*. Likewise, T85 was not used because its signal intensity is attenuated over time by H/D exchange with the deuterated solvent. Signal X1 was nonetheless considered in order to increase the sample population.

**Table 1.** Intensity of selected signals for S/N comparison between the *in situ* and *in vitro* KcsA samples.

	<i>Vitro</i>	<i>Situ</i>	<i>Vitro/Situ</i>
<b>G43</b>	16.34	9.81	1.66
<b>S44</b>	28.62	14.10	2.03
<b>Y45</b>	30.50	14.47	2.11
<b>V48</b>	35.12	13.95	2.52
<b>V70</b>	32.50	10.62	3.06
<b>T74</b>	10.99	7.33	1.50
<b>V76</b>	18.16	5.30	3.43
<b>X1</b>	28.75	10.77	2.67
		<b>average</b>	<b>2.37</b>

Hence, the S/N *in vitro* is approximately twice higher than *in situ*. Since the 2D NH *in situ* was measured with 13.2 times the numbers of scans (NS) as compared with *in vitro*, we can qualitatively derive that the KcsA concentration *in vitro* is  $\sim 7$  times higher than in the native cell membrane, as  $\frac{[KcsA]_{vitro}}{[KcsA]_{situ}} = \sqrt{13.2} \times 2 \approx 7.2$  (to be noted that the S/N increases with  $\sqrt{NS}$ , hence the factor). Since the amount of *in vitro* KcsA in the sample is known (1.25 mg, corresponding to 16 nmol), by comparison the KcsA concentration *in situ* can be estimated, given that the sample volume is the same (1.3 mm rotor). Thus, the *in situ* sample is estimated to have  $\sim 175$   $\mu$ g of KcsA, corresponding to  $\sim 2.5$  nmol. This explains the need for 10.000 scans to acquire a sensitive 2D NH of KcsA in the inner membrane.

## NMR Spectroscopy

### <sup>1</sup>H-detection

All 3D ssNMR experiments were measured at 800 MHz and 60 kHz MAS. The effective sample temperature was set to  $\sim 308$  K. Water suppression was achieved with the MISSISSIPPI scheme.<sup>17</sup> Decoupling was performed with the PISSARRO scheme<sup>18,38</sup>, during all

direct and indirect acquisition periods. For all experiments and all nuclei, the decoupling amplitude was set to one quarter of the MAS frequency, i.e., 15 kHz and not further optimized. Decoupling times were optimized between 50 and 74  $\mu$ s for all nuclei. For all experiments, quadrature-detection in the indirect dimensions was achieved using TPPI. The pulse sequence used to acquire 2D <sup>13</sup>C/<sup>15</sup>N - <sup>1</sup>H spectra was described in reference 4. The recycle delay ('d1 time') was  $\sim$ 0.8 – 1.0 s for all <sup>1</sup>H-detected measurements. For all 2D spectra / planes here shown, it was used a contour level increment of 1.05 – 1.10 and 50 – 60 contour levels. For all 3D measurements, sparse Poisson-Gap15 sampling was used and reconstruction was done with compressed sensing<sup>39</sup> in Topspin 3.2 (Bruker Biospin). Note that all 3D experiments performed on KcsA were done with the D<sub>2</sub>O-incubated in vitro sample. Pulse sequence diagrams for the herein used experiments were already been published elsewhere.<sup>20</sup>

### 3D C $\alpha$ NH

The initial <sup>1</sup>H  $\rightarrow$  <sup>13</sup>C transfer was brought with ramped (20 %) cross polarization with contact times of 450  $\mu$ s and 500  $\mu$ s for iFD ubiquitin and iFD KcsA (D<sub>2</sub>O), respectively. Polarization was further transferred from <sup>13</sup>C $\alpha$   $\rightarrow$  <sup>15</sup>N with SPECIFIC CP<sup>40</sup> using 41 kHz irradiation on <sup>13</sup>C and 20 kHz on <sup>15</sup>N during 6.0 ms for both iFD ubiquitin and iFD KcsA (D<sub>2</sub>O). Despite the relatively strong irradiation on the <sup>13</sup>C channel, the transfer was specific for C $\alpha$ , which was achieved by moving the <sup>13</sup>C carrier upfield (to  $\sim$ 0 ppm), away from the CO signal region. No decoupling on <sup>1</sup>H was necessary during SPECIFIC CP transfer, since heteronuclear dipolar couplings involving <sup>1</sup>H are much reduced at 60 kHz MAS in iFD proteins. The final transfer from <sup>15</sup>N  $\rightarrow$  <sup>1</sup>H was carried out with ramped (10 %) cross-polarization (65 kHz on <sup>15</sup>N, 124 kHz on <sup>1</sup>H, 750  $\mu$ s contact time for iFD ubiquitin, 500  $\mu$ s for iFD KcsA). The measurement time was 14h for ubiquitin and 2d 20h for KcsA using sparse [66 % for ubiquitin / 50 % for KcsA] sampling.

### 3D CONH

Analogous to the C $\alpha$ NH experiment. The <sup>1</sup>H  $\rightarrow$  <sup>13</sup>C CP contact time was 3 ms in iFD KcsA (D<sub>2</sub>O). SPECIFIC CP from CO to <sup>15</sup>N was established with 41 kHz irradiation on <sup>13</sup>C and 20 kHz irradiation on <sup>15</sup>N during 6.0 ms in the absence of <sup>1</sup>H decoupling. The <sup>13</sup>C carrier was placed at  $\sim$ 165 ppm during the SPECIFIC CP step. <sup>15</sup>N  $\rightarrow$  <sup>1</sup>H CP was carried out as described in the C $\alpha$ NH experiment. The measurement time was 2d 11h for KcsA using sparse [54 %] sampling.

### 3D NC $\alpha$ H $\alpha$

After <sup>1</sup>H  $\rightarrow$  <sup>15</sup>N ramped (20 %) CP transfer over 1.5 ms (125 kHz on <sup>1</sup>H, 50 kHz on <sup>15</sup>N), <sup>15</sup>N  $\rightarrow$  <sup>13</sup>C $\alpha$  transfer was performed with SPECIFIC CP over 6.0 ms, during which the <sup>13</sup>C

carrier was placed  $\sim 0$  ppm (as described above). The final transfer from  $^{13}\text{C}\alpha \rightarrow ^1\text{H}$  was done with ramped (10 %) cross-polarization using  $185 \mu\text{s}$  contact time. The measurement time was 2d 12h for iFD ubiquitin using sparse [70 %] sampling.

### 3D $\text{C}\alpha(\text{CO})\text{NH}$

$^1\text{H} \rightarrow ^{13}\text{C}$  CP transfer was performed with  $500 \mu\text{s}$  contact time and the  $^{13}\text{C}$  carrier placed at  $\sim -10$  ppm, which yielded selective transfer to the aliphatic carbons, as described in Refs. (4, 5).  $^{13}\text{C}$ - $^{13}\text{C}$  mixing was brought about with double quantum DREAM<sup>19</sup> recoupling using 27 kHz recoupling amplitude (20 % ramp) over 6.25 ms. Best transfer performance was achieved with the  $^{13}\text{C}$  carrier close to the  $^{13}\text{CO}$  region ( $\sim 170$  ppm) during the transfer. No  $^1\text{H}$ -decoupling was applied during DREAM recoupling, which did not lead to any perceivable transfer losses in comparison to the application of  $^1\text{H}$ -decoupling. The following  $^{13}\text{CO} \rightarrow ^{15}\text{N} \rightarrow ^1\text{H}$  transfer steps were analogous to the ones described in the 3D CONH experiment. The measurement time was 8d 8h for iFD KcsA ( $\text{D}_2\text{O}$ ) using sparse [46 %] sampling.

### 3D $\text{CO}(\text{C}\alpha)\text{NH}$

Analogous to the  $\text{CO}(\text{C}\alpha)\text{NH}$  experiment. The  $^{13}\text{C}$  carrier was placed at  $\sim 185$  ppm during the initial  $^1\text{H} \rightarrow ^{13}\text{C}$  CP step, which yielded selective transfer to the carbonyl carbons.  $^{13}\text{C}$ - $^{13}\text{C}$  mixing was brought about with double quantum DREAM recoupling using 27 kHz recoupling amplitude (20 % ramp) over 4.3 ms. Best transfer performance was achieved with the  $^{13}\text{C}$  carrier close to the  $^{13}\text{C}\alpha$  region ( $\sim 65$  ppm) during the transfer. The following  $^{13}\text{C}\alpha \rightarrow ^{15}\text{N} \rightarrow ^1\text{H}$  transfer steps were analogous to those described in the 3D  $\text{C}\alpha\text{NH}$  experiment. The measurement time was 6d 18h for iFD KcsA ( $\text{D}_2\text{O}$ ) using sparse [50 %] sampling.

### 3D CCH

$^1\text{H} \rightarrow ^{13}\text{C}$  CP transfer was performed with  $450 \mu\text{s}$  contact time in iFD ubiquitin.  $^{13}\text{C}$ - $^{13}\text{C}$  mixing was brought about with double quantum DREAM recoupling using 27 kHz recoupling amplitude (20 % ramp) over 3.5 ms with the  $^{13}\text{C}$  carrier placed at  $\sim 55$  ppm.  $^{13}\text{C} \rightarrow ^1\text{H}$  transfer was done with a short ( $200 \mu\text{s}$ ) CP step to ensure one-bond transfer. The measurement time was 3d 2h in iFD ubiquitin using sparse [60 %] sampling.

### 2D NH of KcsA in cell membranes

This experiment was performed with 9760 scans (i.e., 13.2\*times more scans than for the corresponding experiment with KcsA in vitro) and had a total duration of 5d 16h.

## <sup>13</sup>C-detected

All <sup>13</sup>C-detected experiments were carried out with D<sub>2</sub>O-washed FP KsA.

### 3D NCαCX

This experiment was carried out at 500 MHz and 12 kHz MAS and a real temperature of ~278 K. The initial <sup>1</sup>H → <sup>15</sup>N transfer time was kept very short (250 μs) to select only water-inaccessible residues with protonated backbone nitrogens. The selection was very good, which was verified in a 2D NCα experiment, in which all residues of the water-accessible turret loop were absent. The measurement time was 9d 15h using sparse [72 %] sampling.

### 2D N(CO)CX

This experiment was carried out at 800 MHz and 17 kHz MAS and a real temperature of ~278 K. Analogously to the 3D NCαCX experiment, the initial <sup>1</sup>H → <sup>15</sup>N transfer time was kept very short (250 μs) to select only water-inaccessible residues with protonated backbone nitrogens. The measurement time was 2d 15h using conventional sampling.

## <sup>15</sup>N T1ρ measurements

<sup>1</sup>H-detected <sup>15</sup>N T1ρ measurements were carried out as described in Refs. (32,33) with the below shown pulse sequence (Figure 6). All measurements were performed at 800 MHz magnetic field with 60 kHz MAS using recycle delays of 0.9 s. The <sup>15</sup>N transverse magnetization decay was probed with a <sup>15</sup>N spinlock field of 20 kHz. No <sup>1</sup>H-decoupling was applied during the <sup>15</sup>N spinlock. Note that we found a <sup>15</sup>N T1ρ plateau from ~10–25 kHz spinlock power (Figure S8). Five points with 0, 20, 50, 100, and 200 ms duration of the spinlock were taken. The signals were processed with QSIN 3 window functions in both <sup>1</sup>H and <sup>15</sup>N dimensions to enhance the resolution. Only well-isolated peaks were considered for the analysis, for which we measured the peak intensities. The T1ρ trajectories were fit to single exponentials. Note that for G43, which shows a signal splitting (Figure 5 C,D), we used the maximal intensity of both conformations, given it was not possible to resolve the two conformations in the absence of a relaxation filter.

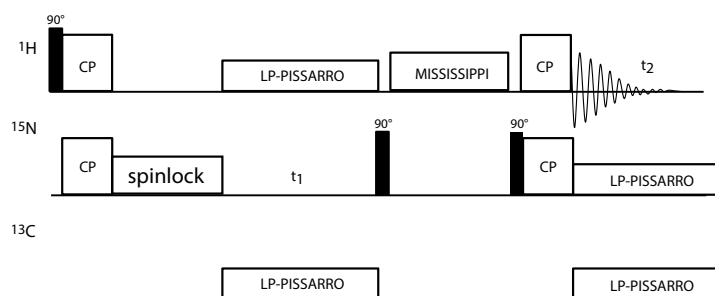


**Figure 8** . NMR pulse sequence to measure site-resolved <sup>15</sup>N T1ρ in the TM part of KcsA.

## Supporting Information

### S1. Spectra comparison between fully protonated (FP) and inversely fractionally deuterated (iFD) ubiquitin

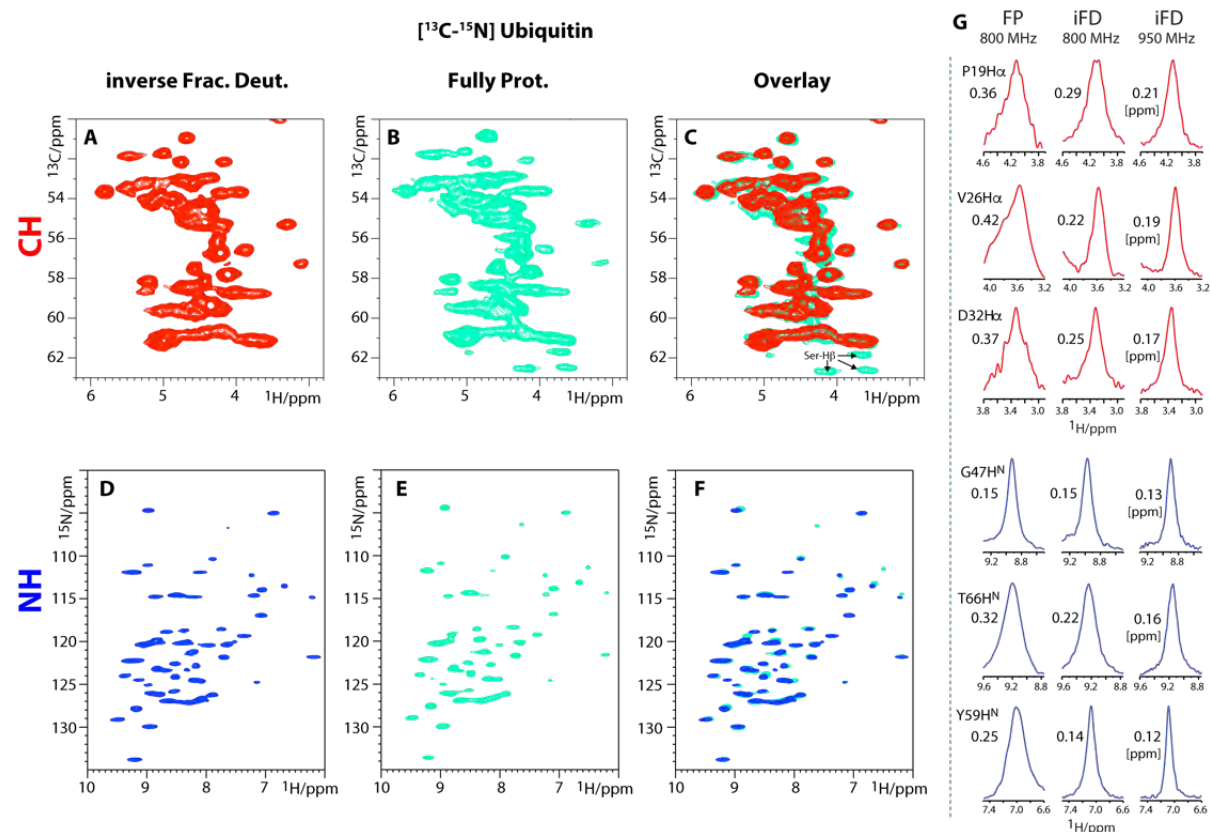


**Figure S1.** A-F) 2D comparison of 2D CH (A,B) and NH (D,E) spectra measured with iFD (A,D) and FP (B,E) ubiquitin at 800 MHz and 60 kHz MAS. Overlays are shown in C and F. Processing parameters are the same for both sample preparations. For the H $\alpha$  protons, it is readily visible that the  $^1\text{H}$ -resolution is improved in iFD ubiquitin. A 2D comparison is less useful for the HN, because they are well-resolved in both sample preparations. G) In 1D cross-sections (see also Figure 1E of the main text), it is however clearly discernible that the resolution is improved in iFD ubiquitin for both H $\text{N}$  and H $\alpha$ . Note that the H $\alpha$  are better resolved because they are closer to the  $^1\text{H}$ -diluted side-chains.

### S2. $^1\text{H}$ -linewidth comparison between fully protonated and inversely fractionally deuterated ubiquitin

Two different samples of FP ubiquitin were prepared and measured in order to diminish the influence of the sample quality on the linewidth. Only the FP sample that gave the best linewidth was considered for the evaluation.

The  $^{15}\text{N}$  linewidth, which is most sensitive to sample heterogeneity, was virtually exactly the same for the iFD and the FP ubiquitin samples that we compared (Figure S3), which strongly corroborates that we compared samples of similar quality.

**Table S2A.** Comparison of the H<sup>N</sup> (I) and H $\alpha$  (II) linewidth in FP and iFD ubiquitin. The linewidth (LW) improvement percentage was calculated as:

$$\text{Improvement [\%]} = \left( \frac{LW^{FP}}{LW^{iFD}} - 1 \right) \times 100.$$

**I) H<sup>N</sup> linewidth comparison:**

Field	950MHz	950MHz	800MHz	800MHz	800MHz	800MHz	800MHz
Residue	iFD [Hz]	iFD [ppm]	iFD [Hz]	iFD [ppm]	FP [Hz]	FP [ppm]	FP/iFD (%)
T9	127	0.134	138	0.173	147	0.184	6.52
G10	135	0.142	135	0.169	143	0.179	6.06
K11	144	0.152	169	0.212	197	0.246	16.42
I13	188	0.198	193	0.241	219	0.274	13.41
S20	139	0.146	149	0.186	197	0.247	32.50
D21	122	0.128	106	0.133	178	0.223	67.31
K33	141	0.148	136	0.170	171	0.214	26.00
I36	205	0.216	206	0.257	242	0.303	17.93
D39	188	0.198	226	0.282	254	0.318	12.50
Q40	161	0.169	198	0.248	289	0.361	45.74
A46	178	0.187	192	0.240	205	0.256	6.63
G47	119	0.125	119	0.149	116	0.145	-2.36
K48	104	0.109	91	0.114	119	0.148	29.76
Q49	183	0.193	166	0.208	213	0.266	28.04
T55	180	0.189	192	0.239	198	0.248	3.55
Y59	119	0.125	110	0.138	201	0.251	81.65
I61	179	0.188	188	0.235	223	0.279	18.62
S65	87	0.092	84	0.105	155	0.193	84.82
T66	156	0.164	179	0.223	257	0.321	43.98
average	150	0.158	156.67	0.196	196	0.245	28.37

## II) Ha linewidth comparison:

Field	950 MHz	950 MHz	800 MHz	800 MHz	800 MHz	800 MHz	800 MHz
Residue	iFD [Hz]	iFD [ppm]	iFD [Hz]	iFD [ppm]	FP [Hz]	FP [ppm]	FP/iFD (%)
L15	135	0.142	140	0.175	230	0.287	64.23
V17	103	0.108	115	0.143	152	0.190	32.25
P19	200	0.211	230	0.288	285	0.356	23.75
V26	184	0.193	177	0.221	340	0.425	92.03
I30	180	0.189	190	0.237	244	0.305	28.90
D32	165	0.174	201	0.252	293	0.366	45.46
K33	125	0.132	123	0.154	138	0.173	12.16
I44	173	0.182	183	0.228	233	0.292	27.73
A46	126	0.133	160	0.200	175	0.219	9.39
E64	216	0.228	245	0.306	293	0.366	19.59
N60	208	0.219	193	0.242	277	0.346	43.33
average	165	0.174	178	0.222	242	0.302	36.26

**Table S2B.** Full list of resolved HN and Ha signals in iFD ubiquitin at 950 MHz and 60 kHz MAS. Signals were analyzed without application of a window function in the <sup>1</sup>H-dimension.

	H <sup>N</sup> 950 MHz [Hz]	H <sup>N</sup> 950 MHz [ppm]		H <sup>α</sup> 950 MHz [Hz]	H <sup>α</sup> 950 MHz [ppm]
I3	149.83	0.16	Q2	150.00	0.16
K6	200	0.21	I3	188.00	0.20
T7	141	0.15	F4	126.14	0.13
T9	127	0.13	K6	226.00	0.24
G10	134.65	0.14	L15	135.14	0.14
K11	143.56	0.15	V17	102.51	0.11
T12	81.54	0.09	E18	177.30	0.19
I13	155.93	0.16	P19	200.07	0.21
T14	102.35	0.11	S20	147.06	0.15
L15	173.77	0.18	V26	183.63	0.19
V17	140.53	0.15	I30	179.87	0.19
S20	141.06	0.15	D32	165.41	0.17
D21	119.04	0.13	K33	125.03	0.13
T22	212.33	0.22	I36	138.41	0.15
V26	193.87	0.20	I44	173.10	0.18
K27	183.87	0.19	F45	260.00	0.27
K29	179	0.19	A46	126.14	0.13
K33	137.44	0.14	G47 α1	148.00	0.16
E34	164.95	0.17	G47 α2	154.00	0.16
I36	191.33	0.20	K48	264.97	0.28
D39	202.26	0.21	K63	201.15	0.21
Q40	173.33	0.18	E64	216.23	0.23
Q41	143.7	0.15	Y59	88.68	0.09
R42	169.38	0.18	N60	208.46	0.22
L43	225.42	0.24	S65	130.99	0.14
I44	234.72	0.25	average	168.65	0.18
F45	155.05	0.16			
A46	177.91	0.19			
G47	118.76	0.13			
K48	104	0.11			
Q49	182	0.19			
E51	216.4	0.23			
D52	123.74	0.13			
R54	122.9	0.13			
T55	180	0.19			
S57	320	0.34			
Y59	119	0.13			
I61	170.59	0.18			
S65	86.72	0.09			
T66	155.87	0.16			
L69	190	0.20			
average	162.07	0.17			

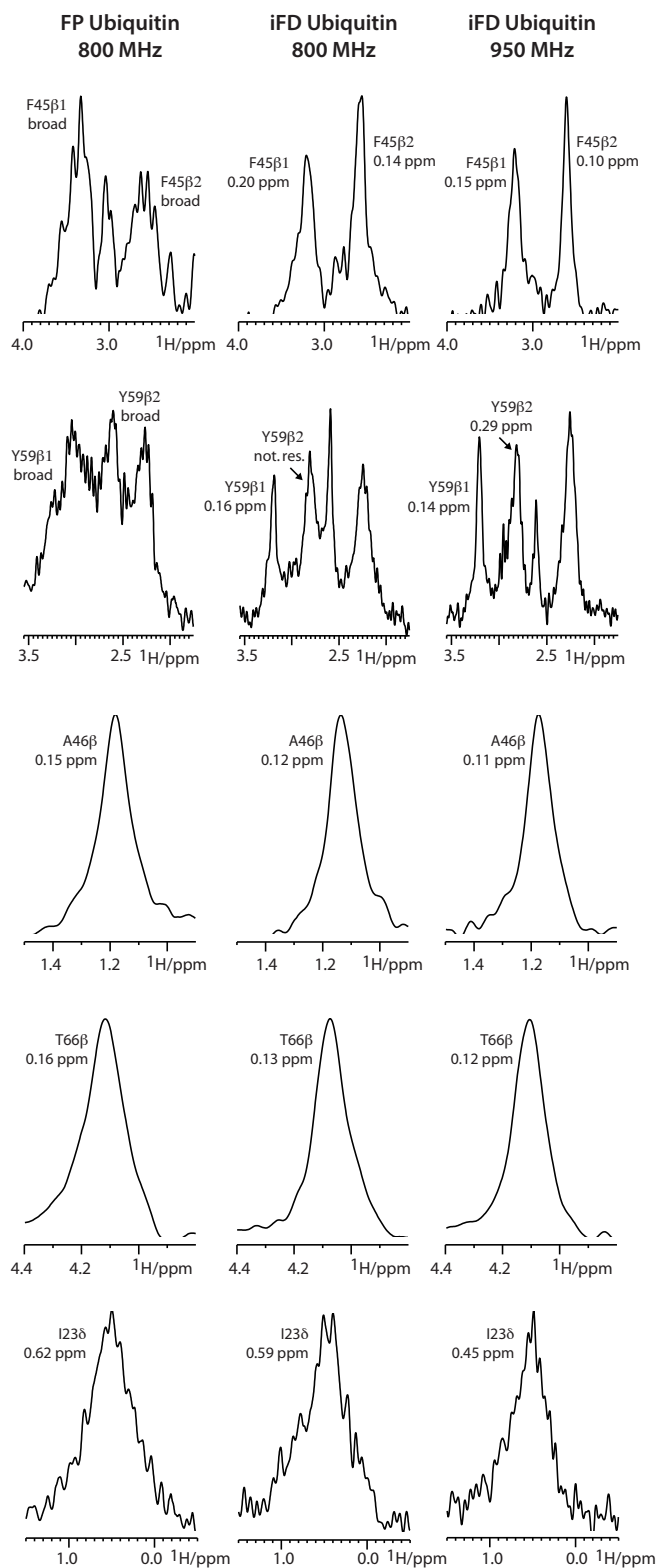


**Figure S2.**  $t_1$  cross-sections extracted from 2D CH experiments measured at 60 kHz MAS, showing the linewidth of side chain  $^1\text{H}$ . We generally found an improved  $^1\text{H}$  linewidth in iFD ubiquitin compared to FP ubiquitin, which is very pronounced for certain residue types such as Phe and Tyr. The improvement was marginal for certain methyl groups (e.g. I23 $\gamma$ ) due to isotopologue effects.

### S3. Assessment of sample quality

To fairly compare the <sup>1</sup>H-linewidth in FP and iFD ubiquitin, it is essential that the analysis is not biased by the sample preparation. We can deduce the sample quality from the <sup>15</sup>N-linewidth, which is most sensitive to sample heterogeneity. Our analysis showed virtually exactly the same <sup>15</sup>N linewidth for the compared ubiquitin samples, also for residues such as D21, Y59, and S65 (Figure S3), which show large gains in <sup>1</sup>H-resolution in iFD ubiquitin. This clearly demonstrates that the <sup>1</sup>H-resolution improvement is caused by the reduction in the <sup>1</sup>H-density.

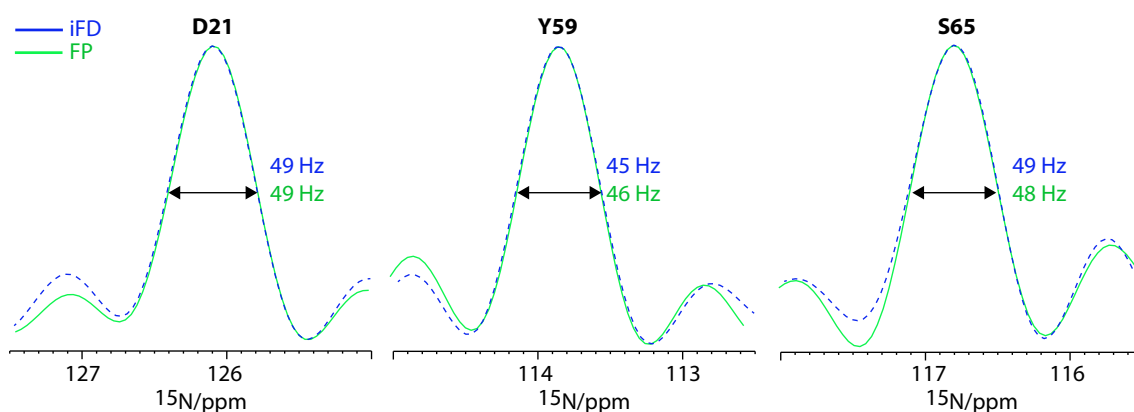


**Figure S3.** Overlay of <sup>15</sup>N cross-sections of FP (green) and iFD (blue) ubiquitin, obtained at 60 kHz MAS in a machine operating at 80 MHz relative to nitrogen.

### S4. Solution state NMR spectra and isotopologue effect

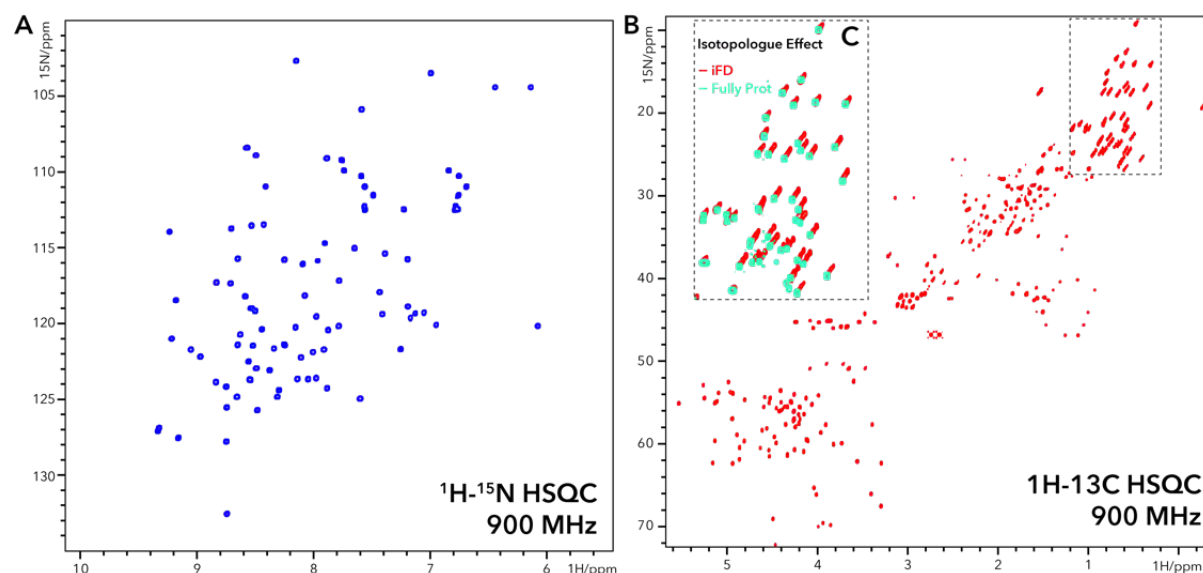


**Figure S4.** 2D <sup>1</sup>H-<sup>15</sup>N HSQC<sup>41</sup> in (A) and <sup>1</sup>H-<sup>13</sup>C HSQC in (B) of iFD ubiquitin in phosphate buffer pH7, measured in a 900 MHz magnet. (C) Overlay of iFD and FP ubiquitin illustrating the isotopologue effect in vinyl and methyl groups. The three signals resulting from -CH<sub>3</sub>, -CH<sub>2</sub>D, -CHD<sub>2</sub> species is detrimental for the resolution of the methyl signal region.

S5. Quantitative analysis of the  $^1\text{H}$  pattern in iFD ubiquitin using solution-state NMR

**Table S5.** Protonation levels [%] of aliphatic carbons were analyzed using  $^{13}\text{C}$ - $^1\text{H}$  HSQC solution-state NMR spectra, measured at 900 MHz. To account for different sample concentrations, the spectra were normalized following the procedure outlined in Ref.<sup>42</sup> by using  $^{15}\text{N}$ - $^1\text{H}$  HSQC<sup>41</sup> spectra. All analysis was based on  $^1\text{H}$ ,  $^{13}\text{C}$  and  $^{15}\text{N}$  solution NMR assignments from Ref.<sup>43</sup>. Note that this is the very same procedure that was applied to analyze the protonation pattern in fractional deuterated (FD) ubiquitin,<sup>20</sup> i.e. iFD (%  $^1\text{H}$ ) = 100 \* signal integral (iFD/FP)

	H $\alpha$	H $\beta$	H $\gamma$	H $\gamma$ 2	H $\delta$	H $\delta$ 2	H $\epsilon$
Ala	95	48					
Arg	96	97	/		87		
Asp	103	78					
Asn	93	74					
*Cys*	*						
Gln	88	93	50				
Glu	94	102	58				
Gly	95						
His	/	89					
Ile	95	99	77	57		70	
Leu	91	98	98		50	53	
Lys	89	79	72		97		94
Met	99	/	72				
Phe	102	70					
Pro	91	95			76		
Ser	93	24					
Thr	99	88	76				
*Trp*	*						
Tyr	97	65					
Val	96	99	55	44			

\* = not present in ubiquitin / = not accessible due to spectral overlap

## S6. Spectral overlay of water -accessible and -inaccessible residues of KcsA

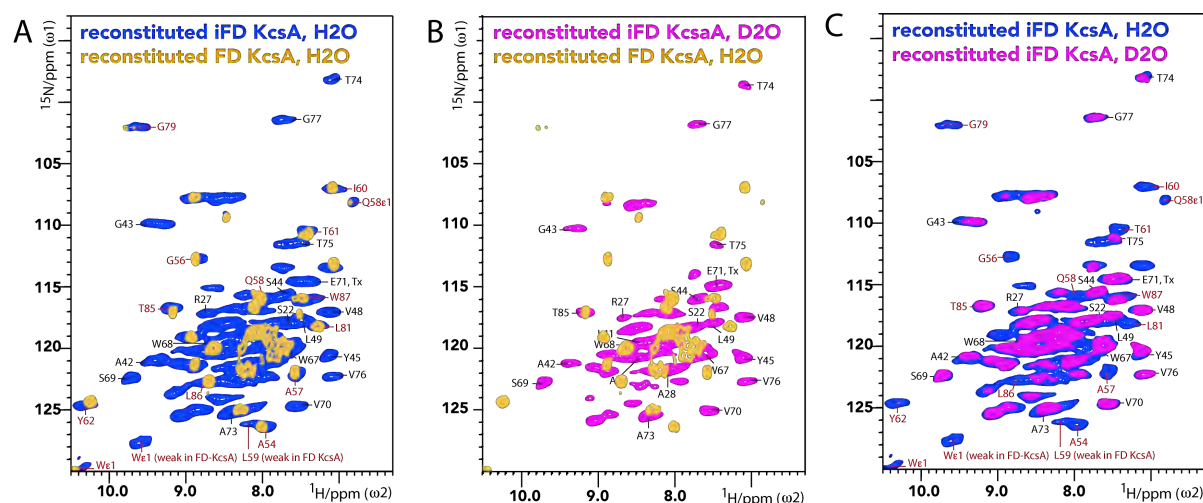


**Figure S6.** Spectral overlay of 2D NH spectra measured with **A)** iFD KcsA in  $\text{H}_2\text{O}$  (blue signals) and  $\text{FD}^{20}$  KcsA in  $\text{H}_2\text{O}$  (yellow signals). iFD KcsA (in  $\text{H}_2\text{O}$ ), which was expressed in protonated solvents, features all HN signals, while FD KcsA (in  $\text{H}_2\text{O}$ ), which was expressed in deuterated solvents, shows only water-accessible residues. Red annotations correspond to signals that were previously assigned in FD KcsA, black signals were assigned with iFD KcsA. **B)** Overlay of FD KcsA and  $\text{D}_2\text{O}$ -washed iFD KcsA. It can be readily seen that all signals of the turret (with exception of T85) as well as G79 of the upper part of the selectivity filter disappear in the iFD KcsA spectrum after  $\text{D}_2\text{O}$ -wash. Therefore, the combination of iFD and FD labelling is also an attractive tool to study membrane protein topology. **C)** Overlay of iFD KcsA before (in blue) and after  $\text{D}_2\text{O}$ -wash (in magenta). It is readily visible that the spectral resolution is improved in the magenta spectrum.

S7.  $^1\text{H}$ -linewidth comparison in iFD KcsA before and after incubation in  $\text{D}_2\text{O}$ 

**Table S7.** Linewidth of  $\text{H}^{\text{N}}$  resonances that were well resolved in the in vitro KcsA ( $\text{D}_2\text{O}$ ) 2D NH spectrum. The linewidth improvement [%] was calculated as  $[(\text{iFD} [\text{H}_2\text{O}]/\text{iFD} [\text{D}_2\text{O}]) - 1] * 100$ . See Figure S7 for signals X1-X4.

Residue	in vitro	in vitro	in vitro	in vitro	Improvement [%]	in situ	in situ
	iFD ( $\text{D}_2\text{O}$ ) LW [Hz]	iFD ( $\text{D}_2\text{O}$ ) [ppm]	iFD ( $\text{H}_2\text{O}$ ) LW [Hz]	iFD ( $\text{H}_2\text{O}$ ) [ppm]		iFD ( $\text{D}_2\text{O}$ ) LW [Hz]	iFD ( $\text{D}_2\text{O}$ ) [ppm]
G43	350	0.44	358	0.45	2.29	249	0.31
S44	194	0.24	overlap	overlap		overlap	overlap
V48	160	0.20	204	0.26	27.50	198	0.25
W68	160	0.20	overlap	overlap		overlap	overlap
S69	107	0.13	135	0.17	26.17	210	0.26
V70	162	0.20	204	0.26	25.89	209	0.26
A73	163	0.20	265	0.33	62.36	321	0.40
T74	227	0.28	238	0.30	4.85	190	0.24
V76	227	0.28	300	0.38	32.16	280	0.35
T75	178	0.22	384	0.48	115.73	416	0.52
G77	244	0.31	288	0.36	18.03	416	0.52
T85	142	0.18	210	0.26	47.89	176	0.22
X1	187	0.23	232	0.29	0.24	151	0.19
X2	169	0.21	overlap	overlap	overlap	overlap	overlap
X3	224	0.28	~400	~0.50	~75	gone	gone
X4	153	0.19	~340	~0.42	~120	overlap	overlap

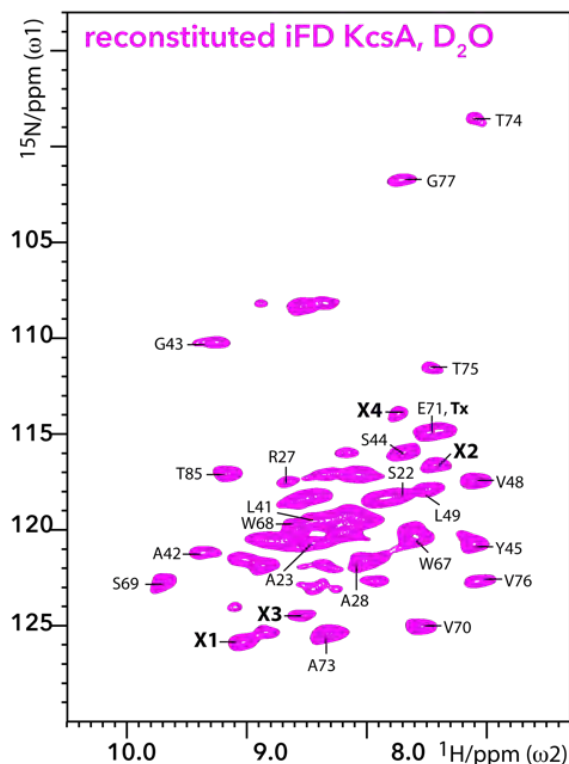


**Figure S7.** 2D NH spectrum of D<sub>2</sub>O-washed iFD KcsA. The unassigned signals X1 – X4, which were included in the linewidth analysis, are indicated in the spectrum.

*S8. Measurement of the bulk <sup>15</sup>N T1ρ as a function of the <sup>15</sup>N spinlock power*

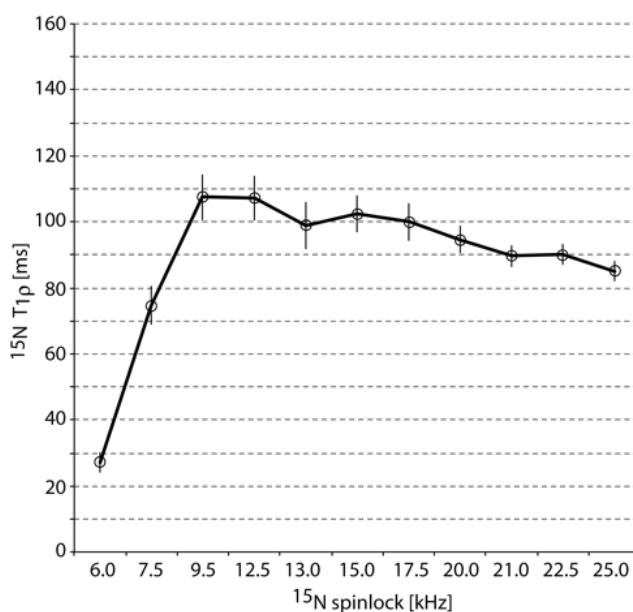


**Figure S8.** Bulk <sup>15</sup>N T1ρ measured in D<sub>2</sub>O-washed iFD KcsA at 800 MHz and 60 kHz MAS. In line with Refs.<sup>32–34</sup>, the graph shows a plateau from ~10–25 kHz <sup>15</sup>N spinlock power with an average <sup>15</sup>N T1ρ of ~100 ms. The relaxation time gets shorter with higher spinlock powers, presumably due to the proximity to the n=1/2 rotary resonance condition.

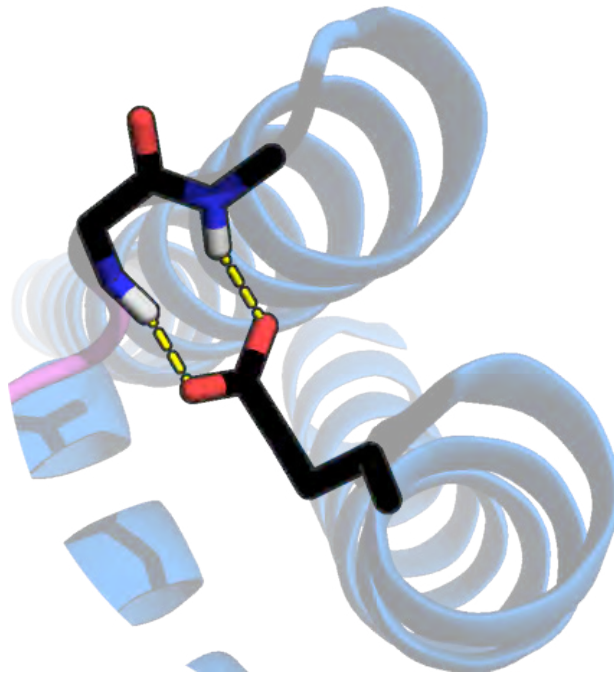
## References

- (1) Ishii, Y.; Tycko, R. Sensitivity Enhancement in Solid State <sup>15</sup>N NMR by Indirect Detection with High-Speed Magic Angle Spinning. *J. Magn. Reson.* **2000**, *142* (1), 199–204.
- (2) Chevelkov, V.; Rehbein, K.; Diehl, A.; Reif, B. Ultrahigh Resolution in Proton Solid-State NMR Spectroscopy at High Levels of Deuteration. *Angew. Chemie Int. Ed.* **2006**, *45* (23), 3878–3881.
- (3) Schanda, P.; Meier, B. H.; Ernst, M. Quantitative Analysis of Protein Backbone Dynamics in Microcrystalline Ubiquitin by Solid-State NMR Spectroscopy. *J. Am. Chem. Soc.* **2010**, *132* (45), 15957–15967.
- (4) Sinnige, T.; Daniëls, M.; Baldus, M.; Weingarth, M. Proton Clouds to Measure Long-Range Contacts between Nonexchangeable Side Chain Protons in Solid-State NMR. *J. Am. Chem. Soc.* **2014**, *136* (12), 4452–4455.
- (5) Chevelkov, V.; Habenstein, B.; Loquet, A.; Giller, K.; Becker, S.; Lange, A. Proton-Detected MAS NMR Experiments Based on Dipolar Transfers for Backbone Assignment of Highly Deuterated Proteins. *J. Magn. Reson.* **2014**, *242*, 180–188.
- (6) Linser, R.; Dasari, M.; Hiller, M.; Higman, V.; Fink, U.; Lopez del Amo, J.-M.; Markovic, S.; Handel, L.; Kessler, B.; Schmieder, P.; et al. Proton-Detected Solid-State NMR Spectroscopy of Fibrillar and Membrane Proteins. *Angew. Chemie Int. Ed.* **2011**, *50* (19), 4508–4512.
- (7) Ward, M. E.; Shi, L.; Lake, E.; Krishnamurthy, S.; Hutchins, H.; Brown, L. S.; Ladizhansky, V. Proton-Detected Solid-State NMR Reveals Intramembrane Polar Networks in a Seven-Helical Transmembrane Protein Proteorhodopsin. *J. Am. Chem. Soc.* **2011**, *133* (43), 17434–17443.
- (8) Dannatt, H. R. W.; Felletti, M.; Jehle, S.; Wang, Y.; Emsley, L.; Dixon, N. E.; Lesage, A.; Pintacuda, G. Weak and Transient Protein Interactions Determined by Solid-State NMR. *Angew. Chemie Int. Ed.* **2016**, *55* (23), 6638–6641.
- (9) Zhou, D. H.; Shah, G.; Cormos, M.; Mullen, C.; Sandoz, D.; Rienstra, C. M. Proton-Detected Solid-State NMR Spectroscopy of Fully Protonated Proteins at 40 KHz Magic-Angle Spinning. *J. Am. Chem. Soc.* **2007**, *129* (38), 11791–11801.
- (10) Marchetti, A.; Jehle, S.; Felletti, M.; Knight, M. J.; Wang, Y.; Xu, Z.-Q.; Park, A. Y.; Otting, G.; Lesage, A.; Emsley, L.; et al. Backbone Assignment of Fully Protonated Solid Proteins by <sup>1</sup>H Detection and Ultrafast Magic-Angle-Spinning NMR Spectroscopy. *Angew. Chemie Int. Ed.* **2012**, *51* (43), 10756–10759.
- (11) Weingarth, M.; van der Crujisen, E. A. W.; Ostmeier, J.; Lievestro, S.; Roux, B.; Baldus, M. Quantitative Analysis of the Water Occupancy around the Selectivity Filter of a K<sup>+</sup> Channel in Different Gating Modes. *J. Am. Chem. Soc.* **2014**, *136* (5), 2000–2007.
- (12) Wang, S.; Parthasarathy, S.; Xiao, Y.; Nishiyama, Y.; Long, F.; Matsuda, I.; Endo, Y.; Nemoto, T.; Yamauchi, K.; Asakura, T.; et al. Nano-Mole Scale Sequential Signal Assignment by <sup>1</sup>H-Detected Protein Solid-State NMR. *Chem. Commun.* **2015**, *51* (81), 15055–15058.
- (13) Xiang, S.; Biernat, J.; Mandelkow, E.; Becker, S.; Linser, R. Backbone Assignment for Minimal Protein Amounts of Low Structural Homogeneity in the Absence of Deuteration. *Chem. Commun.* **2016**, *52* (21), 4002–4005.
- (14) Agarwal, V.; Penzel, S.; Szekely, K.; Cadalbert, R.; Testori, E.; Oss, A.; Past, J.; Samoson, A.; Ernst, M.; Böckmann, A.; et al. De Novo 3D Structure Determination from Sub-Milligram Protein Samples by Solid-State 100 KHz MAS NMR Spectroscopy. *Angew. Chemie Int. Ed.* **2014**, *53* (45), 12253–12256.
- (15) Mroue, K. H.; Nishiyama, Y.; Kumar Pandey, M.; Gong, B.; McNerny, E.; Kohn, D. H.; Morris, M. D.; Ramamoorthy, A. Proton-Detected Solid-State NMR Spectroscopy of Bone with Ultrafast Magic Angle Spinning. *Sci. Rep.* **2015**, *5* (1), 11991.
- (16) Shi, L.; Kawamura, I.; Jung, K.-H.; Brown, L. S.; Ladizhansky, V. Conformation of a Seven-Helical Transmembrane Photosensor in the Lipid Environment. *Angew. Chemie Int. Ed.* **2011**, *50* (6), 1302–1305.
- (17) Zhou, D. H.; Rienstra, C. M. High-Performance Solvent Suppression for Proton Detected Solid-State NMR. *J. Magn. Reson.* **2008**, *192* (1), 167–172.
- (18) Weingarth, M.; Bodenhausen, G.; Tekely, P. Low-Power Decoupling at High Spinning Frequencies in High Static Fields. *J. Magn. Reson.* **2009**, *199* (2), 238–241.
- (19) Verel, R.; Baldus, M.; Ernst, M.; Meier, B. H. A Homonuclear Spin-Pair Filter for Solid-State NMR Based on Adiabatic-Passage Techniques. *Chem. Phys. Lett.* **1998**, *287* (3–4), 421–428.
- (20) Mance, D.; Sinnige, T.; Kaplan, M.; Narasimhan, S.; Daniëls, M.; Houben, K.; Baldus, M.; Weingarth, M. An Efficient Labelling Approach to Harness Backbone and Side-Chain Protons in <sup>1</sup>H-Detected Solid-State NMR Spectroscopy. *Angew. Chemie Int. Ed.* **2015**, *54* (52), 15799–15803.

- (21) Cuello, L. G.; Jogini, V.; Cortes, D. M.; Perozo, E. Structural Mechanism of C-Type Inactivation in K<sup>+</sup> Channels. *Nature* **2010**, *466* (7303), 203–208.
- (22) van der Cruijssen, E. A. W.; Nand, D.; Weingarh, M.; Prokofyev, A.; Hornig, S.; Cukkemane, A. A.; Bonvin, A. M. J. J.; Becker, S.; Hulse, R. E.; Perozo, E.; et al. Importance of Lipid-Pore Loop Interface for Potassium Channel Structure and Function. *Proc. Natl. Acad. Sci. U. S. A.* **2013**, *110* (32), 13008–13013.
- (23) Wylie, B. J.; Bhate, M. P.; McDermott, A. E. Transmembrane Allosteric Coupling of the Gates in a Potassium Channel. *Proc. Natl. Acad. Sci. U. S. A.* **2014**, *111* (1), 185–190.
- (24) Chill, J. H.; Louis, J. M.; Miller, C.; Bax, A. NMR Study of the Tetrameric KcsA Potassium Channel in Detergent Micelles. *Protein Sci.* **2006**, *15* (4), 684–698.
- (25) Renault, M.; Tommassen-van Boxtel, R.; Bos, M. P.; Post, J. A.; Tommassen, J.; Baldus, M. Cellular Solid-State Nuclear Magnetic Resonance Spectroscopy. *Proc. Natl. Acad. Sci.* **2012**, *109* (13), 4863–4868.
- (26) Shahid, S. A.; Nagaraj, M.; Chauhan, N.; Franks, T. W.; Bardiaux, B.; Habeck, M.; Orwick-Rydmark, M.; Linke, D.; van Rossum, B.-J. Solid-State NMR Study of the YadA Membrane-Anchored Domain in the Bacterial Outer Membrane. *Angew. Chemie Int. Ed.* **2015**, *54* (43), 12602–12606.
- (27) Baker, L. A.; Daniëls, M.; van der Cruijssen, E. A. W.; Folkers, G. E.; Baldus, M. Efficient Cellular Solid-State NMR of Membrane Proteins by Targeted Protein Labeling. *J. Biomol. NMR* **2015**, *62* (2), 199–208.
- (28) Schanda, P.; Triboulet, S.; Laguri, C.; Bougault, C. M.; Ayala, I.; Callon, M.; Arthur, M.; Simorre, J.-P. Atomic Model of a Cell-Wall Cross-Linking Enzyme in Complex with an Intact Bacterial Peptidoglycan. *J. Am. Chem. Soc.* **2014**, *136* (51), 17852–17860.
- (29) Chakrapani, S.; Cordero-Morales, J. F.; Jogini, V.; Pan, A. C.; Cortes, D. M.; Roux, B.; Perozo, E. On the Structural Basis of Modal Gating Behavior in K<sup>+</sup> Channels. *Nat. Struct. Mol. Biol.* **2011**, *18* (1), 67–74.
- (30) Takeuchi, K.; Takahashi, H.; Kawano, S.; Shimada, I. Identification and Characterization of the Slowly Exchanging PH-Dependent Conformational Rearrangement in KcsA. *J. Biol. Chem.* **2007**, *282* (20), 15179–15186.
- (31) Ma, P.; Xue, Y.; Coquelle, N.; Haller, J. D.; Yuwen, T.; Ayala, I.; Mikhailovskii, O.; Willbold, D.; Colletier, J.-P.; Skrynnikov, N. R.; et al. Observing the Overall Rocking Motion of a Protein in a Crystal. *Nat. Commun.* **2015**, *6* (1), 8361.
- (32) Lamley, J. M.; Öster, C.; Stevens, R. A.; Lewandowski, J. R. Intermolecular Interactions and Protein Dynamics by Solid-State NMR Spectroscopy. *Angew. Chemie Int. Ed.* **2015**, *54* (51), 15374–15378.
- (33) Lewandowski, J. R.; Sass, H. J.; Grzesiek, S.; Blackledge, M.; Emsley, L. Site-Specific Measurement of Slow Motions in Proteins. *J. Am. Chem. Soc.* **2011**, *133* (42), 16762–16765.
- (34) Good, D. B.; Wang, S.; Ward, M. E.; Struppe, J.; Brown, L. S.; Lewandowski, J. R.; Ladizhansky, V. Conformational Dynamics of a Seven Transmembrane Helical Protein Anabaena Sensory Rhodopsin Probed by Solid-State NMR. *J. Am. Chem. Soc.* **2014**, *136* (7), 2833–2842.
- (35) Chill, J. H.; Louis, J. M.; Baber, J. L.; Bax, A. Measurement of 15N Relaxation in the Detergent-Solubilized Tetrameric KcsA Potassium Channel. *J. Biomol. NMR* **2006**, *36* (2), 123–136.
- (36) Ader, C.; Pongs, O.; Becker, S.; Baldus, M. Protein Dynamics Detected in a Membrane-Embedded Potassium Channel Using Two-Dimensional Solid-State NMR Spectroscopy. *Biochim. Biophys. Acta - Biomembr.* **2010**, *1798* (2), 286–290.
- (37) Sumino, A.; Yamamoto, D.; Iwamoto, M.; Dewa, T.; Oiki, S. Gating-Associated Clustering–Dispersion Dynamics of the KcsA Potassium Channel in a Lipid Membrane. *J. Phys. Chem. Lett.* **2014**, *5* (3), 578–584.
- (38) Weingarh, M.; Demco, D. E.; Bodenhausen, G.; Tekely, P. Improved Magnetization Transfer in Solid-State NMR with Fast Magic Angle Spinning. *Chem. Phys. Lett.* **2009**, *469* (4–6), 342–348.
- (39) Holland, D. J.; Bostock, M. J.; Gladden, L. F.; Nietlispach, D. Fast Multidimensional NMR Spectroscopy Using Compressed Sensing. *Angew. Chemie Int. Ed.* **2011**, *50* (29), 6548–6551.
- (40) BALDUS, M.; PETKOVA, A. T.; HERZFELD, J.; GRIFFIN, R. G. Cross Polarization in the Tilted Frame: Assignment and Spectral Simplification in Heteronuclear Spin Systems. *Mol. Phys.* **1998**, *95* (6), 1197–1207.
- (41) Bodenhausen, G.; Ruben, D. J. Natural Abundance Nitrogen-15 NMR by Enhanced Heteronuclear Spectroscopy. *Chem. Phys. Lett.* **1980**, *69* (1), 185–189.
- (42) Otten, R.; Chu, B.; Krewulak, K. D.; Vogel, H. J.; Mulder, F. A. A. Comprehensive and Cost-Effective NMR Spectroscopy of Methyl Groups in Large Proteins. *J. Am. Chem. Soc.* **2010**, *132* (9), 2952–2960.
- (43) Gabriel Cornilescu; John L. Marquardt; Marcel Ottiger, and; Bax\*, A. Validation of Protein Structure from Anisotropic Carbonyl Chemical Shifts in a Dilute Liquid Crystalline Phase. **1998**.

# CHAPTER 3

Hydrogen Bond Strength in Membrane Proteins  
Probed by time-resolved  $^1\text{H}$ -detected Solid State  
NMR and MD Simulations



## Abstract

$^1\text{H}$ -detected solid-state NMR in combination with  $^1\text{H}/^2\text{H}$  exchange steps allows for the direct identification of very strong hydrogen bonds in membrane proteins. On the example of the membrane-embedded potassium channel KcsA, we quantify the longevity of such very strong hydrogen bonds by combining time-resolved  $^1\text{H}$ -detected solid-state NMR experiments and molecular dynamics simulations. In particular, we show that the carboxyl-side chain of the highly conserved residue Glu51 is involved in ultra-strong hydrogen bonds, which are fully-water-exposed and yet stable for weeks. The astonishing stability of these hydrogen bonds is important for the structural integrity of potassium channels, which we further corroborate by computational studies.

*Based on the publication:*

João Medeiros-Silva, Shehrazade Jekhmane, Marc Baldus and Markus Weingarth  
Hydrogen Bond Strength in Membrane Proteins Probed by Time-Resolved  $^1\text{H}$ -  
Detected Solid-State NMR and MD Simulations.

*Solid State Nuclear Magnetic Resonance*, 2017 87 80-85.

## Introduction

The measurement of hydrogen-deuterium ( $^1\text{H}/^2\text{H}$ ) exchange is a widespread method in solution NMR to probe protein structure,<sup>1,2</sup> folding,<sup>3,4</sup> and protein-ligand interactions.<sup>5</sup> Its principle is straightforward and based on the signal attenuation of exchangeable protons such as amino or hydroxyl protons upon incubation with deuterated solvents. How fast these protons exchange is usually determined by their participation in hydrogen bonds and by their surface exposure. The latter aspect renders  $^1\text{H}/^2\text{H}$  exchange naturally a very attractive method to study membrane protein topology, which has been exploited in a number of solution NMR studies in micelles or detergents.<sup>6-8</sup> In solid-state NMR (ssNMR), however,  $^1\text{H}/^2\text{H}$  exchange could not be directly exploited due a lack of  $^1\text{H}$ -resolution. While the indirect  $^{15}\text{N}$ -detection of  $^1\text{H}/^2\text{H}$  exchange could already be used for elegant ssNMR studies on the topology of 7TM membrane proteins,<sup>9,10</sup> we are likely to see many more applications of the simple  $^1\text{H}/^2\text{H}$  exchange tool with the advent of high-resolution  $^1\text{H}$ -detected ssNMR,<sup>11-19</sup> driven by fast magic angle spinning (MAS). Indeed, as in part described in Chapter 2, we used  $^1\text{H}$ -detected  $^1\text{H}/^2\text{H}$  exchange at fast MAS for the study of the membrane topology and the localization of functionally important water molecules in the ion channel KcsA.<sup>20-22</sup> Furthermore,  $^1\text{H}$ -detected  $^1\text{H}/^2\text{H}$  exchange ssNMR studies were also conducted on the membrane protein proteorhodopsin<sup>23</sup> and on the SH3 domain.<sup>24</sup>

Here we integrate time-resolved  $^1\text{H}$ -detected ssNMR and molecular dynamics simulations to examine unusually strong hydrogen bonds in the membrane-embedded  $\text{K}^+$  channel KcsA. These hydrogen bonds are fully water-exposed and yet stable for many weeks, something that may hint at their potential functional importance.

## Results and discussion

### *The filter residues V84 and T85 form a very strong hydrogen bond network*

The membrane protein KcsA is an archetypical  $\text{K}^+$  channel and a well-accepted model to study the gating of the central pore of  $\text{K}^+$  channels.<sup>25-29</sup> We performed  $^1\text{H}$ -detected studies of KcsA with the complementary labelling schemes fractional deuteration (FD) and inverse fractional deuteration (iFD) (Figure 1). These labelling schemes give access to exchangeable  $\text{H}^{\text{N}}$  only (FD in  $\text{H}_2\text{O}$ ), all  $\text{H}^{\text{N}}$  (iFD in  $\text{H}_2\text{O}$ ), and non-exchangeable  $\text{H}^{\text{N}}$  only (iFD in  $\text{D}_2\text{O}$ ). Combining these labelling schemes represents hence a straightforward and powerful tool to study membrane protein topology. We could readily select residues that belong to the water-exposed outer vestibule (Figure 1A) and the water-shielded transmembrane part (Figure 1C) of KcsA. Note that the water-exposed cytoplasmic domain (CPD) is not visible in our dipolar-based spectra due to increased mobility, as we demonstrated previously.<sup>21</sup> After incubating

iFD KcsA in deuterated buffers for one week, almost all water-exposed residues of the outer vestibule fully exchanged, with the exceptions of V84<sup>N</sup> and T85<sup>N</sup> (Figure 1C, highlighted in red bold letters). Astonishingly these residues did not exchange, in spite of the fact that they are fully accessible by the bulk water (Figure 2). Note that T85 was also protected from exchange in native bacterial membranes (see Figure 4E from chapter 2).

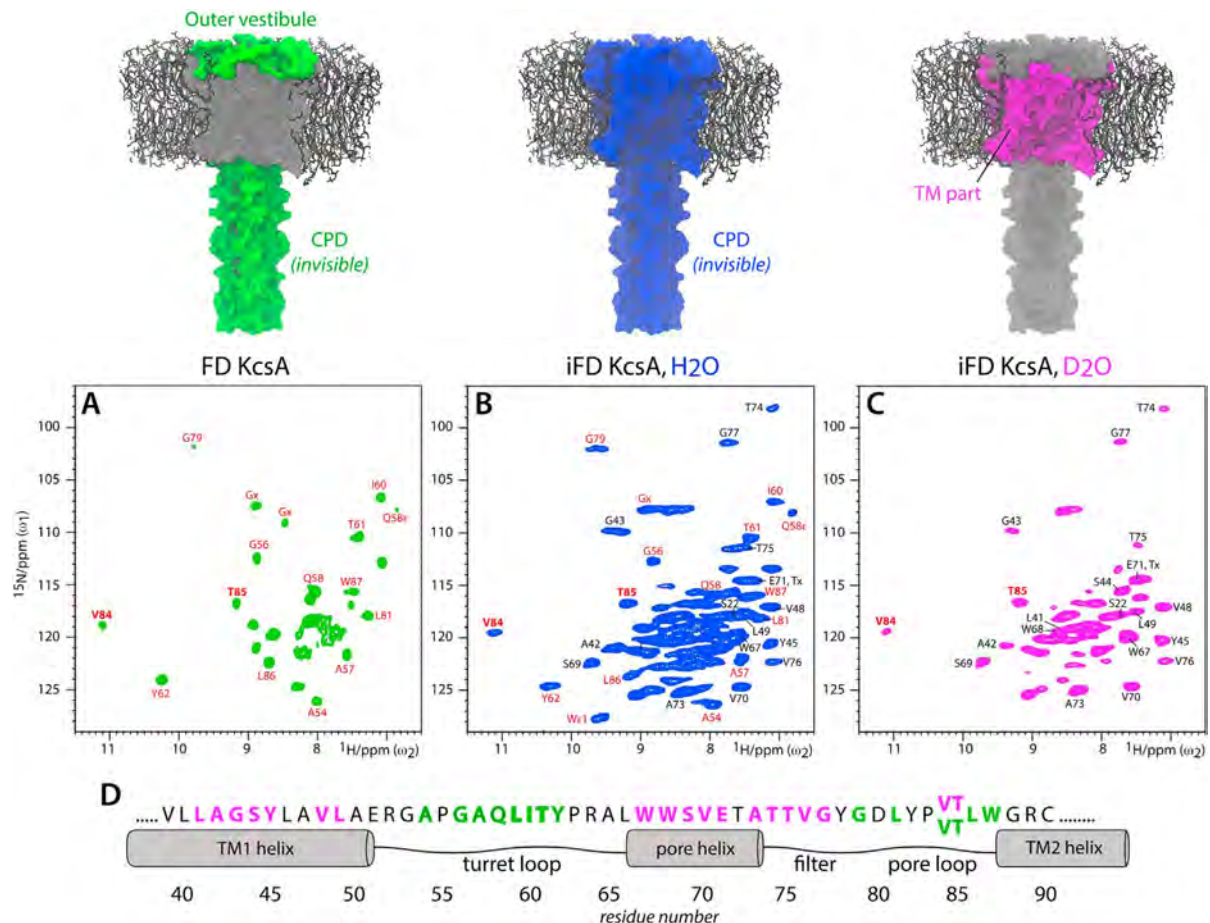


**Figure 1.** <sup>1</sup>H-detected dipolar-based <sup>2</sup>H NH spectra of **A**) FD KcsA, **B**) iFD KcsA in protonated buffers, and **C**) iFD KcsA in deuterated buffers. Spectra were acquired at 800 MHz and with 52 and 60 kHz MAS for FD and iFD KcsA, respectively. Signals of V84 and T85 are annotated in red bold letters. **D**) Illustration of visible H<sup>N</sup> signals in FD KcsA (green) and D<sub>2</sub>O-incubated iFD KcsA (magenta). Residues in black color are not assigned.

This suggested that V84 and T85 are involved in exceptionally strong hydrogen bonds, which may relate to their localization at the water- membrane interface, which is a region of low dielectric permittivity (Figure 2D). In the KcsA crystal structure (pdb 1K4C),<sup>25</sup> the backbone amino protons of both V84 and T85 form hydrogen bonds with the carboxyl side chain of residue E51, connecting the TM1 helix with the pore-loop (P-loop). This hydrogen bond pattern is also present in other K<sup>+</sup> channels, such as in Shaker or the KCNKØ channel, which was demonstrated with cysteine-crosslinking.<sup>30,31</sup> Residue E51 (E418 in Shaker, E28 in KCNKØ) is conserved in most K<sup>+</sup> channels and absolutely conserved in voltage-gated

potassium (Kv) channels (Figure 2A). Several studies have reported that residue E51 is important for slow C-type inactivation in Kv channels, which was demonstrated with mutational studies in Shaker, BK2, and the KCNK $\emptyset$  channel.<sup>30–32</sup> Furthermore, E51 seems relevant for structural integrity, given that certain E51X KcsA mutants failed to express,<sup>33</sup> and E51 was shown to be a pH sensor in the TASK2 channel.<sup>34</sup> It seems hence plausible that the very strong hydrogen bonds formed by the E51 side chain relates to the importance of this residue.

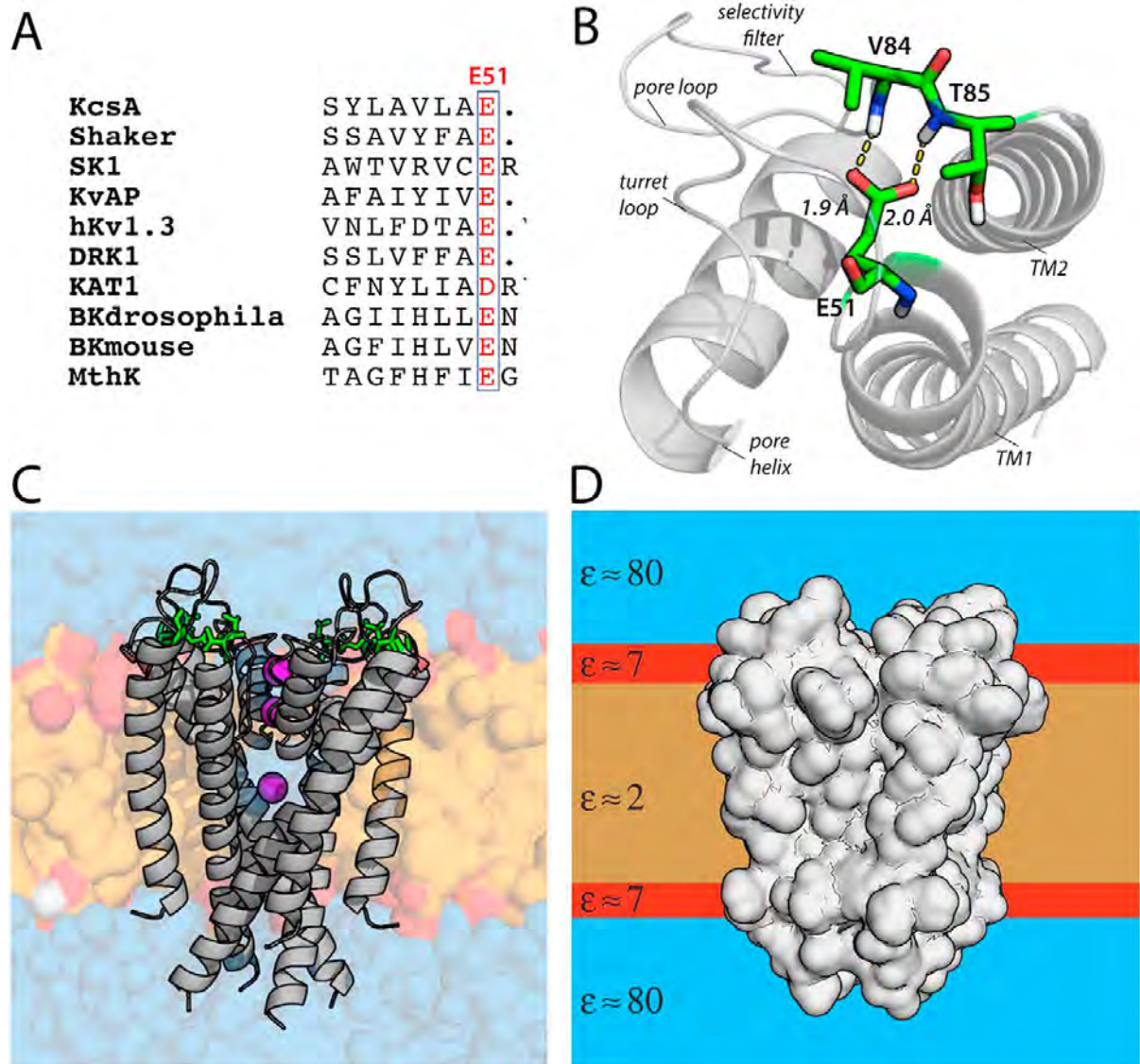


**Figure 2.** A) Sequential alignment of several K<sup>+</sup> channels, showing the absolute conservation of E51 in voltage-gated K<sup>+</sup> channels. B) Illustration of the V84/T85 – E51 hydrogen bond network in KcsA. C) E51 and V84/T85 (shown in green) are fully water exposed and localized at the water-lipid interface. D) Illustration of the profile of dielectric constants  $\epsilon$  across lipid bilayers. The low permittivity at the membrane interface increases Coulomb contributions in hydrogen bonds.

*Time-resolved  $^1\text{H}/^2\text{H}$  exchange*

To quantify the stability of the hydrogen bonds in which V84H<sup>N</sup> and T85 H<sup>N</sup> are involved, we performed time-resolved ssNMR experiments. We measured additional  $^1\text{H}$ -detected 2D NH spectra with iFD KcsA after four and seven weeks of incubation time in deuterated buffers (Figure 3). To quantify the gradual signal decay of V84H<sup>N</sup> and T85 H<sup>N</sup> due to  $^1\text{H}/^2\text{H}$  exchange, we referenced to the water-shielded transmembrane residues V48 and V70, which are not affected by exchange. Our analysis revealed that V84H<sup>N</sup> exchanged substantially faster than T85H<sup>N</sup>. Whereas the T85 signal had lost only about 10% intensity after 4 weeks of incubation time, the V84 signal was reduced by 60% in intensity. This suggested a significant difference in the hydrogen bond strength for these two residues. Such a marked difference is not deducible from the crystal structure 1K4C,<sup>25</sup> in which the V84 – E51 hydrogen bond is actually 0.1 Å shorter than the T85 – E51 hydrogen bond. We hence wondered if the decay differences observed by time-resolved  $^1\text{H}$ -detected ssNMR are directly related to the differential longevity of the V84 – E51 and T85 – E51 hydrogen bonds.

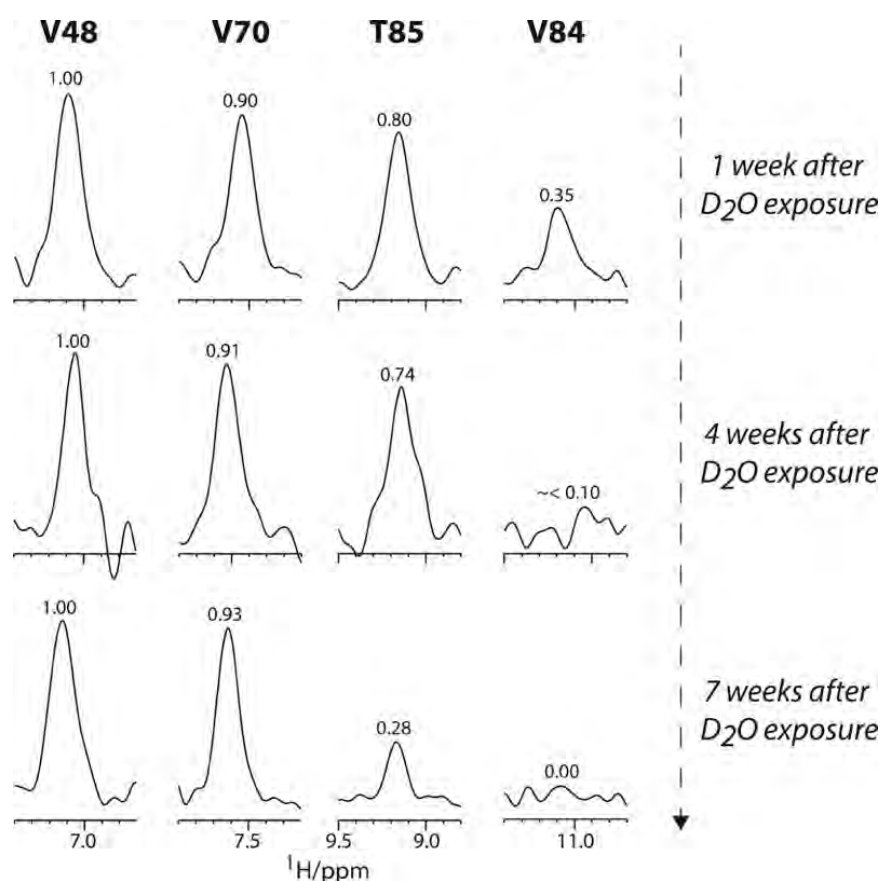


**Figure 3.** The decay of signals V84 and T85 as a function of the incubation time in deuterated buffers. For each measurement point, we referenced the signal heights of V84/T85 to the transmembrane residues V48/V70. The latter are not prone to  $^1\text{H}/^2\text{H}$  exchange. Note that the accelerated decay of T85 between 4 and 7 weeks of  $\text{D}_2\text{O}$ -exposure is presumably due to sample heating effects.

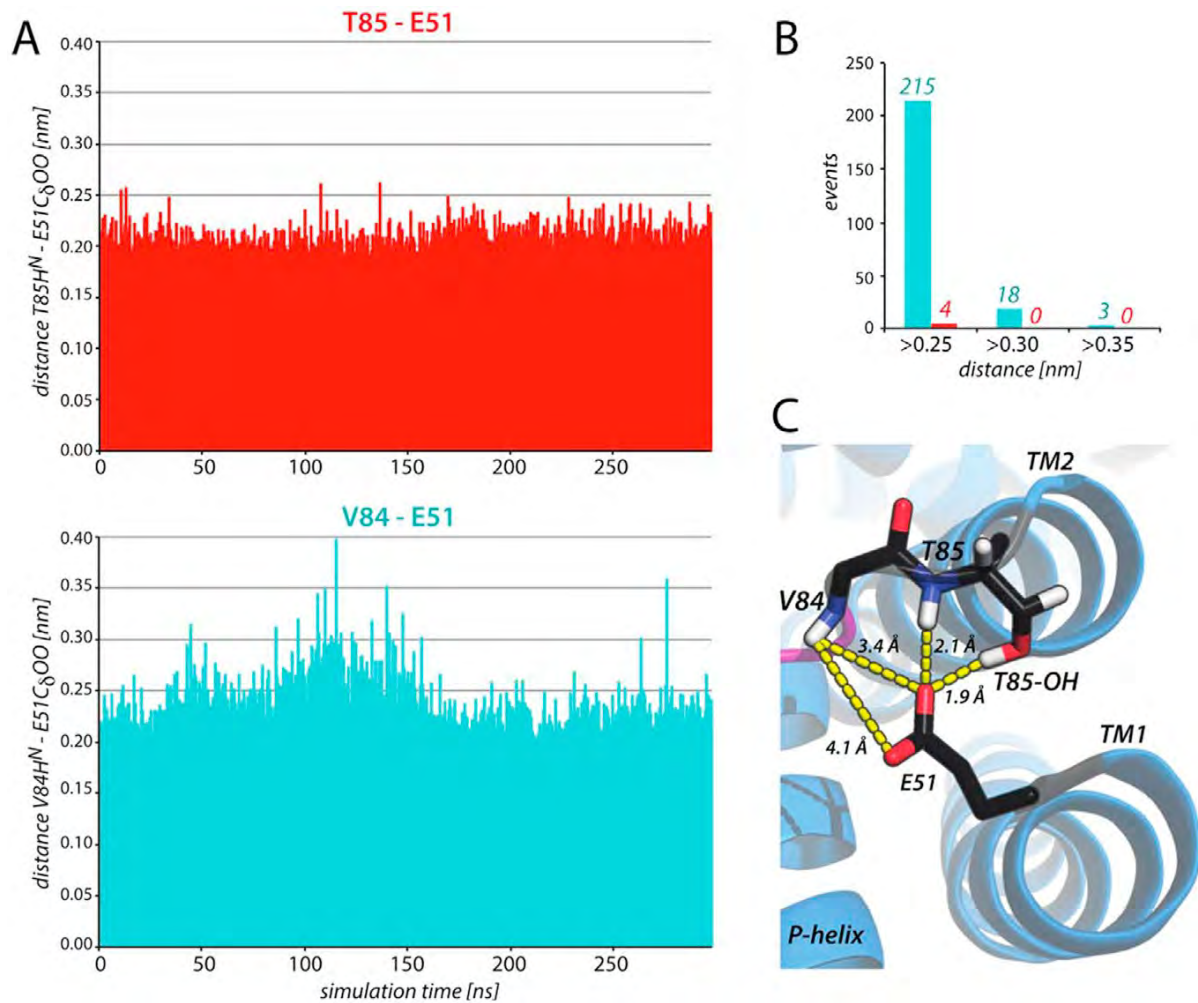


**Figure 4.** Analysis of hydrogen bond stability from MD simulations. **A)** Temporal evolution of the distance between the V84/T85 amino-proton and the carboxyl-oxygen of E51. For each analysis step, the distance to the closer carboxyl oxygen is plotted. The analysis reflects the hydrogen bond distance in one monomer of the tetrameric KcsA channel. Similar pattern were found in the other three protomers. **B)** Summary of the distance evolution shown in A). Distances around 3.5 Å correspond to a loss of hydrogen bonding. **C)** Although a rare event, the V84 – E51 hydrogen bond breaks from time to time, which leaves V84H<sup>N</sup> prone to  $^1\text{H}/^2\text{H}$  exchange. The T85 side chain hydroxyl-group further stabilizes the T85 – E51 hydrogen bond.

Note that an analysis of H<sup>N</sup> – water distances over the trajectory clearly demonstrated that V84H<sup>N</sup> and T85H<sup>N</sup> are refractory to exchange despite the steady presence of close water molecules (Figure S1). We also like to emphasize that the strong V84/T85 signals in FD KcsA (Figure 1A) are not at all in contradiction to our conclusions. While FD KcsA is grown in deuterated buffers, purification and reconstitution steps, which take several days, are performed in protonated buffers. During these steps, signals of the water-accessible outer vestibule fully exchange. Moreover, in the absence of a bilayer, the outer vestibule is less densely packed (absence of bilayer lateral pressure) and the low permittivity environment of the bilayer (Figure 2D) is absent.

To gain further insight in hydrogen bond stability, we performed atomistic molecular dynamics (MD) simulations. We used a closed-conductive KcsA structure (pdb 1K4C) embedded in anionic POPG lipids as starting system. Figure 4A shows the temporal evolution

of the distances between the V84/T85 amino-protons and the closer of the two E51 side chain carboxyl-oxygens, and this is the relevant hydrogen bond distance. The analysis was conducted over 300 ns of MD simulation (Figure 4A,B). We could indeed observe a clear difference in hydrogen bond stability, which is perfectly in line with our time-resolved solid-state NMR data. The T85 hydrogen bond length is extremely steady, and does basically not exceed 2.5 Å over the evaluated period. This is most likely because the T85 hydroxyl side chain further stabilizes the hydrogen bond (Figure 4C). However, for V84, we observe more than 200 times events where distances exceed 2.5 Å, and we even observe a small but significant number of distances that exceed 3.5 Å. Distances around 3.5 Å mark a loss of hydrogen bonding during which V84H<sup>N</sup> is accessible to bulk water and can exchange (Figure 4C). In total, the loss of hydrogen bonding for V84H<sup>N</sup> occurred three times over the evaluated period of 300 ns. The MD simulations hence show that while both V84 and T85 form very tight hydrogen bonds with E51, where the hydrogen bond with T85 is far stronger. Both observations agree remarkably well with our time-resolved <sup>1</sup>H-detected ssNMR data.

#### *Functional relevance of the network*

The enormous stability of the V84/T85 – E51 hydrogen bonds is surprising. In voltage-gated and other K<sup>+</sup> channels, it was shown that loss of interactions with E51 led to a stark acceleration of C-type inactivation.<sup>30–32</sup> In line with this notion, it was demonstrated that linking S5 with the S6-P-loop via E418 in Shaker (E51 in KcsA) greatly stabilizes the inactivation gate.<sup>30</sup> It hence seems plausible that the hydrogen bonds formed by the E51 side chain are therefore tightly controlled. In atomistic MD simulations with a E51A KcsA mutant, we see that loss of the V84/T85 – E51 hydrogen bonds goes along with marked structural alterations in the turret loop (Figure 5). The Baldus group<sup>35</sup> and the Perozo group<sup>36</sup> have recently demonstrated that the turret region modulates KcsA gating, presumably via the selectivity filter. The detailed structural underpinning of the influence of the turret on gating is however yet elusive. However, that the structure or the dynamics of the outer vestibule is linked to channel gating appears obvious, given that specific lipid binding at the outer vestibule modulates channel gating by yet unknown mechanisms.<sup>37–40</sup> Against this backdrop, it is tempting to speculate that the strong hydrogen bonds formed by E51 are a kind of trigger that, via the outer vestibule, act on the selectivity filter.

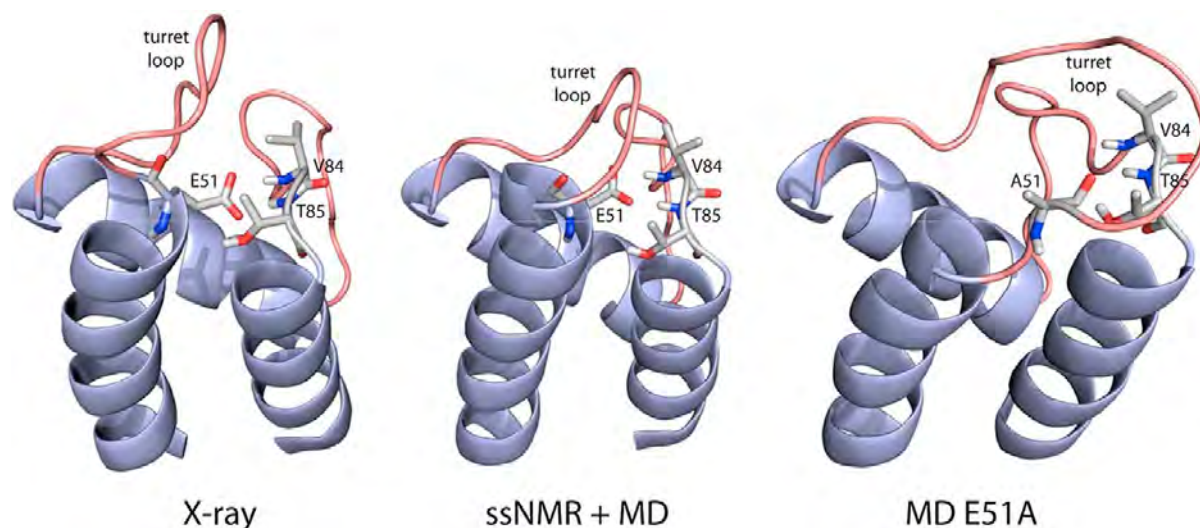


**Figure 5.** KcsA structural alignment of (left) X-ray structure 1K4C, (middle) the ssNMR model<sup>35</sup> from KcsA (after MD simulation), which shows an extended TM1 helix, and (right) the E51A mutant after 90 ns of MD simulations, showing a starkly different turret loop.

## Conclusion

We have reported an approach based on time-resolved  $^1\text{H}$ -detected ssNMR and MD simulations that allows quantifying very strong water-exposed hydrogen bonds. This is particularly interesting, since such bonds are usually not readily identifiable in X-ray structures. Our approach allowed us to identify a network of outstandingly strong hydrogen bonds in the water-exposed turret loop of KcsA. Interestingly, this network appears to be conserved in eukaryotic voltage-gated potassium (Kv) channels. We expect that this approach is amenable to a large number of proteins, especially to membrane proteins. Indeed, the unusual strength of the here described hydrogen bonds likely relates to their location in the interfacial membrane region (Figure 2D). The membrane interface is a zone of low dielectric permittivity (dielectric constant  $\epsilon \sim 7$ , as compared to  $\epsilon \sim 80$  in bulk water), which strengthens the Coulomb interactions in hydrogen bonds. Since any membrane protein features residues at the membrane interface, such ultra-strong, water exposed hydrogen bonds may be rather the rule than the exception, and may be of special structural or functional importance. Notably, it was recently reported in a ssNMR study that a number of residues in the interfacial loops of human aquaporin-1 were protected from  $^1\text{H}/^2\text{H}$  exchange.<sup>41</sup> For future studies, it may be advantageous to use lower temperatures to slow down  $^1\text{H}/^2\text{H}$  exchange, or to use shorter  $\text{D}_2\text{O}$  incubation times to distinguish more nuances of hydrogen bond strength.

## Materials and Methods

### *Sample preparation*

Fractionally deuterated (FD)<sup>21</sup> and inversely fractionally deuterated (iFD)<sup>42</sup> ion channel KcsA were expressed and reconstituted as described in chapter 2. FD [<sup>15</sup>N, <sup>13</sup>C]-KcsA was expressed in deuterated buffers, whereas iFD [<sup>15</sup>N, <sup>13</sup>C]-KcsA was expressed in protonated buffers. Therefore, only water-accessible amino-protons (H<sup>N</sup>) are detectable in FD proteins, whereas also water-inaccessible H<sup>N</sup> can be accessed in iFD proteins. <sup>1</sup>H/<sup>2</sup>H exchange steps were performed with deuterated buffers (99.9% D<sub>2</sub>O), in which the sample was incubated twice, and for one week in total, prior to the first measurement. Supplementary <sup>1</sup>H/<sup>2</sup>H exchange steps were not necessary to back-protonate water-accessible parts of FD KcsA, because purification and reconstitution steps were performed in protonated buffers. All investigated ion channels were reconstituted with E.coli polar lipids (Avanti) in potassium phosphate buffer at pH 7, in the closed-conductive gating mode.

### *Solid-state NMR experiments*

All experiments were performed at 21.1 T static magnetic field (800 MHz <sup>1</sup>H-frequency) and with 52 and 60 kHz MAS frequency for FD and iFD KcsA, respectively. The sample temperature was approximately 303 K. <sup>1</sup>H-detected 2D NH spectra were acquired with a dipolar-based pulse sequence (described in Ref.<sup>15</sup>) using MISSISSIPPI<sup>43</sup> solvent suppression. Low-power PISSARRO<sup>44-46</sup> decoupling (15 kHz decoupling power, pulse length ~70 μs) was applied in both the <sup>15</sup>N dimension and the <sup>1</sup>H dimension.

### *Molecular Dynamics Simulations*

Atomistic MD simulations were run with the g53a6 force field<sup>47</sup> and the GROMACS package version 4.6.3.<sup>48</sup> We used the X-ray structure 1K4C<sup>25</sup> embedded in anionic POPG lipids as starting system. Lipid parameters were obtained from Ref.<sup>49</sup>. The system contained the ion channel, 495 POPG lipids, 27914 water molecules, 513 K<sup>+</sup> and 30 Cl<sup>-</sup> ions, adding up to 114460 atoms. The membrane insertion of the ion channel and further simulation parameters were handled as described previously.<sup>35,37</sup> The internuclear distances to analyze hydrogen bond stability were obtained with the g\_dist tool of the GROMACS package. Distances were extracted in steps of 100 ps over a total simulation length of 300 ns.

## Supporting Information

### S1. Water contact analysis of V84 and T85

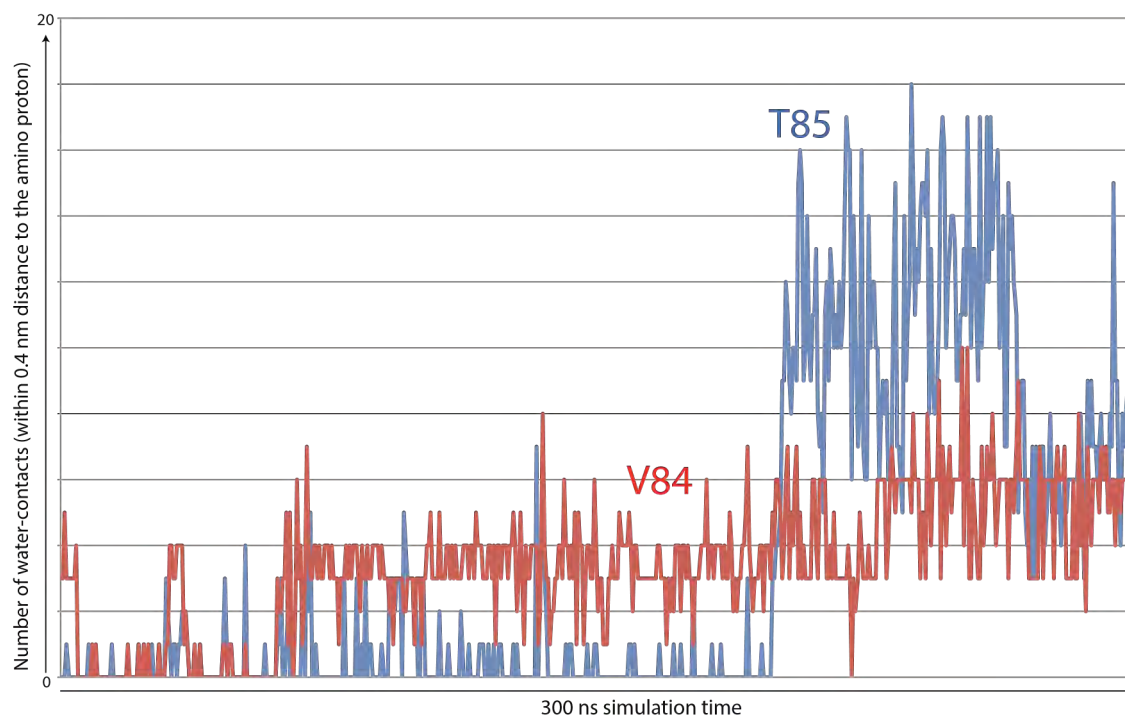


**Figure S1.** Analysis of  $\text{H}^{\text{N}}$  – water contacts over the simulated trajectory. Water molecules within a sphere of 0.4 nm were counted as a contact.

**Video S1.** A movie from a 2 ns trajectory of KcsA in POPG lipids is available in the digital version this chapter, or by following this reference online<sup>50</sup>. The time-resolution is 0.1 ns. At 0.5 ns, i.e. 5 seconds in the movie, the V84–E51 hydrogen bond shortly breaks.

## References

- (1) Wagner, G.; Wüthrich, K. Amide Proton Exchange and Surface Conformation of the Basic Pancreatic Trypsin Inhibitor in Solution: Studies with Two-Dimensional Nuclear Magnetic Resonance. *J. Mol. Biol.* **1982**, *160* (2), 343–361.
- (2) Hoshino, M.; Katou, H.; Hagihara, Y.; Hasegawa, K.; Naiki, H.; Goto, Y. Mapping the Core of the B2-Microglobulin Amyloid Fibril by H/D Exchange. *Nat. Struct. Biol.* **2002**, *9* (5), 332–336.
- (3) Raschle, T.; Rios Flores, P.; Opitz, C.; Müller, D. J.; Hiller, S. Monitoring Backbone Hydrogen-Bond Formation in  $\beta$ -Barrel Membrane Protein Folding. *Angew. Chemie Int. Ed.* **2016**, *55* (20), 5952–5955.
- (4) Englander, S. W.; Mayne, L. Protein Folding Studied Using Hydrogen-Exchange Labeling and Two-Dimensional NMR. *Annu. Rev. Biophys. Biomol. Struct.* **1992**, *21* (1), 243–265.
- (5) Polshakov, V. I.; Birdsall, B.; Feeney, J. Effects of Co-Operative Ligand Binding on Protein Amide NH Hydrogen Exchange. *J. Mol. Biol.* **2006**, *356* (4), 886–903.
- (6) Pinheiro, T. J. .; Cheng, H.; Seeholzer, S. H.; Roder, H. Direct Evidence for the Cooperative Unfolding of Cytochrome c in Lipid Membranes from H-2H Exchange Kinetics. *J. Mol. Biol.* **2000**, *303* (4), 617–626.
- (7) Halskau, Ø.; Frøystein, N. Å.; Muga, A.; Martínez, A. The Membrane-Bound Conformation of  $\alpha$ -Lactalbumin Studied by NMR-Monitored  $^1\text{H}$  Exchange. *J. Mol. Biol.* **2002**, *321* (1), 99–110.
- (8) Yao, X.; Dürr, U. H. N.; Gattin, Z.; Laukat, Y.; Narayanan, R. L.; Brückner, A.-K.; Meisinger, C.; Lange,

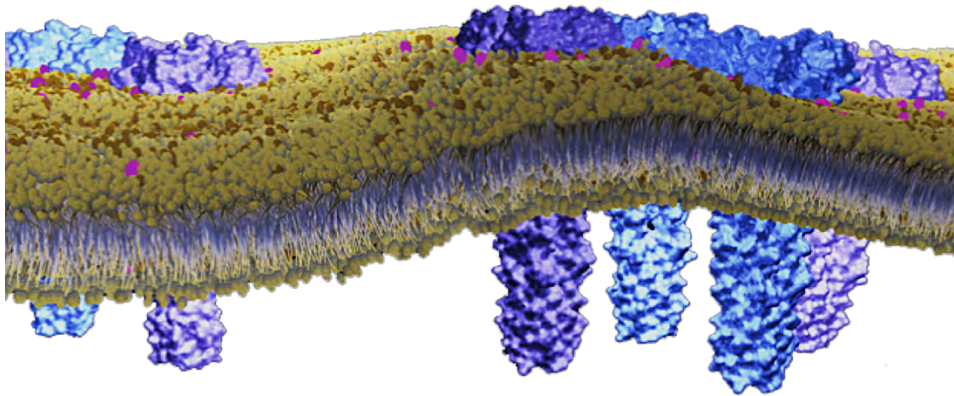
- A.; Becker, S.; Zweckstetter, M. NMR-Based Detection of Hydrogen/Deuterium Exchange in Liposome-Embedded Membrane Proteins. *PLoS One* **2014**, *9* (11), e112374.
- (9) Shi, L.; Kawamura, I.; Jung, K.-H.; Brown, L. S.; Ladizhansky, V. Conformation of a Seven-Helical Transmembrane Photosensor in the Lipid Environment. *Angew. Chemie Int. Ed.* **2011**, *50* (6), 1302–1305.
- (10) Wang, S.; Shi, L.; Kawamura, I.; Brown, L. S.; Ladizhansky, V. Site-Specific Solid-State NMR Detection of Hydrogen-Deuterium Exchange Reveals Conformational Changes in a 7-Helical Transmembrane Protein. *Biophys. J.* **2011**, *101* (3), L23–L25.
- (11) Ishii, Y.; Tycko, R. Sensitivity Enhancement in Solid State <sup>15</sup>N NMR by Indirect Detection with High-Speed Magic Angle Spinning. *J. Magn. Reson.* **2000**, *142* (1), 199–204.
- (12) Chevelkov, V.; Rehbein, K.; Diehl, A.; Reif, B. Ultrahigh Resolution in Proton Solid-State NMR Spectroscopy at High Levels of Deuteration. *Angew. Chemie Int. Ed.* **2006**, *45* (23), 3878–3881.
- (13) Zhou, D. H.; Shah, G.; Cormos, M.; Mullen, C.; Sandoz, D.; Rienstra, C. M. Proton-Detected Solid-State NMR Spectroscopy of Fully Protonated Proteins at 40 KHz Magic-Angle Spinning. *J. Am. Chem. Soc.* **2007**, *129* (38), 11791–11801.
- (14) Agarwal, V.; Penzel, S.; Szekely, K.; Cadalbert, R.; Testori, E.; Oss, A.; Past, J.; Samoson, A.; Ernst, M.; Böckmann, A.; et al. De Novo 3D Structure Determination from Sub-Milligram Protein Samples by Solid-State 100 KHz MAS NMR Spectroscopy. *Angew. Chemie Int. Ed.* **2014**, *53* (45), 12253–12256.
- (15) Sinnige, T.; Daniëls, M.; Baldus, M.; Weingarth, M. Proton Clouds to Measure Long-Range Contacts between Nonexchangeable Side Chain Protons in Solid-State NMR. *J. Am. Chem. Soc.* **2014**, *136* (12), 4452–4455.
- (16) Chevelkov, V.; Habenstein, B.; Loquet, A.; Giller, K.; Becker, S.; Lange, A. Proton-Detected MAS NMR Experiments Based on Dipolar Transfers for Backbone Assignment of Highly Deuterated Proteins. *J. Magn. Reson.* **2014**, *242*, 180–188.
- (17) Lamley, J. M.; Öster, C.; Stevens, R. A.; Lewandowski, J. R. Intermolecular Interactions and Protein Dynamics by Solid-State NMR Spectroscopy. *Angew. Chemie Int. Ed.* **2015**, *54* (51), 15374–15378.
- (18) Ma, P.; Xue, Y.; Coquelle, N.; Haller, J. D.; Yuwen, T.; Ayala, I.; Mikhailovskii, O.; Willbold, D.; Colletier, J.-P.; Skrynnikov, N. R.; et al. Observing the Overall Rocking Motion of a Protein in a Crystal. *Nat. Commun.* **2015**, *6* (1), 8361.
- (19) Andreas, L. B.; Jaudzems, K.; Stanek, J.; Lalli, D.; Bertarello, A.; Le Marchand, T.; Cala-De Paepe, D.; Kotelovica, S.; Akopjana, I.; Knott, B.; et al. Structure of Fully Protonated Proteins by Proton-Detected Magic-Angle Spinning NMR. *Proc. Natl. Acad. Sci. U. S. A.* **2016**, *113* (33), 9187–9192.
- (20) Weingarth, M.; van der Crujisen, E. A. W.; Ostmeyer, J.; Lievestro, S.; Roux, B.; Baldus, M. Quantitative Analysis of the Water Occupancy around the Selectivity Filter of a K<sup>+</sup> Channel in Different Gating Modes. *J. Am. Chem. Soc.* **2014**, *136* (5), 2000–2007.
- (21) Mance, D.; Sinnige, T.; Kaplan, M.; Narasimhan, S.; Daniëls, M.; Houben, K.; Baldus, M.; Weingarth, M. An Efficient Labelling Approach to Harness Backbone and Side-Chain Protons in <sup>1</sup>H-Detected Solid-State NMR Spectroscopy. *Angew. Chemie Int. Ed.* **2015**, *54* (52), 15799–15803.
- (22) Medeiros-Silva, J.; Mance, D.; Daniëls, M.; Jekhmane, S.; Houben, K.; Baldus, M.; Weingarth, M. <sup>1</sup>H-Detected Solid-State NMR Studies of Water-Inaccessible Proteins In Vitro and In Situ. *Angew. Chemie Int. Ed.* **2016**, *55* (43), 13606–13610.
- (23) Ward, M. E.; Shi, L.; Lake, E.; Krishnamurthy, S.; Hutchins, H.; Brown, L. S.; Ladizhansky, V. Proton-Detected Solid-State NMR Reveals Intramembrane Polar Networks in a Seven-Helical Transmembrane Protein Proteorhodopsin. *J. Am. Chem. Soc.* **2011**, *133* (43), 17434–17443.
- (24) del Amo, J.-M. L.; Fink, U.; Reif, B. Quantification of Protein Backbone Hydrogen-Deuterium Exchange Rates by Solid State NMR Spectroscopy. *J. Biomol. NMR* **2010**, *48* (4), 203–212.
- (25) Zhou, Y.; Morais-Cabral, J. H.; Kaufman, A.; MacKinnon, R. Chemistry of Ion Coordination and Hydration Revealed by a K<sup>+</sup> Channel–Fab Complex at 2.0 Å Resolution. *Nature* **2001**, *414* (6859), 43–48.
- (26) Lange, A.; Giller, K.; Hornig, S.; Martin-Eauclaire, M.-F.; Pongs, O.; Becker, S.; Baldus, M. Toxin-Induced Conformational Changes in a Potassium Channel Revealed by Solid-State NMR. *Nature* **2006**, *440* (7086), 959–962.
- (27) Ader, C.; Schneider, R.; Hornig, S.; Velisetty, P.; Wilson, E. M.; Lange, A.; Giller, K.; Ohmert, I.; Martin-Eauclaire, M.-F.; Trauner, D.; et al. A Structural Link between Inactivation and Block of a K<sup>+</sup> Channel. *Nat. Struct. Mol. Biol.* **2008**, *15* (6), 605–612.
- (28) Cordero-Morales, J. F.; Cuello, L. G.; Zhao, Y.; Jogini, V.; Cortes, D. M.; Roux, B.; Perozo, E. Molecular

- Determinants of Gating at the Potassium-Channel Selectivity Filter. *Nat. Struct. Mol. Biol.* **2006**, *13* (4), 311–318.
- (29) Ader, C.; Schneider, R.; Hornig, S.; Velisetty, P.; Vardanyan, V.; Giller, K.; Ohmert, I.; Becker, S.; Pongs, O.; Baldus, M. Coupling of Activation and Inactivation Gate in a K<sup>+</sup>-Channel: Potassium and Ligand Sensitivity. *EMBO J.* **2009**, *28* (18), 2825–2834.
- (30) Larsson, H. P.; Elinder, F. A Conserved Glutamate Is Important for Slow Inactivation in K<sup>+</sup> Channels. *Neuron* **2000**, *27* (3), 573–583.
- (31) Zilberberg, N.; Ilan, N.; Goldstein, S. A. . KCNKØ: Opening and Closing the 2-P-Domain Potassium Leak Channel Entails “C-Type” Gating of the Outer Pore. *Neuron* **2001**, *32* (4), 635–648.
- (32) Ortega-Sáenz, P.; Pardal, R.; Castellano, A.; López-Barneo, J. Collapse of Conductance Is Prevented by a Glutamate Residue Conserved in Voltage-Dependent K(+) Channels. *J. Gen. Physiol.* **2000**, *116* (2), 181–190.
- (33) Imai, S.; Osawa, M.; Takeuchi, K.; Shimada, I. Structural Basis Underlying the Dual Gate Properties of KcsA. *Proc. Natl. Acad. Sci. U. S. A.* **2010**, *107* (14), 6216–6221.
- (34) Morton, M. J.; Abohamed, A.; Sivaprasadarao, A.; Hunter, M. PH Sensing in the Two-Pore Domain K<sup>+</sup> Channel, TASK2. *Proc. Natl. Acad. Sci. U. S. A.* **2005**, *102* (44), 16102–16106.
- (35) van der Crujisen, E. A. W.; Nand, D.; Weingarth, M.; Prokofyev, A.; Hornig, S.; Cukkemane, A. A.; Bonvin, A. M. J. J.; Becker, S.; Hulse, R. E.; Perozo, E.; et al. Importance of Lipid-Pore Loop Interface for Potassium Channel Structure and Function. *Proc. Natl. Acad. Sci.* **2013**, *110* (32), 13008–13013.
- (36) Raghuraman, H.; Islam, S. M.; Mukherjee, S.; Roux, B.; Perozo, E. Dynamics Transitions at the Outer Vestibule of the KcsA Potassium Channel during Gating. *Proc. Natl. Acad. Sci. U. S. A.* **2014**, *111* (5), 1831–1836.
- (37) Weingarth, M.; Prokofyev, A.; van der Crujisen, E. A. W.; Nand, D.; Bonvin, A. M. J. J.; Pongs, O.; Baldus, M. Structural Determinants of Specific Lipid Binding to Potassium Channels. *J. Am. Chem. Soc.* **2013**, *135* (10), 3983–3988.
- (38) Weingarth, M.; Baldus, M. Solid-State NMR-Based Approaches for Supramolecular Structure Elucidation. *Acc. Chem. Res.* **2013**, *46* (9), 2037–2046.
- (39) Marius, P.; de Planque, M. R. R.; Williamson, P. T. F. Probing the Interaction of Lipids with the Non-Annular Binding Sites of the Potassium Channel KcsA by Magic-Angle Spinning NMR. *Biochim. Biophys. Acta - Biomembr.* **2012**, *1818* (1), 90–96.
- (40) van der Crujisen, E. A. W.; Prokofyev, A. V.; Pongs, O.; Baldus, M. Probing Conformational Changes during the Gating Cycle of a Potassium Channel in Lipid Bilayers. *Biophys. J.* **2017**, *112* (1), 99–108.
- (41) Wang, S.; Ing, C.; Emami, S.; Jiang, Y.; Liang, H.; Pomès, R.; Brown, L. S.; Ladizhansky, V. Structure and Dynamics of Extracellular Loops in Human Aquaporin-1 from Solid-State NMR and Molecular Dynamics. *J. Phys. Chem. B* **2016**, *120* (37), 9887–9902.
- (42) Medeiros-Silva, J.; Mance, D.; Daniëls, M.; Jekhmane, S.; Houben, K.; Baldus, M.; Weingarth, M. 1-Detektierete Festkörper-NMR-Studien Wasserunzugänglicher Proteine in Vitro Und in Situ. **2016**.
- (43) Zhou, D. H.; Rienstra, C. M. High-Performance Solvent Suppression for Proton Detected Solid-State NMR. *J. Magn. Reson.* **2008**, *192* (1), 167–172.
- (44) Weingarth, M.; Bodenhausen, G.; Tekely, P. Probing the Quenching of Rotary Resonance by PISSARRO Decoupling. *Chem. Phys. Lett.* **2011**, *502* (4–6), 259–265.
- (45) Weingarth, M.; Bodenhausen, G.; Tekely, P. Low-Power Decoupling at High Spinning Frequencies in High Static Fields. *J. Magn. Reson.* **2009**, *199* (2), 238–241.
- (46) Weingarth, M.; Tekely, P.; Bodenhausen, G. Efficient Heteronuclear Decoupling by Quenching Rotary Resonance in Solid-State NMR. *Chem. Phys. Lett.* **2008**, *466* (4–6), 247–251.
- (47) Soares, T. A.; Hünenberger, P. H.; Kastenholz, M. A.; Krätzler, V.; Lenz, T.; Lins, R. D.; Oostenbrink, C.; van Gunsteren, W. F. An Improved Nucleic Acid Parameter Set for the GROMOS Force Field. *J. Comput. Chem.* **2005**, *26* (7), 725–737.
- (48) Hess, B.; Kutzner, C.; van der Spoel, D.; Lindahl, E. GROMACS 4: Algorithms for Highly Efficient, Load-Balanced, and Scalable Molecular Simulation. *J. Chem. Theory Comput.* **2008**, *4* (3), 435–447.
- (49) Kukol, A. Lipid Models for United-Atom Molecular Dynamics Simulations of Proteins. *J. Chem. Theory Comput.* **2009**, *5* (3), 615–626.
- (50) Medeiros-Silva, J.; Jekhmane, S.; Baldus, M.; Weingarth, M. Hydrogen Bond Strength in Membrane Proteins Probed by Time-Resolved <sup>1</sup>H-Detected Solid-State NMR and MD Simulations. *Solid State Nucl. Magn. Reson.* **2017**, *87*, 80–85.



# CHAPTER 4

Shifts in the selectivity filter dynamics cause modal gating in  $K^+$  channels



## Abstract

Spontaneous activity shifts at constant experimental conditions represent a widespread regulatory mechanism in ion channels. The molecular origins of these modal gating shifts are poorly understood. In the K<sup>+</sup> channel KcsA, a multitude of fast activity shifts that emulate the native modal gating behaviour can be triggered by point-mutations in the hydrogen bonding network that controls the selectivity filter. Using solid-state NMR and molecular dynamics simulations in a variety of KcsA mutants, here we show that modal gating shifts in K<sup>+</sup> channels are associated with important changes in the channel dynamics that strongly perturb the selectivity filter equilibrium conformation. Furthermore, our study reveals a drastically different motional and conformational selectivity filter landscape in a mutant that mimics voltage-gated K<sup>+</sup> channels, which provides a foundation for an improved understanding of eukaryotic K<sup>+</sup> channels. Altogether, our results provide a high-resolution perspective on some of the complex functional behaviour of K<sup>+</sup> channels.

*Based on the publication:*

Shehrazade Jekhmane\*, João Medeiros-Silva\*, Jing Li, Felix Kümmerer, Christoph Müller-Hermes, Marc Baldus, Benoît Roux and Markus Weingarth

Shifts in the selectivity filter dynamics cause modal gating in K<sup>+</sup> channels.

*Nature communications*, 2019, 10, 123.

\*equal contribution

## Introduction

Potassium (K<sup>+</sup>) channels are of fundamental importance for the functioning of excitable cells.<sup>1</sup> They allow selective and rapid flux of K<sup>+</sup> across the cell membrane through a central pore, which is regulated by the interplay between a cytoplasmic activation gate and an extracellular C-type inactivation gate known as selectivity filter. The selectivity filter sequence TVGYG is highly conserved, and its backbone carbonyl-groups together with the threonine hydroxyl group line up to form the five K<sup>+</sup> coordination sites (S0–S4).<sup>2,3</sup>

Extensive crystallographic studies in the well-accepted model K<sup>+</sup> channel KcsA showed that C-type inactivation is governed by a complex hydrogen bond network behind the selectivity filter.<sup>4,5</sup> Residue E71 is at the centre of this network, and modulates the selectivity filter by coordinating to the backbone of Y78 and, mediated via a water molecule, the D80 as well as the W67 side chains (Figure 1A). While W67 and D80 are highly conserved in K<sup>+</sup> channels, E71 is commonly replaced by a valine or isoleucine in eukaryotes (Figure 1B), which is assumed to critically modulate selectivity filter gating. Indeed, electrophysiological measurements showed that point-mutations at E71 lock the KcsA channel into different, natively occurring gating modes, which are best represented by a high-open probability (E71A), a low-open probability (E71I), and a high-frequency flicker (E71Q) mode.<sup>6</sup> Random shifts between such gating modes, known as modal gating shifts, were observed in various eukaryotic and prokaryotic K<sup>+</sup> channels, and are a widespread regulatory mechanism of channel activity.<sup>4,7–11</sup> Yet, despite their broad functional importance, the structural correlates and triggers of modal gating shifts are unknown. Modal gating shifts were suggested to relate to selectivity filter rearrangements; however, a series of X-ray structures of E71X mutants showed no changes in the filter (RMSD relative to WT KcsA is <0.25 Å)<sup>6</sup> despite the marked functional heterogeneity of these mutants. Curiously, for the E71A mutant, a well-established model to study K<sup>+</sup> channel gating,<sup>12,13</sup> a second, strongly different filter conformation of uncertain functional relevance was crystallised.<sup>4,14</sup> Besides the lack of clarity on the selectivity filter conformation, it was further assumed that changes in the filter dynamics could cause modal gating shifts.<sup>6</sup> However, also here, whether the selectivity filter dynamics change in reference to the gating mode is unknown, and experimental data are scarce to resolve this question. Altogether, there is a fundamental lack of knowledge on how the hydrogen bond network surrounding the selectivity filter modulates its gating, which critically limits our understanding of modal gating shifts of Kv channels.

Here, we use modern proton-detected (<sup>1</sup>H-detected)<sup>15–20</sup> solid-state NMR (ssNMR) in native-like membranes to compare the selectivity filter in WT KcsA and the three mutants (E71A, E71I, E71Q) that are best representatives of modal gating. We show that E71 point-mutations cause marked changes in the selectivity filter conformational dynamics, in contrast to previous crystallographic studies that revealed virtually no changes in structure.<sup>6</sup> By

combining ssNMR with molecular dynamics (MD) simulations, we demonstrate that altered structural dynamics in E71X mutants drive the selectivity filter into new conformational equilibria that represent the molecular origin of modal gating. Furthermore, we show that modal gating goes hand in hand with fluctuations in the hydrogen bonding and water network behind the filter, which are triggers of sudden mode shifts. Altogether, these results provide a high-resolution perspective on the complex kinetic behaviour of the selectivity filter of K<sup>+</sup> channels. Importantly, the pronounced conformational and motional changes that we observe in E71I KcsA provide a foundation for future elucidation of the selectivity filter of eukaryotic K<sup>+</sup> channels.

## Results

### *NMR assignments of the channels at near-native conditions*

We assigned the <sup>1</sup>H, <sup>13</sup>C, and <sup>15</sup>N ssNMR chemical shifts of WT KcsA and the E71A, E71I, E71Q mutants in order to analyse their conformational dynamics in membranes. First, we prepared uniformly [<sup>13</sup>C,<sup>15</sup>N]-labelled inversely Fractionally Deuterated<sup>17</sup> channels in liposomes composed of *Escherichia coli* lipids. Samples were prepared in buffer conditions (pH 7.4, 100 mM K<sup>+</sup>) at which WT KcsA is in the closed-conductive state,<sup>21</sup> i.e., a state with a closed activation gate and a conductive selectivity filter. De novo backbone chemical shift assignments were obtained for mutant E71A using a set of four dipolar-based three-dimensional (3D) <sup>1</sup>H-detected ssNMR experiments (CANH, CONH, CAcoNH, COcaNH) (Figure 1C and Figure S1). The high spectral quality enabled us to almost fully assign residues L41–W87, which include the complete selectivity filter and pore helix, the pore loop, larger parts of the outer transmembrane 1 (TM1) helix, and a few residues of the inner transmembrane 2 (TM2) helix. Since we used dipolar-based magnetisation transfer steps that decrease in efficiency with increasing molecular mobility, the cytoplasmic domain (F125–R160) and the membrane-associated M0 helix (M1–H20) were not detectable at our experimental temperatures of 300–310 K.<sup>22</sup> Assignments were then transferred to KcsA mutants E71I and E71Q and confirmed with a reduced set of 3D ssNMR experiments (CANH, CONH). The reduced set was also used to complement our previous WT KcsA assignments.<sup>17</sup> For the flicker mutant E71Q, spectral sensitivity was significantly lower, indicative of increased mobility, which averages dipolar magnetisation transfer efficiency. Furthermore, for all mutants and WT KcsA, we acquired two-dimensional (2D) <sup>13</sup>C–<sup>13</sup>C experiments. Moreover, we acquired dipolar 2D <sup>15</sup>N–<sup>1</sup>H ssNMR spectra, in which each signal relates to one <sup>15</sup>N–<sup>1</sup>H backbone or side chain unit, and which represent spectral fingerprints.

## Modal gating relates to changes in the filter conformation

NMR chemical shifts are sensitive reporters of protein conformation. Therefore, comparing the chemical shifts of the mutants to WT KcsA enables the analysis of the structural impact of the substitutions at E71. The 2D  $^{15}\text{N}$ - $^1\text{H}$  and  $^{13}\text{C}$ - $^{13}\text{C}$  spectra of all E71X mutants superimposed very well onto WT KcsA, demonstrating that the global protein fold is conserved (Figure S2). However, for all mutants, we observed remarkably large  $^1\text{H}$  and  $^{15}\text{N}$  (HN) as well as  $^{13}\text{C}$  chemical shift perturbations (CSPs) across the selectivity filter (Figure 1D,E and Figure S3). For all mutants, we observed very important HN CSPs for the essential residues W67, Y78, and D80 behind the filter, demonstrating changes in their hydrogen bond interactions. At the same time, the large Ca and CO CSPs that we observed for residues G77, Y78, and D80 imply pronounced conformational filter backbone changes, which likely have implications for the  $K^+$  occupancy. Intriguingly, all mutants also exhibited a large CSP for V76CO, which is immediately involved in  $K^+$  binding and key residue for C-type inactivation (Figure 1E).<sup>3</sup>

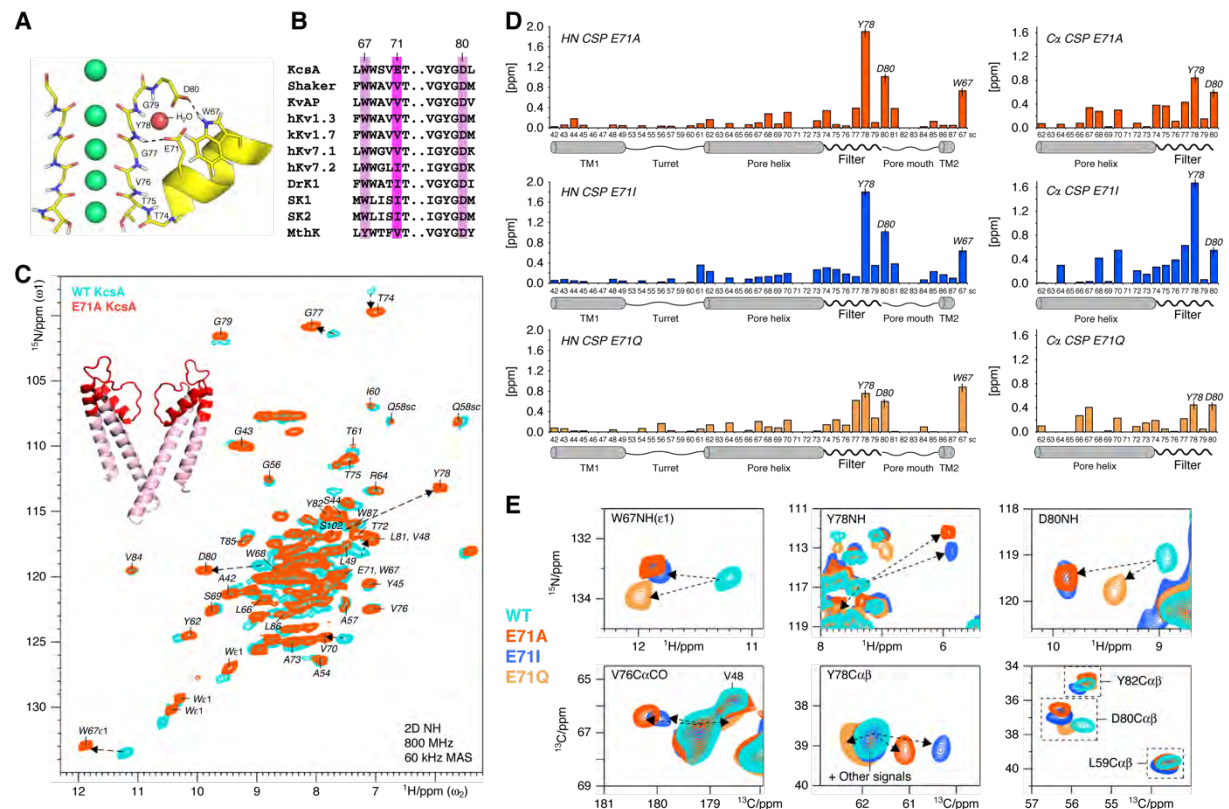


**Figure 1.** E71X point-mutations cause large conformational changes in the KcsA selectivity filter. **A)** The selectivity filter of  $K^+$  channel KcsA (1K4C) is regulated by a hydrogen bond network with the triad W67–E71–D80 at the centre.<sup>5</sup> **B)** W67 and D80 are highly conserved, while E71 is commonly replaced by a nonpolar valine or isoleucine in Kv channels. **C)** 2D NH ssNMR spectra of WT KcsA (cyan) and mutant E71A (red) acquired in membranes. Arrows indicate major signal shifts of key residues. Residues L41–W87 are annotated in the E71A spectrum and highlighted in red on the X-ray structure. **D)** Chemical shift perturbations (CSPs) of E71A (red), E71I (blue), and E71Q (orange) in

reference to WT KcsA. Combined HN CSPs (left) of amino-protons and backbone-nitrogens and (right) Ca CSPs. The strongest NH CSPs in E71A are highlighted in C). **E**) 2D NH (upper panel) and 2D CC spectra (lower) showing large CSPs of key residues W67, V76, Y78, and D80 in E71A (red), E71I (blue), and E71Q (orange) relative to WT KcsA (cyan).

Mutants E71A and E71I showed a strikingly similar CSP pattern. Here, the HN and  $^{13}\text{C}$  signal shifts of W67, V76, Y78, and D80 are all similar in magnitude and in the same direction. This similarity appears plausible, given that neither alanine nor isoleucine is able to mimic the hydrogen bonding capacities of the E71 carboxyl group. However, although the CSP pattern is similar, E71I shows a much larger Y78Ca CSP than E71A, which implies conformational differences.

While we also observed CSP maxima at W67, G77, Y78, and D80 in E71Q, these signal shifts were partially in opposite direction relative to E71A and E71I, and less strong. In general, among the three mutants, the chemical shifts of E71Q deviated the least from WT KcsA. Considering that a glutamine can partly substitute for some of the hydrogen bonds of a glutamate, it is likely that the E71Q filter conformation is relatively close to WT KcsA. Indeed, the D80 side chain and the Y78 backbone showed by far the smallest CSPs for E71Q, which strongly suggests that Q71–D80 and Q71–Y78 maintain interactions analogous to WT KcsA, while these interactions are lost in E71A and E71I (Figs. 2A and 1E).

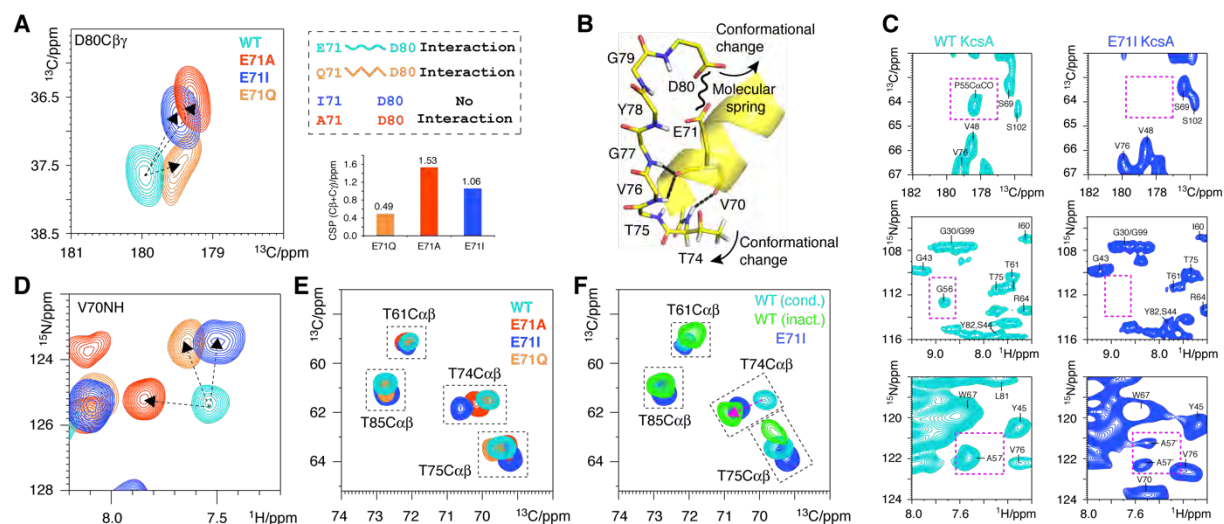


**Figure 2.** Loss of the E71–D80 interaction causes extended rearrangements behind the filter. **A**) Zoom into (left) 2D CC ssNMR spectra of WT KcsA (cyan), E71A (red), E71I (blue), and E71Q (orange) showing the D80 side chain CSPs. E71Q (right) mimics the E71–D80 interaction, which is lost in E71A and E71I. The D80 side chain CSPs are large in E71A and E71I, while they are small in E71Q. **B**) Structural representation (1K4C) of the stabilisation of filter residues T74–G77 by hydrogen bonds with V70 and E71 of the pore helix. **C**) The E71I turret is disordered, which causes signals to disappear or split. Spectral zooms are shown for WT KcsA (cyan) and E71I (blue). **D**) Overlay of 2D NH spectra showing a strong CSP for V70 of the pore helix. **E**) Overlay of 2D CC spectra, showing CSPs of the functionally critical T74 side chain in E71X mutants. **F**) The large T74 CSP in E71I (pH 7.4, 100 mM  $\text{K}^+$ ) is reminiscent of the inactivated filter in WT KcsA (pH 4, 0 mM  $\text{K}^+$ ).

Next to conformational changes in the filter, the mutants showed moderate to larger CSPs around residues W67–V70. These changes presumably relate to modulations in the aromatic belt W67, W68, and Y78 that surrounds the filter, and to the loss or modulation of interaction E71–D80, which acts as a molecular spring that couples the pore helix to the pore mouth in WT KcsA (Figure 2B).<sup>5</sup> Our data show that the pore helices in all mutant channels exhibit, compared to WT KcsA, local changes (Figure 2D) that modulate the residues T74–T75–V76–G77 at the N-terminal end of the selectivity filter, which are directly coordinated to the pore helix by hydrogen bonds. Indeed, all mutants show clear perturbations at V76 and G77 (Figure 1D,E). We observed the largest CSPs in the E71I pore helix, which correlates with strong signal shifts of the T74 side chain. Since conformational changes of the T74 side chain relate to C-type inactivation,<sup>23,24</sup> this perturbation could be functionally important for E71I, which favours transitions to a non-conductive state.<sup>6</sup> This assumption is corroborated by 2D CC spectra, which show that the T74 side chain conformation in E71I (pH 7.4, 100 mM K<sup>+</sup>) and in the inactivated filter of WT KcsA (pH 4, 0 mM K<sup>+</sup>) are close to each other (Figure 2E,F).

Furthermore, we observed remarkable conformational changes in the turret G53–T61. The turret is an important drug binding site<sup>25</sup> and responds to gating changes<sup>26</sup>; however, the structural underpinning is unclear and inaccessible from X-ray structures because of intense interactions between turret and Fab fragments.<sup>4</sup> In our ssNMR experiments, the CSPs in the turret are small. However, to our surprise, residues P55, G56, and A57 in E71I disappeared or showed signal splittings, strongly indicative of stark structural heterogeneity (Figure 2C). This implies that the replacement of E71 by isoleucine causes long-range effect that are felt ~2 nm away from the mutation site. Note that CSPs for the TM1 and TM2 helices, as well as for un-annotated TM residues, were very small, confirming that the global WT KcsA fold is conserved in the mutants.

### *Changes in the filter dynamics and modal gating shifts*

Historically, the selectivity filter was thought to form a stiff framework in order to allow fast conduction of K<sup>+</sup> together with high selectivity over Na<sup>+</sup>.<sup>2</sup> More recent studies point to a more dynamic filter,<sup>27</sup> and hypothesise that modal gating shifts relate to changes in the motional behaviour of the filter.<sup>6</sup> However, quantitative experimental data on selectivity filter dynamics are not available in membranes, critically limiting our understanding of K<sup>+</sup> channel function. Here we probe the filter dynamics in reference to the gating mode with ssNMR relaxation, which is an ideal approach to measure the internal dynamics of membrane proteins at native conditions.<sup>17,28</sup> Site-resolved ssNMR relaxation can be probed with 2D <sup>15</sup>N–<sup>1</sup>H experiments that include a relaxation element that is sensitive to dynamics on a certain time-scale. A series of spectra is then acquired with increasing duration of the relaxation element,

and the signal sensitivity decreases according to the motion for a given residue. The signal decay is then converted into a relaxation rate  $R$ , and higher rates indicate enhanced dynamics. We probed the  $^{15}\text{N}$  slow rotating-frame relaxation ( $R_{1\rho}$ ) for WT KcsA and the mutants (Figure 3) using extensive series of  $^1\text{H}$ -detected 2D  $^{15}\text{N}$ - $^1\text{H}$  experiments.<sup>29</sup>  $^{15}\text{N}$   $R_{1\rho}$  relaxation is sensitive to dynamics in the nanosecond–millisecond range but dominated by motion with slow correlation times in the microsecond range.<sup>30</sup> The high sensitivity with  $^1\text{H}$ -detection enabled us to measure relaxation rates with high accuracy. In all investigated channels, our study unravelled strikingly different filter dynamics that clearly correlate with the CSP maxima, thereby linking conformational and motional changes. In WT KcsA, the filter ( $\sim 15 \text{ ms}^{-1} R_{1\rho}$ ) is the most dynamic membrane-embedded region, with G79 as a distinct local maximum. The dynamics of the pore helix is slightly lower, TM1 residues show the least dynamics, while the extracellular turret is by far the most mobile region. These results agree with our previous relaxation studies in WT KcsA.<sup>17</sup>

The global dynamics of mutant E71I, which mimics certain Kv channels, is particularly interesting. Surprisingly, compared to WT KcsA, we measured strongly enhanced dynamics at the filter entrance Y78-D80 ( $\sim 25 \text{ ms}^{-1} R_{1\rho}$ ). These residues also showed the largest CSPs, demonstrating again that local conformational and motional changes correlate. Furthermore, we observed sizeable stiffening at G77 in the middle of the E71I filter. Intriguingly, the selectivity filter dynamics is very different in the E71A mutant, in which the middle and upper filter regions (V76–D80) drastically rigidified ( $\sim 8 \text{ ms}^{-1} R_{1\rho}$ ). This means that E71A and E71I exhibit clearly different filter dynamics in spite of similar CSP patterns. It is easy to imagine that these differential dynamics are at the origin of some of the heterogeneous gating kinetics observed in KcsA and other  $\text{K}^+$  channels. As for the CSPs, the flicker mutant E71Q behaved very differently and featured substantially and globally enhanced  $R_{1\rho}$  values with a maximum at V76. This means that the entire channel undergoes pronounced large-scale slow motions, which explains the strongly reduced sensitivity in our dipolar experiments with E71Q. Altogether, our data hence strongly suggest that the rapid flickering between open and closed states in KcsA, and observed in all  $\text{K}^+$  channels,<sup>6,10</sup> relates to large-scale dynamics of the pore domain.

Another noteworthy observation was the stark change in the dynamics of the turret, which rigidified in E71A and E71I. As we concluded above (Figure 2C), this implies that the loss of the E71–D80 interaction causes allosteric changes 2 nm distal from the mutation site, presumably by successive changes of hydrogen bonding partners. A likely starting point for this chain reaction could be D80, which adopts a clearly different conformation in E71A and E71I compared to WT KcsA (Figure 2A).

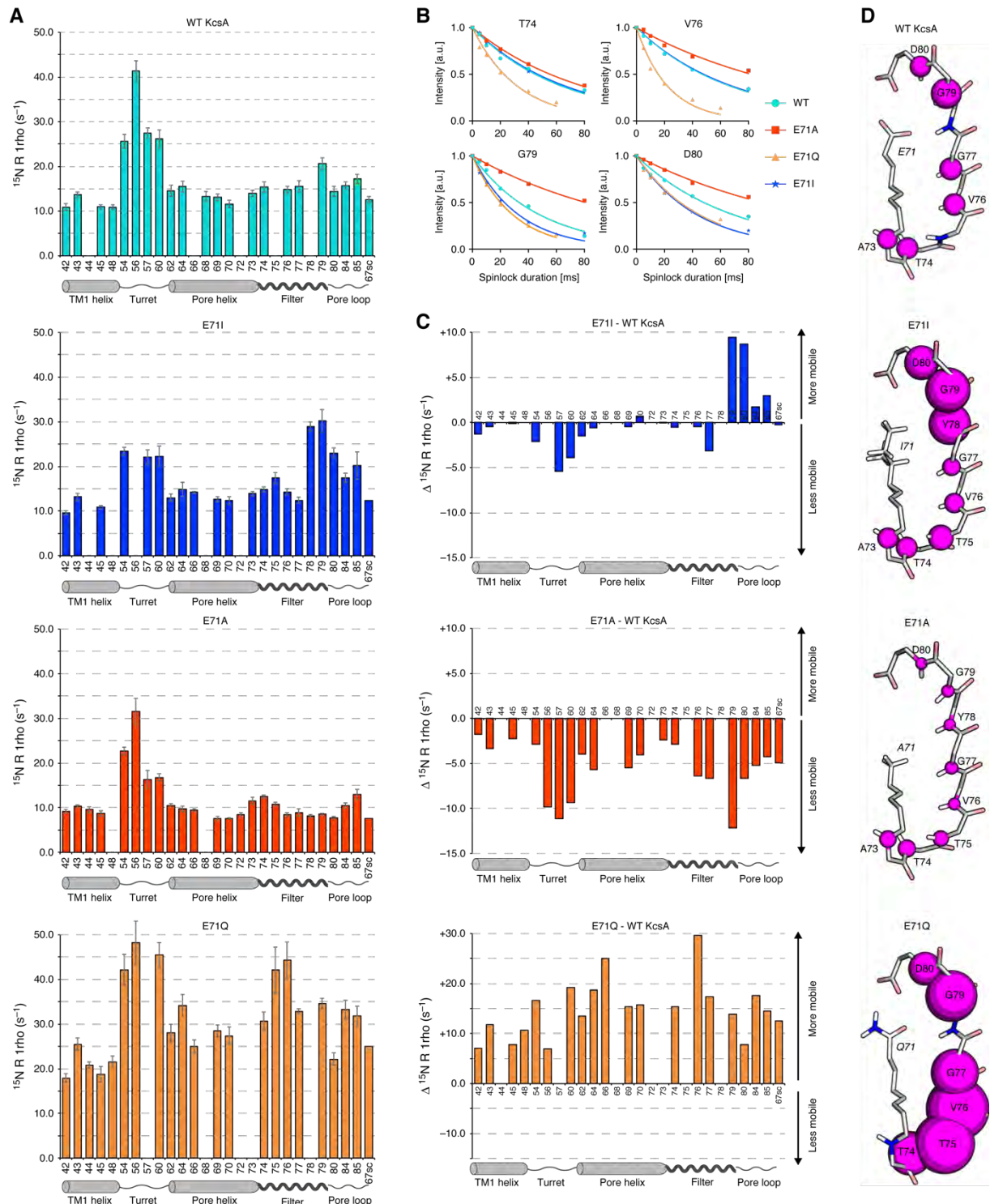


**Figure 3.** E71X point-mutations strongly change the selectivity filter dynamics. **A)**  $^{15}\text{N}$  rotating-frame ssNMR relaxation rates ( $R_{1\rho}$ ) that report on slow molecular motions in WT KcsA (cyan), E71A (red), E71I (blue), and E71Q (orange) measured at 700 MHz and 58 kHz MAS. The error bars show the standard error of the fit. **B)**  $R_{1\rho}$  signal decay curves for selected filter residues. Symbols mark data points and lines represent best fits. **C)** Plots of the differences in the dynamics between E71X mutants and WT KcsA. **D)** Illustration of the site-resolved selectivity filter dynamics. The size of the magenta spheres represents the  $R_{1\rho}$  relaxation rates.

*Fluctuations in a critical water cavity trigger modal gating*

The strongly different filter dynamics in the E71X mutants raise the question which molecular events could cause spontaneous mode shifts. One potential trigger could be buried water, localised in a cavity behind the filter, which is a decisive gating determinant in  $K^+$  channels, relating to C-type inactivation and recovery.<sup>22,31,32</sup> Previous X-ray studies suggested that changes in the size of the water cavity could trigger modal gating shifts. In these and other previous studies, two water molecules were resolved behind the filter of E71I and E71A,<sup>6,12</sup> while the presence of buried water molecules in E71Q was unclear due to insufficient resolution.

Here, we revisit the water distribution behind the selectivity filter using H/D exchange ssNMR,<sup>17,33,34</sup> for which we acquired 2D  $^{15}\text{N}$ - $^1\text{H}$  spectra in fully deuterated buffers. At these conditions, exchange with deuterons strongly attenuates signals of water-exposed amino-protons, which provides high-resolution information on the water cavity size.<sup>22</sup> The channels were incubated in deuterated buffers for 2 days, and the completeness of the exchange was confirmed on the fully water-exposed turret, which entirely disappeared from the 2D NH spectra (Figure 4A, right panel). In WT KcsA, G79 is the only filter residue that disappeared in deuterated buffers while Y78–T74 showed no signs of H/D exchange (Figure 4A,B). The lack of exchange for Y78 in WT KcsA is astonishing, given that a water molecule is in direct proximity in the X-ray structure (Figure 1A), and strongly suggests that a tight hydrogen bond with E71 protects Y78 from H/D exchange. In line with this conclusion, Y78 showed attenuated intensity in both E71I (–33%) and E71A (–81%) (Figure 4B,C), in which the X71–Y78 hydrogen bond is lost. Intriguingly, the much faster exchange of Y78 in E71A implies a larger water cavity, which agrees with the smaller size of alanine relative to isoleucine. The widened water cavity is also corroborated by the high rigidity of E71A (Figure 3), which renders enhanced molecular fluctuations an unlikely cause for increased H/D exchange. Strikingly, in the flickery E71Q channel, G79 did not exchange (Figure 4A). Similarly, L81 did not exchange in E71Q, while it disappeared in E71A, E71I, and WT KcsA, which confirms that the water cavity is smaller or fully absent behind the E71Q filter. Altogether, our NMR data demonstrate that, in membranes, E71X point-mutations change the size of the water cavity in reference to the gating mode, analogous to the crucial change of the water cavity during C-type inactivation.<sup>31</sup> Note that long MD simulations, which are discussed in detail in the following sections, also show widened water cavities and higher exchange-rates with bulk water for E71A and E71I (Figure S4 and Table S1).



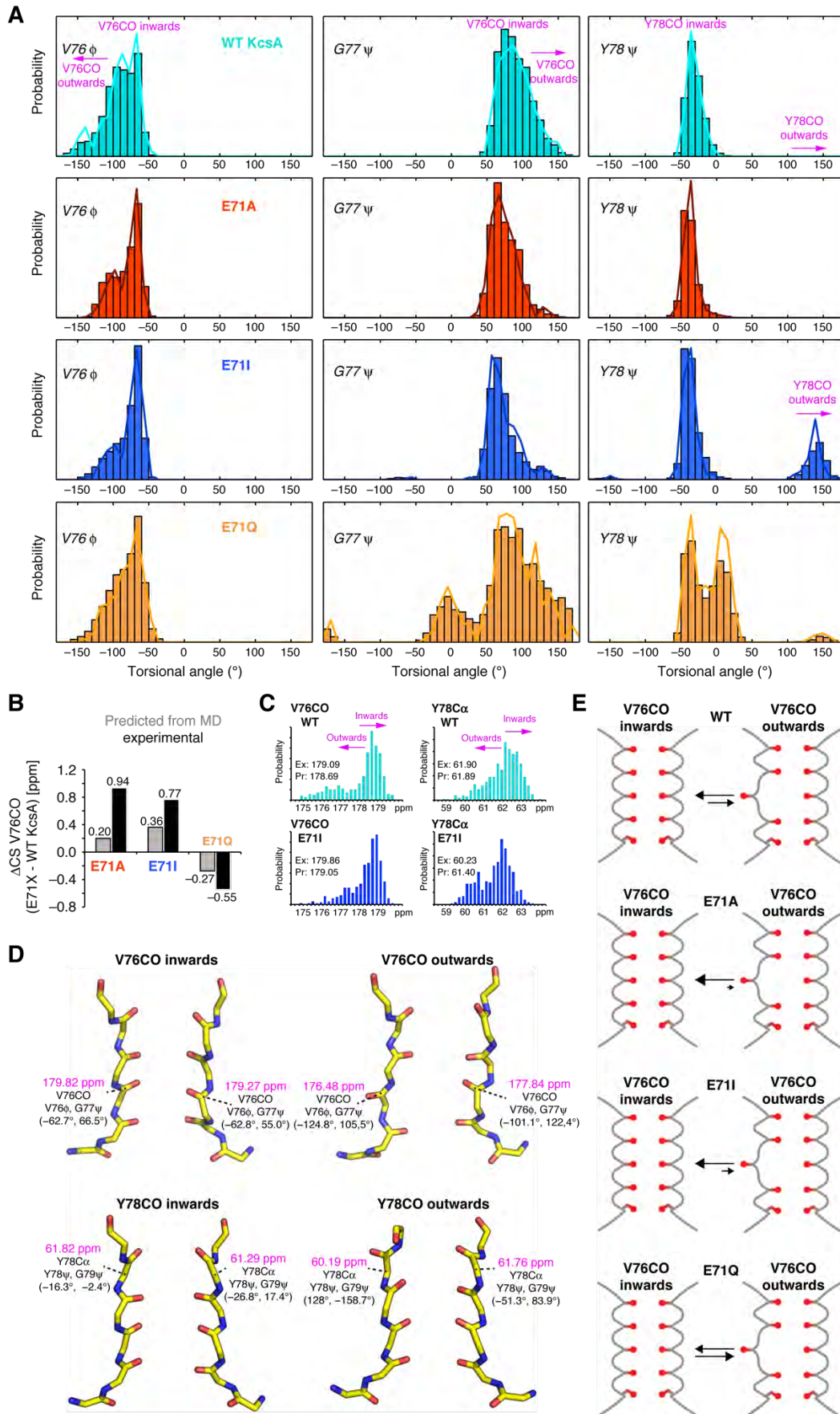


Figure 5. E71X mutations shift the equilibrium between inwards and outwards filter states.

**A)** Dihedral angle distribution of filter residues of WT (cyan), E71A (red), E71I (blue), and E71Q (orange) derived from 1- $\mu$ s-long MD simulations. Characteristic angular spaces for inwards conformations, with the carbonyl group oriented towards the filter pore, and outwards states are highlighted. **B)** Comparison of V76CO CSPs derived from experiments (black bars) and back-calculated<sup>35</sup> from MD simulations (grey bars). **C)** Histogram of back-calculated chemical shifts for V76CO and Y78Ca of WT KcsA (cyan) and E71I (blue). The V76CO (left) inwards state is stabilised in E71I, leading to higher V76CO chemical shifts, while the Y78CO (right) inwards state is destabilised in E71I, leading to lower Y78Ca chemical shifts. **D)** Representative MD snapshots of WT KcsA and E71I showing inwards and outwards states of V76CO and Y78CO. The chemical shifts (in magenta) of V76CO and Y78Ca strongly differ between inwards and outwards conformations. **E)** Illustration of the stabilisation of the V76CO inwards state in E71A and E71I, and the destabilisation in E71Q.

### *Shifts in the equilibrium structure of the filter*

Our ssNMR data demonstrate that E71 point-mutations cause large CSPs in the selectivity filter, with maxima at Y78Ca and V76CO; the latter forming the S2 and S3 sites that are critically involved in C-type inactivation.<sup>3</sup> Such large perturbations in the heart of the filter are astonishing, given that E71A and E71I show a sharply reduced extent of C-type inactivation.<sup>6</sup> To gain a structural understanding of the ssNMR CSPs, we performed a series of 1- $\mu$ s-long MD simulations for each WT KcsA and the mutants (Figure 5A and Figure S5). For WT KcsA, simulations show that the selectivity filter samples two conformations in which V76CO points either towards (inwards conformation) or away (outwards) from the filter pore.<sup>36</sup> The equilibrium between these two, most likely rapidly converting, conformations was recently confirmed by 2D IR data that showed a 60:40 ratio between inwards:outwards conformations. Remarkably, simulations also indicate that E71X mutations perturb this equilibrium, stabilising the V76CO inwards conformation in E71I and E71A, while the outwards state is favoured in E71Q.

To probe if the V76CO CSPs could be explained by a change in the average conformation of the filter, we back-calculated<sup>35</sup> the <sup>13</sup>C ssNMR chemical shifts over the MD simulations (Figure 5B,C). These calculations yielded a much lower V76CO chemical shift in the outwards conformation (predicted  $\Delta V76CO_{\text{inwards-outwards}} = +2$  to  $+3$  ppm) (Figure 5D); a result that agrees with the much lower chemical shift of V76CO at low [K<sup>+</sup>] in the collapsed filter with a flipped V76–G77 plane (experimental  $\Delta V76CO_{\text{conductive filter-collapsed filter}} = +3.3$  ppm).<sup>21,37</sup> Hence, these results show that the V76CO inwards conformation is strongly stabilised in E71A (V76CO CSP =  $+0.94$  ppm relative to WT KcsA) and E71I ( $+0.77$  ppm), while the sampling of the outwards conformation is enhanced in E71Q ( $-0.55$  ppm) (Figure 5E). This conclusion also agrees with our relaxation data, which show reduced dynamics for V76 and G77 in E71A and E71I, whereas both residues show much higher mobility in E71Q. Notably, the stabilisation of the V76CO inwards state correlates with the decrease of C-type inactivation in E71A and E71I.<sup>6</sup>

Similarly, we could derive a structural understanding of the stark Y78Ca CSPs. In MD simulations, WT KcsA exclusively adopts the Y78CO inwards conformation that is stabilised by the E71–Y78 hydrogen bond. However, in E71I, the Y78 backbone is no longer stabilised and we observe sizeable sampling of an outwards conformation (Figure 5A). Here again, back-calculated chemical shifts show a much lower Y78Ca signal in the Y78CO outwards conformation (predicted  $\Delta Y78Ca_{\text{inwards-outwards}} = + 2$  ppm) (Figure 5C,D). These results imply that a Y78CO outwards state is frequently sampled in E71I (Y78Ca CSP =  $-1.94$  ppm relative to WT KcsA) and less frequently or only partially in E71A (Y78Ca CSP =  $-0.84$  ppm). Note that we could not observe a Y78CO outwards state in E71A simulations, presumably due to insufficient sampling.

#### *Destabilisation of the critical interaction D80–W67*

An especially remarkable finding in our study is the drastically increased filter dynamics in E71I compared to E71A despite similar nonpolar E71 substitutions, and this surge in flexibility most likely causes increased sampling of the Y78CO outwards state in E71I. We used MD simulations to gain a molecular understanding of the enhanced E71I filter dynamics. In our simulations, the conformational space of the D80 side chain is an event of particular interest (Figure S6). In WT KcsA, the interaction with E71 locks D80 in a down conformation (Figure 6A), and only this conformation enables the W67–D80 interaction, which is critical for gating in Kv channels.<sup>38,39</sup> The down conformation prevails in E71A, enabling a steady W67–D80 interaction (Figure 6B,D). However, in E71I simulations, the bulky isoleucine sterically destabilises the W67–D80 interaction and causes D80 to increasingly sample middle and up conformations (Figure 6C). We validated the loss of the W67–D80 interaction in E71I with ssNMR  $^{15}\text{N}$   $T_1$  relaxation experiments that are sensitive to the fast pico-to-nanosecond motion of unbound side chains. These experiments clearly show markedly enhanced W67 side chain dynamics in E71I, confirming an unstable W67–D80 interaction in this mutant (Figure 6D,E). To compensate, D80 increasingly engages in interactions with the functionally important residues R64 and Y82<sup>4,31</sup> that are hardly sampled in WT KcsA. The D80 promiscuity is pronounced in MD simulations of E71I and E71Q and agrees with the enhanced ssNMR  $R_{1\rho}$  dynamics at the filter entrance of E71I and E71Q (Figure 3). In E71A, however, a steady D80–W67 interaction stabilises the filter, as demonstrated by strongly reduced  $R_{1\rho}$  dynamics, and this stabilisation is most likely the reason why the Y78CO outwards state is much less frequently sampled in E71A than in E71I. Interestingly, our extensive MD analysis also demonstrates that the E71 point-mutations and the D80 promiscuity cause long-range modulations in the turret (Figure S6), which presumably relate to the turret heterogeneity in the mutants (Figures 2C and 3).

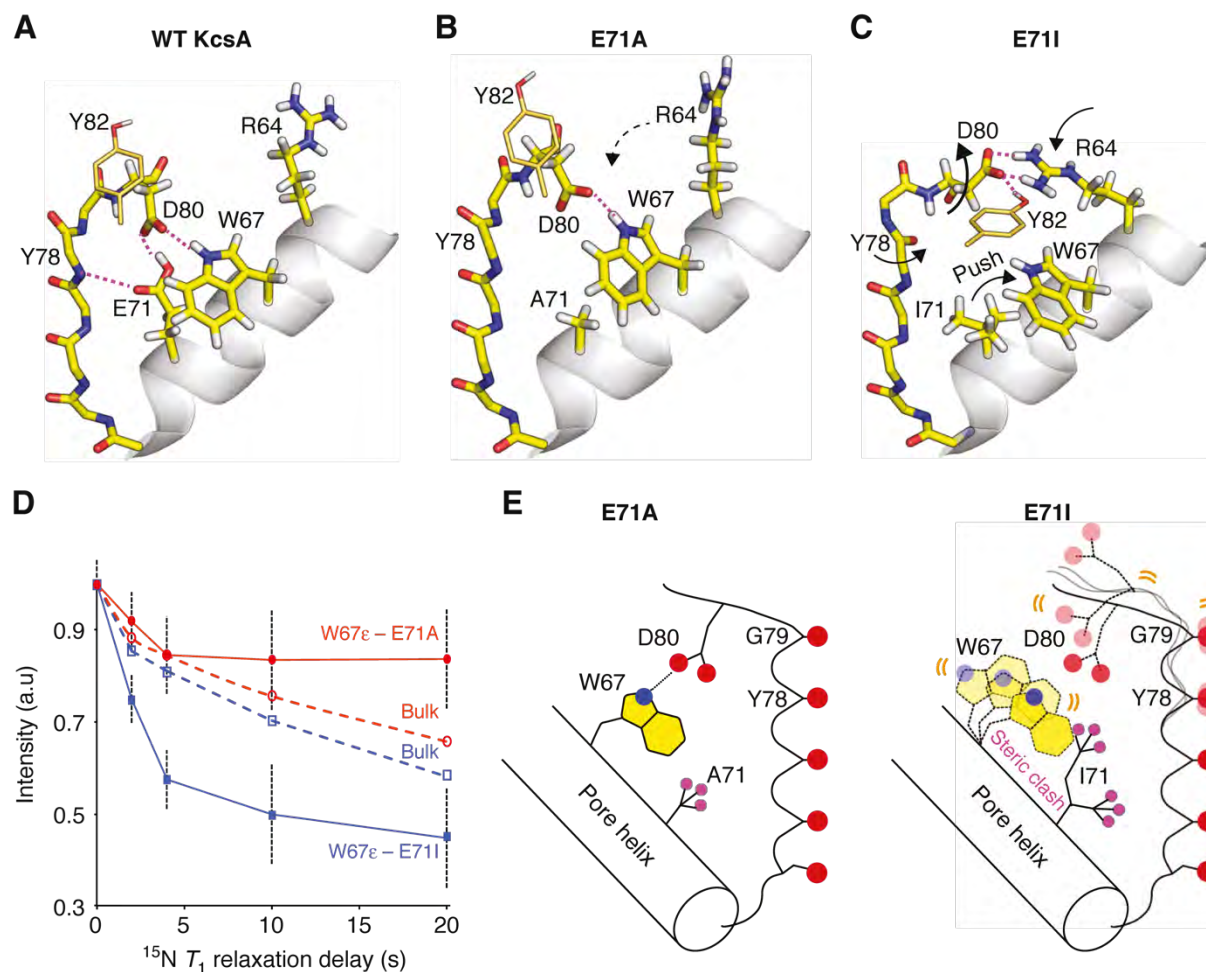


**Figure 6.** The functionally critical W67–D80 interaction is destabilised in E71I KcsA. **A**) WT KcsA MD simulation: the tight interaction with E71 locks the D80 side chain in a down configuration that enables hydrogen bonding with W67 (snapshot after 270 ns). **B**) E71A simulation: the down conformation prevails, enabling the W67–D80 interaction, which stabilises the filter entrance (snapshot after 600 ns). **C**) E71I simulation: I71 impedes the W67–D80 interaction which destabilises the filter entrance. D80 engages in interactions with Y82 (from a neighbouring channel subunit) and R64 (snapshot after 600 ns). **D**) Longitudinal relaxation times ( $^{15}\text{N}$   $T_1$ ) that report on fast motion of the W67 side chain for E71A (red circles) and E71I (blue squares), measured at 950 MHz and 60 kHz MAS. The error shows the signal-to-noise ratio for W67Ne at a given data point. **E**) (left) The W67–D80 interaction is maintained in E71A; (right) I71 hinders the W67–D80 hydrogen bond, which entails increased dynamics at the pore mouth.

## Discussion

Modal gating shifts at constant experimental conditions have been observed in  $K^+$ ,<sup>4,6–10</sup>  $\text{Na}^+$ ,<sup>40</sup>  $\text{Ca}^{2+}$ ,<sup>41,42</sup> and other ion channels,<sup>43,44</sup> and are considered a widespread regulatory mechanism,<sup>11,45</sup> potentially to achieve intermediate activity levels. While known for a long-time, the molecular underpinning of modal gating behaviour is poorly understood. In KcsA, E71 point-mutations emulate modal gating shifts; however, X-ray structures of E71X mutants showed no differences compared to WT KcsA.<sup>6</sup> These seemingly disparate perspectives of

functional heterogeneity and of structural similarity raise critical problems for our understanding of modal gating and also of Kv channel function (Figure 1B). Our ssNMR study in native-like conditions paints a strikingly different picture, demonstrating that E71 substitutions lock the selectivity filter in characteristic conformational and motional landscapes that markedly diverge from WT KcsA. These landscapes strongly depend on the nature of residue 71 and directly relate to the heterogeneous functional behaviour observed in K<sup>+</sup> channels.<sup>6</sup>

By integrating ssNMR and MD simulations, we show that E71 point-mutations rearrange the network behind the filter and perturb the K<sup>+</sup> binding sites V76 and Y78 (Figure 1A,E). Thereby, we show that E71X mutations change the equilibrium between intrinsically sampled filter states (Figure 5E), which agrees with 2D IR data<sup>36</sup> and the so-called ‘flipped’ E71A structure that points towards a complex selectivity filter landscape that includes dynamical flips of K<sup>+</sup> coordinating peptide planes.<sup>36</sup> Our data demonstrate a stabilisation of the V76CO inwards state in E71A and E71I relative to WT KcsA, which correlates with a sharply reduced entry into the C-type inactivated state. Furthermore, our data clearly show Y78 conformational perturbations in E71I and E71A. Such perturbations could not be observed in WT KcsA X-ray structures;<sup>3</sup> however, there is strong evidence from previous ssNMR studies that Y78 modulations can accompany filter gating. Indeed, ssNMR data show that Y78Ca exhibits a drastically lower signal in the open-collapsed state (experimental  $\Delta Y78Ca_{\text{conductive filter-collapsed filter}} = +4.3$  ppm),<sup>37</sup> which unambiguously argues that the Y78 conformation can change in reference to the filter mode. This notion is also corroborated by the ‘flipped’ E71A X-ray structure (2ATK), which also features a Y78CO partial outward state,<sup>4,46</sup> and it is in line with a recent cryo-EM structure of the hERG channel.<sup>47</sup> While the exact role in KcsA is unclear, we surmise that Y78 backbone modulations may relate to a non-conductive state that is favoured by E71I, which agree with the strongly reduced K<sup>+</sup> occupancy at S0–S2 in E71I.<sup>6</sup>

Importantly, the marked conformational changes in the E71I selectivity filter, and especially the destabilisation of the W67–D80 interaction (Figure 6D,E), suggest to be of broad relevance for Kv channels (Figure 1B) where the W67–D80 interaction plays a defining role in the inactivation process. Mutational studies showed that the inability to establish this highly conserved interaction entails severe functional perturbations for KcsA, Shaker, and Kv1.2.<sup>38,39</sup> Moreover, in line with the effect of the weakening of the W67–D80 interaction in E71I, the destabilisation of the analogous interaction W434–E447 in Shaker modulates the equilibrium between conducting and non-conducting filter states.<sup>48</sup>

On the basis of our set of results, we show that modal gating shifts in K<sup>+</sup> channels relate to changes in the statistical weighting of pre-existing selectivity filter states which are triggered by fluctuations in the hydrogen bonding (Figure 6) and water network (Figure 4).

Notably, we show that modulations in this network cause changes in the turret over more than 2 nm (Figures 2C and 3), which opens a pathway how turret-binding drugs, lipids, or other proteins can allosterically modulate the filter.<sup>21,25,49–51</sup> The question arises why most of these conformational subtypes could not be crystallised. Here, the reason is most likely the interaction with Fab fragments that act as crystallographic chaperons and attach to KcsA X-ray structures. In agreement with electrophysiological measurements,<sup>4</sup> these artificial Fab interactions lock the selectivity filter in a specific conformation, and thereby hinder the capturing of transient configurations, masking the effect of E71 point-mutations. Interestingly, the lack of non-canonical filter conformations in X-ray structures was mirrored by additional torsional or position restraints in MD simulations to stabilise a conductive filter conformation.<sup>52,53</sup> At least for KcsA, such potentials could mask the physiological filter plasticity, as demonstrated in this study and previously with 2D IR.<sup>36</sup>

## Conclusion

In conclusion, our work establishes the shifts in the conformational dynamics of the selectivity filter as the key physiological determinant of modal gating behaviour. At the same time, our work provides a long-needed quantitative description of the selectivity filter dynamics in a native environment, which is of fundamental importance to understand ion channel function.<sup>54</sup> Given that the here-described filter dynamics are strongly different in mutant E71I, our study may ultimately help to better understand eukaryotic Kv channels. Finally, we like to emphasise that further experiments with open channels under inactivating conditions will be critically required to fully comprehend how E71X mutations modulate channel open probability and C-type inactivation.

## Materials and Methods

### *Sample preparation*

WT KcsA and E71X mutant channels were expressed in *E. coli* M15 cells (Qiagen) using standard H<sub>2</sub>O-based M9 medium supplemented with 0.5 g/L <sup>15</sup>NH<sub>4</sub>Cl and 2 g/L D-glucose-<sup>13</sup>C6-d7 in order to improve the spectral resolution in <sup>1</sup>H-detected ssNMR experiments.<sup>17</sup> Cells were subsequently harvested, treated with lysozyme, and lysed via French press. The membranes containing the KcsA channels were collected by centrifugation (100,000×g) and proteins were extracted with 40 mM DM (Anatrace).<sup>26</sup> KcsA channels were purified using Ni-NTA agarose beads (Qiagen), resulting in a final yield of 10 mg/L for WT KcsA and 5 mg/L for the E71X KcsA mutants. Liposome reconstitution was performed using *E. coli* polar lipids (Avanti) at 1:100 protein:lipid molar ratio, in which the detergent was removed using polystyrene beads (Bio-Beads SM-2).<sup>26</sup> Before the ssNMR measurements, reconstituted samples were suspended in fully protonated phosphate buffer (pH 7.4, 100 mM K<sup>+</sup>). For

spectral assignments, a fully protonated buffer was used in order to observe the entire channel in  $^1\text{H}$ -detected ssNMR experiments. For proton/deuterium (H/D) exchange ssNMR spectroscopy, ion channels were incubated in fully deuterated buffers (pH 7.4, 100 mM  $\text{K}^+$ ) for a total of 2 days prior to the measurements.

### *Solid-state NMR experiments*

3D ssNMR experiments for sequential backbone chemical shift assignments were performed at 800 MHz ( $^1\text{H}$ -frequency) using 60 kHz magic angle spinning (MAS) frequency and a real temperature of approximately 305 K. In total, we ran ten dipolar-based 3D ssNMR experiments to assign the three mutant channels and WT KcsA. The pulse sequences and experimental setups were performed as previously described.<sup>17</sup> 2D  $^{13}\text{C}$ - $^{13}\text{C}$  PARISxy<sup>55</sup> ( $N = 1/2$ ,  $m = 1$ ) experiments for side chain chemical shift assignments were performed at 700 MHz using 42 kHz MAS and a  $^{13}\text{C}$ - $^{13}\text{C}$  mixing time of 110 ms.  $^{15}\text{N}$   $T_{\text{rho}}$  relaxation experiments were performed as described for the water-inaccessible part of KcsA and measured at 700 MHz and 58 kHz MAS using a  $^{15}\text{N}$  spin lock amplitude of 17.5 kHz.<sup>17</sup> We used  $^1\text{H}$ -detected 2D experiments together with relaxation increments of 0, 5, 10, 20, 40, and 80 ms. For the much faster relaxing flicker E71Q channel, we used increments of 0, 5, 10, 20, 40, and 60 ms.  $^{15}\text{N}$   $T_1$  measurements were performed at 950 MHz and 60 kHz MAS using relaxation elements of 0, 2, 4, 10, and 20 s. The W67 side chain is spectrally isolated in E71A and E71I (Figure S2) and could be readily analysed in a series of 1D experiments. For the analysis of H/D exchange data from 2D NH spectra acquired in protonated and deuterated buffers, we used the signal intensities, which were normalised to the water-inaccessible residues S69 and V70 that are not subjected to H/D exchange. PISSARRO<sup>56</sup> decoupling was used as decoupling method in all direct and indirect dimensions. Chemical shifts were back-calculated from MD simulations with the SPARTA<sup>+</sup> program.<sup>35</sup> Channels structures were extracted from MD simulations with a time-increment of 10 ns, yielding a total of 400 monomer structures. Compared to our experimental data, the SPARTA<sup>+</sup> predictions give systematically lower chemical shifts for the V76 backbone carbonyl carbon, which we aligned by adding 2.5 ppm to the predicted carbonyl chemical shifts for all channels.

### *Molecular Dynamics Simulations*

Atomic models of KcsA were constructed based on crystal structures (1K4C<sup>3</sup> and 3OR6<sup>6</sup>) that represent a structural state with closed inner gate. Considering the high similarity between crystal structures of WT (1K4C), E71A (1ZWI), and E71I (3OR7), the simulation systems for E71A and E71I are built based on the fully equilibrated WT system by introducing respective single mutation. With more substantial difference compared with WT, the crystal

structure for E71Q (3OR6) was used to build its simulation system. For all MD simulations, the channel was embedded in a bilayer of 3:1 POPC:POPG lipids and solvated in 150 mM or 200 mM KCl using the web service CHARMM-GUI.<sup>57,58</sup> Most residues were assigned their standard protonation state at pH 7. The total number of atoms in the MD systems is on the order of  $\sim 49,000$ . The CHARMM force field PARAM36 for protein,<sup>59</sup> lipids,<sup>60</sup> and ions<sup>61</sup> was used. Explicit water was described with the TIP3P model. In WT, the residue Glu71 is protonated to form a key hydrogen bond with Asp80.<sup>32,62</sup> The models of KcsA were refined using energy minimization for at least 2000 steps, and the ions and non-filter backbone atoms were kept fixed throughout the minimization procedure. After energy minimisation, the conductive filter was restrained for 10–20 ns to relax any unfavourable contacts destabilising the filter. All the simulations were performed under constant NPT conditions at 310 K and 1 atmosphere, and periodic boundary conditions with electrostatic interactions were treated by the particle-mesh Ewald (PME) method and a real-space cutoff of 12 Å. The simulations use a time step of 2 fs. After minimization and equilibration with harmonic positional restraints on all of the C atoms, MD simulations were performed for 1  $\mu$ s for wild type and all mutants, by using either NAMD version 2.11,<sup>63</sup> or on the special purpose computer Anton (Pittsburgh Supercomputer Center).<sup>64</sup>

## Supporting Information

### Sequential ssNMR assignments with $^1\text{H}$ -detected 3D experiments

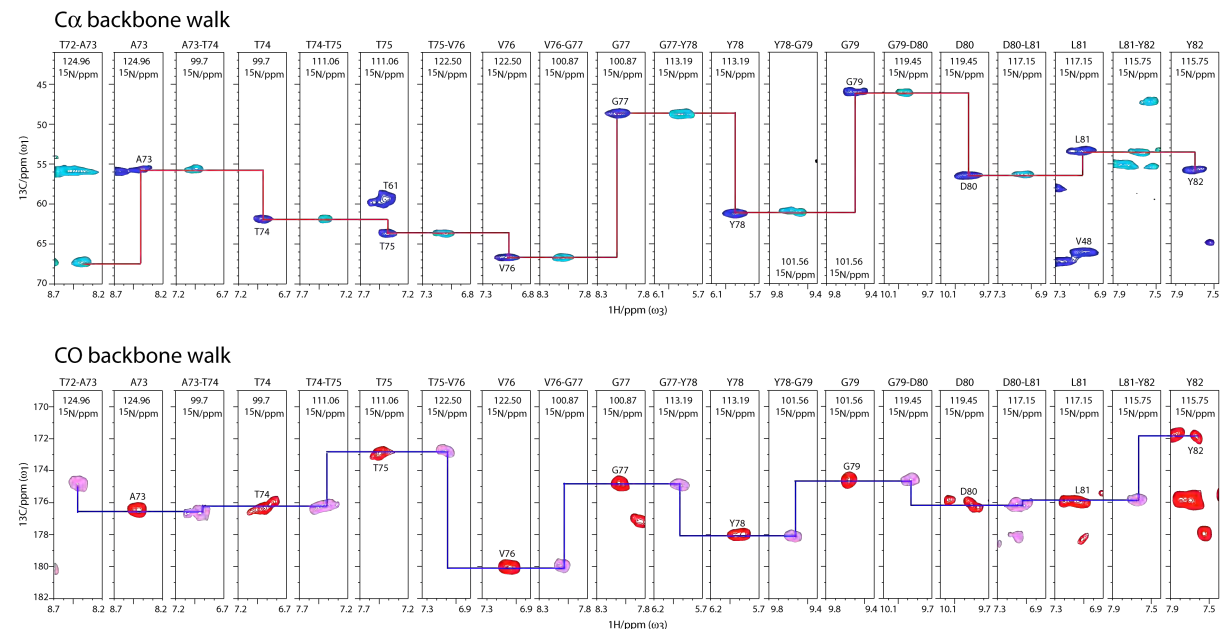


**Figure S1.** Upper panel:  $\text{Ca-Ca}^{+1}$  backbone walk showing full connectivity for residues T72 – Y82 in KcsA mutant E71A. Dark Blue signals show CAH planes from a 3D CANH experiment, cyan CAH planes were taken from a 3D CACO NH experiment. Lower panel:  $\text{CO-CO}^{+1}$  backbone walk showing full connectivity for residues T72 – Y82 in E71A. Magenta signals show COH planes from a 3D CONH experiment, red COH planes were taken from a 3D COCANH experiment.

## Comparison of 2D NH and 2D CC ssNMR spectra of WT KcsA and the E71X mutants

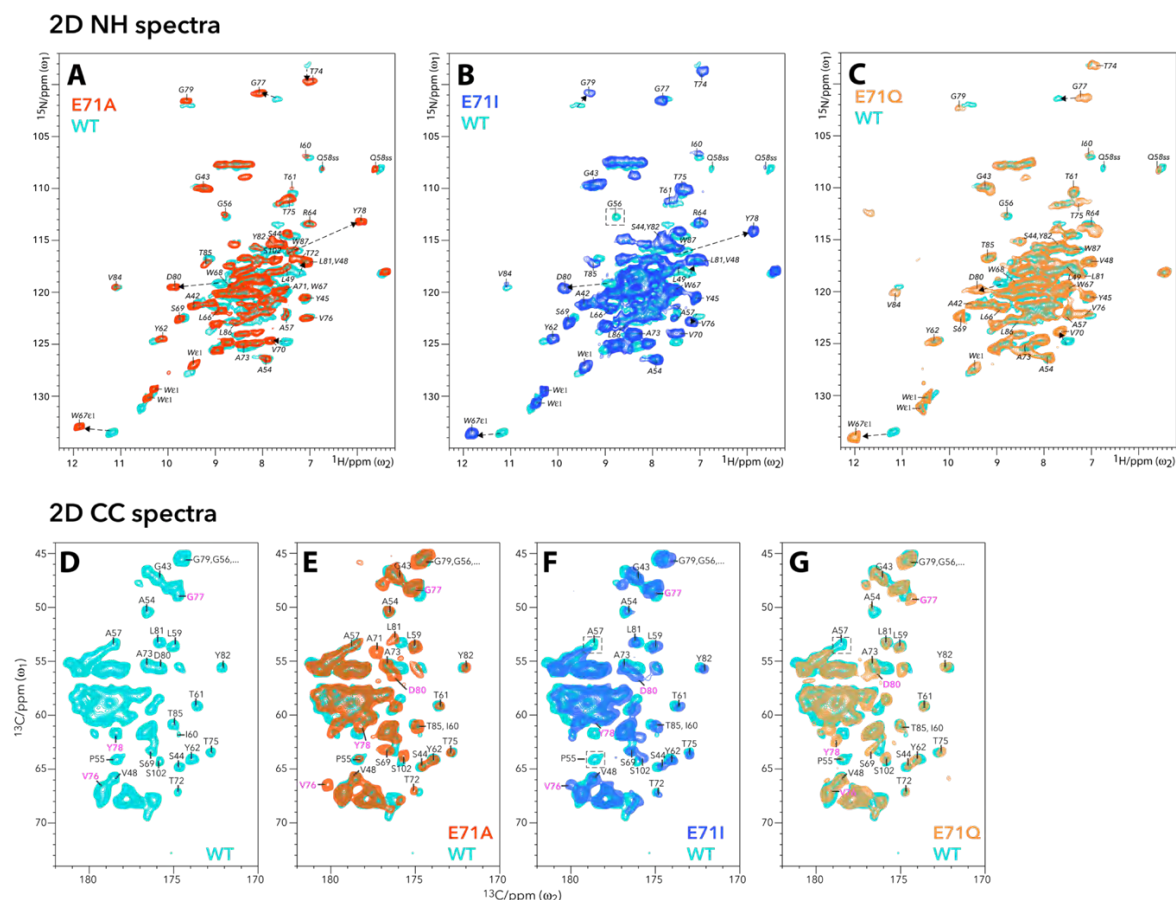


**Figure S2.** Upper row: Overlay of 2D NH spectra of WT KcsA (cyan) onto A) E71A (red), B) E71I (blue), and C) E71Q (orange). Lower row: Zoom into the carbonyl-region of 2D PARISxy<sup>55</sup> CC experiments. D) WT KcsA (cyan), E) E71A (red) and WT KcsA, F) E71I (blue) and WT KcsA, G) E71Q (orange) and WT KcsA. Signals of V76-Y78 and D80 that show larger chemical shift perturbations are highlighted in magenta. Signals of P55-A57 that disappear or split in E71I due to conformational heterogeneity are highlighted in dashed boxes.

## Ca and CO ssNMR chemical shift perturbations of the E71X KcsA mutants

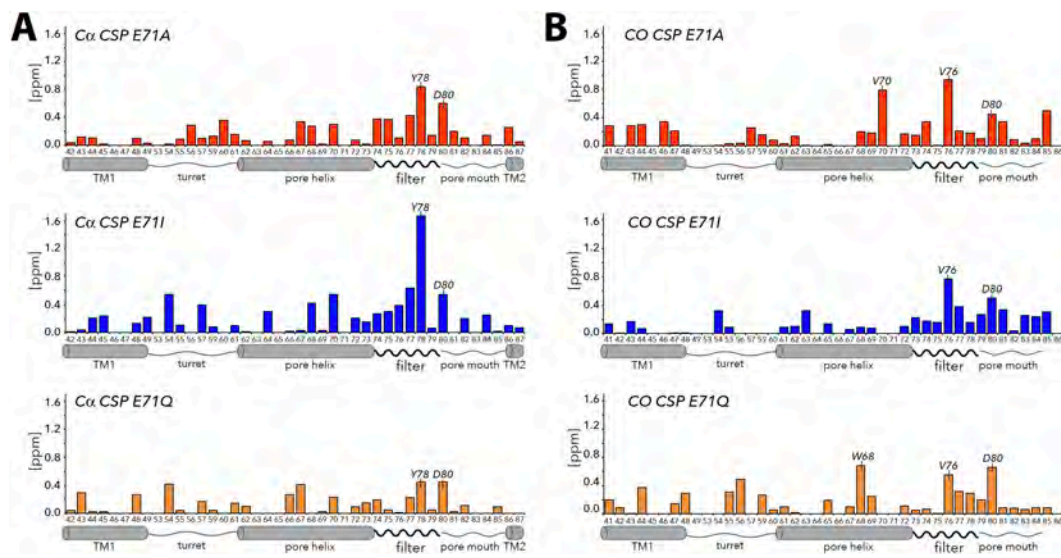


**Figure S3.** A) Ca CSPs for E71A (in red), E71I (blue), and E71Q (orange). B) Respective CO CSPs.

## Water distribution derived from long MD simulations / Structural changes in the water-lid

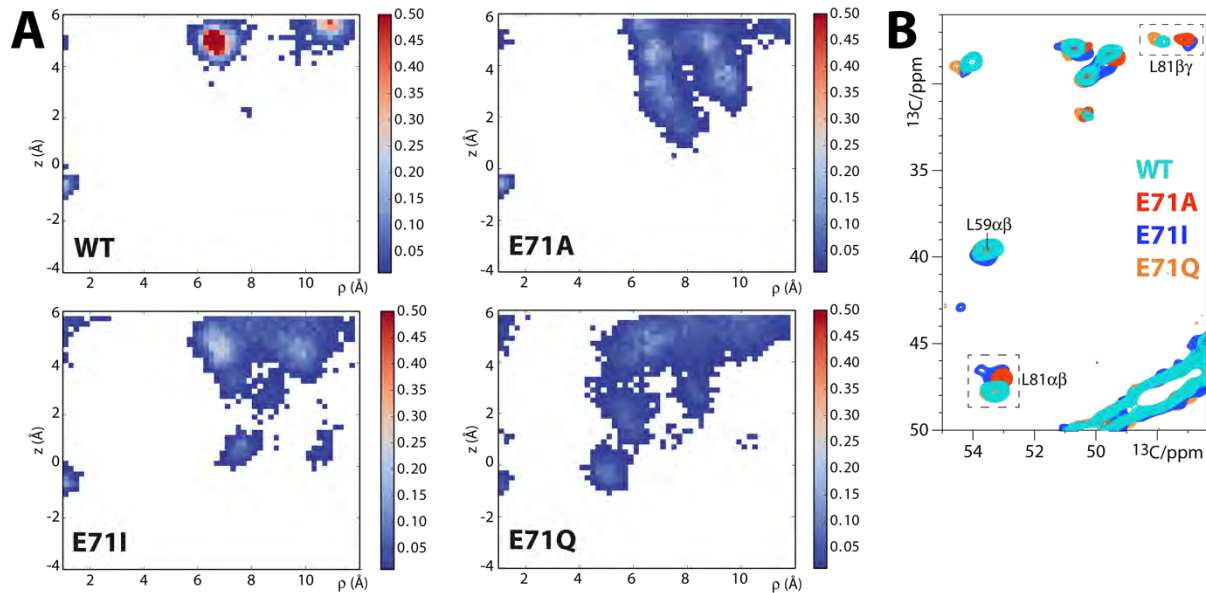


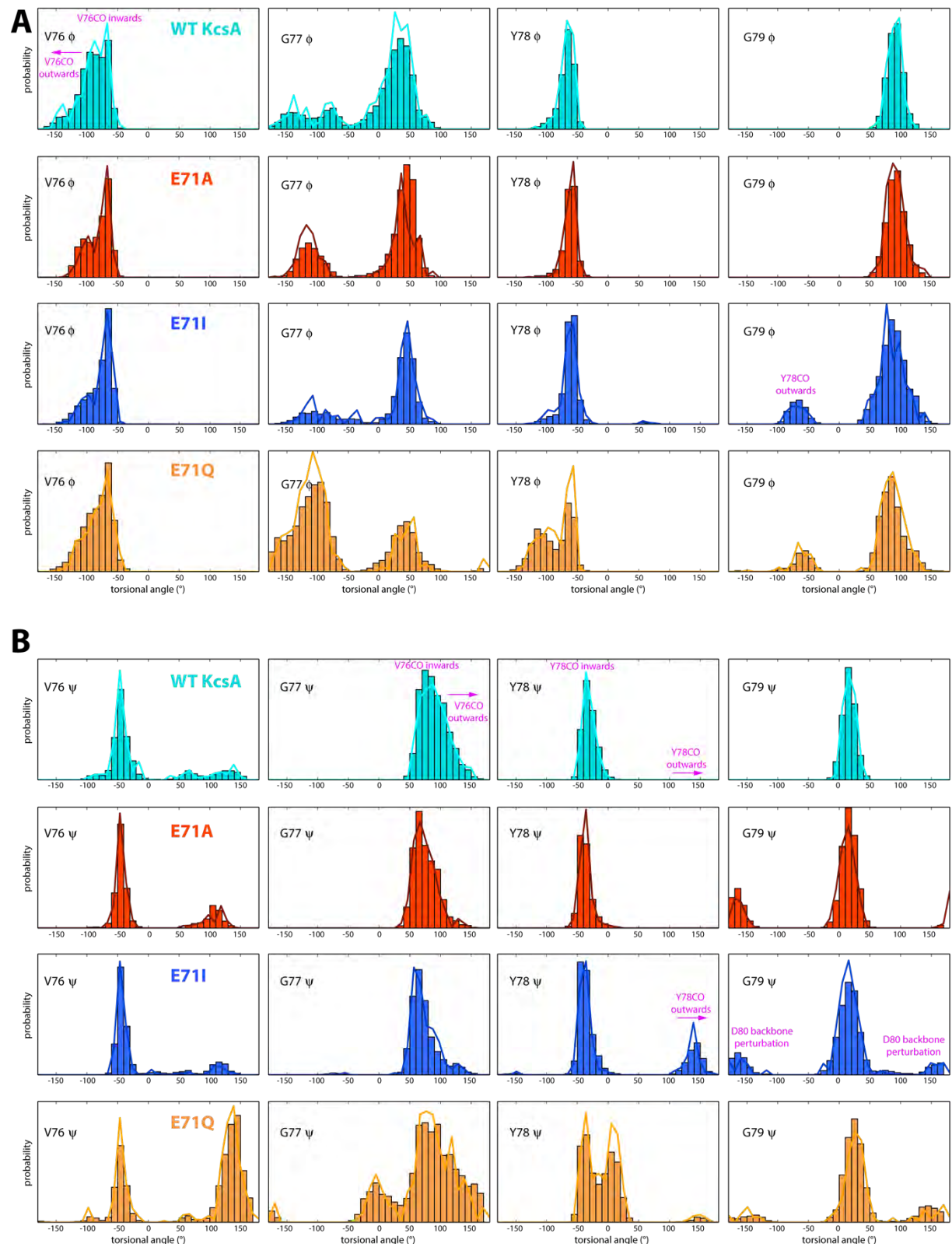
**Figure S4.** A) 2D average occupancy map for all four subunits during 1000ns MD simulations. The x-axis describes the radius to the center of the selectivity filter, and the y-axis is the z-coordinate of water molecules. In agreement with our ssNMR data, MD simulations show a widening of the water cavity for mutant channels E71I and especially E71A. In these channels, the cavity water also exhibits a higher mobility, as described by higher exchange-rates with bulk water (see Table S1). For E71Q, the simulations could not reproduce the smaller water cavity that we unambiguously detect in solid-state NMR experiments. Potential reasons for the mismatch between ssNMR and MD simulations for E71Q could be a suboptimal MD starting structure (which was derived from WT KcsA) and insufficient sampling. B) The increased exchange with bulk water in mutants E71A and E71I most likely relates to structural and dynamical changes of residues D80 – Y82, which act as lid of the water cavity.<sup>31</sup> Indeed, we observe marked structural changes in the L81 side-chain conformation in 2D CC ssNMR spectra of mutants E71A and E71I.

**Table S1.** MD derived water exchange rates with bulk water

	WT	E71I	E71A	E71Q
# of water molecules	$0.81 \pm 0.12$	$1.47 \pm 0.21$	$2.30 \pm 0.16$	$1.58 \pm 0.16$
Turnover time (ns)	$51.9 \pm 40.9$	$7.51 \pm 4.82$	$18.5 \pm 8.9$	$6.7 \pm 1.9$

The water-binding cavity within each subunit is defined as the space with a distance less than 7 Å from both the nitrogen (or substituted ester oxygen) atom from Gly77 and the C-alpha from E71 in the same monomer. The number of water molecules within each subunit was determined as the average water number within this pocket during specific trajectory. The mean turnover time of water molecules within each subunit is defined as  $T_{MD} \langle N \rangle = n_d$ , where  $T_{MD}$  is the length of the trajectory,  $\langle N \rangle$  is the average number of water molecules in one cavity, and  $n_d$  is the number of distinct water molecules that visited the cavity at least once during the simulation. Each of the four subunits was treated as an individual sample to estimate the average and SD. This kind of analysis was also used in previous studies.<sup>32</sup>

Simulated dihedral angle profiles of WT KcsA and the E71X mutant channels



## Distance measurement between side chains derived from MD simulations

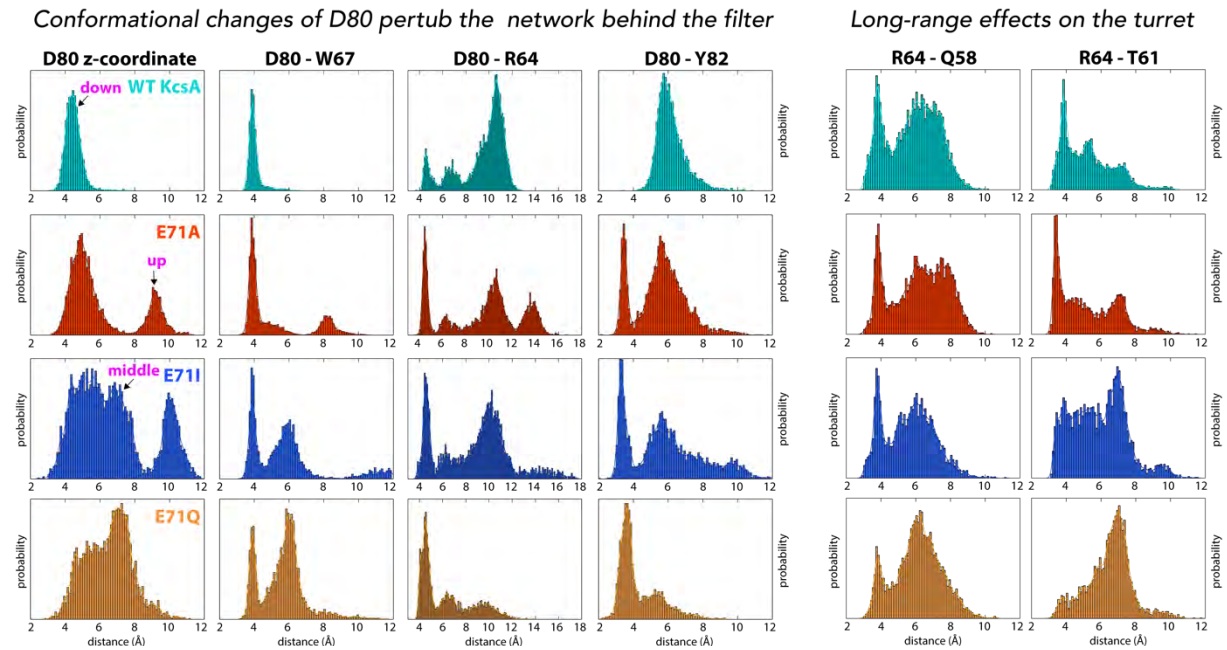


**Figure S6.** Distance measurement between side chains derived from 1  $\mu$ s-long MD simulations of WT KcsA (cyan), E71A (red), E71I (blue), and E71Q (orange). The D80 side chain conformation is shown as the distribution of its z-coordinate (the centre of mass of carboxyl group). For distance measurement, the atom selections are D80 (C $\gamma$ ), Y82 (OH), W67 (N $\epsilon$ 1), T61 (O $\gamma$ 1), Q58 (backbone carbonyl oxygen), and R64 (C $\zeta$ ). Q58, T61, R64, W67, and D80 are from the same subunit, while Y82 is from an adjacent subunit.

## Data availability

The solid-state NMR assignments were deposited in the BMRB, with the accession numbers 27676 for WT KcsA, 27678 for E71A KcsA, 27679 for E71I KcsA, and 27680 for E71Q KcsA. The source data underlying Figures 1, 3, 5, 6 and S3 can be accessed online the respective publication (Ref. <sup>65</sup>) or in the digital version of this thesis.

## References

- (1) Yellen, G. The Voltage-Gated Potassium Channels and Their Relatives. *Nature* **2002**, *419* (6902), 35–42.
- (2) Doyle, D. A.; Cabral, J. M.; Pfuetzner, R. A.; Kuo, A.; Gulbis, J. M.; Cohen, S. L.; Chait, B. T.; MacKinnon, R. The Structure of the Potassium Channel: Molecular Basis of K<sup>+</sup> Conduction and Selectivity. *Science* (80-.). **1998**, *280* (5360), 69–77.
- (3) Zhou, Y.; Morais-Cabral, J. H.; Kaufman, A.; MacKinnon, R. Chemistry of Ion Coordination and Hydration Revealed by a K<sup>+</sup> Channel–Fab Complex at 2.0 Å Resolution. *Nature* **2001**, *414* (6859), 43–48.
- (4) Cordero-Morales, J. F.; Cuello, L. G.; Zhao, Y.; Jogini, V.; Cortes, D. M.; Roux, B.; Perozo, E. Molecular Determinants of Gating at the Potassium-Channel Selectivity Filter. *Nat. Struct. Mol. Biol.* **2006**, *13* (4), 311–318.
- (5) Cordero-Morales, J. F.; Jogini, V.; Lewis, A.; Vásquez, V.; Cortes, D. M.; Roux, B.; Perozo, E. Molecular Driving Forces Determining Potassium Channel Slow Inactivation. *Nat. Struct. Mol. Biol.* **2007**, *14* (11), 1062–1069.
- (6) Chakrapani, S.; Cordero-Morales, J. F.; Jogini, V.; Pan, A. C.; Cortes, D. M.; Roux, B.; Perozo, E. On the

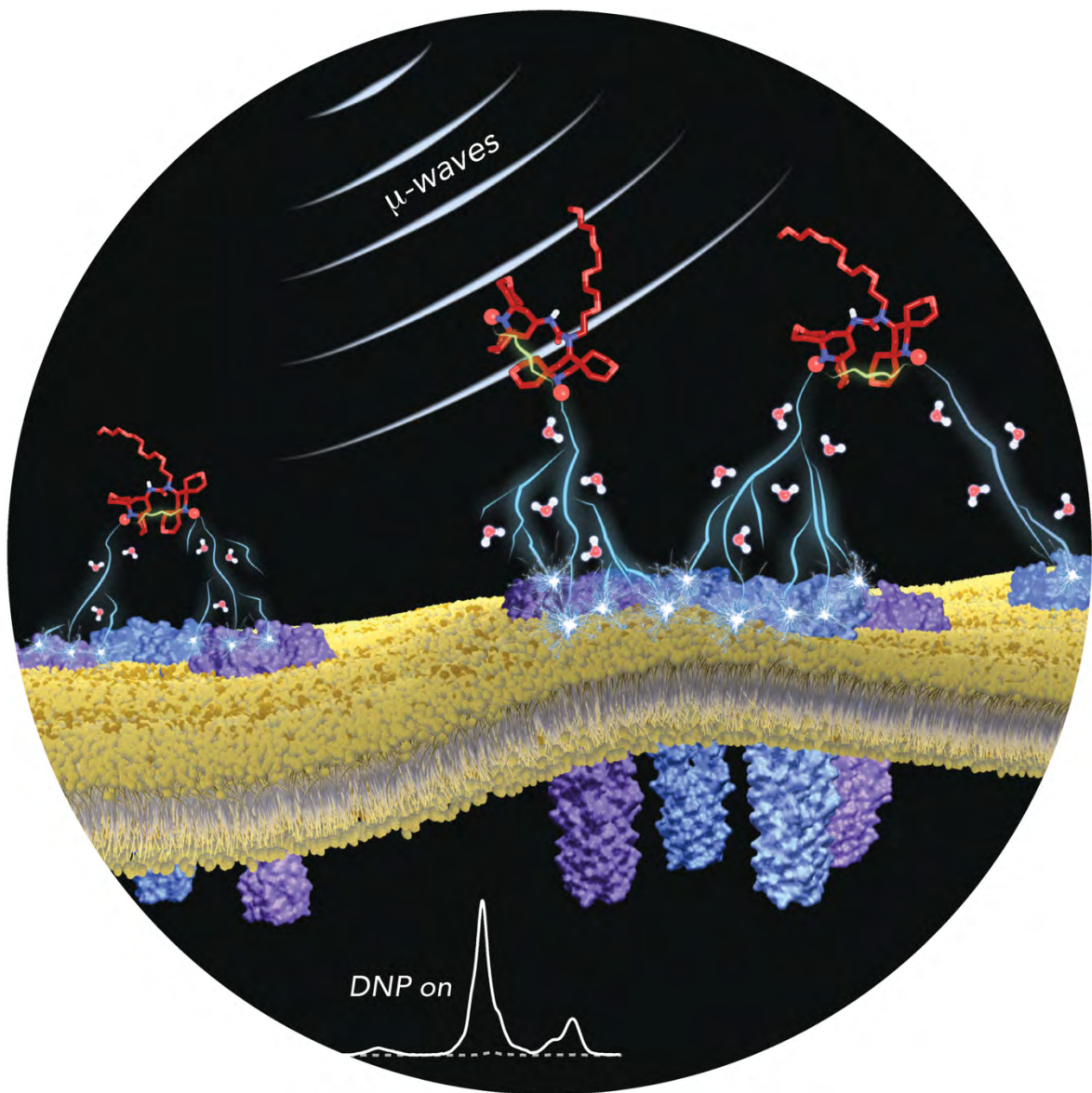
- Structural Basis of Modal Gating Behavior in K<sup>+</sup> Channels. *Nat. Struct. Mol. Biol.* **2011**, *18* (1), 67–74.
- (7) Zagotta, W. N.; Hoshi, T.; Aldrich, R. W. Shaker Potassium Channel Gating III: Evaluation of Kinetic Models for Activation. *J. Gen. Physiol.* **1994**, *103* (2), 321–362.
- (8) Zheng, J.; Sigworth, F. J. Selectivity Changes during Activation of Mutant Shaker Potassium Channels. *J. Gen. Physiol.* **1997**, *110* (2), 101–117.
- (9) Schoppa, N. E.; Sigworth, F. J. Activation of Shaker Potassium Channels: I. Characterization of Voltage-Dependent Transitions. *J. Gen. Physiol.* **1998**, *111* (2), 271–294.
- (10) Chakrapani, S.; Cordero-Morales, J. F.; Perozo, E. A Quantitative Description of KcsA Gating II: Single-Channel Currents. *J. Gen. Physiol.* **2007**, *130* (5), 479–496.
- (11) Bicknell, B. A.; Goodhill, G. J. Emergence of Ion Channel Modal Gating from Independent Subunit Kinetics. *Proc. Natl. Acad. Sci. U. S. A.* **2016**, *113* (36), E5288–E5297.
- (12) Cuello, L. G.; Cortes, D. M.; Perozo, E. The Gating Cycle of a K<sup>+</sup> Channel at Atomic Resolution. *Elife* **2017**, *6*.
- (13) Heer, F. T.; Posson, D. J.; Wojtas-Niziuski, W.; Nimigean, C. M.; Bernèche, S. Mechanism of Activation at the Selectivity Filter of the KcsA K<sup>+</sup> Channel. *Elife* **2017**, *6*.
- (14) Cheng, W. W. L.; McCoy, J. G.; Thompson, A. N.; Nichols, C. G.; Nimigean, C. M. Mechanism for Selectivity-Inactivation Coupling in KcsA Potassium Channels. *Proc. Natl. Acad. Sci.* **2011**, *108* (13), 5272–5277.
- (15) Chevelkov, V.; Rehbein, K.; Diehl, A.; Reif, B. Ultrahigh Resolution in Proton Solid-State NMR Spectroscopy at High Levels of Deuteration. *Angew. Chemie Int. Ed.* **2006**, *45* (23), 3878–3881.
- (16) Agarwal, V.; Penzel, S.; Szekely, K.; Cadalbert, R.; Testori, E.; Oss, A.; Past, J.; Samoson, A.; Ernst, M.; Böckmann, A.; et al. DeNovo 3D Structure Determination from Sub-Milligram Protein Samples by Solid-State 100kHz MAS NMR Spectroscopy. *Angew. Chemie - Int. Ed.* **2014**, *53* (45), 12253–12256.
- (17) Medeiros-Silva, J.; Mance, D.; Daniëls, M.; Jekhmane, S.; Houben, K.; Baldus, M.; Weingarth, M. 1 H-Detected Solid-State NMR Studies of Water-Inaccessible Proteins In Vitro and In Situ. *Angew. Chemie Int. Ed.* **2016**, *55* (43), 13606–13610.
- (18) Andreas, L. B.; Jaudzems, K.; Stanek, J.; Lalli, D.; Bertarello, A.; Le Marchand, T.; Cala-De Paepe, D.; Kotelovica, S.; Akopjana, I.; Knott, B.; et al. Structure of Fully Protonated Proteins by Proton-Detected Magic-Angle Spinning NMR. *Proc. Natl. Acad. Sci. U. S. A.* **2016**, *113* (33), 9187–9192.
- (19) Retel, J. S.; Nieuwkoop, A. J.; Hiller, M.; Higman, V. A.; Barbet-Massin, E.; Stanek, J.; Andreas, L. B.; Franks, W. T.; Van Rossum, B.-J.; Vinothkumar, K. R.; et al. Structure of Outer Membrane Protein G in Lipid Bilayers. *Nat. Commun.* **2017**, *8* (1).
- (20) Medeiros-Silva, J.; Jekhmane, S.; Paioni, A. L.; Gawarecka, K.; Baldus, M.; Swiezewska, E.; Breukink, E.; Weingarth, M. High-Resolution NMR Studies of Antibiotics in Cellular Membranes. *Nat. Commun.* **2018**, *9* (1), 3963.
- (21) Ader, C.; Schneider, R.; Hornig, S.; Velisetty, P.; Wilson, E. M.; Lange, A.; Giller, K.; Ohmert, I.; Martin-Eauclaire, M.-F.; Trauner, D.; et al. A Structural Link between Inactivation and Block of a K<sup>+</sup> Channel. *Nat. Struct. Mol. Biol.* **2008**, *15* (6), 605–612.
- (22) Weingarth, M.; van der Cruijnsen, E. A. W.; Ostmeier, J.; Lievestro, S.; Roux, B.; Baldus, M. Quantitative Analysis of the Water Occupancy around the Selectivity Filter of a K<sup>+</sup> Channel in Different Gating Modes. *J. Am. Chem. Soc.* **2014**, *136* (5), 2000–2007.
- (23) Pan, A. C.; Cuello, L. G.; Perozo, E.; Roux, B. Thermodynamic Coupling between Activation and Inactivation Gating in Potassium Channels Revealed by Free Energy Molecular Dynamics Simulations. *J. Gen. Physiol.* **2011**, *138* (6), 571–580.
- (24) Cuello, L. G.; Jogini, V.; Cortes, D. M.; Pan, A. C.; Gagnon, D. G.; Dalmas, O.; Cordero-Morales, J. F.; Chakrapani, S.; Roux, B.; Perozo, E. Structural Basis for the Coupling between Activation and Inactivation Gates in K<sup>+</sup> Channels. *Nature* **2010**, *466* (7303), 272–275.
- (25) Lange, A.; Giller, K.; Hornig, S.; Martin-Eauclaire, M.-F.; Pongs, O.; Becker, S.; Baldus, M. Toxin-Induced Conformational Changes in a Potassium Channel Revealed by Solid-State NMR. *Nature* **2006**, *440* (7086), 959–962.
- (26) van der Cruijnsen, E. A. W.; Nand, D.; Weingarth, M.; Prokofyev, A.; Hornig, S.; Cukkemane, A. A.; Bonvin, A. M. J. J.; Becker, S.; Hulse, R. E.; Perozo, E.; et al. Importance of Lipid-Pore Loop Interface for Potassium Channel Structure and Function. *Proc. Natl. Acad. Sci.* **2013**, *110* (32), 13008–13013.
- (27) Baker, K. A.; Tzitzilonis, C.; Kwiatkowski, W.; Choe, S.; Riek, R. Conformational Dynamics of the KcsA Potassium Channel Governs Gating Properties. *Nat. Struct. Mol. Biol.* **2007**, *14* (11), 1089–1095.

- (28) Good, D. B.; Wang, S.; Ward, M. E.; Struppe, J.; Brown, L. S.; Lewandowski, J. R.; Ladizhansky, V. Conformational Dynamics of a Seven Transmembrane Helical Protein Anabaena Sensory Rhodopsin Probed by Solid-State NMR. *J. Am. Chem. Soc.* **2014**, *136* (7), 2833–2842.
- (29) Lewandowski, J. R.; Sass, H. J.; Grzesiek, S.; Blackledge, M.; Emsley, L. Site-Specific Measurement of Slow Motions in Proteins. *J. Am. Chem. Soc.* **2011**, *133* (42), 16762–16765.
- (30) Lewandowski, J. R. Advances in Solid-State Relaxation Methodology for Probing Site-Specific Protein Dynamics. *Acc. Chem. Res.* **2013**, *46* (9), 2018–2027.
- (31) Ostmeyer, J.; Chakrapani, S.; Pan, A. C.; Perozo, E.; Roux, B. Recovery from Slow Inactivation in K<sup>+</sup> Channels Is Controlled by Water Molecules. *Nature* **2013**, *501* (7465), 121–124.
- (32) Li, J.; Ostmeyer, J.; Boulanger, E.; Rui, H.; Perozo, E.; Roux, B. Chemical Substitutions in the Selectivity Filter of Potassium Channels Do Not Rule out Constricted-like Conformations for C-Type Inactivation. *Proc. Natl. Acad. Sci. U. S. A.* **2017**, *114* (42), 11145–11150.
- (33) Shi, L.; Kawamura, I.; Jung, K.-H.; Brown, L. S.; Ladizhansky, V. Conformation of a Seven-Helical Transmembrane Photosensor in the Lipid Environment. *Angew. Chemie Int. Ed.* **2011**, *50* (6), 1302–1305.
- (34) Medeiros-Silva, J.; Jekhmane, S.; Baldus, M.; Weingarh, M. Hydrogen Bond Strength in Membrane Proteins Probed by Time-Resolved <sup>1</sup>H-Detected Solid-State NMR and MD Simulations. **2017**.
- (35) Shen, Y.; Bax, A. SPARTA+: A Modest Improvement in Empirical NMR Chemical Shift Prediction by Means of an Artificial Neural Network. *J. Biomol. NMR* **2010**, *48* (1), 13–22.
- (36) Kratochvil, H. T.; Carr, J. K.; Matulef, K.; Annen, A. W.; Li, H.; Maj, M.; Ostmeyer, J.; Serrano, A. L.; Raghuraman, H.; Moran, S. D.; et al. Instantaneous Ion Configurations in the K<sup>+</sup> ion Channel Selectivity Filter Revealed by 2D IR Spectroscopy. *Science (80-. )*. **2016**, *353* (6303), 1040–1044.
- (37) Wylie, B. J.; Bhate, M. P.; McDermott, A. E. Transmembrane Allosteric Coupling of the Gates in a Potassium Channel. *Proc. Natl. Acad. Sci.* **2014**, *111* (1), 185–190.
- (38) Perozo, E.; MacKinnon, R.; Bezanilla, F.; Stefani, E. Gating Currents from a Nonconducting Mutant Reveal Open-Closed Conformations in Shaker K<sup>+</sup> Channels. *Neuron* **1993**, *11* (2), 353–358.
- (39) Cordero-Morales, J. F.; Jogini, V.; Chakrapani, S.; Perozo, E. A Multipoint Hydrogen-Bond Network Underlying KcsA C-Type Inactivation. *Biophys. J.* **2011**, *100* (10), 2387–2393.
- (40) Howe, J. R.; Ritchie, J. M. Multiple Kinetic Components of Sodium Channel Inactivation in Rabbit Schwann Cells. *J. Physiol.* **1992**, *455* (1), 529–566.
- (41) Delcour, A. H.; Tsien, R. W. Altered Prevalence of Gating Modes in Neurotransmitter Inhibition of N-Type Calcium Channels. *Science (80-. )*. **1993**, *259* (5097), 980–984.
- (42) Ionescu, L.; White, C.; Cheung, K.-H.; Shuai, J.; Parker, I.; Pearson, J. E.; Foskett, J. K.; Mak, D.-O. D. Mode Switching Is the Major Mechanism of Ligand Regulation of InsP<sub>3</sub> Receptor Calcium Release Channels. *J. Gen. Physiol.* **2007**, *130* (6), 631–645.
- (43) Popescu, G.; Auerbach, A. Modal Gating of NMDA Receptors and the Shape of Their Synaptic Response. *Nat. Neurosci.* **2003**, *6* (5), 476–483.
- (44) Popescu, G.; Robert, A.; Howe, J. R.; Auerbach, A. Reaction Mechanism Determines NMDA Receptor Response to Repetitive Stimulation. *Nature* **2004**, *430* (7001), 790–793.
- (45) Geng, Y.; Magleby, K. L. Modal Gating of Endplate Acetylcholine Receptors: A Proposed Mechanism. *J. Gen. Physiol.* **2015**, *146* (6), 435–439.
- (46) Cordero-Morales, J. F.; Jogini, V.; Chakrapani, S.; Perozo, E. A Multipoint Hydrogen-Bond Network Underlying KcsA C-Type Inactivation. *Biophys. J.* **2011**, *100* (10), 2387–2393.
- (47) Wang, W.; MacKinnon, R. Cryo-EM Structure of the Open Human Ether-à-Go-Go-Related K<sup>+</sup> Channel HERG. *Cell* **2017**, *169* (3), 422–430.e10.
- (48) Lueck, J. D.; Mackey, A. L.; Infield, D. T.; Galpin, J. D.; Li, J.; Roux, B.; Ahern, C. A. Atomic Mutagenesis in Ion Channels with Engineered Stoichiometry. *Elife* **2016**, *5* (OCTOBER2016).
- (49) Bohlen, C. J.; Priel, A.; Zhou, S.; King, D.; Siemens, J.; Julius, D. A Bivalent Tarantula Toxin Activates the Capsaicin Receptor, TRPV1, by Targeting the Outer Pore Domain. *Cell* **2010**, *141* (5), 834–845.
- (50) Visscher, K. M.; Medeiros-Silva, J.; Mance, D.; Rodrigues, J. P. G. L. M.; Daniëls, M.; Bonvin, A. M. J. J.; Baldus, M.; Weingarh, M. Supramolecular Organization and Functional Implications of K<sup>+</sup> Channel Clusters in Membranes. **2017**.
- (51) Weingarh, M.; Prokofyev, A.; van der Crujisen, E. A. W.; Nand, D.; Bonvin, A. M. J. J.; Pongs, O.; Baldus, M. Structural Determinants of Specific Lipid Binding to Potassium Channels. *J. Am. Chem. Soc.* **2013**, *135* (10), 3983–3988.
- (52) Jensen, M. Ø.; Jogini, V.; Borhani, D. W.; Leffler, A. E.; Dror, R. O.; Shaw, D. E. Mechanism of Voltage

- Gating in Potassium Channels. *Science* (80-. ). **2012**, 336 (6078), 229–233.
- (53) Köpfer, D. A.; Song, C.; Gruene, T.; Sheldrick, G. M.; Zachariae, U.; De Groot, B. L. Ion Permeation in K<sup>+</sup> Channels Occurs by Direct Coulomb Knock-On. *Science* (80-. ). **2014**, 346 (6207), 352–355.
- (54) Shi, C.; He, Y.; Hendriks, K.; De Groot, B. L.; Cai, X.; Tian, C.; Lange, A.; Sun, H. A Single NaK Channel Conformation Is Not Enough for Non-Selective Ion Conduction. *Nat. Commun.* **2018**, 9 (1).
- (55) Weingarth, M.; Bodenhausen, G.; Tekely, P. Broadband Magnetization Transfer Using Moderate Radio-Frequency Fields for NMR with Very High Static Fields and Spinning Speeds. *Chem. Phys. Lett.* **2010**, 488 (1–3), 10–16.
- (56) Weingarth, M.; Bodenhausen, G.; Tekely, P. Low-Power Decoupling at High Spinning Frequencies in High Static Fields. *J. Magn. Reson.* **2009**, 199 (2), 238–241.
- (57) Jo, S.; Kim, T.; Iyer, V. G.; Im, W. CHARMM-GUI: A Web-Based Graphical User Interface for CHARMM. *J. Comput. Chem.* **2008**, 29 (11), 1859–1865.
- (58) Jo, S.; Lim, J. B.; Klauda, J. B.; Im, W. CHARMM-GUI Membrane Builder for Mixed Bilayers and Its Application to Yeast Membranes. *Biophys. J.* **2009**, 97 (1), 50–58.
- (59) Best, R. B.; Zhu, X.; Shim, J.; Lopes, P. E. M.; Mittal, J.; Feig, M.; MacKerell Jr., A. D. Optimization of the Additive CHARMM All-Atom Protein Force Field Targeting Improved Sampling of the Backbone  $\phi$ ,  $\psi$  and Side-Chain X1 and X2 Dihedral Angles. *J. Chem. Theory Comput.* **2012**, 8 (9), 3257–3273.
- (60) Klauda, J. B.; Venable, R. M.; Freites, J. A.; O'Connor, J. W.; Tobias, D. J.; Mondragon-Ramirez, C.; Vorobyov, I.; MacKerell Jr., A. D.; Pastor, R. W. Update of the CHARMM All-Atom Additive Force Field for Lipids: Validation on Six Lipid Types. *J. Phys. Chem. B* **2010**, 114 (23), 7830–7843.
- (61) Beglov, D.; Roux, B. Finite Representation of an Infinite Bulk System: Solvent Boundary Potential for Computer Simulations. *J. Chem. Phys.* **1994**, 100 (12), 9050–9063.
- (62) Bhate, M. P.; McDermott, A. E. Protonation State of E71 in KcsA and Its Role for Channel Collapse and Inactivation. *Proc. Natl. Acad. Sci. U. S. A.* **2012**, 109 (38), 15265–15270.
- (63) Phillips, J. C.; Braun, R.; Wang, W.; Gumbart, J.; Tajkhorshid, E.; Villa, E.; Chipot, C.; Skeel, R. D.; Kalé, L.; Schulten, K. Scalable Molecular Dynamics with NAMD. *J. Comput. Chem.* **2005**, 26 (16), 1781–1802.
- (64) Shaw, D. E.; Dror, R. O.; Salmon, J. K.; Grossman, J. P.; MacKenzie, K. M.; Bank, J. A.; Young, C.; Deneroff, M. M.; Batson, B.; Bowers, K. J.; et al. Millisecond-Scale Molecular Dynamics Simulations on Anton. In *Proceedings of the Conference on High Performance Computing Networking, Storage and Analysis, SC '09*; 2009.
- (65) Jekhmane, S.; Medeiros-Silva, J.; Li, J.; Kümmerer, F.; Müller-Hermes, C.; Baldus, M.; Roux, B.; Weingarth, M. Shifts in the Selectivity Filter Dynamics Cause Modal Gating in K<sup>+</sup> Channels. *Nat. Commun.* **2019**, 10 (1), 123.

# CHAPTER 5

Supramolecular organization and functional implications of  $K^+$  channel clusters in membranes



## Abstract

The segregation of cellular surfaces in heterogeneous patches is considered to be a common motif in bacteria and eukaryotes that is underpinned by the observation of clustering and cooperative gating of signaling membrane proteins such as receptors or channels. Such processes could represent an important cellular strategy to shape signaling activity. Hence, structural knowledge of the arrangement of channels or receptors in supramolecular assemblies represents a crucial step towards a better understanding of signaling across membranes. We herein report on the supramolecular organization of clusters of the K<sup>+</sup> channel KcsA in bacterial membranes, which was analyzed by a combination of DNP enhanced solid-state NMR experiments and MD simulations. We used solid-state NMR spectroscopy to determine the channel–channel interface and to demonstrate the strong correlation between channel function and clustering, which suggests a yet unknown mechanism of communication between K<sup>+</sup> channels.

*Based on the publication:*

Koen M. Visscher, João Medeiros-Silva, Deni Mance, João P. G. L. M. Rodrigues, Mark Daniëls, Alexandre M. J. J. Bonvin, Marc Baldus, and Markus Weingarth

Supramolecular organization and functional implications of K<sup>+</sup> channel clusters in membranes.

*Angewandte Chemie International Edition*, 2017, 56 (43), 13222–13227.

## Introduction

Multiple lines of experimental evidence highlight the lateral patchiness of cellular surfaces, suggesting that membranes are organized in heterogeneous domains.<sup>1,2</sup> This corroborates the notion that membrane signaling proteins such as channels or receptors are assembled in supramolecular clusters, in which protein function is coupled,<sup>3–5</sup> possibly to achieve an optimal response to a single stimulus. Indeed, clustering and coupled gating have been reported for a number of ion channels, including mammalian K<sup>+</sup>,<sup>6–8</sup> Na<sup>+</sup>,<sup>9,10</sup> and Ca<sub>2</sub><sup>+</sup><sup>4</sup> channels. However, the principles of the arrangement of channel clusters and the implications of clustering for channel gating remain largely unknown.

KcsA is an archetypical K<sup>+</sup> channel and widely used to study ion channel gating. The KcsA pore is conserved across all K<sup>+</sup> channels and regulated by a cytoplasmic activation gate and an extracellular inactivation gate.<sup>11</sup> It has been demonstrated *in vitro*<sup>12–14</sup> and *in vivo* in *E. coli*<sup>15</sup> and in the native host *S. lividans*<sup>16</sup> that KcsA can form clusters. Herein, we have studied the supramolecular arrangement of KcsA clusters in *E. coli* membranes by conventional and dynamic nuclear polarization (DNP) enhanced solid-state NMR (ssNMR) experiments and coarse-grained molecular dynamics (CGMD) simulations. We demonstrate that KcsA channels assemble into clusters in native-like lipid membranes, and provide structural details on the channel–channel interface, disclosing an unexpected role of a membrane-associated helix as a key element for clustering. Intriguingly, we demonstrate with DNP-ssNMR experiments that channel function and cluster formation are correlated, which suggests a thus far unknown mechanism of inter-channel communication.

## Results and discussion

### *KcsA clustering in membranes*

ssNMR spectroscopy provides a straightforward means for studying the clustering of membrane proteins by mixing proteins that carry different NMR-active nuclei X and Y (e.g., X = <sup>15</sup>N and Y = <sup>13</sup>C).<sup>17,18</sup> Magnetization transfer between spin species X and Y necessitates the formation of clusters that are stable on the experimental timescale, which is in the range of μs to ms for dedicated dipolar transfer schemes. We reconstituted an equimolar mixture of <sup>15</sup>N-labeled KcsA [U-<sup>15</sup>N-KcsA] and <sup>13</sup>C-labeled KcsA [U-<sup>13</sup>C-KcsA] in *E. coli* lipids at a 1:100 protein/lipid (P/L) molar ratio. We initially prepared the samples in neutral buffers (pH 7, 50 mM K<sup>+</sup>), in which channels are in the closed–conductive gating mode, which we validated with a ssNMR 2D <sup>13</sup>C–<sup>13</sup>C PARIS<sup>19</sup> spectrum (Figure S1). In line with previous results,<sup>20</sup> the KcsA channels exhibited a parallel topology in this preparation (Figure S3). To probe KcsA clustering, we carried out a series of one-dimensional (1D) NHHC experiments,<sup>17</sup> in which magnetization is initially created on <sup>15</sup>N nuclei (i.e., of U-<sup>15</sup>N-KcsA) and transferred via short

heteronuclear transfer steps and a longer  $^1\text{H}$ – $^1\text{H}$  dipolar mixing unit to  $^{13}\text{C}$  nuclei (of U- $^{13}\text{C}$ -KcsA; Figure 1 A). We observed pronounced transfer to  $^{13}\text{C}$  nuclei in the 1D NHHC spectra (Figure 1 B), which strongly indicated the formation of KcsA clusters that are stable on the sub-millisecond timescale and probably beyond. As the  $^1\text{H}$ -mediated magnetization transfer from  $^{15}\text{N}$  to  $^{13}\text{C}$  is short- ranged with an upper barrier of approximately 5 Å, the NHHC spectra strongly suggest that the clustered channels are in direct contact. Furthermore, while most of our ssNMR experiments were carried out at low temperature (at 255 K) for sensitivity reasons, cluster formation also occurred at higher temperature (293 K; Figure 1 C). Note that magnetization transfer from  $^{15}\text{N}$  to  $^{13}\text{C}$  was virtually abolished in a mixture of U- $^{15}\text{N}$ -KcsA and unlabeled KcsA, which means that putative spurious  $^{13}\text{C}$  natural-abundance contributions can be neglected (Figure 1 D), validating our experimental setup. We would also like to emphasize that the homotetrameric KcsA is of outstanding stability in liposomes, and tetramers do not dissociate neither at elevated temperatures, up to 80 °C,<sup>21</sup> nor in harsh detergents such as SDS.<sup>22</sup> Therefore, signal intensity in NHHC experiments must result from contacts between different channels.

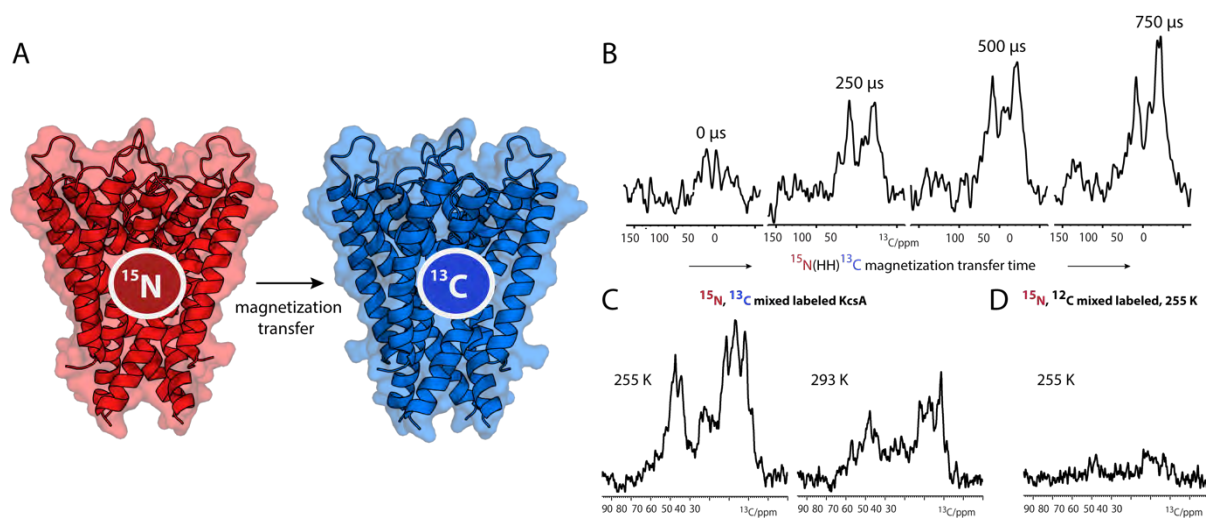


**Figure 1.** ssNMR demonstrates that KcsA channels form clusters in *E. coli* lipids. **A)** KcsA clustering can be probed with an equimolar mixture of  $^{15}\text{N}$ - and  $^{13}\text{C}$ -labeled channels and dedicated ssNMR experiments such as NHHC.<sup>17</sup> **B)** A series of 1D NHHC experiments with increasing  $^1\text{H}$ – $^1\text{H}$  magnetization transfer times applied to mixed-labeled channels show the presence of KcsA clusters. **C)** Cluster formation occurred at low (255 K) and high (293 K) temperature. The lower intensity at 293 K is due to increased local motion, which decreases the dipolar transfer efficiency. **D)** The virtual absence of signals without  $^{13}\text{C}$  labeling shows that natural-abundance contributions can be neglected.

*KcsA clustering relates to gating*

As a next step, we investigated if clustering correlates with KcsA function. It is currently not clear if or how clustering modulates KcsA function, and contradicting studies have been published in recent years. Molina and co-workers showed by electrophysiological measurements in liposomes that clustered channels open together in a concerted manner, and that clustering strongly increases channel open probability.<sup>12</sup> However, in stark contrast to the studies by Molina and co-workers, AFM experiments, using truncated channels in zwitterionic lipids exposed to a mica surface, came to the conclusion that open channels do not form clusters.<sup>14</sup> We tried to settle this striking conflict with a series of comparative 1D NHHc measurements with closed and open full-length channels embedded in *E. coli* lipids. For these studies it was critical to work at a low P/L ratio; 1) to allocate enough space so that channels could potentially dissociate upon opening,<sup>14</sup> and 2) to exclude random channel–channel contacts. However, as a 1D NHHc experiment with a P/L ratio of 1:100 (Figure 1) already required a measurement time of about one day, substantially lower P/L ratios were prohibitive with conventional NMR spectroscopy. We overcame this issue with the DNP technique, which can provide sensitivity gains of two orders of magnitude, and thereby enables otherwise infeasible ssNMR experiments with lowly concentrated membrane proteins (for examples, see Refs. (18,23–30)). We prepared vesicles with mixed <sup>15</sup>N or <sup>13</sup>C-labeled channels and ran experiments using a 263 GHz/400 MHz DNP/ssNMR setup at 100 K. We obtained signal enhancement factors  $\epsilon$  of 20–55, which are comparable to those in our previous DNP applications with KcsA.<sup>25</sup> Importantly, this enhancement allowed us to work at a much lower P/L ratio of 1:400, ensuring that the DNP-ssNMR results reflect specific channel–channel contacts in reference to the gating mode. We first conducted DNP-ssNMR experiments with closed channels (at pH 7), which confirmed the formation of clusters. Afterwards, we washed exactly the same sample in acidic (pH 4) buffers, which is a well-known means to open the activation gate of KcsA.<sup>11,31,32</sup> Unexpectedly, we obtained drastically increased NHHc transfer efficiencies with open channels (Figure 2 A). We confirmed this result by “shuttling” the channels back to the closed state (pH 7), for which the NHHc transfer was again much weaker (Figure 2 B). Hence, our DNP-ssNMR experiments in native bacterial lipids revealed that cluster formation is a reversible, dynamic process that is correlated with the gating cycle of KcsA. Moreover, our study unambiguously demonstrates that open channels form clusters, which explains previous results from Molina and co-workers.<sup>12</sup> Furthermore, our study reveals that the opening of the activating gate strongly stimulates cluster formation.

But what causes the surprising increase in cluster formation upon channel opening, and how can clustered channels communicate to open simultaneously? Our data demonstrate that the channel–channel interface is modulated during the closed-to-open transition. This very

strongly suggests that a structural element that is involved in channel opening is also involved in the channel–channel interface. The major structural event upon channel opening is a conformational change of the inner transmembrane (TM2) helix, and this unseals the cytoplasmic gate. However, it appears hardly possible that the TM2 helix, which is hidden in the interior of KcsA, contributes to channel–channel interactions. Another structural element that responds to the closed-to-open transition is the membrane-associated M0 helix, formed by the N-terminal residues M1–G21.<sup>33</sup> Indeed, it seems much more likely that M0 helices are involved in cluster formation, given that they are by far the most protruding element of the KcsA channel in the membrane plane.

Upon channel opening, in a mechanism dubbed “roll and stabilize”, the M0 helix undergoes a major conformational change that buries hydrophobic M0 residues in the bilayer and exposes charged residues to lipid head groups.<sup>33</sup> The M0 helix could hence be a switch to modulate clustering, and we therefore hypothesized that these helices contribute to the channel–channel interface.

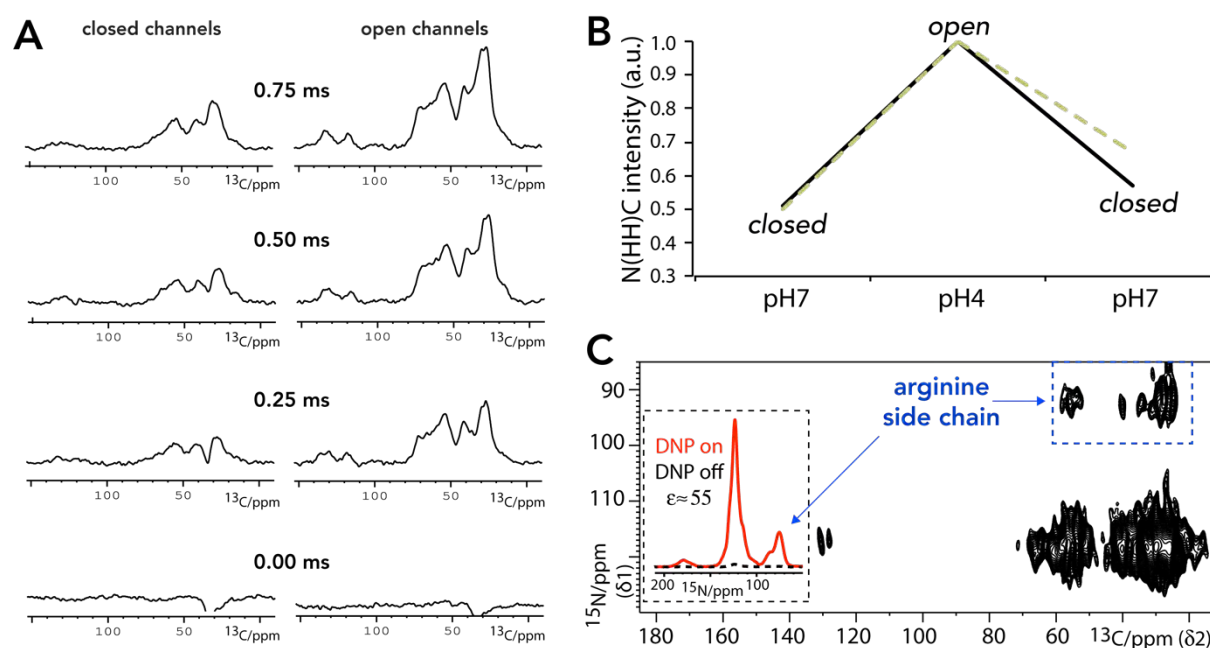


**Figure 2.** DNP-ssNMR experiments to probe KcsA clustering in reference to function. **A)** A series of 1D NHHC spectra for closed–conductive (left) and open–inactivated (right) mixed-labeled channels (see also Figure S2). Spectra are normalized (see S4) and ordered according to the  $^1\text{H}$ – $^1\text{H}$  mixing time. **B)** Comparison of NHHC spectra measured with a  $^1\text{H}$ – $^1\text{H}$  mixing time of 0.75 ms. Spectra were normalized according to the highest intensity at the signal maxima at  $\delta(^{13}\text{C})=27$  ppm (black continuous lines) and  $\delta(^{13}\text{C})=54$  ppm (golden dashed lines). The intensity values are from the same sample used in Figures 2A,C. **C)** DNP-enhanced 2D NHHC spectrum, measured with mixed-labeled closed (pH 7) KcsA channels. The comparison of 1D  $^{15}\text{N}$  cross-polarization spectra in the insert illustrates the DNP enhancement of 55. The blue dashed box marks the channel–channel contacts that involve arginine side chains. To save experimental time, the arginine signals at  $\delta(^{15}\text{N})\approx 75$  ppm were back-folded to  $\delta(^{15}\text{N})=95$  ppm in the 2D NHHC spectrum.

### The M0 helix domain mediates channel-channel contacts

To investigate the channel–channel interface in further detail, we resorted to coarse-grained molecular dynamics (CGMD) simulations using the MARTINI force field.<sup>34</sup> Such simulations have both the long temporal and large spatial scale to study membrane protein clustering.<sup>35,36</sup> However, we would like to note that CGMD simulations only provide limited insight into cluster formation. First, such simulations are necessarily less accurate than all-atom simulations, and this may lead to an overestimation of intermolecular interactions. Second, the MARTINI force field is limited in its response to changes in the simulated environment, and secondary structure changes, for example, are not permitted. However, we would like to emphasize that overestimations of channel–channel interactions are of lesser concern, given that we have clearly demonstrated that KcsA forms clusters in membranes. Moreover, ssNMR studies of KcsA in *E. coli* membranes, in which KcsA forms clusters (Figures 1 and 2), show only minimal secondary-structure changes as compared to the crystal structures.<sup>37</sup> Finally, it is not realistic to study channel clustering with all-atom simulations on the relevant timescales.

We performed CGMD simulations in which 16 closed KcsA channels, derived from PDB No. 1K4C (comprising residues S22–H124), were initially equidistantly placed in a large membrane composed of 3280 DOPE, 944 DOPG, and 480 cardiolipin lipids, approximating the composition of the inner *E. coli* membrane.<sup>38</sup> The P/L ratio was approximately 1:300. To probe the influence of the M0 helix on clustering, we simulated these channels in the absence and presence of this helix (Figure 3 A, B). For the latter case, the M0 helix was added with MODELLER. Each simulation was run for a total duration of 37.5 ms. Indeed, the simulations clearly showed that the M0 helices modulate clustering. In the absence of the M0 helix, only small dimeric or trimeric clusters formed. However, the presence of M0 helices much accelerated clustering, with M0 helices acting as flexible tentacles that initiate channel–channel contacts. Intriguingly, M0 helices of clustered channels cast a kind of elongated mesh of 40 nm width, in which channels are entangled and from which they cannot easily escape. Such large assemblies are in line with *in vivo* and *in vitro* measurements, which revealed large KcsA clusters of 50 nm width.<sup>13,16</sup> Notably, channel–channel contacts are relatively dynamic in this mesh (see Video S5), and this is likely necessary so that channel–channel interactions can respond to gating transitions (Figure 2). Note that we did not consider the cytoplasmic domain (CPD) of KcsA in the simulations as previous studies had shown that the CPD does not take part in clustering.<sup>12,13</sup> In line with these findings, an alignment of full-length KcsA<sup>39</sup> to our model of clusters shows that the CPDs of clustered channels are far away from each other (Figure S5).

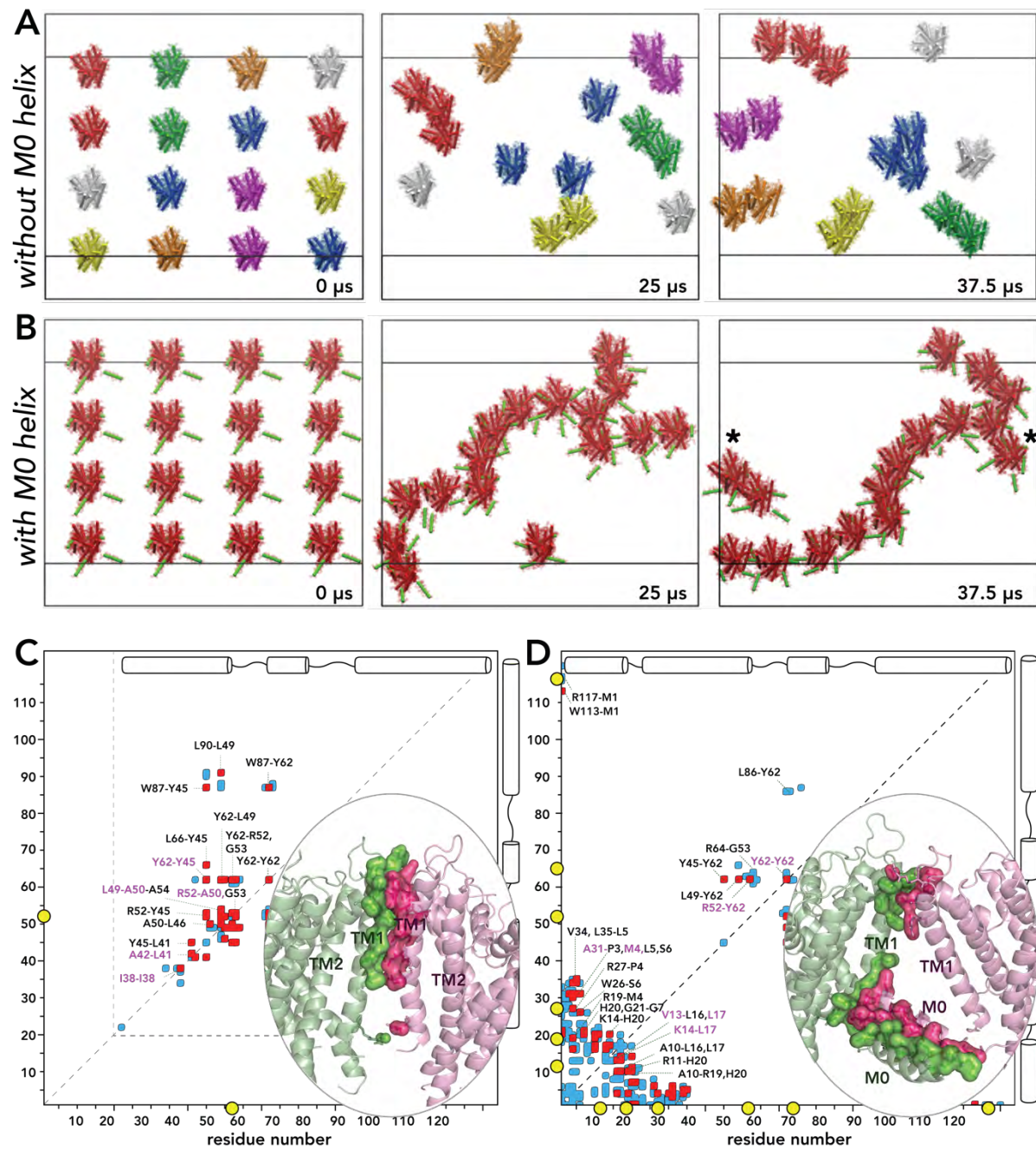


**Figure 3.** KcsA cluster formation probed by CGMD simulations. **A)** Evolution of channels without the M0 helix. Channels in the same clusters are shown in the same colors. **B)** Evolution of channels with the M0 helix, highlighted in green. Channels marked with asterisks form clusters over periodic boundaries. The snapshot after 37.5 ms was laterally translated by 5 nm. **C,D)** Contact maps derived from back-transformed<sup>40</sup> atomic-resolution interfaces sampled over the last 7.5 ms of the simulations. The maps show residue pairs of interacting channels within 5 Å distance without (C) and with (D) M0 helices. Pairs that were populated by >30% and <30% in comparison to the most populated pair are shown in red and blue, respectively. The five most populated pairs are shown in magenta. Pairs populated by <10% are not shown. Yellow circles highlight arginine residues at the interface. Representative high-resolution interfaces are shown in the bottom-right corners.

Importantly, the M0 helix also has a strong influence on the channel–channel interface. In the absence of this helix (Figure 3 C), the interface is dominated by the TM1 helix. As we had assumed, the inner TM2 helix does not contribute to the interface. In the presence of the M0 helices, the interface is dominated by the mutually interacting M0 helices, which sterically prevent the TM1 helix from taking part in clustering. Moreover the turret, which connects the TM1 to the selectivity filter, is also involved in the interface (Figure 3 D). We sought to corroborate our structural model with a 2D NHHc ssNMR experiment, which critically required DNP enhancement for sensitivity reasons. An enhancement of  $\epsilon = 55$  enabled the acquisition of a 2D NHHc spectrum in only three days (Figure 2 C). While the resolution of the backbone amino protons ( $\delta(^{15}\text{N}) = 100\text{--}130$  ppm) in the 2D experiment did not permit the assignment of specific contacts, we observed very strong correlations characteristic for polarization transfer from the arginine guanidinium group (resonating at  $\delta(^{15}\text{N}) = 75\text{--}80$  ppm) to  $^{13}\text{C}$  atoms in the backbone and side chains. The strong arginine contribution at the interface strongly corroborates the presence of the M0 helix at the interface (Figure 3 D). Indeed, with the M0 helix, a total of six arginine residues (R11, R19, R27, R52, R64, R117) are heavily involved in channel–channel contacts. However, without the M0 helix (Figure 3 C), the interface is dominated by the hydrophobic TM1 helix, and only a single arginine (R52) contributes to interchannel contacts. Aside from this experimental evidence, it is sterically hardly possible that the protruding M0 helices are not present at the interface.

Note that the use of 800 MHz DNP<sup>25</sup> would have provided little additional information in this study because its application would have been limited to 1D experiments for sensitivity reasons. Likewise, 2D or 3D experiments of the N(HH)CC type, which may provide precious information on the interface, were prohibited by the low spectral sensitivity in our strongly diluted membrane preparations.

## Conclusion

In conclusion, we have dissected the anatomy of KcsA clusters in native bacterial lipids. By combining DNP-ssNMR experiments with MD simulations, we demonstrated that K<sup>+</sup> channel gating and clustering are correlated in membranes, which hints at a relationship between KcsA localization and function. Thereby, our study solves a striking conflict<sup>13</sup> in the growing KcsA cluster literature, and strongly supports previous reports that KcsA channels can open in a concerted manner.<sup>12</sup> Intriguingly, our study discloses that the membrane-associated M0 helix is a key element for cluster formation, and likely also for interchannel communication. In this context, our study highlights the importance of understanding how membrane proteins interact at high resolution, especially as protein assemblies are ubiquitous in crowded biological membranes.

## Materials and Methods

### *Sample preparation*

The uniformly (U)  $^{13}\text{C}^{14}\text{N}$  or  $^{12}\text{C}^{15}\text{N}$  labeled KcsA samples were expressed in a medium containing U- $^{13}\text{C}$  or U- $^{12}\text{C}$  glucose and  $^{14}\text{NH}_4\text{Cl}$  or  $^{15}\text{NH}_4\text{Cl}$ , respectively. Purification and reconstitution steps were done following earlier work, see refs. (37,41). Ion channels were reconstituted in *E. coli polar* lipids (Avanti) using a protein/lipid (P/L) molar ratio of 1/100 and 1/400 for conventional and DNP-enhanced ssNMR experiments, respectively. For the conventional ssNMR experiments, the reconstituted samples were washed twice for 1.5 h in 50 mM sodium phosphate buffer, 50 mM  $\text{K}^+$ , 50 mM  $\text{Na}^+$  (pH 7).

For DNP-ssNMR experiments, the KcsA liposome samples were re-suspended in a 50  $\mu\text{l}$  solution containing the biradical AMUPol.<sup>42</sup> This solution consisted of 15 mM AMUPol dissolved in 1:2:2 (v/v/v)  $\text{d}_8$ -glycerol: $\text{D}_2\text{O}$ : $\text{H}_2\text{O}$ (buffered). The pH7 buffer was composed by 50 mM sodium phosphate, 50 mM NaCl and 50mM KCl, at final concentration; and the pH 4 buffer was composed by 10 mM sodium citrate and 120 mM NaCl, at final concentration. Subsequently, samples were collected by centrifugation at 130,000  $\times g$  for 30 min. Pellets were collected and the procedure was repeated again. Pellet were then packed into 3.2 mm sapphire rotors.

### *Solid-state NMR experiments*

#### Conventional ssNMR

NHHC<sup>17,43</sup> experiments were carried out in a magnetic field of 16.4 T (700 MHz  $^1\text{H}$  frequency, Bruker BioSpin) and a magic angle spinning (MAS) frequency of 7.2 kHz, respectively. The second and third cross-polarization steps of NHHC experiments were kept short (100 - 300  $\mu\text{s}$ ). The effective sample temperature was set to 255 K, unless indicated otherwise. A 2D  $^{13}\text{C}$ - $^{13}\text{C}$  PARIS spectrum<sup>41,44</sup> was acquired at 700 MHz and 12 kHz MAS at 270 K.

#### Conventional ssNMR

DNP-enhanced NHHC experiments were carried out at a proton/electron frequency of 400 MHz/263 GHz (Bruker BioSpin). All DNP experiments were performed at 100 K using a MAS rate of 8 kHz. For the DNP-enhanced 2D NHHC experiment, we used very short (100  $\mu\text{s}$ ) contact times for the second and third cross-polarization steps and a  $^1\text{H}$ - $^1\text{H}$  spin diffusion time of 600  $\mu\text{s}$ . For the spectral comparison of DNP-enhanced 1D NHHC spectra of closed and open channels (Figure 2A,B), we scaled the spectra according to their intensities (see S4).

Importantly, we used the same sample preparation for the data acquired in Figure 2A,B.

The samples were retrieved from the rotor and washed twice with acidic (pH4) or neutral (pH7) buffers to obtain open or closed channels, respectively. The samples were then re-washed with the appropriate AMUPol buffer as described.

### *Molecular Dynamics Simulations*

CGMD simulations were carried out using the GROMACS package version 4.5.4<sup>45</sup> and the MARTINI force field version 2.2<sup>34</sup> together with an integration step of 20 fs and the standard settings<sup>34</sup> for nonbonded interactions in a NPT ensemble. For nonbonded interactions, we used the potentials described in the original MARTINI publication,<sup>34</sup> i.e., potentials for LJ and Coulomb interactions that are shifted (using the Gromacs shifting function) to zero between 0.9 – 1.2 nm and 0.0 - 1.2 nm, respectively. The system was semi-isotropically coupled to a pressure bath at 1 bar ( $\tau_p = 3$  ps) using the Berendsen Barostat<sup>46</sup> and coupled ( $\tau_T = 0.3$  ps) to a heat bath using the Berendsen Thermostat.<sup>46</sup> A solvated mixed DOPE : DOPG : Cardiolipin (7 : 2 : 1 molar ratio) bilayer, consisting of 205 DOPE, 59 DOPG lipids and 30 Cardiolipin, together with 4415 water beads and 95 sodium counter ions was equilibrated and one KcsA channel inserted. This system was expanded four times in both x and y dimensions, yielding a total system of dimensions 42.8 x 42.8 x 9.3 nm<sup>3</sup> (xyz) and a total number of beads of 158080. Cardiolipin parameters were taken from ref. (47). The CG KcsA structure was derived from a closed-conductive channel (pdb code 1K4C<sup>48</sup>) using the martinize.py script. An elastic network approach<sup>49</sup> with a force constant of 1000 kJ mol<sup>-1</sup> nm<sup>-2</sup> and a cutoff of 0.9 nm was used together with the MARTINI force field to ensure long-time stability of the protein fold. Independent elastic networks were used for each of the four KcsA subunits. No elastic bonds were applied between M0 helix and TM part of KcsA. The M0 helix was modelled using secondary structure restraints in MODELLER v9.12.<sup>46</sup>

## Supporting Information

## S1.2. Gating states of KcsA by ssNMR

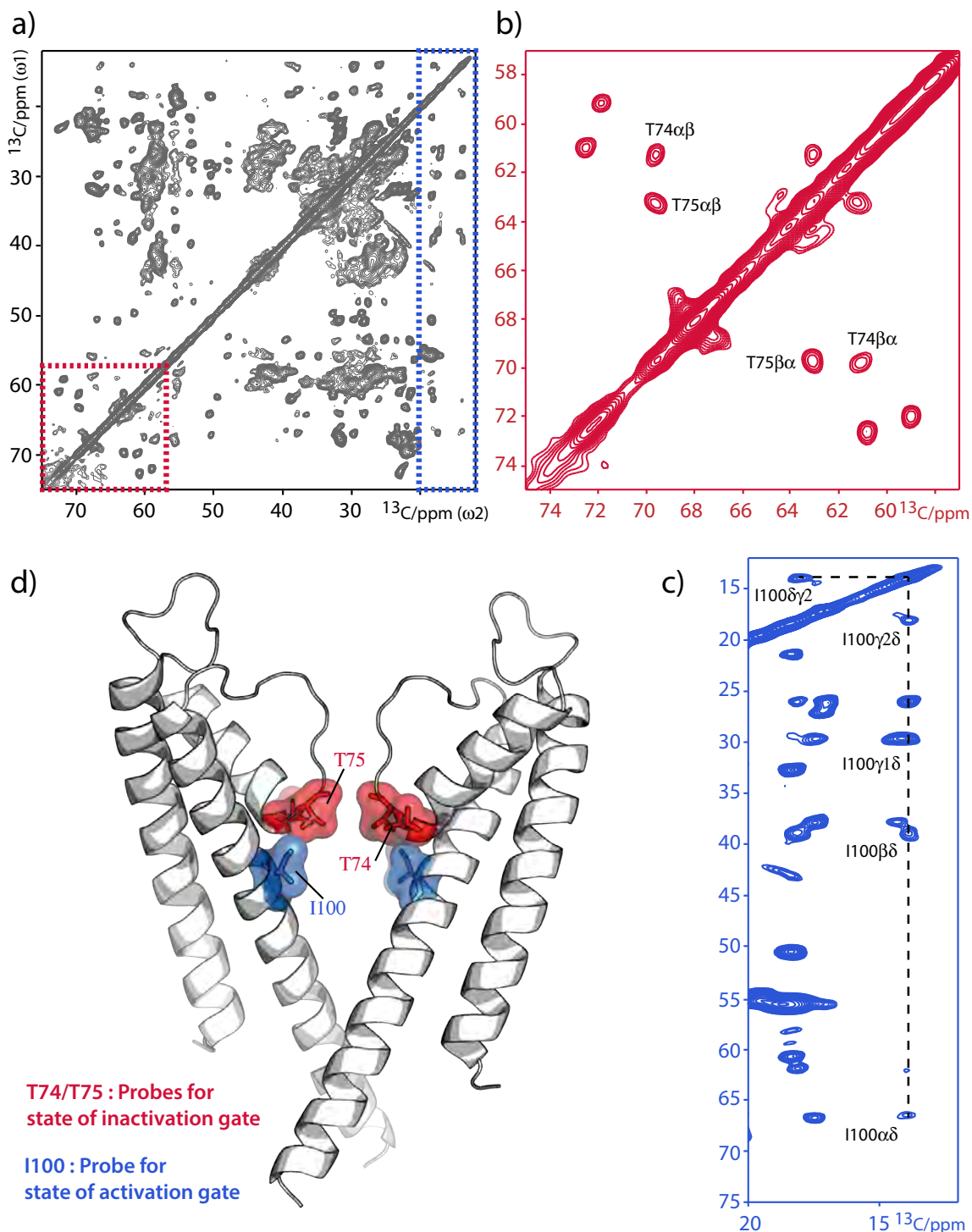


**Figure S1.** Cutouts of a) a 2D  $^{13}\text{C}$ - $^{13}\text{C}$  PARIS<sup>19</sup> spectrum, measured with full-length KcsA, showing signal patterns that are characteristic<sup>41,50-52</sup> for b) the *conductive* inactivation gate (also called selectivity filter) and c) the *closed* activation gate. d) Illustration of the molecular positions of the spectral probes (T74, T75, and I100) for the gating mode of KcsA.

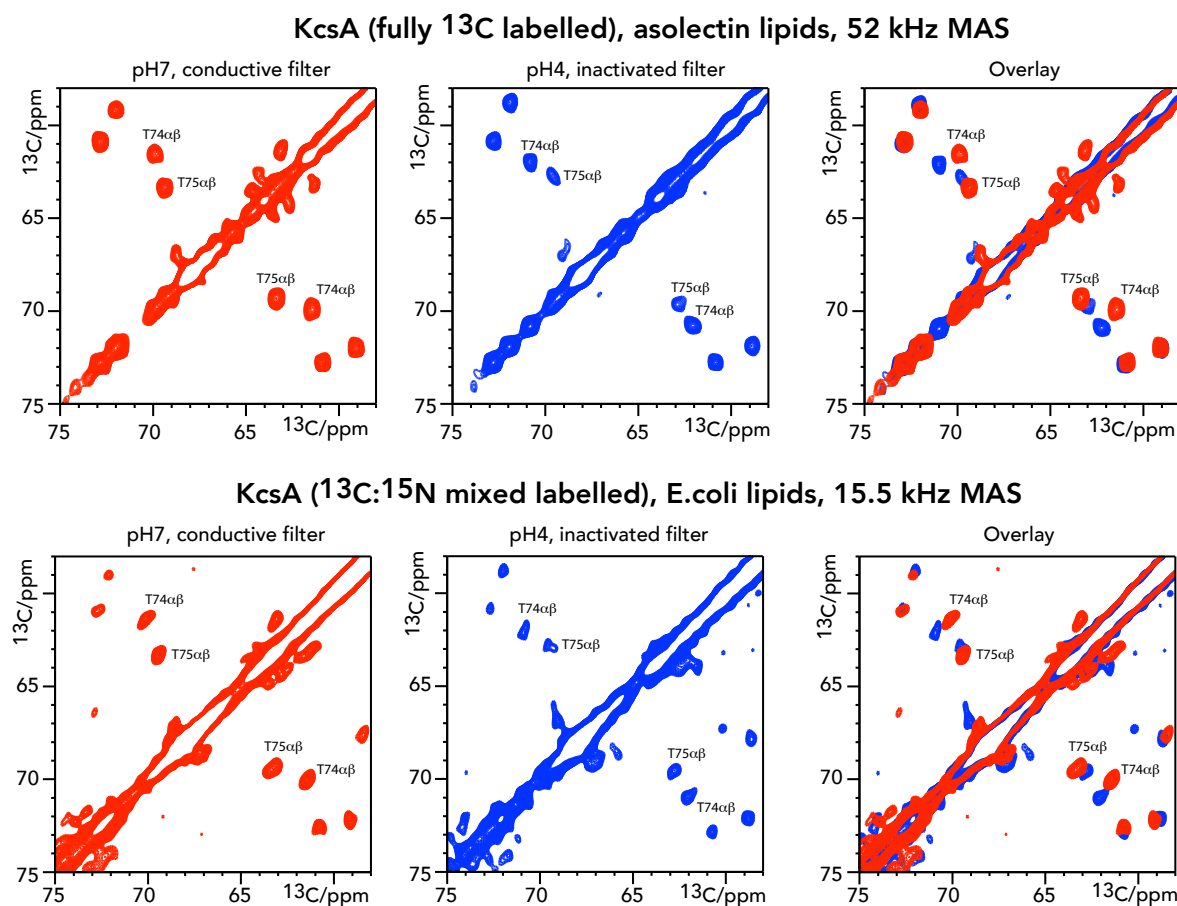
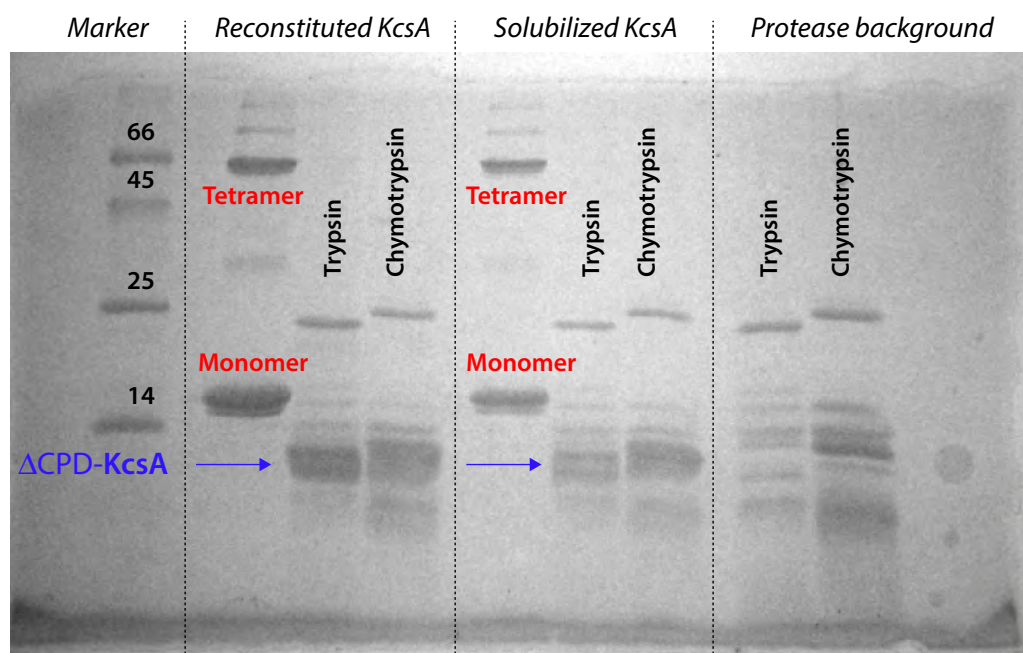


**Figure S2.**  $^{13}\text{C}$ - $^{13}\text{C}$  PARIS spectra acquired at pH7 (left panel) and pH4 (middle panel). The spectra were acquired with the mixed-labeled sample used for Figure 1 (lower row), and with the sample described in Ref (31).

### S3. Topology of KcsA in the E.coli liposomes

Treatment of reconstituted KcsA channels with proteases resulted in an almost homogenous truncated construct of about 10-12 kDa, consistent with a uniform cleavage of the C-terminal cytoplasmic domain (CPD), resulting in the dissociation of KcsA subunits (Figure S2). The parallel KcsA topology is illustrated by the complete lack of intact tetramers and monomers of KcsA, which would be present if channels adopted an antiparallel or random orientation that inhibited cleavage of the CPDs for a certain number of channels. The size of the  $\Delta\text{CPD}$ -KcsA construct is highlighted by protease treatment of randomly orientated, DM-solubilized KcsA, which leads to a complete cleavage of the hydrophilic CPD. The position of trypsin-cleavage sites which are accessible for the enzymes are shown in bold. Analogously, cleavage sites of Chymotrypsin are restricted to the C- and N-termini.



**Trypsin-cleavage sites in KcsA (residue-number):**

**11** (100%); **14** (100%); **19** (100%); 27 (100%); 52 (100%); 64 (100%); 89 (100%); 117 (100%); **121** (100%); **122** (77.3%); **127** (100%); **131** (94.4%); **139** (100%); **142** (100%); **147** (100%); **150** (79.4%); **153** (100%)

**Figure S3.** In accordance with previous reports,<sup>20,53</sup> an enzymatic cleavage assay reveals a parallel topology of KcsA channels in our reconstituted liposome preparation. The figure shows SDS-PAGE gels at 12.5% acrylamide with a molecular weight marker (kDa) in the first left-most lane. The three-lane groups contain respectively *left*) KcsA reconstituted in lipid vesicles; *middle*) KcsA solubilized with decyl- $\beta$ -D-maltoside,<sup>54</sup> *right*) protease background profile.

#### S4. Comparison of the DNP spectra shown in Figure 2

In Figures 2A,B we compared signal intensities of 1D NHHC spectra of open and closed channels. Since the sample was washed with different buffers to ‘shuttle’ the channels between closed and open states, the ratio of  $^{13}\text{C}$  and  $^{15}\text{N}$  labeled channels was the same for each experiment. However, it was necessary to scale intensities for the comparison due to i) different DNP-enhancements, and ii) loss of sample after the washing steps. To scale the spectra, we measured and compared intensities of DNP-enhanced 1D  $^{15}\text{N}$  cross-polarization spectra for each buffer condition. These scaling factors were applied to each experimental series shown in Figures 2A,B.

## S5. Channel clustering simulation by CGMD

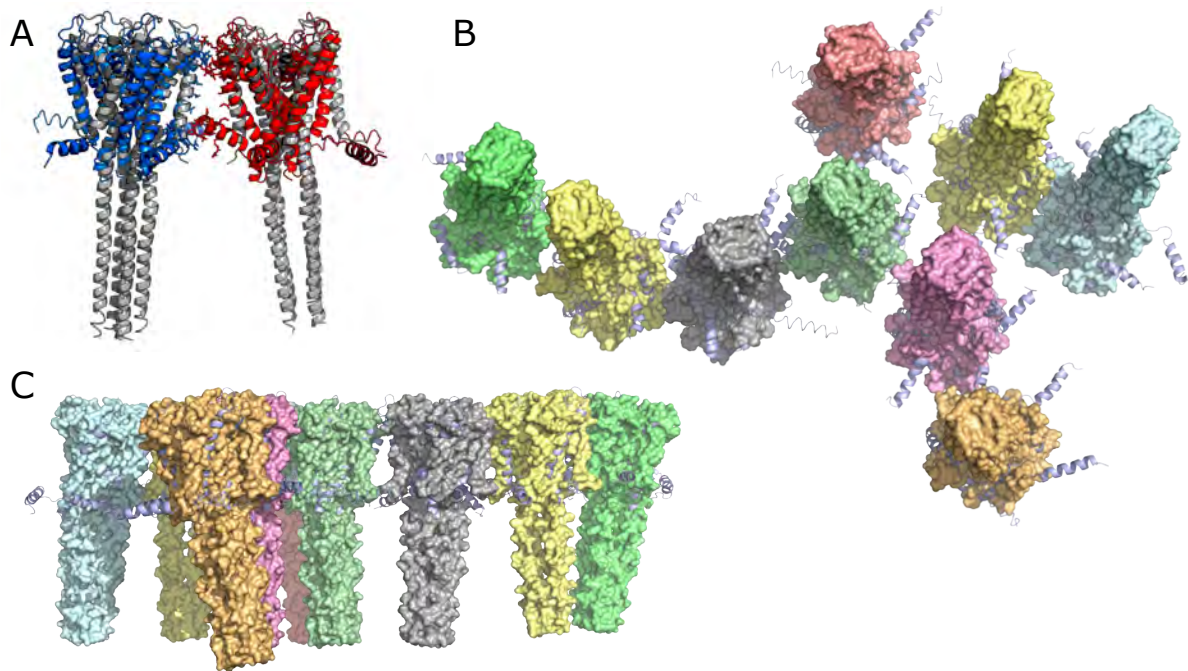


**Figure S5.** In (A), alignment of full-length KcsA crystal structures (pdb code 3EFF)<sup>39</sup> to a KcsA dimer that is representative for the contact map of Figure 3D. The KcsA dimer was taken from the end of the 37.5  $\mu$ s CGMD simulation (Figure 3B) and back-transformed to atomistic coordinates using the Backward<sup>40</sup> tool. As can be seen from the alignment, the C-terminal cytoplasmic domains (CPDs; residues 125 – 160) of KcsA channels in clusters are far away from each other, which is also evident in (B) and (C), showing the same superposition for a larger ensemble of nine simulated KcsA channels from two different perspectives. This is in good agreement with previous studies, which reported that CPDs are neither necessary for nor involved in KcsA clusters.<sup>12,13</sup>

**Video S5.** The evolution of the 16 coarse-grained KcsA channels in presence of the M0 helix in *E. coli* lipids over 37.5  $\mu$ s. Lipids, water and ions are left out for clarity. The time-resolution of the video is 100 ns. The coloring of the channels is arbitrary.

## References

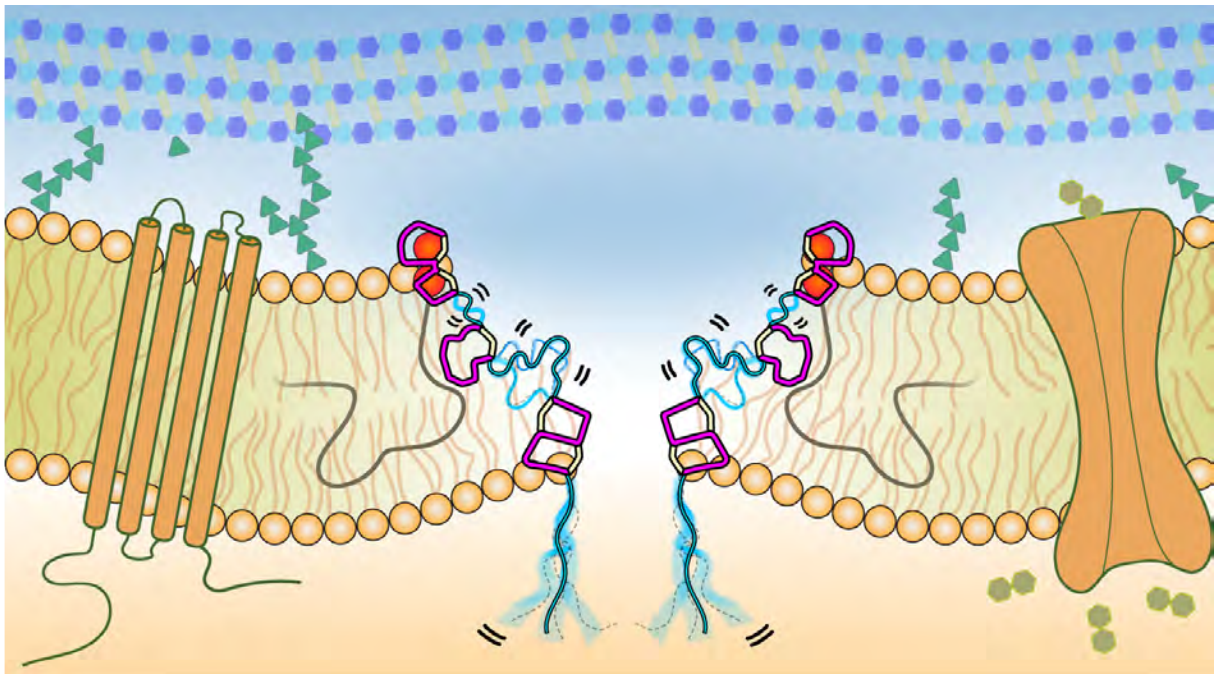
- (1) Spira, F.; Mueller, N. S.; Beck, G.; Von Olshausen, P.; Beig, J.; Wedlich-Söldner, R. Patchwork Organization of the Yeast Plasma Membrane into Numerous Coexisting Domains. *Nat. Cell Biol.* **2012**, *14* (6), 640–648.
- (2) Sharma, P.; Varma, R.; Sarasij, R. C.; Ira; Gousset, K.; Krishnamoorthy, G.; Rao, M.; Mayor, S. Nanoscale Organization of Multiple GPI-Anchored Proteins in Living Cell Membranes. *Cell* **2004**, *116* (4), 577–589.
- (3) Marx, S. O.; Gaburjakova, J.; Gaburjakova, M.; Henrikson, C.; Ondrias, K.; Marks, A. R. Coupled Gating between Cardiac Calcium Release Channels (Ryanodine Receptors). *Circ. Res.* **2001**, *88* (11), 1151–1158.
- (4) Navedo, M. F.; Cheng, E. P.; Yuan, C.; Votaw, S.; Molkenin, J. D.; Scott, J. D.; Santana, L. F. Increased Coupled Gating of L-Type Ca<sup>2+</sup> Channels during Hypertension and Timothy Syndrome. *Circ. Res.* **2010**, *106* (4), 748–756.
- (5) Sieber, J. J.; Willig, K. I.; Kutzner, C.; Gerding-Reimers, C.; Harke, B.; Donnert, G.; Rammner, B.; Eggeling, C.; Hell, S. W.; Grubmüller, H.; et al. Anatomy and Dynamics of a Supramolecular Membrane Protein Cluster. *Science* (80-.). **2007**, *317* (5841), 1072–1076.
- (6) Lim, S. T.; Antonucci, D. E.; Scannevin, R. H.; Trimmer, J. S. A Novel Targeting Signal for Proximal Clustering of the Kv2.1 K<sup>+</sup> Channel in Hippocampal Neurons. *Neuron* **2000**, *25* (2), 385–397.
- (7) O’Connell, K. M. S.; Loftus, R.; Tamkun, M. M. Localization-Dependent Activity of the Kv2.1 Delayed-Rectifier K<sup>+</sup> Channel. *Proc. Natl. Acad. Sci. U. S. A.* **2010**, *107* (27), 12351–12356.
- (8) Horio, Y.; Hibino, H.; Inanobe, A.; Yamada, M.; Ishii, M.; Tada, Y.; Satoh, E.; Hata, Y.; Takai, Y.; Kurachi, Y. Clustering and Enhanced Activity of an Inwardly Rectifying Potassium Channel, Kir4.1, by an Anchoring Protein, PSD-95/SAP90. *J. Biol. Chem.* **1997**, *272* (20), 12885–12888.
- (9) Naundorf, B.; Wolf, F.; Volgushev, M. Unique Features of Action Potential Initiation in Cortical Neurons. *Nature* **2006**, *440* (7087), 1060–1063.
- (10) Freeman, S. A.; Desmazières, A.; Fricker, D.; Lubetzki, C.; Sol-Foulon, N. Mechanisms of Sodium Channel Clustering and Its Influence on Axonal Impulse Conduction. *Cell. Mol. Life Sci.* **2016**, *73* (4), 723–735.
- (11) Yellen, G. The Voltage-Gated Potassium Channels and Their Relatives. *Nature* **2002**, *419* (6902), 35–42.
- (12) Molina, M. L.; Barrera, F. N.; Fernández, A. M.; Poveda, J. A.; Renart, M. L.; Encinar, J. A.; Riquelme, G.; González-Ros, J. M. Clustering and Coupled Gating Modulate the Activity in KcsA, a Potassium Channel Model. *J. Biol. Chem.* **2006**, *281* (27), 18837–18848.
- (13) Sumino, A.; Yamamoto, D.; Iwamoto, M.; Dewa, T.; Oiki, S. Gating-Associated Clustering–Dispersion Dynamics of the KcsA Potassium Channel in a Lipid Membrane. *J. Phys. Chem. Lett.* **2014**, *5* (3), 578–584.
- (14) Yanagisawa, M.; Iwamoto, M.; Kato, A.; Yoshikawa, K.; Oiki, S. Oriented Reconstitution of a Membrane Protein in a Giant Unilamellar Vesicle: Experimental Verification with the Potassium Channel KcsA. *J. Am. Chem. Soc.* **2011**, *133* (30), 11774–11779.
- (15) Giudici, A. M.; Molina, M. L.; Ayala, J. L.; Montoya, E.; Renart, M. L.; Fernández, A. M.; Encinar, J. A.; Ferrer-Montiel, A. V.; Poveda, J. A.; González-Ros, J. M. Detergent-Labile, Supramolecular Assemblies of KcsA: Relative Abundance and Interactions Involved. *Biochim. Biophys. Acta - Biomembr.* **2013**, *1828* (2), 193–200.
- (16) Hegermann, J.; Overbeck, J.; Schrempf, H. In Vivo Monitoring of the Potassium Channel KcsA in *Streptomyces lividans* Hyphae Using Immunoelectron Microscopy and Energy-Filtering Transmission Electron Microscopy. *Microbiology* **2006**, *152* (9), 2831–2841.
- (17) Etzkorn, M.; Böckmann, A.; Lange, A.; Baldus, M. Probing Molecular Interfaces Using 2D Magic-Angle-Spinning NMR on Protein Mixtures with Different Uniform Labeling. *J. Am. Chem. Soc.* **2004**, *126* (45), 14746–14751.
- (18) Maciejko, J.; Mehler, M.; Kaur, J.; Lieblein, T.; Morgner, N.; Ouari, O.; Tordo, P.; Becker-Baldus, J.; Glaubitz, C. Visualizing Specific Cross-Protomer Interactions in the Homo-Oligomeric Membrane Protein Proteorhodopsin by Dynamic-Nuclear-Polarization-Enhanced Solid-State NMR. *J. Am. Chem. Soc.* **2015**, *137* (28), 9032–9043.
- (19) Weingarth, M.; Bodenhausen, G.; Tekely, P. Broadband Carbon-13 Correlation Spectra of Microcrystalline Proteins in Very High Magnetic Fields. *J. Am. Chem. Soc.* **2009**, *131* (39), 13937–13939.
- (20) Cuello, L. G.; Romero, J. G.; Marien Cortes, D.; Perozo, E. pH-Dependent Gating in the *Streptomyces lividans* K<sup>+</sup> Channel. *Biochemistry* **1998**, *37* (10), 3229–3236.
- (21) Van Dalen, A.; Hegger, S.; Killian, J. A.; De Kruijff, B. Influence of Lipids on Membrane Assembly and Stability

- of the Potassium Channel KcsA. *FEBS Lett.* **2002**, *525* (1–3), 33–38.
- (22) Cortes, D. M.; Perozo, E. Structural Dynamics of the Streptomyces Lividans K<sup>+</sup> Channel (SKC1): Oligomeric Stoichiometry and Stability. *Biochemistry* **1997**, *36* (33), 10343–10352.
- (23) Bajaj, V. S.; Mak-Jurkauskas, M. L.; Belenky, M.; Herzfeld, J.; Griffin, R. G. Functional and Shunt States of Bacteriorhodopsin Resolved by 250 GHz Dynamic Nuclear Polarization-Enhanced Solid-State NMR. *Proc. Natl. Acad. Sci. U. S. A.* **2009**, *106* (23), 9244–9249.
- (24) Jacso, T.; Franks, W. T.; Rose, H.; Fink, U.; Broecker, J.; Keller, S.; Oschkinat, H.; Reif, B. Characterization of Membrane Proteins in Isolated Native Cellular Membranes by Dynamic Nuclear Polarization Solid-State NMR Spectroscopy without Purification and Reconstitution. *Angew. Chemie Int. Ed.* **2012**, *51* (2), 432–435.
- (25) Koers, E. J.; Van Der Cruijisen, E. A. W.; Rosay, M.; Weingarth, M.; Prokofyev, A.; Sauvée, C.; Ouari, O.; Van Der Zwan, J.; Pongs, O.; Tordo, P.; et al. NMR-Based Structural Biology Enhanced by Dynamic Nuclear Polarization at High Magnetic Field. *J. Biomol. NMR* **2014**, *60* (2–3), 157–168.
- (26) Voinov, M. A.; Good, D. B.; Ward, M. E.; Milikisiyants, S.; Marek, A.; Caporini, M. A.; Rosay, M.; Munro, R. A.; Ljumovic, M.; Brown, L. S.; et al. Cysteine-Specific Labeling of Proteins with a Nitroxide Biradical for Dynamic Nuclear Polarization NMR. *J. Phys. Chem. B* **2015**, *119* (32), 10180–10190.
- (27) Liao, S. Y.; Lee, M.; Wang, T.; Sergeyev, I. V.; Hong, M. Efficient DNP NMR of Membrane Proteins: Sample Preparation Protocols, Sensitivity, and Radical Location. *J. Biomol. NMR* **2016**, *64* (3), 223–237.
- (28) Lehnert, E.; Mao, J.; Mehdipour, A. R.; Hummer, G.; Abele, R.; Glaubitz, C.; Tampé, R. Antigenic Peptide Recognition on the Human ABC Transporter TAP Resolved by DNP-Enhanced Solid-State NMR Spectroscopy. *J. Am. Chem. Soc.* **2016**, *138* (42), 13967–13974.
- (29) Becker-Baldus, J.; Bamann, C.; Saxena, K.; Gustmann, H.; Brown, L. J.; Brown, R. C. D.; Reiter, C.; Bamberg, E.; Wachtveitl, J.; Schwalbe, H.; et al. Enlightening the Photoactive Site of Channelrhodopsin-2 by DNP-Enhanced Solid-State NMR Spectroscopy. *Proc. Natl. Acad. Sci. U. S. A.* **2015**, *112* (32), 9896–9901.
- (30) Kaplan, M.; Narasimhan, S.; de Heus, C.; Mance, D.; van Doorn, S.; Houben, K.; Popov-Čeleketić, D.; Damman, R.; Katrukha, E. A.; Jain, P.; et al. EGFR Dynamics Change during Activation in Native Membranes as Revealed by NMR. *Cell* **2016**, *167* (5), 1241–1251.e11.
- (31) Weingarth, M.; van der Cruijisen, E. A. W.; Ostmeier, J.; Lievestro, S.; Roux, B.; Baldus, M. Quantitative Analysis of the Water Occupancy around the Selectivity Filter of a K<sup>+</sup> Channel in Different Gating Modes. *J. Am. Chem. Soc.* **2014**, *136* (5), 2000–2007.
- (32) van der Cruijisen, E. A. W.; Prokofyev, A. V.; Pongs, O.; Baldus, M. Probing Conformational Changes during the Gating Cycle of a Potassium Channel in Lipid Bilayers. *Biophys. J.* **2017**, *112* (1), 99–108.
- (33) Iwamoto, M.; Oiki, S. Amphipathic Antenna of an Inward Rectifier K<sup>+</sup> Channel Responds to Changes in the Inner Membrane Leaflet. *Proc. Natl. Acad. Sci.* **2013**, *110* (2), 749–754.
- (34) De Jong, D. H.; Singh, G.; Bennett, W. F. D.; Arnarez, C.; Wassenaar, T. A.; Schäfer, L. V.; Periole, X.; Tieleman, D. P.; Marrink, S. J. Improved Parameters for the Martini Coarse-Grained Protein Force Field. *J. Chem. Theory Comput.* **2013**, *9* (1), 687–697.
- (35) Van Den Bogaart, G.; Meyenberg, K.; Risselada, H. J.; Amin, H.; Willig, K. I.; Hubrich, B. E.; Dier, M.; Hell, S. W.; Grubmüller, H.; Diederichsen, U.; et al. Membrane Protein Sequestering by Ionic Protein-Lipid Interactions. *Nature* **2011**, *479* (7374), 552–555.
- (36) Periole, X.; Knepp, A. M.; Sakmar, T. P.; Marrink, S. J.; Huber, T. Structural Determinants of the Supramolecular Organization of G Protein-Coupled Receptors in Bilayers. *J. Am. Chem. Soc.* **2012**, *134* (26), 10959–10965.
- (37) van der Cruijisen, E. A. W.; Nand, D.; Weingarth, M.; Prokofyev, A.; Hornig, S.; Cukkemane, A. A.; Bonvin, A. M. J. M. J. J.; Becker, S.; Hulse, R. E.; Perozo, E.; et al. Importance of Lipid-Pore Loop Interface for Potassium Channel Structure and Function. *Proc. Natl. Acad. Sci.* **2013**, *110* (32), 13008–13013.
- (38) Huijbregts, R. P. H.; De Kroon, A. I. P. M.; De Kruijff, B. Topology and Transport of Membrane Lipids in Bacteria. *Biochim. Biophys. Acta - Rev. Biomembr.* **2000**, *1469* (1), 43–61.

- (39) Uysal, S.; Vasquez, V.; Tereshko, V.; Esaki, K.; Fellouse, F. A.; Sidhu, S. S.; Koide, S.; Perozo, E.; Kossiakoff, A. Crystal Structure of Full-Length KcsA in Its Closed Conformation. *Proc. Natl. Acad. Sci.* **2009**, *106* (16), 6644–6649.
- (40) Wassenaar, T. A.; Pluhackova, K.; Böckmann, R. A.; Marrink, S. J.; Tieleman, D. P. Going Backward: A Flexible Geometric Approach to Reverse Transformation from Coarse Grained to Atomistic Models. *J. Chem. Theory Comput.* **2014**, *10* (2), 676–690.
- (41) Lange, A.; Giller, K.; Hornig, S.; Martin-Eauclaire, M.-F.; Pongs, O.; Becker, S.; Baldus, M. Toxin-Induced Conformational Changes in a Potassium Channel Revealed by Solid-State NMR. *Nature* **2006**, *440* (7086), 959–962.
- (42) Sauvée, C.; Rosay, M.; Casano, G.; Aussenac, F.; Weber, R. T.; Ouari, O.; Tordo, P. Highly Efficient, Water-Soluble Polarizing Agents for Dynamic Nuclear Polarization at High Frequency. *Angew. Chemie Int. Ed.* **2013**, *52* (41), 10858–10861.
- (43) Lange, A.; Luca, S.; Baldus, M. Structural Constraints from Proton-Mediated Rare-Spin Correlation Spectroscopy in Rotating Solids †. *J. Am. Chem. Soc.* **2002**, *124* (33), 9704–9705.
- (44) Weingarh, M.; Demco, D. E.; Bodenhausen, G.; Tekely, P. Improved Magnetization Transfer in Solid-State NMR with Fast Magic Angle Spinning. *Chem. Phys. Lett.* **2009**, *469* (4–6), 342–348.
- (45) Hess, B.; Kutzner, C.; van der Spoel, D.; Lindahl, E. GROMACS 4: Algorithms for Highly Efficient, Load-Balanced, and Scalable Molecular Simulation. *J. Chem. Theory Comput.* **2008**, *4* (3), 435–447.
- (46)  $\llcorner$ ali, A. Comparative Protein Modeling by Satisfaction of Spatial Restraints. *Mol. Med. Today* **1995**, *1* (6), 270–277.
- (47) Dahlberg\*, M. Polymorphic Phase Behavior of Cardiolipin Derivatives Studied by Coarse-Grained Molecular Dynamics. **2007**.
- (48) Zhou, Y.; Morais-Cabral, J. H.; Kaufman, A.; Mackinnon, R. Chemistry of Ion Coordination and Hydration Revealed by a K<sup>+</sup> Channel-Fab Complex at 2.0 Å Resolution. *Nature* **2001**, *414* (6859), 43–48.
- (49) Periole, X.; Cavalli, M.; Marrink, S.-J.; Ceruso, M. A. Combining an Elastic Network With a Coarse-Grained Molecular Force Field: Structure, Dynamics, and Intermolecular Recognition. *J. Chem. Theory Comput.* **2009**, *5* (9), 2531–2543.
- (50) Ader, C.; Schneider, R.; Hornig, S.; Velisetty, P.; Wilson, E. M.; Lange, A.; Giller, K.; Ohmert, I.; Martin-Eauclaire, M.-F.; Trauner, D.; et al. A Structural Link between Inactivation and Block of a K<sup>+</sup> Channel. *Nat. Struct. Mol. Biol.* **2008**, *15* (6), 605–612.
- (51) Schneider, R.; Ader, C.; Lange, A.; Giller, K.; Hornig, S.; Pongs, O.; Becker, S.; Baldus, M. Solid-State NMR Spectroscopy Applied to a Chimeric Potassium Channel in Lipid Bilayers. *J. Am. Chem. Soc.* **2008**, *130* (23), 7427–7435.
- (52) Wylie, B. J.; Bhate, M. P.; McDermott, A. E. Transmembrane Allosteric Coupling of the Gates in a Potassium Channel. *Proc. Natl. Acad. Sci.* **2014**, *111* (1), 185–190.
- (53) Heginbotham, L.; LeMasurier, M.; Kolmakova-Partensky, L.; Miller, C. Single *Streptomyces lividans* K(+) Channels: Functional Asymmetries and Sidedness of Proton Activation. *J. Gen. Physiol.* **1999**, *114* (4), 551–560.
- (54) Gradmann, S.; Ader, C.; Heinrich, I.; Nand, D.; Dittmann, M.; Cukkemane, A.; van Dijk, M.; Bonvin, A. M. J. J.; Engelhard, M.; Baldus, M. Rapid Prediction of Multi-Dimensional NMR Data Sets. *J. Biomol. NMR* **2012**, *54* (4), 377–387.

# CHAPTER 6

## High-resolution NMR studies of antibiotics in cell membranes



## Abstract

The alarming rise of antimicrobial resistance requires antibiotics with unexploited mechanisms. Ideal templates could be antibiotics that target the peptidoglycan precursor lipid II, known as the bacterial Achilles heel, at an irreplaceable pyrophosphate group. Such antibiotics would kill multidrug-resistant pathogens at nanomolar concentrations without causing antimicrobial resistance. However, due to the challenge of studying small membrane-embedded drug–receptor complexes in native conditions, the structural correlates of the pharmaceutically relevant binding modes are unknown. Here, using advanced highly sensitive solid-state NMR setups, we present a high-resolution approach to study lipid II-binding antibiotics directly in cell membranes. On the example of nisin, the preeminent lantibiotic, we show that the native antibiotic-binding mode strongly differs from previously published structures, and we demonstrate that functional hotspots correspond to plastic drug domains that are critical for the cellular adaptability of nisin. Thereby, our approach provides a foundation for an improved understanding of powerful antibiotics.

*Based on the publication:*

João Medeiros-Silva, Shehrazade Jekhmane, Alessandra Lucini Paioni, Marc Baldus, Eefjan Breukink and Markus Weingarth

High-Resolution NMR Studies of Antibiotics in Cellular Membranes.

*Nature Communications*, **2018**, 9 (1), 3963.

## Introduction

The rapid growth of antimicrobial resistance (AMR) is a severe threat to global health. To date, AMR has been observed against all clinically used antibiotics, which is forecast to cause a staggering 10 million annual human deaths by year 2050.<sup>1</sup> It is hence of pressing need to develop antibiotics that operate via unexploited mechanisms and that are robust to resistance development.

Structural information is decisive for antibiotic design. However, resolving structural information that is relevant for drug development is complicated by the potentially critical influence of the medium on drug-binding modes. Structural data on antibiotic–receptor interactions are therefore ideally obtained under native conditions, which guarantees that the most relevant antibiotic state is studied. This tenet is of special importance for antimicrobial peptides (AMPs) that target bacterial membranes, which are media of enormous complexity. Most of these antibiotics are active in the micromolar concentration range and non-specifically target bacterial membranes. A smaller number of AMPs are active in the nanomolar concentration range, which is achieved by specifically targeting a membrane component such as the essential cell wall precursor lipid II.<sup>2</sup> These lipid II-binding compounds, such as vancomycin, plectasin,<sup>3</sup> tridecaptin,<sup>4</sup> or the recently discovered teixobactin,<sup>5</sup> can kill multidrug-resistant bacteria while resistance development is extraordinarily difficult. Native structural information is of particular relevance for antibiotics that target lipid II, whose accessibility and structure vary across bacteria,<sup>6,7</sup> which can modulate drug activity strongly.<sup>3,4,8</sup> However, structural data on lipid II-binding antibiotics are scarce and usually only available in artificial media such as micelles. Altogether, it is largely unknown how native conditions modulate membrane-binding antibiotics. This is because quantitative structural studies of small (10 kDa) drug–receptor complexes in cell membranes present major technical challenges that are yet to be overcome.

In principle, solid-state NMR (ssNMR) allows for structural studies directly in cell membranes.<sup>9–11</sup> However, native ssNMR studies are enormously challenging due to the low cellular concentration of the target system and the resulting poor spectral sensitivity. This problem is even more strongly exacerbated for cellular drug-binding studies with lipid II, whose minute native concentration cannot be increased recombinantly. In this work, using a state-of-the-art ssNMR approach that integrates the highly sensitive methods <sup>1</sup>H-detection and high-field dynamic nuclear polarization (DNP), we show high-resolution studies of an antibiotic–lipid II complex directly in cellular membranes on the example of the lantibiotic nisin.<sup>12</sup> Nisin employs a unique dual mode of antimicrobial action<sup>12</sup> and is effective against multidrug-resistant pathogens. Previous solution NMR studies in organic solvents reported a nisin:lipid II complex structure (1WCO),<sup>13</sup> which served as template for many drug design

efforts.<sup>14–17</sup> Here, we show that the native lipid II-bound state of nisin in cell membranes strongly differs from the previously published structure. We rationalize the native conformational space of lipid II-bound nisin and identify plastic domains that enable the antibiotic to adapt to the cellular environment. Intriguingly, these plastic domains correspond to pharmaceutical hotspots that allow to improve nisin’s activity, establishing a link between antimicrobial activity and cellular adaptability. These insights provide a foundation for design strategies for lipid II-targeting antibiotics and demonstrate the high potential of our native structural biology approach to obtain an improved understanding of antibiotics that target membrane constituents.

## Results

### *The nisin : Lipid II pore only forms in membranes*

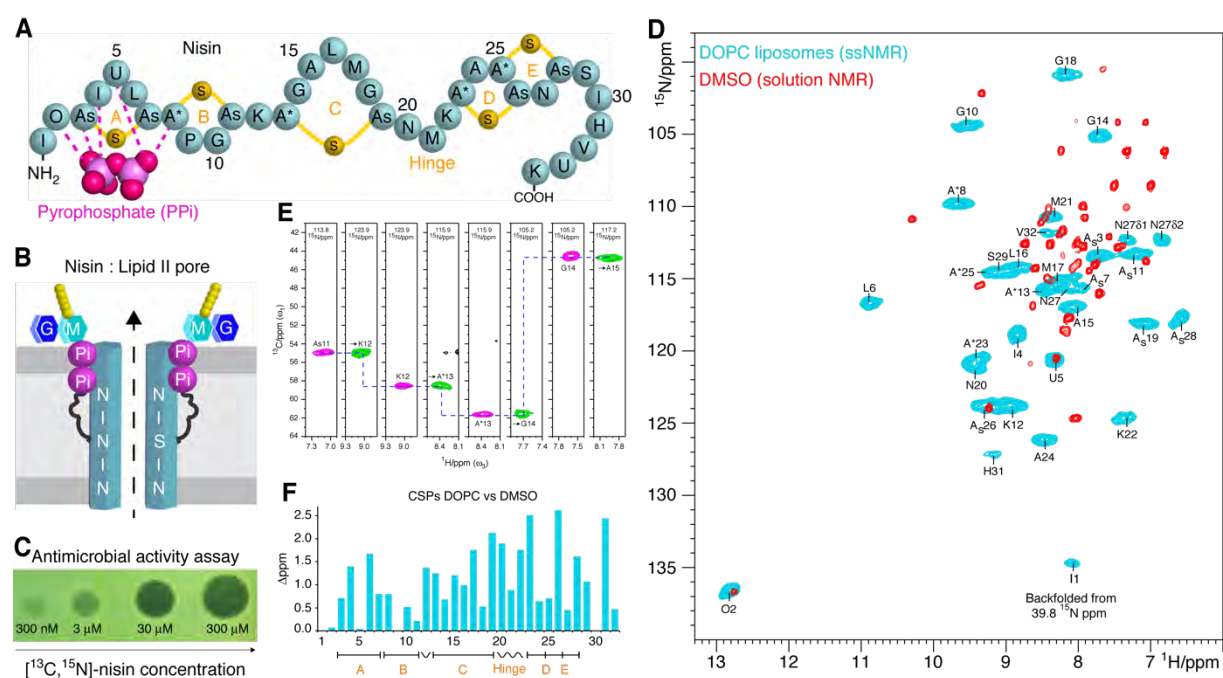


**Figure 1.** ssNMR experiments of the lipid II–nisin complex in DOPC liposomes. **A)** Illustration of the nisin Z peptide–antibiotic. The thio-ether rings are named A–E. Rings A–B are supposed to interact via five hydrogen bonds with lipid II.<sup>13</sup> The non-canonical residues A<sub>s</sub>, A\*, O, and U are described in Supplementary Figure S3A. **B)** Nisin and lipid II form a defined pore that spans the bacterial plasmamembrane. See Supplementary Figure S3B for the lipid II structure. **C)** A “spot-on-the-lawn” assay shows antimicrobial activity of [<sup>13</sup>C, <sup>15</sup>N]-labeled nisin. **D)** Overlay of <sup>1</sup>H-detected 2D <sup>15</sup>N–<sup>1</sup>H spectra of the nisin–lipid II complex in DOPC (blue) and DMSO (red). We measured the ssNMR spectrum of nisin bound to lipid II in the pore state (2:1 stoichiometry) in DOPC at 950 MHz (<sup>1</sup>H-frequency) and 60 kHz MAS. The solution NMR spectrum in DMSO was previously published<sup>13</sup> and shows a 1:1 nisin:lipid II complex. **E)** Sequential assignments of lipid II-bound nisin in liposomes. Strip plots are shown from 3D CANH (magenta) and CAcoNH (green) ssNMR experiments. **F)** Chemical shift perturbations (CSPs) comparing lipid II-bound nisin in DOPC and DMSO. CSPs were calculated according to  $CSP = \sqrt{(\Delta^1H)^2 + (\Delta^{15}N/6.51)^2}$ .

The heavily modified lantibiotic nisin (34 residues) is characterized by five thio-ether rings named A–E (Figure 1A). Nisin employs a unique antimicrobial dual mode of action that combines pore formation and inhibition of the peptidoglycan biosynthesis analogously to vancomycin.<sup>12</sup> These two functions are structurally separated. Via hydrogen bonds with the backbone amino protons, the N-terminal rings A–B directly bind lipid II at the pyrophosphate (PPi) group, thereby blocking the peptidoglycan synthesis.<sup>13</sup> The PPi group is deemed irreplaceable, and nisin is therefore highly robust against AMR development. The C-terminal part, containing rings D–E, is essential for the subsequent pore formation, in which eight nisin and four lipid II are assumed to span a hole across the plasmamembrane (Figure 1B).<sup>18</sup> N- and C-terminal domains are connected via a “hinge” linker, which is common to type A(I) lantibiotics.<sup>19</sup> The hinge is of high pharmacological interest, and mutations / extensions / deletions of hinge residues improve or reduce the pore-forming of nisin.<sup>15,16,20,21</sup> However, in the absence of high-resolution data for the pore, it is unknown how mutations modulate the native state of nisin, critically limiting its use as a template. The only information available is a nisin:lipid II complex solved in DMSO at a 1:1 stoichiometry.<sup>13</sup> Interestingly, the 2:1 stoichiometry, found in lipid membranes,<sup>18</sup> could not be detected in DMSO.

To investigate the structure of nisin bound to lipid II in the pore state, we first produced [<sup>13</sup>C, <sup>15</sup>N]-labeled nisin in the native nisin producer *Lactococcus lactis*. [<sup>13</sup>C, <sup>15</sup>N]-labeled nisin showed strong activity in standard assays (Figure 1C) and minimum inhibitory concentration (MIC) values comparable to previously reported values (see Supplementary Figure S4).<sup>22,23</sup> Afterwards, we co-assembled the nisin:lipid II pore at a 2:1 ratio in DOPC liposomes, and acquired a <sup>1</sup>H-detected 2D <sup>15</sup>N–<sup>1</sup>H spectrum with 60 kHz magic angle spinning (MAS) (Figure 1D). We could readily identify the spectrally well-separated signal of residue O2, which interacts with the PPi group and exhibits the same very high <sup>1</sup>H chemical shift of 12.85 ppm as in DMSO.<sup>13</sup> This demonstrates that nisin is bound to lipid II under our experimental conditions, which is also clearly evidenced by a lipid II-free control sample (Figure 2A). Lipid II-bound nisin featured sharp, well-resolved NMR signals in DOPC, implying an ordered pore state. Strikingly, the spectra of lipid II-bound nisin in DOPC and in DMSO drastically deviated (Figure 1D). To analyze this difference, we de novo assigned the backbone chemical shifts of lipid II-bound nisin in liposomes using 3D experiments (Figure 1E). The chemical shift perturbations (CSPs) profile that compares NMR signals in DOPC and DMSO indeed shows a marked overall conformational change in liposomes. The largest CSPs occur in the C-terminal rings D–E, which is likely diagnostic for pore formation in the DOPC membrane opposed to a non-pore state in DMSO. Moreover, we also observed stark CSPs for rings A–B, which strongly suggests that the critical interaction with the PPi group is altered in liposomes. Intriguingly, in liposomes, we could detect the N-terminal residue I1, which is of high importance for nisin’s activity for uncertain reasons,<sup>24,25</sup> and which remained invisible in

DMSO.<sup>13</sup> Altogether, we succeeded to capture the lipid II-bound state of nisin in the pore at high spectral resolution. Our data demonstrate that a previously solved structure<sup>13</sup> did not report on a physiologically relevant state. However, given that the medium strongly influences the conformation of lipid II-bound nisin (Figure 1D), we set out to extend our liposomal studies of the nisin:lipid II pore to cellular bacterial membranes.

### *The native nisin : Lipid II pore at high-resolution*

SSNMR studies in cellular membranes suffer from low molecular concentration, resulting in poor sensitivity. We recently demonstrated that <sup>1</sup>H-detection can provide the ssNMR sensitivity required to study recombinantly overexpressed proteins in cell membranes at physiological temperatures.<sup>26</sup> However, studying native lipid II–peptide interactions is much more challenging because the lipid II concentration is minute in bacterial membranes (0.5mol % compared to plasmamembrane phospholipids)<sup>27</sup> and cannot be increased recombinantly.

To study the native lipid II-bound state of nisin in the pore by <sup>1</sup>H-detected ssNMR, we added nisin to membrane vesicles derived from the Gram-positive bacterium *Micrococcus flavus*, a nisin-sensitive bacteria (MIC =  $2.7 \pm 0.75$  nM),<sup>22,23</sup> which contain all inherent membrane components (lipids, proteins, and other biomolecules).<sup>27</sup> Our sample contained ~25 μg, i.e., less than 10 nmol of antibiotic. Despite of this 15–20-fold concentration reduction compared to the DOPC sample, we could acquire a sensitive 2D <sup>15</sup>N–<sup>1</sup>H spectrum of lipid II-bound nisin (Figure 2A). The native spectrum reproduced our DOPC data, and we could annotate most signals, strongly suggesting that we had captured the native state of lipid II-bound nisin in the pore in both membrane systems. However, subtle differences, which we discuss below, between the spectra of the two membrane systems indicated that the cellular environment modulates the pore conformation. We also detected a second set of signals, which can be seen by the signals splitting for G14 and A<sub>s</sub>28. As it became clear from a negative control spectrum in DOPG/DOPC without lipid II (Fig. 2a, in gray), these signals originate from nonspecifically bound nisin, present in slight excess over lipid II, whose exact native concentration is difficult to measure. Note that anionic lipids were used to enhance non-specific binding in the control sample.<sup>28</sup>

Despite the simultaneous presence of lipid II-bound and nonspecifically attached nisin, a number of residues (O2, A<sub>s</sub>3, I4, U5, L6, G10, A<sub>s</sub>11, K12, G14, A<sub>s</sub>19, K22, and A<sub>s</sub>28) give unambiguous signals for the native state of lipid II-bound nisin. Interestingly, the amino group of residue I1 was not detectable. This suggests that the I1 amino group has a high mobility, given that we used dipolar ssNMR experiments, in which signal sensitivity decreases with increased dynamics. Generally, rings A–B (O2–G10) showed marginal CSPs in cell membranes compared to DOPC, which is in agreement with their tight interaction with the PPI group, rendering these rings less susceptible to the medium. Exceptions were residues L6

and especially I4, which both showed  $^{15}\text{N}$  CSPs between 0.6 and 1.0 ppm. Furthermore, the  $^1\text{H}$ -signals of residues L6, G10, and A\*8 were broadened, potentially due to heterogeneous PPI interactions. Ring C (A\*13–A<sub>s</sub>19) showed clear CSPs in cellular membranes, which are most notable for G14 and A<sub>s</sub>19. Further CSPs for L16–M17 are consistent with the native spectrum but could not be unambiguously resolved. This suggests that the cellular membrane subtly changes the C ring conformation, which is essential for nisin activity for unexplained structural reasons.<sup>29</sup>

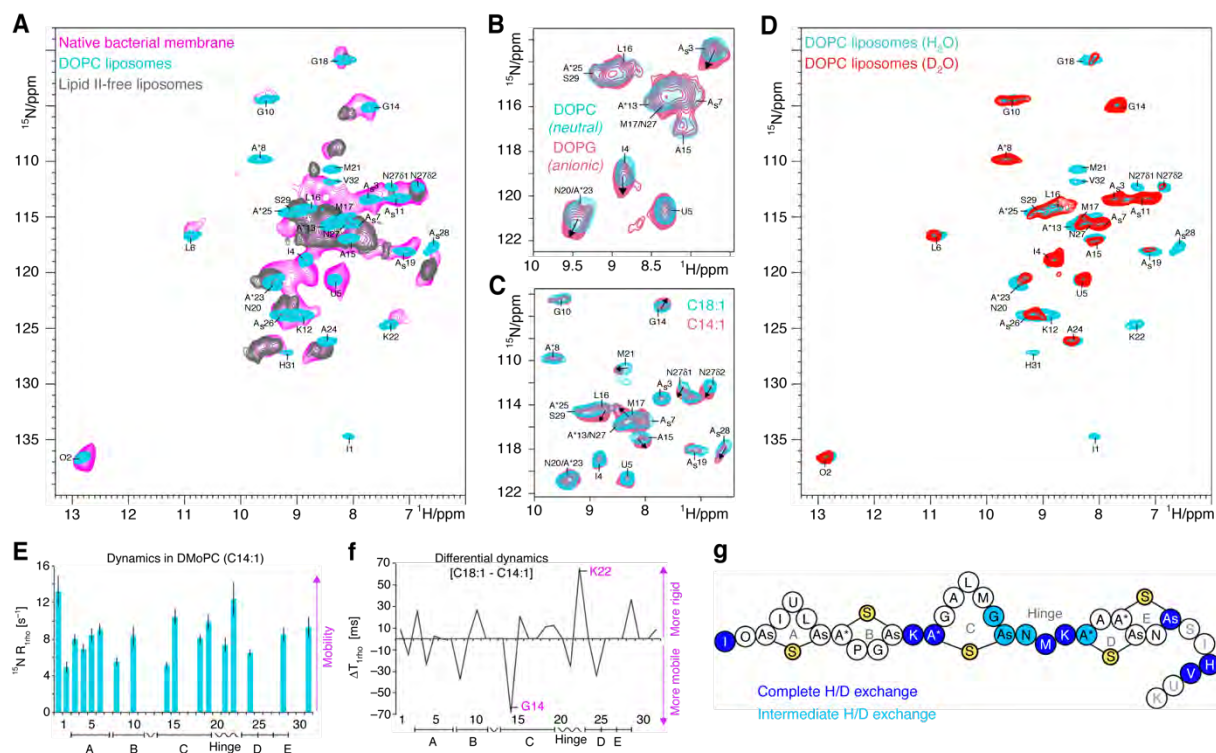


**Figure 2.** The lipid II–nisin complex in cellular membranes. **A)** Comparison of  $^1\text{H}$ -detected 2D  $^{15}\text{N}$ – $^1\text{H}$  spectra of lipid II-bound nisin in native *M. flavus* membranes (magenta) and in DOPC (cyan). The gray spectrum shows nisin non-specifically bound to DOPG:DOPC liposomes (7:3 ratio) in the absence of lipid II. **B)** Overlay of 2D  $^{15}\text{N}$ – $^1\text{H}$  spectra of lipid II-bound nisin acquired in zwitterionic DOPC (cyan) and anionic DOPG:DOPC (7:3 ratio) (pink) liposomes. **C)** Overlay of 2D  $^{15}\text{N}$ – $^1\text{H}$  spectra of lipid II-bound nisin acquired in C18:1 DOPC (cyan) and C14:1 DMOPC (pink) liposomes. **D)**  $^1\text{H}/^2\text{H}$  exchange: 2D  $^{15}\text{N}$ – $^1\text{H}$  spectra of lipid II-bound nisin acquired in DOPC in fully protonated (cyan) and deuterated (red) buffers. **E)**  $^{15}\text{N}$   $R_{1\rho}$  relaxation rates of lipid II-bound nisin acquired in DOPC. The error bars indicate the standard deviation of the fit. **F)** Differential  $^{15}\text{N}$   $T_{1\rho}$  times comparing dynamics in C18:1 DOPC and C14:1 DMOPC liposomes. **G)**  $^1\text{H}/^2\text{H}$  ssNMR exchange results. Dark and light blue beads represent residues that showed complete and intermediate exchange in deuterated buffers, respectively. Residues S29/I30 and U33/K34 could not be analyzed due to spectral overlap and fast dynamics, respectively.

Intriguingly, the hinge (N20–K22) and C-terminal domain (A\*23–A<sub>s</sub>28), which form the actual transmembrane (TM) pore, featured consistent signal shifts in the cellular membrane compared to DOPC. The hinge is the only TM element that is not restraint in thio-rings and

is assumed to play a special role.<sup>30</sup> Drug development efforts have concentrated on the hinge, yielding nisin derivatives with enhanced bioactivity.<sup>14–16</sup> The hinge residues and A\*23–A24 in direct proximity, showed clear CSPs in cellular membranes. Intriguingly, M21 either strongly shifted or disappeared in the cellular spectrum due to increased mobility. Altogether, this suggests that the hinge is plastic and important for the adaption of nisin : lipid II pore to bacterial membranes. Furthermore, also the pore-forming rings D–E are sensitive to the membrane environment, as shown by the marked CSP of residue A<sub>5</sub>28. Residues H31–V32 disappeared in the dipolar-based cellular spectrum, pointing to an increased mobility of the C terminus.

#### *Adaptation of the pore structure to native environment.*

The differences between the spectra from DOPC or *M. flavus* membranes indicate that the nisin pore structure adapts to the membrane environment. A likely source of this modulation is the complex composition of lipid tails and headgroups in cellular *M. flavus* membranes. In the following, we investigated the impact of the membrane composition on the conformation and dynamics of lipid II-bound nisin, focusing on two key aspects, i.e., bilayer charge and thickness. Furthermore, we varied the length of the prenyl-chain of lipid II.

Gram-positive membranes generally are highly enriched in anionic lipids that constitute usually >50% of the bilayer.<sup>31</sup> To test the effect of an anionic bilayer, we acquired ssNMR data of the lipid II-bound state of nisin in the pore in mixed liposomes composed of anionic DOPG and zwitterionic DOPC lipids (Figure 2B). Globally, the ssNMR spectrum shows that nisin is only weakly modulated by the membrane charge, in agreement with its high specificity for lipid II<sup>20</sup>. Nonetheless, we observed smaller but clear <sup>15</sup>N CSPs around 0.5–1 ppm for residues A<sub>5</sub>3–I4, which correspond in direction and magnitude to the signal perturbations in *M. flavus* membranes. This means that ring A at the membrane–water interface is modulated by anionic lipids in cell membranes. Interestingly, this observation agrees with mutagenesis studies that showed that replacing I4 by a cationic residue favorably affects nisin’s activity.<sup>32</sup> Equally interesting, also residues N20 and A\*23–A24 at and around the hinge showed significant CSPs in anionic membranes. These residues all showed significant CSPs in *M. flavus* vesicles. Given that the hinge is most likely located in the membrane core and not directly interacting with lipid headgroups,<sup>33</sup> these findings suggest that the hinge conformations change in order to adapt the pore structure to the membrane charge.

Membrane thickness has been shown to be very important for the pore-forming activity of some lantibiotics.<sup>34,35</sup> Micrococcal membranes contain mainly branched C15:0 fatty acids and are therefore thinner compared to a DOPC bilayer. To explore the modulatory influence of the bilayer thickness, we acquired spectra of the lipid II-bound state of nisin in the pore in liposomes formed of C14:1 DMoPC that is much shorter compared to DOPC (18:1) (Figure

2C). While rings A–B, that are not in contact with the lipid tails, did not show CSPs in DMOPC, almost all residues of ring C (e.g., G14 and A15) showed CSPs in the thinner membrane, and these CSPs are consistent with the cellular *M. flavus* spectrum (Figure 2A). Equally in agreement with the cellular spectrum, residues N27–A<sub>s</sub>28 of the TM part also exhibited clear CSPs in DMOPC. To better rationalize these signal changes, we acquired <sup>15</sup>N T<sub>1rho</sub> ssNMR relaxation data in order to compare the mobility of the nisin pore in DOPC and DMOPC liposomes (Figure 2E,F). From this comparison, we sought to understand if the membrane thickness modulates the conformational dynamics of the pore structure. We observed a striking stiffening of G14 of ring C in DMOPC, which correlated with a stark mobility increase of K22 in the hinge. This corroborates our observation that the hinge is plastic, and suggests that the hinge conformation is coupled to the functionally critical<sup>29</sup> conformation of the adjacent C ring. Moreover, the C-terminal A<sub>s</sub>28 showed enhanced dynamics in DMOPC, which agrees with the reduced thickness of DMOPC membranes and corroborates our conclusion that the nisin C terminus pierces through the membrane surface. The enhanced C terminus mobility also explains the absence of the H31–V32 signals in *M. flavus* vesicles.

The dodecaprenyl-(C55) prenyl-chain of lipid II is highly conserved in bacteria. Since we used a slightly shorter heptaprenyl-(C35) lipid II for ssNMR measurements in DOPC liposomes, the longer length of the C55-prenyl-chain in the native *M. flavus* membrane could potentially modulate our cellular ssNMR spectra. However, such an influence is not likely, given that previous leakage studies strongly suggest that the tail of the prenyl-chain is neither involved in pore formation nor interacts with nisin.<sup>23</sup> Indeed, the nisin:(C35)–lipid II and nisin:(C55)–lipid II complexes give exactly the same 2D NH spectra in DOPC liposomes (Supplementary Figure S2).

### *Linker regions enable the cellular adaptability of the pore*

So far, our results pointed to an important role of the hinge plasticity, which may be required for the adaption of the pore to the thickness and charge of the target membrane. In a pore structure, this may mean that the hinge would be accessible by the water phase through the pore lumen. Provided the hinge is not involved in strong inter- or intramolecular interactions, which is expected as it needs to stay flexible, the hinge residues should be sensitive to deuterium exchange.<sup>26,36,37</sup> Indeed, after 1d of incubation in deuterated buffers, signal of G18–A24 around the hinge had either disappeared or showed strongly decreased intensity in a 2D <sup>15</sup>N–<sup>1</sup>H spectrum (Figure 2D,G). This demonstrates that the hinge has the required conformational flexibility to enable the adaption of the pore structure to the cellular environment, and it also demonstrates that hinge residues line the pore lumen. Surprisingly, we also observed a complete exchange of K12, and most likely A\*13, that link rings B–C. This

suggests that these residues also line the pore lumen, and that the orientation between rings B and C exhibits some degree of flexibility, matching with the rearrangement of ring C that we observed in *M. flavus* membranes and shorter lipids (Figure 2A,C). Notably, just like the hinge, residue K12 was identified as pharmaceutical hotspot.<sup>38</sup> Altogether, this shows that drug domains of high functional significance relate to nisin's plasticity.

Residues O2–G10 did not exchange in deuterated buffers, which is in excellent agreement with the direct interaction of rings A–B with the PPI group, protecting them from <sup>1</sup>H/<sup>2</sup>H exchange. Surprisingly, the critical residue I1,<sup>24</sup> thought to tightly interact with the PPI group,<sup>25</sup> disappeared in deuterated buffers. This result makes a strong hydrogen bond between I1 and the PPI group unlikely. To further investigate the role of the I1 amino group, we measured the nanosecond dynamics (<sup>15</sup>N T<sub>1</sub>) of lipid II-bound nisin in DOPC, which indeed confirmed the high flexibility of the I1 amino group (Supplementary Figure S1), and which also explains the absence of the I1 amino group in cellular conditions (Figure 2A).

#### *The nisin - Lipid II complex as seen by DNP ssNMR*

With the data presented so far, we could capture the native lipid II-bound state of nisin in the pore and rationalize the influence of cellular membranes on nisin's lipid II-binding mode. However, the <sup>1</sup>H-detected cellular spectrum did not allow investigating all nisin residues, and did not provide side chain data, which can often be critical for drug binding. In order to obtain this complementary information, we sought to use DNP enhancement, which can boost the NMR signals of biomolecules by orders of magnitude.<sup>39–46</sup> Combined with a high-field 800 MHz magnet,<sup>47,48</sup> we envisioned that DNP would provide sufficient sensitivity and resolution to study the nisin pore in cell membranes. Therefore, we used a similar sample preparation as for cellular <sup>1</sup>H-detection, where we could clearly detect the native state of nisin in the pore. We obtained a DNP enhancement  $\epsilon$  of 8 in *M. flavus* vesicles, which enabled the acquisition of a well-resolved 2D <sup>13</sup>C–<sup>13</sup>C spectrum of the lipid II-bound state of nisin in the pore in 4 days of measurement time (Figure 3).

Given that DNP measurements require very low temperatures (100 K), we first explored the impact of cryogenic temperatures in order to subsequently study the influence of cellular membranes on the nisin:lipid II pore. This is because at 100 K, conformational dynamics can result in signal broadening and solvents effects can lead to signal shifts.<sup>49–52</sup> Thereby, DNP spectra can provide valuable information on molecular motions and surface exposure. We first acquired a so-called 2D <sup>13</sup>C–<sup>13</sup>C “spin diffusion” experiment at 280 K in DOPC to assign the nisin side chain <sup>13</sup>C signals (Figure 3A, in blue). <sup>13</sup>C-signals of residues I1–V32 could be fully assigned (see Supplementary Figure S5 and Supplementary Table1). Notably, while the C-terminal residues I30–K34 gave only faint signals at 280 K temperature; we could detect these residues at 250 K (Figure 3G). This confirms the enhanced dynamics of the C terminus

that we observed in the  $^1\text{H}$ -detected *M. flavus* spectrum, implying that C terminus sticks out of the membrane.

After obtaining the  $^{13}\text{C}$ -assignments, we acquired a DNP-enhanced 2D  $^{13}\text{C}$ - $^{13}\text{C}$  experiment of lipid II-bound nisin in DOPC at 800 MHz and 100 K as reference spectrum (Figure 3A, in orange), and compared it to the same type of spectrum acquired in cell membranes (Figure 3B, magenta). The DNP spectrum in DOPC was of appealing resolution, and globally followed the room temperature (280 K) spectrum closely, which enabled us to analyze most signals at DNP conditions. Figure 3C shows the ( $\text{C}\alpha + \text{C}\beta$ ) CSPs in DOPC membranes comparing 280 K and cryogenic (100 K) DNP conditions, which enables us to study which side chains are water-exposed or conformationally heterogeneous. While most nisin residues show minor signal shifts, we see clear maxima for O2 and I4, which is similar in the cellular DNP spectrum. These CSPs likely relate to hydration effects, since ring A presumably localizes on top of the membrane.<sup>13</sup> Note that we also verified with further 2D measurements at 280 K that these CSPs relate to the cryogenic temperatures and are not caused by the DNP radical.<sup>53</sup> Surprisingly, while I4 showed CSPs and signal broadening, the I1 side chain featured intense, defined signals in both DOPC and cellular DNP spectra. This suggests that the I1 side chain is rigid and water shielded in the native pore. This assumption could be further corroborated in a series of dipolar-based 2D spectra at 280 K, showing a much faster built-up for I1 side chain signals compared to I4 (Figure 3F). This suggests that the I1 side chain, rather than the backbone, may be important for nisin's pore structure. Note that highly conserved<sup>32</sup> residue P9 showed intense signals without CSPs in DNP spectra in DOPC and *M. flavus* membranes, demonstrating that the ring B conformation is highly defined, which is presumably critical for efficient PPI binding. Intriguingly, the hinge and adjacent residues like A\*23 showed strongly decreased intensities due to signal broadening at DNP conditions in DOPC, which was even exacerbated in cellular membranes (Figure 3E). This again demonstrates the conformational heterogeneity of the hinge, which is in very good agreement with our  $^1\text{H}$ -detected experiments. Notably, the A\*13 signals disappeared on both sides of the diagonal in the cellular DNP spectrum, while these signals were visible in DOPC. This broadening most likely relates to an increased conformational plasticity of residues K12–A\*13 that connect ring C to the PPI-binding motif, which is in excellent agreement with the absence of these residues in  $^1\text{H}/^2\text{H}$  exchange experiments. This highlights that ring C is modulated by the membrane complexity, as we showed above (Figure 2C). Furthermore, at 100 K, residue S29 showed severe line broadening in DOPC and cellular membranes, confirming that the C terminus is dynamically disordered in the native pore. This finding, yet again, underscores the importance of flexible regions for nisin's activity, given that mutations of S29 increase nisin's activity.<sup>54</sup>

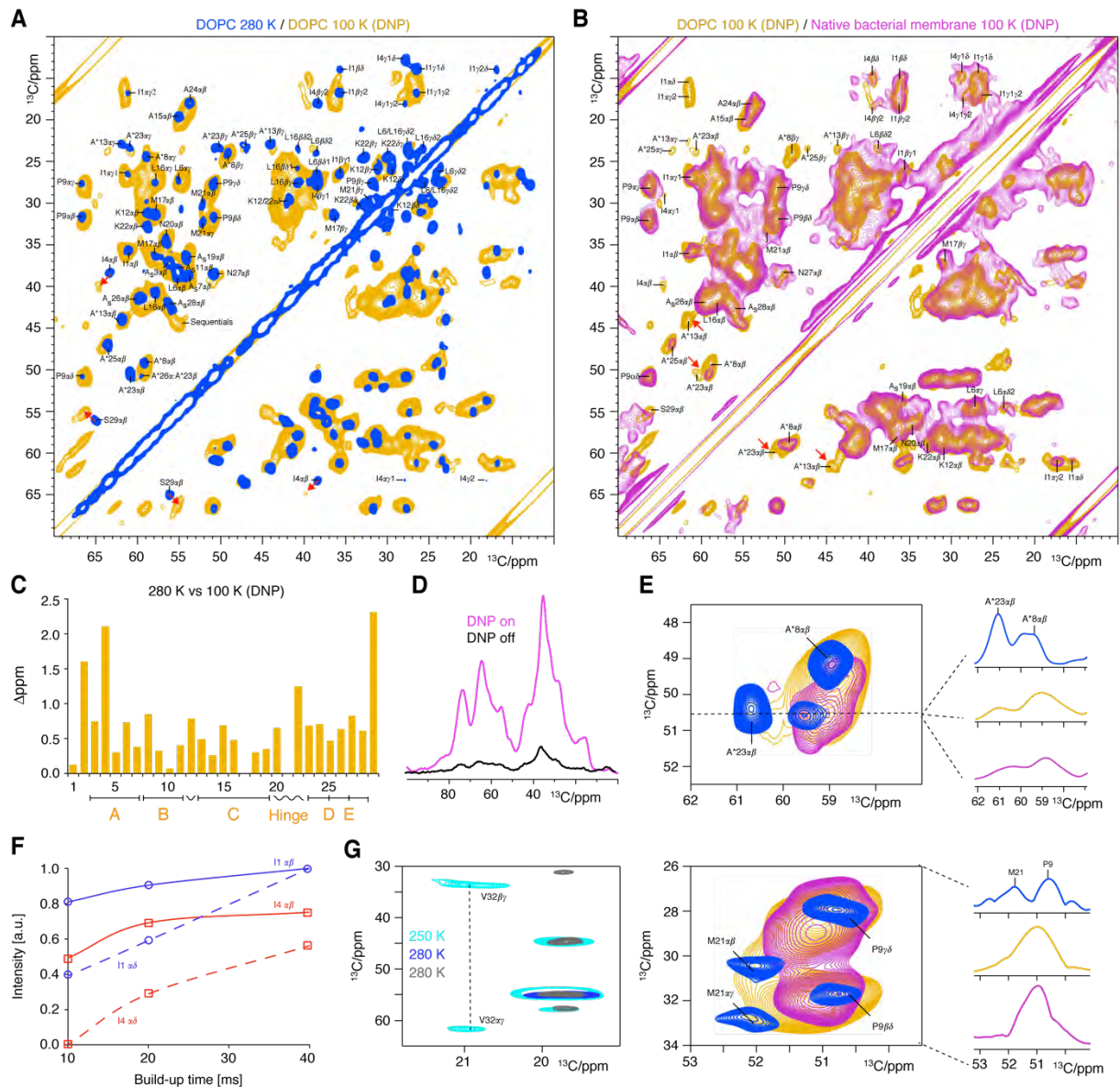


**Figure 3.** DNP-enhanced ssNMR on the lipid II-bound state of nisin in the pore. **A)** 2D  $^{13}\text{C}$ - $^{13}\text{C}$  ssNMR spin diffusion spectra of the lipid II-bound state of nisin in the pore in DOPC acquired at 280 K sample temperature (blue) and at 100 K with DNP enhancement (orange). Red arrows highlight strong CSPs. **B)** Overlay of DNP-ssNMR 2D  $^{13}\text{C}$ - $^{13}\text{C}$  spectra of nisin in the pore acquired in DOPC (orange) and in cellular *M. flavus* vesicles (magenta). Both spectra were acquired at identical conditions using 10.6 kHz MAS, 800 MHz and 40 ms  $^{13}\text{C}$ - $^{13}\text{C}$  mixing. **C)** Combined (Ca + C $\beta$ ) CSPs comparing lipid II-bound nisin in DOPC at 280 K against 100 K temperature (DNP conditions). **D)**  $^{13}\text{C}$  cross-polarization spectra of lipid II-bound nisin in *M. flavus* vesicles with (magenta) and without (black) DNP enhancement. **E)** The hinge domain is conformationally flexible and broadens out at DNP conditions in DOPC (orange). This is even more pronounced in cellular membranes (magenta). Upper panel: (left) zoom into A\*23 adjacent to the hinge; (right) slice through the A\*23 $\alpha\beta$  signal. Lower panel: (left) zoom into M21; (right) projection along the indirect dimension (26–34  $^{13}\text{C}$  ppm). **F)**  $^{13}\text{C}$ - $^{13}\text{C}$  PSDS spin diffusion buildup curves of the Ca $\beta$  (continuous lines) and Ca $\delta$  (dashed lines) cross-peaks for residues I1 (in blue) and I4 (red). **G)** The mobile nisin C terminus gives faint signals in dipolar 2D  $^{13}\text{C}$ - $^{13}\text{C}$  spectra at 280 K (in gray and dark blue with 100 ms and 30 ms  $^{13}\text{C}$ - $^{13}\text{C}$  mixing, respectively), while stronger signals appear at 250 K (in cyan, 50 ms mixing).

## Discussion

Antimicrobial resistance is a severe problem and the development of antibiotics is of high urgency. Drugs that target lipid II, the bacterial “Achilles heel,” are promising templates for next-generation antibiotics that are robust against AMR.<sup>2</sup> However, the native, i.e., pharmaceutically relevant binding modes of these drugs are scarcely understood because the major technical challenges to study small drug–receptor complexes in cell membranes at the atomic level are yet to be overcome. In the present study, we introduced a cutting-edge ssNMR approach that enables comprehensive high-resolution studies of antibiotic–lipid II complexes directly in native bacterial membranes. We demonstrated our approach on the example of the lantibiotic nisin, which uses a unique dual mode of action of targeted pore formation and vancomycin-like blockage of the peptidoglycan synthesis.

A previous solution NMR study in DMSO already provided a nisin:lipid II complex structure,<sup>13</sup> which has been the gold standard for the structural understanding of nisin and similar lantibiotics. The present ssNMR data conclusively showed that the conformation of lipid II bound nisin is drastically different in membranes, i.e., the physiologically / pharmacologically relevant environment. De novo ssNMR assignments demonstrated that the membrane environment markedly modulates the nisin:lipid II complex structure, which is because nisin forms a pore complex with lipid II in membranes, as opposed to a non-pore state in DMSO (Figure 1D,F).

Given the marked influence of the membrane environment on the binding mode, it seemed plausible that the functional state of the nisin pore is modulated by the cellular membrane complexity. Therefore, as a next step, using <sup>1</sup>H-detected ssNMR, we could acquire a spectrum of the lipid II-bound state of nisin in the pore directly in native *M. flavus* membranes at physiological temperatures (Figure 2A). The obtained cellular spectrum globally reproduced our data in DOPC, and demonstrated that we had discovered the functional state of the pore. Intriguingly, we observed that specific regions of lipid II-bound nisin were modulated by cellular conditions (Figure 4A). Using studies in different membrane types, we showed that the membrane compositions modulate the conformational space of nisin. This modulation is especially visible around the linker K12 and the hinge N20–K22 that connect both lipid II-binding and pore-forming functional motifs of nisin. Using <sup>1</sup>H/<sup>2</sup>H exchange experiments, we showed that these linker domains are not involved in strong intermolecular interactions, which is required for the plasticity of the linkers (Figure 2D,E). These observations could be confirmed in high-field DNP-enhanced experiments in native bacterial membranes, where signals of linker domains and the C terminus exhibited severe signal broadening due to conformational heterogeneity. Intriguingly, the linker domains and the C terminus were identified as pharmacological hotspots,<sup>15,32,38,54</sup> and modifications of these plastic elements can

strongly increase nisin's bioactivity, even against Gram-negative pathogens (Figure 4B).<sup>14, 54</sup> Thereby, our study suggests that these flexible linker regions are critical for nisin to adapt to the target membrane of a given bacterium. This is in excellent agreement with a recent study that indicated that substitutions/ extensions of the linker domains change the bioactivity of nisin in a strain-specific manner.<sup>30</sup> Furthermore, our <sup>1</sup>H/<sup>2</sup>H exchange experiments demonstrate that hinge residues line the pore lumen, which provides the first high-resolution topological insights in the hitherto elusive pore state (Figure 4A).

Our studies also conclusively showed that the nisin ring A, and especially the conserved ring B,<sup>32</sup> are least modulated by the environment, which is consistent with nisin's high specificity for the PPI group. Surprisingly, <sup>1</sup>H/<sup>2</sup>H exchange studies and measurements of nisin's dynamics suggest that the critical residue I1 does not engage in strong hydrogen bonding with the PPI group.<sup>13, 25</sup> While we cannot rule out that the N-terminal I1 amino group transiently interacts with the PPI group, our data hint at an important role for the I1 side chain, which adopts a well-defined and presumably water-shielded conformation in the native nisin pore (Figure 3). This assumption is supported by mutational studies that showed a twofold activity reduction upon replacing I1 by a tryptophan.<sup>55</sup>

## Conclusion

To summarize, our native structural study provides high-resolution insights into the dual activity of the preeminent lantibiotic nisin. Given the uniqueness of nisin's binding mode, its high activity and robustness against AMR development, the use of nisin as a template could be a promising strategy for the construction of antibiotics. As demonstrated in this work, the combination of advanced highly sensitive ssNMR methods paves the way to obtain comprehensive molecular insights into small antibiotic-receptor complexes in a cellular membrane environment. Such native studies may be particularly important to understand the pharmaceutically relevant states of lipid II-binding drugs with a high exposure to the membrane surface.<sup>3,5</sup>

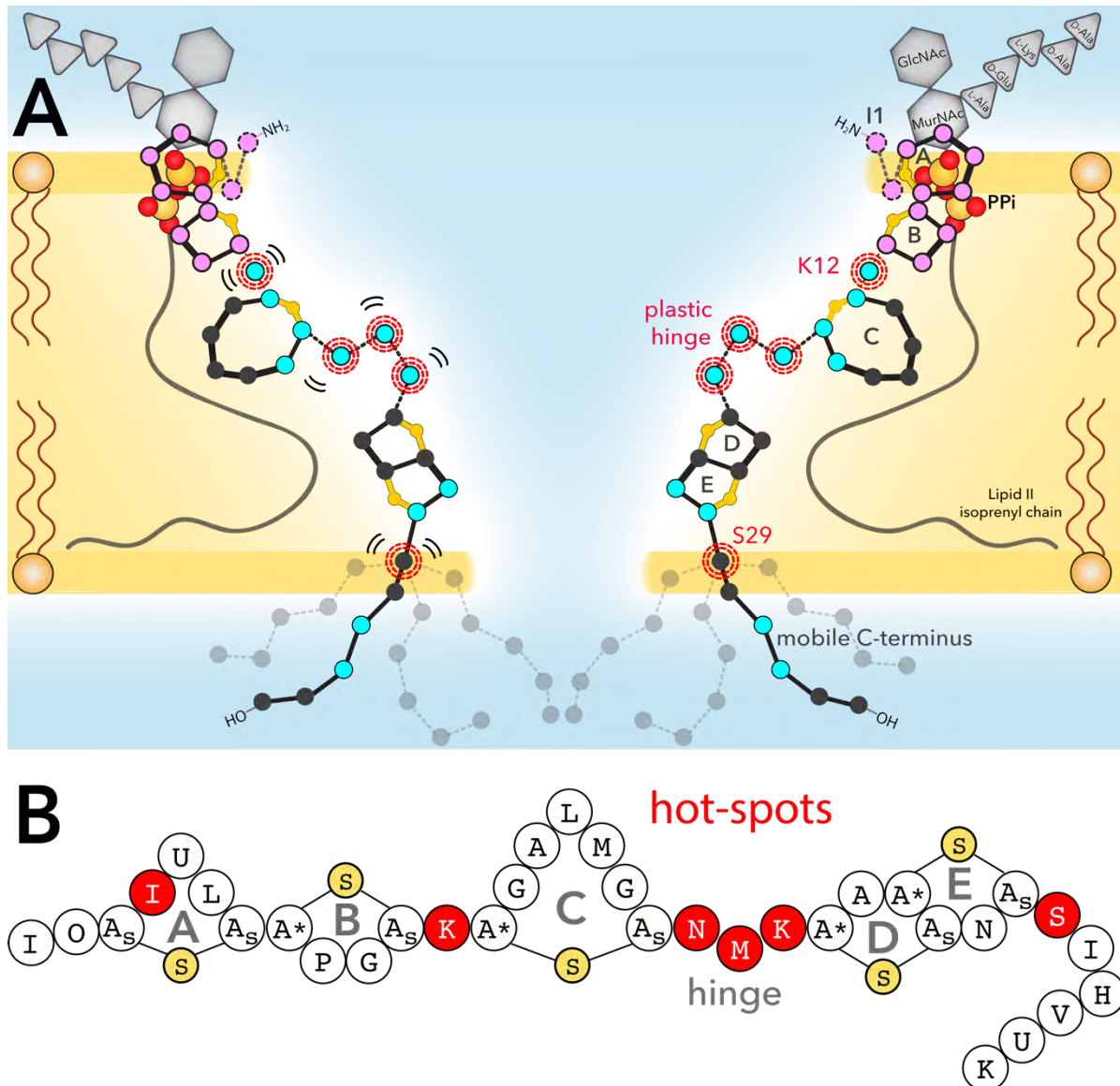


**Figure 4.** The nisin:lipid II pore topology. **A)** Membrane arrangement of the nisin:lipid II topology as seen by ssNMR. Plastic residues that are required to adapt to the bacterial target membrane are highlighted with red circles. Residues that showed  $^1\text{H}/^2\text{H}$  exchange are colored in blue and align the pore lumen. The C terminus is dynamically disordered and resides at the water–membrane interface. The A–B rings (in magenta) interact with the lipid II PPi group. **B)** Residues I4,<sup>32</sup> K12,<sup>38</sup> N20–K22,<sup>15,16,20,21,30</sup> and S29<sup>54</sup> are pharmaceutical hotspots that enable to improve nisin’s activity upon mutation. These residues were all identified as important for nisin’s cellular adaptability in this study.

## Materials and Methods

### *Sample preparation*

The *Lactococcus lactis* NIZO 22186 strain carrying the *nisZ* gene was used for nisin production. Uniformly labeled [ $^{13}\text{C}$ , $^{15}\text{N}$ ]-nisin Z was obtained using [ $^{13}\text{C}$ , $^{15}\text{N}$ ]-enriched medium.<sup>56</sup> Nisin was extracted from the growth medium using Amberlite XAD-16N (Sigma-Aldrich) resin and purified with RP-HPLC (Discovery C18, L.  $\times$  I.D. 150 mm  $\times$  2.1 mm, 5  $\mu\text{m}$  particle size). The column was equilibrated with [ $\text{H}_2\text{O}$  95:5 ACN, 0.05% TFA] and elution was carried out with a linear gradient 50–100% of [ACN 95:5  $\text{H}_2\text{O}$ , 0.05% TFA] at RT and 0.75 ml flow rate. The absorbance of the eluent was monitored at 214 nm and the fractions containing nisin were subsequently lyophilized. The presence and purity of nisin in the eluted fractions was confirmed by ESI-MS (Finnigan LCQ Deca XP). See Figure S4 for an HPLC elution profile and an ESI ionization trace. The concentration of nisin was measured using the Micro BCA Protein Assay (Thermo Scientific) and cross-validated by  $^1\text{H}$ -solution NMR using DSS as an internal standard. Accordingly, the specific absorbance for nisin Z at 220 nm was  $1.214 \text{ mg}^{-1} \text{ ml mm}^{-1}$  in 0.05% acetic acid solution.

Antimicrobial activity of nisin was monitored by a bioassay against *Staphylococcus simulans* 22 (Figure 1C). Accordingly, *S. simulans* was grown in TSB medium (Sigma-Aldrich) at 37  $^\circ\text{C}$  under aerobic conditions. Bacteria were seeded at 1% dilution into soft TSB agar medium (0,6% agar, cooled to 37  $^\circ\text{C}$ ), plated and dried. Aliquot of 10  $\mu\text{l}$  of each test sample was pipetted onto surface of the seeded agar plate, which was afterward dried and incubated overnight at 37  $^\circ\text{C}$ . The test samples containing nisin were prepared in Tris buffer (15 mM Tris-HCl, 25 mM NaCl, pH 7.0).

Lipid II (lysine form) was purified using published protocols,<sup>23</sup> using heptaprenyl-phosphate as the polyisoprenyl substrate, as this guarantees optimal pore formation by nisin in DOPC membranes.<sup>23</sup>

Phospholipids 1,2-dioleoyl-sn-glycero-3-phosphocholine (C18:1, DOPC), 1,2-dimyristoleoyl-sn-glycero-3-phosphocholine (C14:1, DMOPC), and 1,2-dioleoyl-sn-glycero-3-phosphoglycerol (C18:1, DOPG) were purchased from Avanti Polar Lipids, Inc.

Dry lipid films containing the lipid II/phospholipids mixture (4% mol/mol) were hydrated by vortexing with 1.5 ml of a nisin solution (15 mM Tris-HCl, 25 mM NaCl, pH 7.0). The correspondent samples contained exact stoichiometric amounts for a 2:1 nisin–lipid II complex. Subsequently, in order to complete nisin–lipid II pore complex formation, the lipid suspension containing the pore complex was incubated at room temperature for 90 min. Liposomes were collected by centrifugation (20,000  $\times g$ ) and loaded into Bruker 1.3 or 3.2 mm zirconia rotors. Afterward, supernatants were virtually free of nisin, as we tested with

antimicrobial activity assays. In total, the samples contained ~0.60 mg and 2.60 mg (150 and 750 nmol) of nisin in the 1.3 and 3.2 mm rotors, respectively. Note that we did not observe chemical shift differences for the nisin–lipid II complex in DOPC liposomes with different concentrations (1, 2, or 4 %) of lipid II.

For  $^1\text{H}/^2\text{H}$  exchange studies, reconstituted liposomes containing the nisin–lipid II pores were resuspended in deuterated buffer (99.8%  $\text{D}_2\text{O}$ , 25 mM NaCl, 15 mM Tris-HCl, pH 7.0) and incubated for 1 day before ssNMR measurements.

Native membrane vesicles (MVs) preparations were obtained from *Micrococcus flavus* DSM 1790 strain based on the method described previously.<sup>23</sup> Accordingly, the bacteria were grown in TSB medium (6L) up to an OD600 of 5 (mid log phase). Cells were harvested and washed with 50 mM Tris-Cl, pH 8.0, resuspended in the same buffer (30–50 ml per liter of culture), and lysed over eight runs using a cell disruptor (Constant Systems). The remaining intact cells were removed by a low-speed centrifugation of the mixture at 600  $\times g$  and the clear supernatant was centrifuged at 20,000  $\times g$  to collect the membranes. The resulting membrane pellet was resuspended in the same buffer, flash-frozen in liquid nitrogen, and stored at  $-20^\circ\text{C}$ .

During the MVs preparation, a large fraction of the lipid II pool is naturally consumed by the active enzymes present in the membrane. Therefore, the lipid II content in the *M. flavus* MVs was restored to maximal natural amounts by incubating the membranes in a suspension with the corresponding lipid II precursors UDP-MurNAc-pentapeptide and UDP-GlcNAc.<sup>12</sup> The lipid II concentration in the *M. flavus* membrane preparations was estimated to be 0.5% of its total phospholipids molar content,<sup>27</sup> which was calculated via an inorganic phosphate determination. Briefly, membrane lipids were extracted and isolated according to the Bligh–Dyer procedure<sup>57</sup> and the amount of organic phosphate present was subsequently determined according to the method described by Rouser et al.<sup>58</sup> Nisin was accordingly added to the lipid II-replenished MVs considering a 2:1 nisin:lipid II stoichiometry.

For the cellular  $^1\text{H}$ -detected ssNMR experiments, *M. flavus* MVs samples contained ~10 nmol of nisin which were loaded in a Bruker 1.3 mm zirconia rotor. For the cellular DNP-ssNMR experiments, *M. flavus* MVs samples contained ~55 nmol of nisin which were loaded in a Bruker 3.2 mm sapphire rotor.

Reconstituted lipid II-bound nisin in DOPC liposomes (4% lipid II) for the DNP samples were prepared using 300 nmol lipid II and 600 nmol of nisin. Prior to the measurements, all DNP samples were suspended in 60% glycerol- $d_8$ , 35% buffer solution (25 mM NaCl, 15 mM Tris-HCl pH 7.0 final concentration), and 5% 15 mM AMUPol<sup>53</sup> (final concentration) in  $\text{D}_2\text{O}$ . Samples were filled in a Bruker 3.2 mm sapphire rotor.

*NMR spectroscopy*

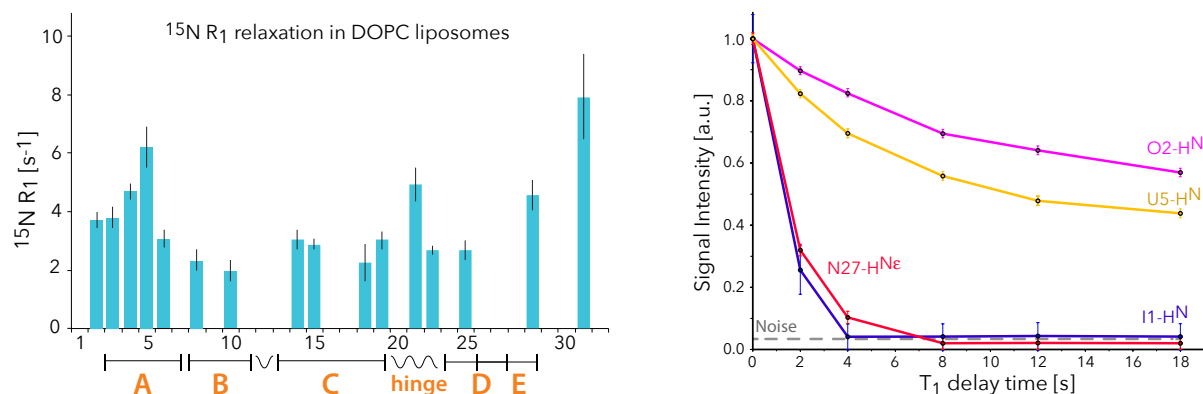
$^1\text{H}$ -detected ssNMR experiments were performed at 60 kHz MAS frequency at static magnetic fields of 18.8 and 22.2 T (800 and 950 MHz  $^1\text{H}$ -frequency, Bruker Biospin). All experiments were performed using dipolar-based sequences at a sample temperature of about 310 K. Sequential backbone chemical shift assignments were performed using 3D CANH, 3D CONH, and 3D CAcoNH experiments.<sup>26</sup> For the latter experiment, one-bond polarization  $^{13}\text{C}$ – $^{13}\text{C}$  transfer between CA and CO was achieved with DREAM<sup>59</sup> recoupling. For all cross-polarization (CP) steps, we used ramped (10–20%) contact pulses. All 3D experiments were acquired with sparse sampling (40–50%). In all  $^1\text{H}$ -detected experiments, the last transfer step from  $^{15}\text{N}$  to  $^1\text{H}$  was kept short (500–700  $\mu\text{s}$ ) to exclusively obtain intra-residual transfer. PISSARRO<sup>60</sup> low-power (15 kHz decoupling amplitude, 70  $\mu\text{s}$  pulse length) decoupling was used during all indirect and direct detection periods.

Two-dimensional  $^{13}\text{C}$ - $^{13}\text{C}$  spin diffusion experiments at room temperature (280 K) were performed with PARIS<sup>61</sup> recoupling at 950 MHz and 17 kHz MAS frequency. The PARIS recoupling amplitude was 10 kHz, the mixing time 45 ms, and we used the standard phase inversion time of half a rotor period ( $N = 1/2$ , i.e., 29.41  $\mu\text{s}$ ). SPINAL64<sup>62</sup> was used in both indirect and direct detection periods. For the dipolar magnetization transfer buildup curves (Figure 3F), we used 2D PDS  $^{13}\text{C}$ - $^{13}\text{C}$  experiments, i.e., we did not apply a recoupling sequence on the protons in order to emphasize the effect of local molecular motions.

DNP-enhanced 2D  $^{13}\text{C}$ - $^{13}\text{C}$  spin diffusion ssNMR experiments were carried out using an 800 MHz/527 GHz setup (Bruker Biospin) at 100 K experimental temperature and 10.6 kHz MAS. A  $^{13}\text{C}$ - $^{13}\text{C}$  mixing time of 40 ms was used for all DNP experiments without recoupling irradiation on the proton channel. SPINAL64 decoupling was used in all detection periods.

$^1\text{H}$ -detected  $^{15}\text{N}$   $T_{1\rho}$  and  $T_1$  relaxation experiments were carried out at 950 MHz and 800 MHz magnetic field, respectively, using 60 kHz MAS.<sup>26</sup> The  $^{15}\text{N}$  transverse magnetization decay was probed with a  $^{15}\text{N}$  spinlock field of 17.5 kHz, without application of  $^1\text{H}$ -decoupling during the  $^{15}\text{N}$  spinlock. We measured six points for both  $T_1$  (0, 2, 4, 6, 8, 12, and 18 s) and  $T_{1\rho}$  (0, 10, 25, 50, 100, and 130 ms). Only well-isolated peaks were considered for the analysis, for which we measured the peak intensities. The  $T_1$  and  $T_{1\rho}$  trajectories were fit to single exponentials.

## Supporting Information

S1.  $^{15}\text{N}$   $R_1$  relaxation measurements in Lipid II-bound nisin in DOPC.

**Figure S1.** (left)  $^{15}\text{N}$   $R_1$  relaxation rates of Lipid-II bound nisin acquired in DOPC liposomes. The error bars indicate the standard deviation of the fit. (right) The N-terminal I1 amino-group (in blue) relaxed very fast, comparable to the N27 side chain (red). Such a fast relaxation is typical for highly flexible side chains that are not, or only weakly, involved in hydrogen bonding. Note that I1 relaxed so fast that we could not fit it, and hence not derive a  $^{15}\text{N}$   $R_1$  rate. The T<sub>1</sub> trajectories were fit to single exponentials according to  $I = I^0 + e^{-\frac{t}{T_1}}$ .

## S2. Evaluation of the influence of the length of the Lipid II prenyl-chain on Lipid II-bound nisin.

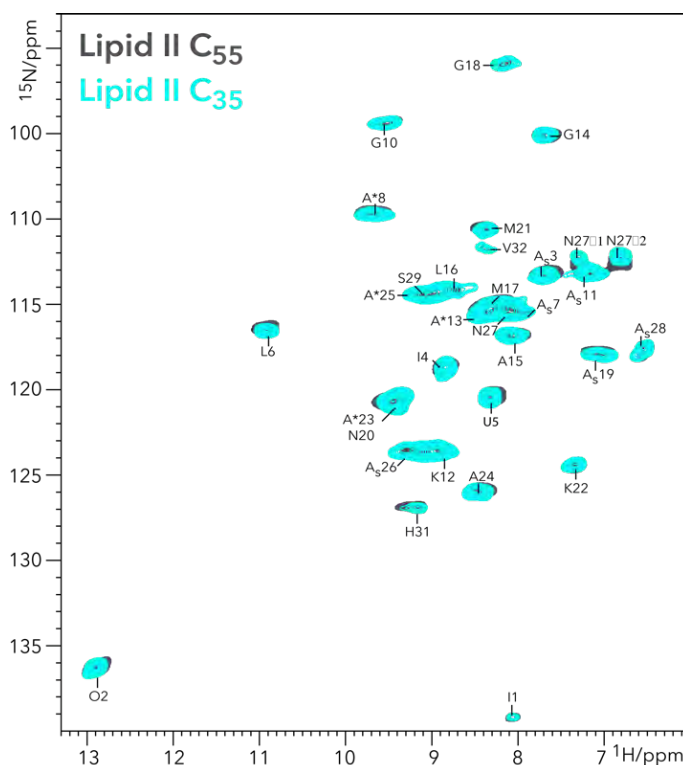


**Figure S2.** In the cyan 2D NH ssNMR spectrum, we used heptaprenyl-(C35) Lipid II, and dodecaprenyl-(C55) Lipid II in the black spectrum. The spectra, both acquired in DOPC liposomes, show no difference, which demonstrates that the tail of the Lipid II prenyl-chain does not strongly interact with nisin.

## S3. Chemical structures of lipid II and non-canonical aminoacids

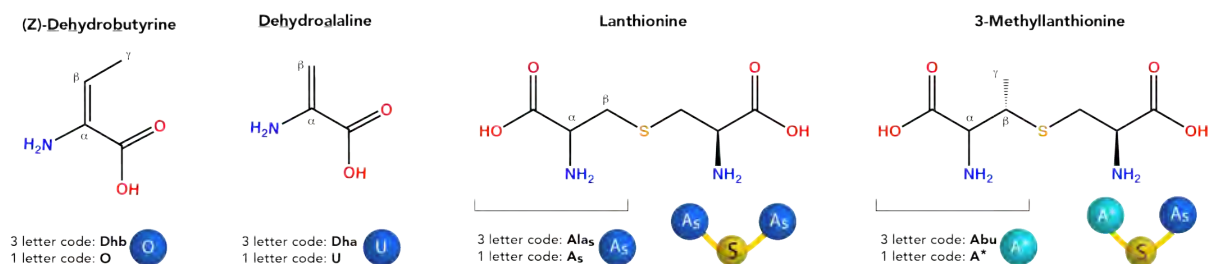


**Figure S3A.** Chemical structures and conventions adopted in this manuscript for the non-canonical amino acids present in nisin.

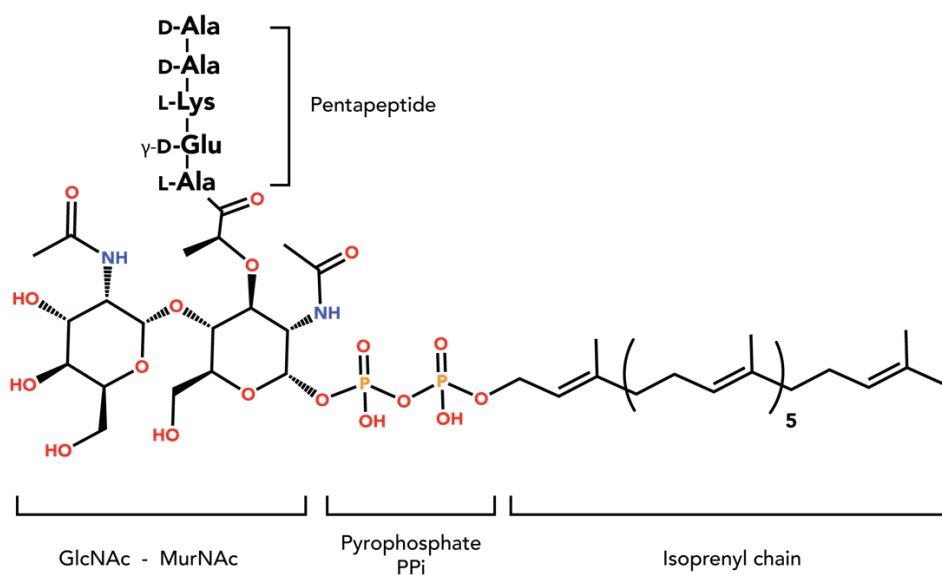


**Figure S3B.** Chemical structure of the Lipid II used for this study.

## S4. Nisin purification and evaluation

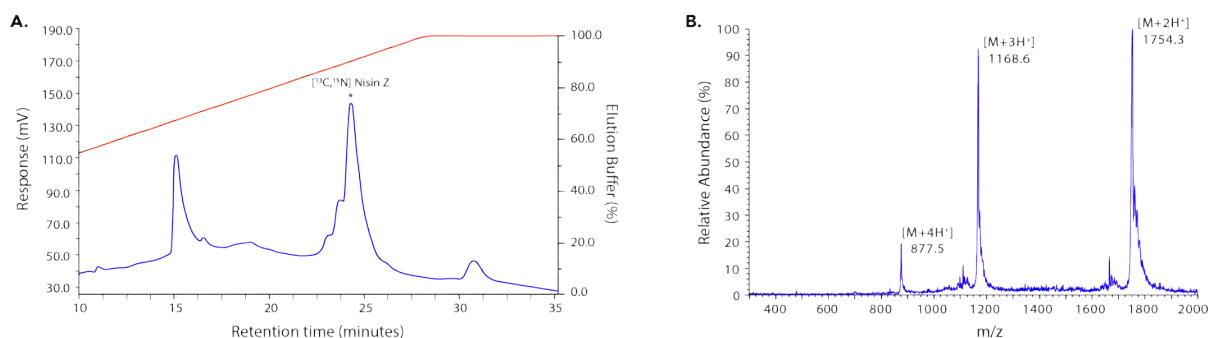


**Figure S4.** (A) C18 RP-HPLC elution profile of the *L. lactis* growth medium extract. Fractions collected between 24-25 min displayed antimicrobial activity. (B) ESI ionization trace of the eluted fraction annotated in (A).

The purified nisin displayed a MIC of  $3.4 \pm 0.75$  nM ( $12.0 \pm 2.5$   $\mu\text{g/L}$ ) against *Micrococcus flavus*, which matched that of unlabeled nisin with  $2.7 \pm 0.75$  nM ( $9.0 \pm 2.5$   $\mu\text{g/L}$ ). These values are consistent with the reported MIC in the literature for *M. flavus*.<sup>20,22</sup>



## S6. Chemical Shift assignments of Lipid II bound-nisin in DOPC liposomes

**Table S1.** Chemical shift values for nisin Z bound to lipid II in DOPC at pH 7 and approx. 280 K. Values in parts per million (ppm)

Residue	#	N <sup>H</sup>	H <sup>N</sup>	H <sup>α</sup>	CO	C <sub>α</sub>	C <sub>β</sub>	C <sub>γ</sub>	C <sub>δ</sub>	C <sub>ε</sub>
Ile	1	39.8	8.05	4.59	170.6	61.12	35.68	26.56; 16.8	13.83	
Dhb	2	136.6	12.85	---	166.9	131.1	134.5	16.03		
D-Ala(s)	3	113.5	7.65	5.8	174.2	56.13	37.2			
Ile	4	119.1	8.83	4.16	174.3	63.3	38.34	27.65; 18.16	12.67	
Dha	5	120.73	8.28	---	167.3	134.6	107.8			
Leu	6	116.7	10.85	4-4.3	175.8	55.01	38.68	27.2	26.37; 24.11	
Ala(s)	7	116.5	7.95	5.43	172.9	53.9	38.63			
Abu	8	104.5	9.55	5.05	175.6	59	49.1	24		
Pro	9	138.3	---	4.61	177.3	66.61	31.66	27.58	50.75	
Gly	10	104.6	9.49	4-4.5	171.6	44.7				
Ala(s)	11	113.8	7.05	4-4.3	177.5	55.1	38.8			
Lys	12	123.8	9.05	4.4-4.6	177.7	58.73	31.14	26.02	29.56	41.59
Abu	13	115.9	8.32	4.72	174.3	61.87	43.93	22.96		
Gly	14	105.4	7.64	4-4.5	176.15	45.15				
Ala	15	117.3	7.97	4-4.3	180	55.01	19.66			
Leu	16	114.6	8.49	4.2	176.1	57.8	40.76	27.52	25.85; 23.51	
Met	17	115.3	8.25	4.2	176.5	57.8	36.34	31.43		18.2
Gly	18	101.2	8.14	4.12	174.26	44.8				
Ala(s)	19	117.9	7.05	5.2-5.5	173.7	54.06	36.5			
Asp	20	120.8	9.3	4.5-5	173.6	56.59	34.63	177		
Met	21	111.85	8.36	5.2	176.9	52	30	32.3		17.25
Lys	22	124.8	7.33	4.4-4.6	176.6	58.73	32.73	24.53	30.08	42.01
Abu	23	121	9.4	5.11	176.8	60.8	50.5	23.35		
Ala	24	126.1	8.41	3.9	179	53.5	17.97			
Abu	25	114.7	9.05	4.76	176.7	63.5	46.85	23.35		
Ala(s)	26	123.6	9	5.32	173.9	59.7	41.5			
Asp	27	115.6 <sup>a</sup>	8	5.25	175.1	50.73	38.5	178.4		
Ala(s)	28	118.2	6.55	4.5-5	173	55.95	42.42			
Ser	29	114.4	8.78	4.5-5	172.8	56.1	64.95			
Ile	30	124.5	9.3	n.d. *	174.2	59.4	38.2	27.78; 17.68	17.68	
His	31	126.4	9.1	n.d. *	174.4	54.72	30.79	129.9**	115.9**	137.5**
Val	32	111.8	8.37	n.d. *	n.d. *	61.60; 60.15	33.3	20.3		
Dha	33	n.d. *	n.d. *		n.d. *	n.d. *	n.d. *			
Lys	34	n.d.*	n.d.*	n.d.*	n.d.*	n.d.*	n.d.*	n.d.*	n.d.*	n.d.*

\*n.d. = not defined.

<sup>a</sup> N $\delta$  = 113.3 ppm

\*\*Values obtained via DNP (at 100 K temperature).

## References

- (1) O'Neill, J. Antimicrobial Resistance: Tackling a Crisis for the Health and Wealth of Nations. *Review on Antimicrobial Resistance*. 2016, pp 1–16.
- (2) Breukink, E.; de Kruijff, B. Lipid II as a Target for Antibiotics. *Nat. Rev. Drug Discov.* **2006**, *5* (4), 321–323.
- (3) Schneider, T.; Kruse, T.; Wimmer, R.; Wiedemann, I.; Sass, V.; Pag, U.; Jansen, A.; Nielsen, A. K.; Mygind, P. H.; Raventós, D. S.; et al. Plectasin, a Fungal Defensin, Targets the Bacterial Cell Wall Precursor Lipid II. *Science* (80-. ). **2010**, *328* (5982), 1168–1172.
- (4) Cochrane, S. A.; Findlay, B.; Bakhtiary, A.; Acedo, J. Z.; Rodriguez-Lopez, E. M.; Mercier, P.; Vederas, J. C. Antimicrobial Lipopeptide Tridecaptin A1selectively Binds to Gram-Negative Lipid II. *Proc. Natl. Acad. Sci. U. S. A.* **2016**, *113* (41), 11561–11566.
- (5) Ling, L. L.; Schneider, T.; Peoples, A. J.; Spoering, A. L.; Engels, I.; Conlon, B. P.; Mueller, A.; Schäberle, T. F.; Hughes, D. E.; Epstein, S.; et al. A New Antibiotic Kills Pathogens without Detectable Resistance. *Nature* **2015**, *517* (7535), 455–459.
- (6) Münch, D.; Engels, I.; Müller, A.; Reder-Christ, K.; Falkenstein-Paul, H.; Bierbaum, G.; Grein, F.; Bendas, G.; Sahl, H. G.; Schneider, T. Structural Variations of the Cell Wall Precursor Lipid II and Their Influence on Binding and Activity of the Lipoglycopeptide Antibiotic Oritavancin. *Antimicrob. Agents Chemother.* **2015**, *59* (2), 772–781.
- (7) Scheffers, D. J.; Tol, M. B. LipidII: Just Another Brick in the Wall? *PLoS Pathog.* **2015**, *11* (12), e1005213.
- (8) Münch, D.; Roemer, T.; Lee, S. H.; Engeser, M.; Sahl, H. G.; Schneider, T. Identification and in Vitro Analysis of the GatD/MurT Enzyme-Complex Catalyzing Lipid II Amidation in Staphylococcus Aureus. *PLoS Pathog.* **2012**, *8* (1), e1002509.
- (9) Linden, A. H.; Lange, S.; Franks, W. T.; Akbey, Ü.; Specker, E.; Van Rossum, B. J.; Oschkinat, H. Neurotoxin II Bound to Acetylcholine Receptors in Native Membranes Studied by Dynamic Nuclear Polarization NMR. *J. Am. Chem. Soc.* **2011**, *133* (48), 19266–19269.
- (10) Renault, M.; Tommassen-Van Boxtel, R.; Bos, M. P.; Post, J. A.; Tommassen, J.; Baldus, M. Cellular Solid-State Nuclear Magnetic Resonance Spectroscopy. *Proc. Natl. Acad. Sci. U. S. A.* **2012**, *109* (13), 4863–4868.
- (11) Ward, M. E.; Wang, S.; Munro, R.; Ritz, E.; Hung, I.; Gor'Kov, P. L.; Jiang, Y.; Liang, H.; Brown, L. S.; Ladizhansky, V. In Situ Structural Studies of Anabaena Sensory Rhodopsin in the E. Coli Membrane. *Biophys. J.* **2015**, *108* (7), 1683–1696.
- (12) Breukink, E.; Wiedemann, I.; van Kraaij, C.; Kuipers, O. P.; Sahl, H. G.; de Kruijff, B. Use of the Cell Wall Precursor Lipid II by a Pore-Forming Peptide Antibiotic. *Science* **1999**, *286* (5448), 2361–2364.
- (13) Hsu, S.-T. D.; Breukink, E.; Tischenko, E.; Lutters, M. A. G.; de Kruijff, B.; Kaptein, R.; Bonvin, A. M. J. J.; van Nuland, N. A. J. The Nisin–Lipid II Complex Reveals a Pyrophosphate Cage That Provides a Blueprint for Novel Antibiotics. *Nat. Struct. Mol. Biol.* **2004**, *11* (10), 963–967.
- (14) Yuan, J.; Zhang, Z. Z.; Chen, X. Z.; Yang, W.; Huan, L. D. Site-Directed Mutagenesis of the Hinge Region of NisinZ and Properties of NisinZ Mutants. *Appl. Microbiol. Biotechnol.* **2004**, *64* (6), 806–815.
- (15) Field, D.; Connor, P. M. O.; Cotter, P. D.; Hill, C.; Ross, R. P. The Generation of Nisin Variants with Enhanced Activity against Specific Gram-Positive Pathogens. *Mol. Microbiol.* **2008**, *69* (1), 218–230.
- (16) Healy, B.; Field, D.; O'Connor, P. M.; Hill, C.; Cotter, P. D.; Ross, R. P. Intensive Mutagenesis of the Nisin Hinge Leads to the Rational Design of Enhanced Derivatives. *PLoS One* **2013**, *8* (11), e79563.
- (17) Koopmans, T.; Wood, T. M.; 'T Hart, P.; Kleijn, L. H. J.; Hendrickx, A. P. A.; Willems, R. J. L.; Breukink, E.; Martin, N. I. Semisynthetic Lipopeptides Derived from Nisin Display Antibacterial Activity and Lipid II Binding on Par with That of the Parent Compound. *J. Am. Chem. Soc.* **2015**, *137* (29), 9382–9389.
- (18) Hasper, H. E.; De Kruijff, B.; Breukink, E. Assembly and Stability of Nisin-Lipid II Pores. *Biochemistry* **2004**, *43* (36), 11567–11575.
- (19) Héchar, Y.; Sahl, H. G. Mode of Action of Modified and Unmodified Bacteriocins from Gram-Positive Bacteria. *Biochimie* **2002**, *84* (5–6), 545–557.
- (20) Wiedemann, I.; Breukink, E.; Van Kraaij, C.; Kuipers, O. P.; Bierbaum, G.; De Kruijff, B.; Sahl, H. G. Specific Binding of Nisin to the Peptidoglycan Precursor Lipid II Combines Pore Formation and Inhibition of Cell Wall Biosynthesis for Potent Antibiotic Activity. *J. Biol. Chem.* **2001**, *276* (3), 1772–1779.
- (21) Ross, A. C.; Vederas, J. C. Fundamental Functionality: Recent Developments in Understanding the Structure-Activity Relationships of Lantibiotic Peptides. *J. Antibiot. (Tokyo)*. **2011**, *64* (1), 27–34.
- (22) Bonelli, R. R.; Schneider, T.; Sahl, H. G.; Wiedemann, I. Insights into in Vivo Activities of Lantibiotics

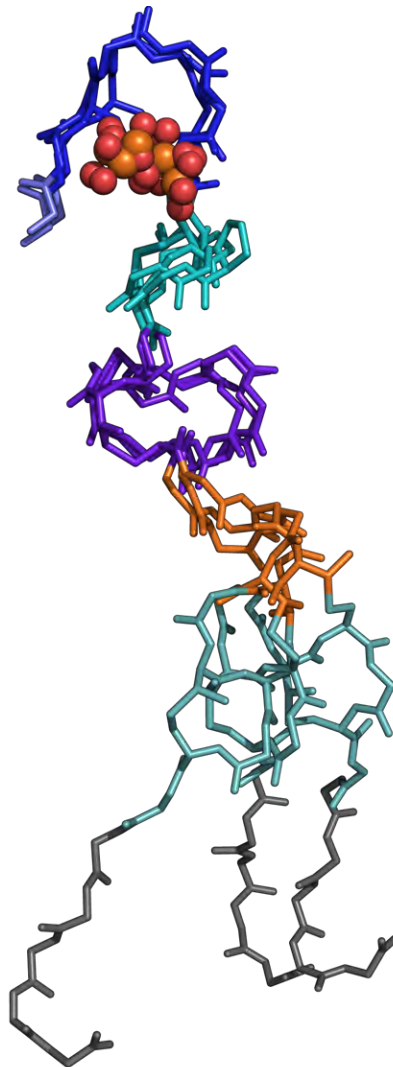
- from Gallidermin and Epidermin Mode-of-Action Studies. *Antimicrob. Agents Chemother.* **2006**, *50* (4), 1449–1457.
- (23) Breukink, E.; van Heusden, H. E.; Vollmerhaus, P. J.; Swiezewska, E.; Brunner, L.; Walker, S.; Heck, A. J. R.; de Kruijff, B. Lipid II Is an Intrinsic Component of the Pore Induced by Nisin in Bacterial Membranes. *J. Biol. Chem.* **2003**, *278* (22), 19898–19903.
- (24) Kuipers, O. P.; Rollema, H. S.; de Vos, W. M.; Siezen, R. J. Biosynthesis and Secretion of a Precursor of Nisin Z by *Lactococcus Lactis*, Directed by the Leader Peptide of the Homologous Lantibiotic Subtilin from *Bacillus Subtilis*. *FEBS Lett.* **1993**, *330* (1), 23–27.
- (25) Bonev, B. B.; Breukink, E.; Swiezewska, E.; De Kruijff, B.; Watts, A. Targeting Extracellular Pyrophosphates Underpins the High Selectivity of Nisin. *FASEB J.* **2004**, *18* (15), 1862–1869.
- (26) Medeiros-Silva, J.; Mance, D.; Daniëls, M.; Jekhmane, S.; Houben, K.; Baldus, M.; Weingarth, M. <sup>1</sup>H-Detected Solid-State NMR Studies of Water-Inaccessible Proteins In Vitro and In Situ. *Angew. Chemie Int. Ed.* **2016**, *55* (43), 13606–13610.
- (27) Kramer, N. E.; Smid, E. J.; Kok, J.; De Kruijff, B.; Kuipers, O. P.; Breukink, E. Resistance of Gram-Positive Bacteria to Nisin Is Not Determined by Lipid II Levels. *FEMS Microbiol. Lett.* **2004**, *239* (1), 157–161.
- (28) Demel, R. A.; Peelen, T.; Siezen, R. J.; De Kruijff, B.; Kuipers, O. P. Nisin Z, Mutant Nisin Z and Lacticin 481 Interactions with Anionic Lipids Correlate with Antimicrobial Activity: A Monolayer Study. *Eur. J. Biochem.* **1996**, *235* (1–2), 267–274.
- (29) Van Kraaij, C.; Breukink, E.; Rollema, H. S.; Bongers, R. S.; Kusters, H. A.; De Kruijff, B.; Kuipers, O. P. Engineering a Disulfide Bond and Free Thiols in the Lantibiotic Nisin Z. *Eur. J. Biochem.* **2000**, *267* (3), 901–909.
- (30) Zhou, L.; van Heel, A. J.; Kuipers, O. P. The Length of a Lantibiotic Hinge Region Has Profound Influence on Antimicrobial Activity and Host Specificity. *Front. Microbiol.* **2015**, *6* (JAN).
- (31) Ratledge, C.; Wilkinson, S. G. *Microbial Lipids Vol. 1; Microbial Lipids*; Academic Press, 1988.
- (32) Rink, R.; Wierenga, J.; Kuipers, A.; Kluskens, L. D.; Driessen, A. J. M.; Kuipers, O. P.; Moll, G. N. Dissection and Modulation of the Four Distinct Activities of Nisin by Mutagenesis of Rings A and B and by C-Terminal Truncation. *Appl. Environ. Microbiol.* **2007**, *73* (18), 5809–5816.
- (33) Van Heusden, H. E.; De Kruijff, B.; Breukink, E. Lipid II Induces a Transmembrane Orientation of the Pore-Forming Peptide Lantibiotic Nisin. *Biochemistry* **2002**, *41* (40), 12171–12178.
- (34) Smith, L.; Zachariah, C.; Thirumoorthy, R.; Rocca, J.; Novák, J.; Hillman, J. D.; Edison, A. S. Structure and Dynamics of the Lantibiotic Mutacin 1140. *Biochemistry* **2003**, *42* (35), 10372–10384.
- (35) Paiva, A. D.; Breukink, E.; Mantovani, H. C. Role of Lipid II and Membrane Thickness in the Mechanism of Action of the Lantibiotic Bovicin HC5. *Antimicrob. Agents Chemother.* **2011**, *55* (11), 5284–5293.
- (36) Shi, L.; Kawamura, I.; Jung, K. H.; Brown, L. S.; Ladizhansky, V. Conformation of a Seven-Helical Transmembrane Photosensor in the Lipid Environment. *Angew. Chemie - Int. Ed.* **2011**, *50* (6), 1302–1305.
- (37) Medeiros-Silva, J.; Jekhmane, S.; Baldus, M.; Weingarth, M. Hydrogen Bond Strength in Membrane Proteins Probed by Time-Resolved <sup>1</sup>H-Detected Solid-State NMR and MD Simulations. *Solid State Nucl. Magn. Reson.* **2017**, *87*, 80–85.
- (38) Molloy, E. M.; Field, D.; Connor, P. M. O.; Cotter, P. D.; Hill, C.; Ross, R. P. Saturation Mutagenesis of Lysine 12 Leads to the Identification of Derivatives of Nisin A with Enhanced Antimicrobial Activity. *PLoS One* **2013**, *8* (3), e58530.
- (39) Bajaj, V. S.; Mak-Jurkauskas, M. L.; Belenky, M.; Herzfeld, J.; Griffin, R. G. Functional and Shunt States of Bacteriorhodopsin Resolved by 250 GHz Dynamic Nuclear Polarization-Enhanced Solid-State NMR. *Proc. Natl. Acad. Sci. U. S. A.* **2009**, *106* (23), 9244–9249.
- (40) Voinov, M. A.; Good, D. B.; Ward, M. E.; Milikisiyants, S.; Marek, A.; Caporini, M. A.; Rosay, M.; Munro, R. A.; Ljumovic, M.; Brown, L. S.; et al. Cysteine-Specific Labeling of Proteins with a Nitroxide Biradical for Dynamic Nuclear Polarization NMR. *J. Phys. Chem. B* **2015**, *119* (32), 10180–10190.
- (41) Liao, S. Y.; Lee, M.; Wang, T.; Sergeev, I. V.; Hong, M. Efficient DNP NMR of Membrane Proteins: Sample Preparation Protocols, Sensitivity, and Radical Location. *J. Biomol. NMR* **2016**, *64* (3), 223–237.
- (42) Joedicke, L.; Mao, J.; Kuenze, G.; Reinhart, C.; Kalavacherla, T.; Jonker, H. R. A.; Richter, C.; Schwalbe, H.; Meiler, J.; Preu, J.; et al. The Molecular Basis of Subtype Selectivity of Human Kinin G-Protein-Coupled Receptors. *Nat. Chem. Biol.* **2018**, *14* (3), 284–290.
- (43) Kaplan, M.; Narasimhan, S.; de Heus, C.; Mance, D.; van Doorn, S.; Houben, K.; Popov-Čeleketić, D.; Damman, R.; Katrukha, E. A.; Jain, P.; et al. EGFR Dynamics Change during Activation in Native Membranes as Revealed by NMR. *Cell* **2016**, *167* (5), 1241–1251.e11.

- (44) Frederick, K. K.; Michaelis, V. K.; Corzilius, B.; Ong, T. C.; Jacavone, A. C.; Griffin, R. G.; Lindquist, S. Sensitivity-Enhanced NMR Reveals Alterations in Protein Structure by Cellular Milieus. *Cell* **2015**, *163* (3), 620–628.
- (45) Lilly Thankamony, A. S.; Wittmann, J. J.; Kaushik, M.; Corzilius, B. Dynamic Nuclear Polarization for Sensitivity Enhancement in Modern Solid-State NMR. *Prog. Nucl. Magn. Reson. Spectrosc.* **2017**, *102–103*, 120–195.
- (46) Visscher, K. M.; Medeiros-Silva, J.; Mance, D.; Rodrigues, J. P. G. L. M.; Daniëls, M.; Bonvin, A. M. J. J.; Baldus, M.; Weingarth, M. Supramolecular Organization and Functional Implications of K<sup>+</sup> Channel Clusters in Membranes. *Angew. Chemie - Int. Ed.* **2017**, *56* (43), 13222–13227.
- (47) Fricke, P.; Mance, D.; Chevelkov, V.; Giller, K.; Becker, S.; Baldus, M.; Lange, A. High Resolution Observed in 800 MHz DNP Spectra of Extremely Rigid Type III Secretion Needles. *J. Biomol. NMR* **2016**, *65* (3–4), 121–126.
- (48) Koers, E. J.; Van Der Crujisen, E. A. W.; Rosay, M.; Weingarth, M.; Prokofyev, A.; Sauvée, C.; Ouari, O.; Van Der Zwan, J.; Pongs, O.; Tordo, P.; et al. NMR-Based Structural Biology Enhanced by Dynamic Nuclear Polarization at High Magnetic Field. *J. Biomol. NMR* **2014**, *60* (2–3), 157–168.
- (49) Sergeev, I. V.; Itin, B.; Rogawski, R.; Day, L. A.; McDermott, A. E. Efficient Assignment and NMR Analysis of an Intact Virus Using Sequential Side-Chain Correlations and DNP Sensitization. *Proc. Natl. Acad. Sci. U. S. A.* **2017**, *114* (20), 5171–5176.
- (50) Debelouchina, G. T.; Bayro, M. J.; Van Der Wel, P. C. A.; Caporini, M. A.; Barnes, A. B.; Rosay, M.; Maas, W. E.; Griffin, R. G. Dynamic Nuclear Polarization-Enhanced Solid-State NMR Spectroscopy of GNNQQNY Nanocrystals and Amyloid Fibrils. *Phys. Chem. Chem. Phys.* **2010**, *12* (22), 5911–5919.
- (51) Bauer, T.; Dotta, C.; Balacescu, L.; Gath, J.; Hunkeler, A.; Böckmann, A.; Meier, B. H. Line-Broadening in Low-Temperature Solid-State NMR Spectra of Fibrils. *J. Biomol. NMR* **2017**, *67* (1), 51–61.
- (52) Ni, Q. Z.; Markhasin, E.; Can, T. V.; Corzilius, B.; Tan, K. O.; Barnes, A. B.; Daviso, E.; Su, Y.; Herzfeld, J.; Griffin, R. G. Peptide and Protein Dynamics and Low-Temperature/DNP Magic Angle Spinning NMR. *J. Phys. Chem. B* **2017**, *121* (19), 4997–5006.
- (53) Sauvée, C.; Rosay, M.; Casano, G.; Aussenac, F.; Weber, R. T.; Ouari, O.; Tordo, P. Highly Efficient, Water-Soluble Polarizing Agents for Dynamic Nuclear Polarization at High Frequency. *Angew. Chemie Int. Ed.* **2013**, *52* (41), 10858–10861.
- (54) Field, D.; Begley, M.; O'Connor, P. M.; Daly, K. M.; Hugenholtz, F.; Cotter, P. D.; Hill, C.; Ross, R. P. Bioengineered Nisin A Derivatives with Enhanced Activity against Both Gram Positive and Gram Negative Pathogens. *PLoS One* **2012**, *7* (10), e46884.
- (55) Zhou, L.; Shao, J.; Li, Q.; Van Heel, A. J.; De Vries, M. P.; Broos, J.; Kuipers, O. P. Incorporation of Tryptophan Analogues into the Lantibiotic Nisin. *Amino Acids* **2016**, *48* (5), 1309–1318.
- (56) Kuipers, O. P.; Rollema, H. S.; Yap, W. M. G. J.; Boot, H. J.; Siezen, R. J.; De Vos, W. M. Engineering Dehydrated Amino Acid Residues in the Antimicrobial Peptide Nisin. *J. Biol. Chem.* **1992**, *267* (34), 24340–24346.
- (57) Bligh, E. G.; Dyer, W. J. A RAPID METHOD OF TOTAL LIPID EXTRACTION AND PURIFICATION. *Can. J. Biochem. Physiol.* **1959**, *37* (8), 911–917.
- (58) Rouser, G.; Fleischer, S.; Yamamoto, A. Two Dimensional Thin Layer Chromatographic Separation of Polar Lipids and Determination of Phospholipids by Phosphorus Analysis of Spots. *Lipids* **1970**, *5* (5), 494–496.
- (59) Verel, R.; Baldus, M.; Ernst, M.; Meier, B. H. A Homonuclear Spin-Pair Filter for Solid-State NMR Based on Adiabatic-Passage Techniques. *Chem. Phys. Lett.* **1998**, *287* (3–4), 421–428.
- (60) Weingarth, M.; Bodenhausen, G.; Tekely, P. Low-Power Decoupling at High Spinning Frequencies in High Static Fields. *J. Magn. Reson.* **2009**, *199* (2), 238–241.
- (61) Weingarth, M.; Demco, D. E.; Bodenhausen, G.; Tekely, P. Improved Magnetization Transfer in Solid-State NMR with Fast Magic Angle Spinning. *Chem. Phys. Lett.* **2009**, *469* (4–6), 342–348.
- (62) Fung, B. M.; Khitritin, A. K.; Ermolaev, K. An Improved Broadband Decoupling Sequence for Liquid Crystals and Solids. *J. Magn. Reson.* **2000**, *142* (1), 97–101.



# CHAPTER 7

## Progress on the Nisin-Lipid II pore structure



In this chapter, I describe the latest progress towards the structure determination of the nisin – lipid II pore complex. This chapter is the experimental continuation of chapter 6, therefore the reader is referred to chapters 1 and 6 for an introduction about the nisin – lipid II system.



*Nisin : Lipid II interface*

The binding of nisin to the pyrophosphate group of lipid II was demonstrated with  $^{31}\text{P}$  experiments (Figure 2 A,B) conducted in liposomes. In the presence of nisin, the phosphate signals of lipid II display large chemical shift perturbations that demonstrate binding of the antibiotic. A dipolar-based 2D HP spectrum provided site-resolved drug - pyrophosphate contacts, displaying clear correlations between the lipid II phosphate groups and nisin's amide protons O2, A\*8 and U5/A<sub>s</sub>7. This allows us to pin-point the binding site of nisin to lipid II.

We are currently investigating the full binding interface between lipid II and nisin. Here, we succeeded to derive an approach to  $^{13}\text{C}$ - $^{15}\text{N}$  isotope-label lipid II, which is a big step for structural studies of drug – lipid II complex, and will, for the first time ever, enable to determine the role of the lipid II sugar-pentapeptide headgroup for nisin-pore formation at atomic scale. In general, these antibiotic – headgroup interactions are critical for the mode of action of many other promising antibiotics and understanding these interactions at atomic scale will significantly improve our capacity to use lipid II binding drugs as templates for drug design. These measurements with labelled lipid II will, for example, finally explain the role of the critical hydrophobic interaction of nisin residue Ile1, postulated in the previous chapter and recently supported by mutagenesis studies.<sup>2</sup>,

Thus far, our ssNMR measurements of labelled lipid II, acquired with dipolar-based experiments (Figure 2D) in complex with unlabeled nisin, clearly demonstrate that both sugars are rigid in the pore complex and are most likely directly involved in nisin – lipid II interactions. The penta-peptide domain is however mobile in the complex, as only two of these residues (Ala1 and D- $\gamma$ Glu2) are observable in the dipolar-based spectrum. The flexibility of the pentapeptide domain was confirmed by using J-based experiments, which are sensitive to high mobility (Figure 2C). Accordingly, the J-based spectrum displays several NH signals that correspond to the pentapeptide and presumably also one of the the NAc groups.

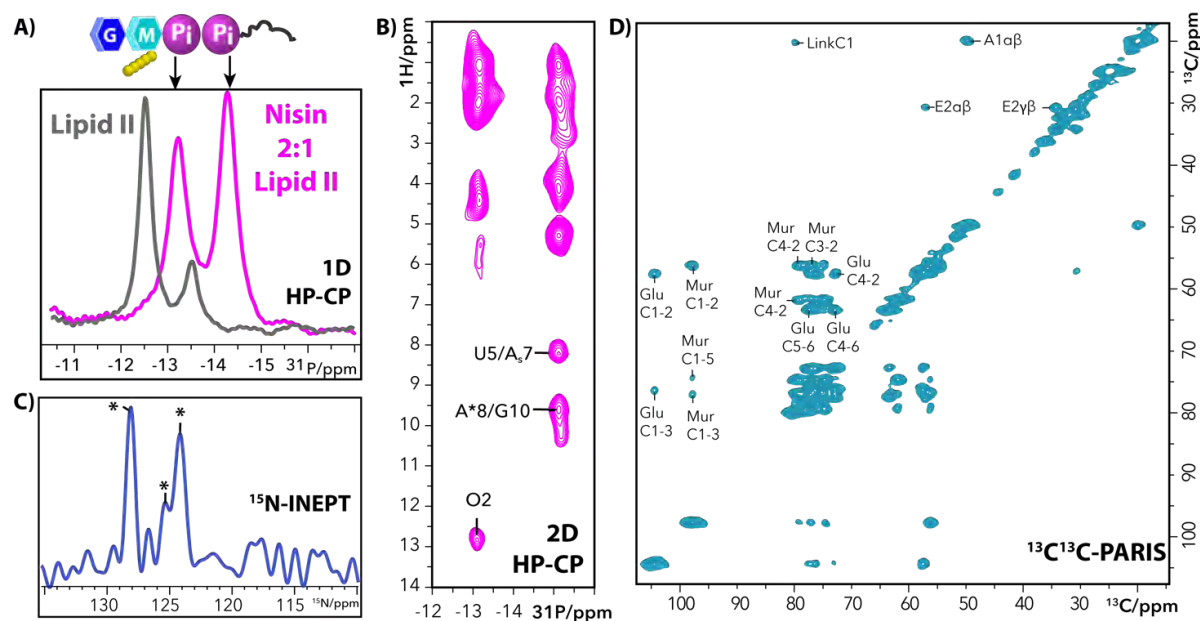


**Figure 2.** A) 1D  $^1\text{H}^{31}\text{P}$  CP spectrum of lipid II in its free state (gray) and after addition of 2 molar equivalents of nisin (magenta), measured in DOPC liposomes at 11.7 T and 10 kHz MAS B) 2D  $^1\text{H}^{31}\text{P}$ -CP spectrum of lipid II – nisin complex, measured in DOPC liposomes at 18.8 T and 60 kHz MAS C)  $^{15}\text{N}$  INEPT spectrum of  $^{15}\text{N}$ - $^{13}\text{C}$  labelled lipid II in the pore-complex, measured at 16.4 T and 60kHz MAS. The spectrum displays several NH signals that correspond to the pentapeptide residues and NAc groups of the sugars. D)  $^{13}\text{C}$ - $^{13}\text{C}$  spin diffusion spectrum of the pore complex using  $^{15}\text{N}$ - $^{13}\text{C}$  labelled lipid II and unlabeled Nisin, measured in DOPC liposomes at 16.4 T and 42 kHz MAS. We can readily assign the GlucNAc and MurNAc sugars groups, as well as the first two aminoacids Ala-1 and D- $\gamma$ -Glu-2 from the pentapeptide. The last three residues of the pentapeptide (Lys-3, D-Ala-4 and D-Ala-5) are highly mobile and not visible in this spectrum.

### Nisin Monomer Structure

The calculation of the nisin monomer structure relied on distance constraints obtained through carbon spin diffusion experiments. The strategy consisted on gradually measuring longer range carbon-carbon contacts by increasing the spin diffusion mixing times, i.e., short spin diffusion mixing times (50 ms) provide intra-residue contacts, while longer mixing times (600 ms) provide inter-residual long-range contacts (i.e.  $\geq 5$  residues). For example, in Figure 3 B, P9 Ca shows clear contacts to residues L16 and M17, implying that these residues are spatially close (less than 0.8 nm apart), which is very precious information on the mutual orientation of the thioether rings B and C. Contacts between nisin monomers were, at this stage, filtered out by mixing  $^{13}\text{C}$  and  $^{12}\text{C}$  labelled nisin, thereby significantly reducing the likelihood that two  $^{13}\text{C}$  -labelled monomers are next to each other in the pore (Figure 3). In total, we used four different  $^{13}\text{C}$  - $^{13}\text{C}$  mixing times of 50, 300, 600, and 1000 ms in order to obtain a total of 105 medium-range (i.e. 2-4 residues away) and 55 long-range unambiguous contacts, added to the 5 nisin – Lipid II pyrophosphate contacts obtained with the 2D HP experiment.

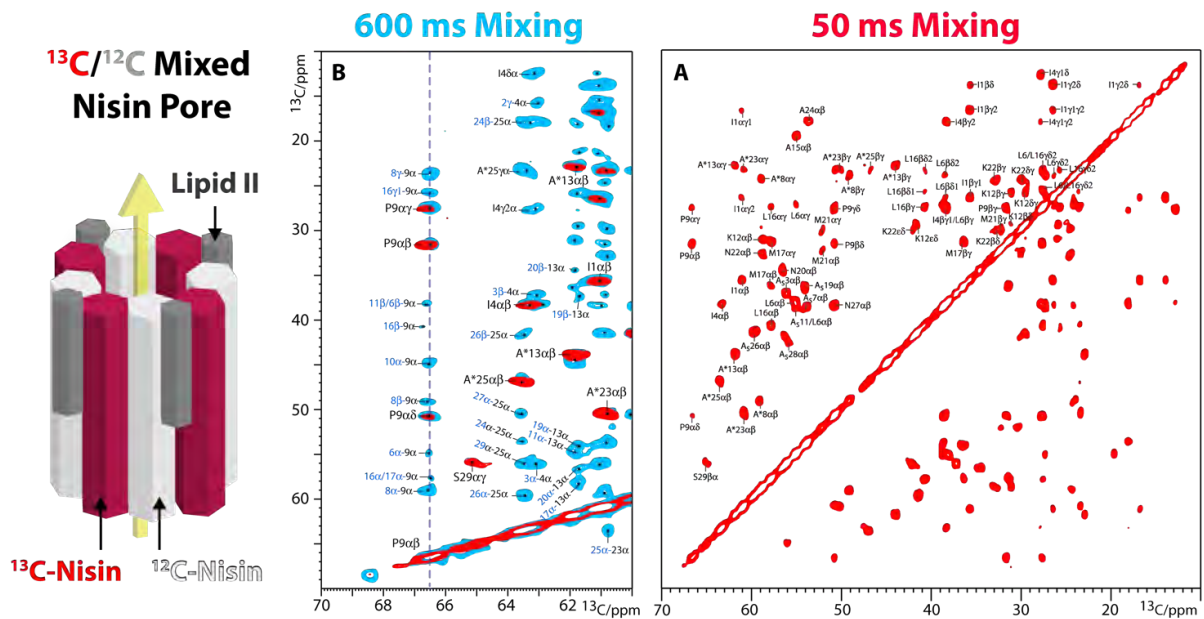


**Figure 3.** (Left) Labelling strategy for the selective measurement of intramolecular nisin distance restraints. (Right) Example of two 2D  $^{13}\text{C}$ - $^{13}\text{C}$  spin diffusion experiments using PARIS recoupling<sup>3</sup> with (A) 50 ms mixing time, providing intra-residue contacts and (B) 600 ms mixing time, providing long range contacts ( $> 4$  residues away). Not all resonances were annotated for simplicity, but full assignments are shown in Figure S1. Measurements were performed in DOPC liposomes and recorded at 950 MHz (proton frequency) with 17 kHz MAS frequency, at 280K sample temperature.

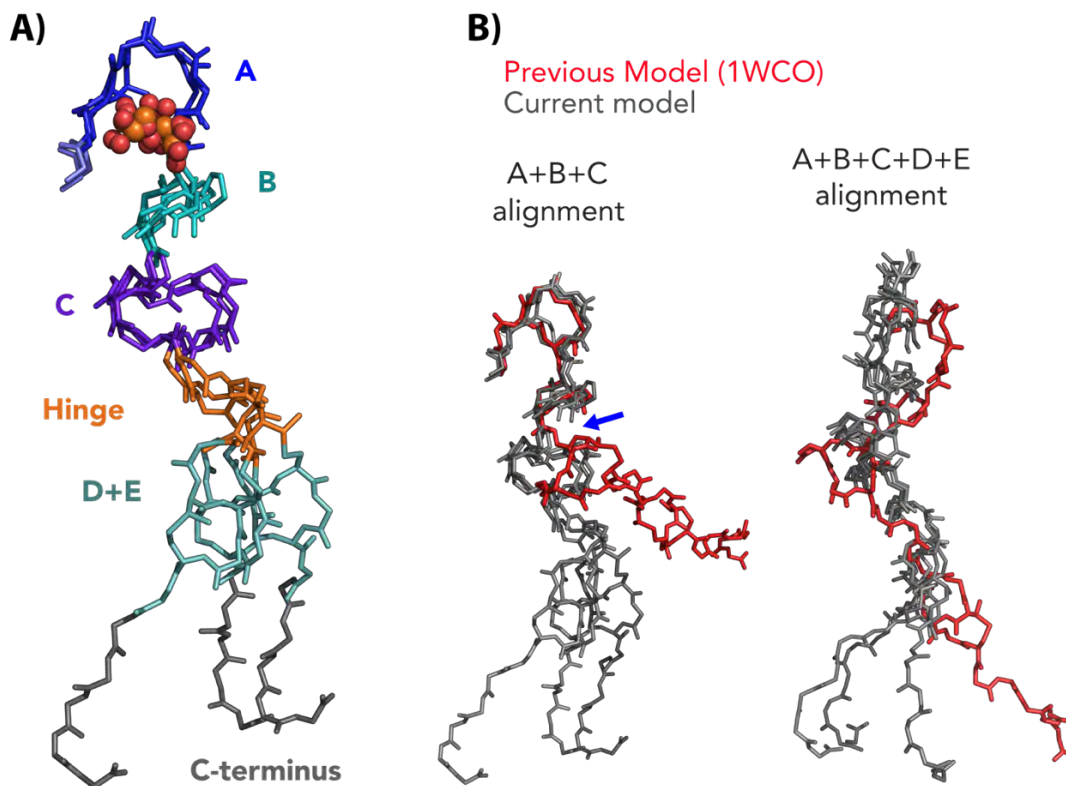


**Figure 4.** A) ssNMR structure of nisin inserted in the lipid II pore-complex. B) Comparison between the ssNMR structure, solved in DOPC liposomes, and the published 1WCO structure solved in DMSO. Our structure demonstrates major conformational changes in the presence of a bilayer.

Figure 4 A shows the nisin monomer structure calculated in the pore complex, i.e. the physiologically relevant conformation. We obtained an average backbone RMSD of 3.5 Å for residues 1-29, which shows a well-defined conformation for this part of the peptide. Our structure in lipid bilayers shows very important alterations in comparison to the previous structure of nisin calculated in DMSO (1WCO). Specifically, we observe major conformational alterations at the linker residue K12 and the entire C-ring, as well as drastic differences at the hinge and rings D+E (Figure 4B). The implications of these structural differences for the pore assembly will be more evident when the complete pore structure is obtained.

### *Nisin : Nisin Interface*

The nisin : nisin interface was defined by using intermolecular nisin – nisin distance restraints obtained via dipolar couplings between two different nisin monomers. The experimental design consisted in mixing exclusively  $^{15}\text{N}$ -labelled nisin monomers and exclusively  $^{13}\text{C}$ -labelled nisin monomers in equimolar ratio to form  $^{15}\text{N}/^{13}\text{C}$  mixed-labelled pores. Using a so-called 2D  $^{13}\text{C}$ - $^{15}\text{N}$  PAIN experiment,<sup>4</sup> acquired at 950 MHz and 12 kHz MAS, Magnetization was then transferred from nitrogen to carbon nuclei in to obtain the interchain nisin contacts (Figure 5 B). As a result, we obtained 30 ambiguous and 4 unambiguous restraints that define the oligomerization interface. The majority of these contacts at the interface are related to the D+E rings, which are essential for pore formation.<sup>5</sup> At the moment of writing, the nisin – nisin interface in the pore is being calculated using multi-body docking in collaboration with Dr. João Rodrigues from the Levitt group at Stanford University.

## **Conclusion and outlook**

We successfully obtained the long-sought-after structure of nisin in the pore-complex, which is the pharmaceutically relevant state. The calculated structure shows stark differences to the previously published one, which used to be the gold standard for many drug-design studies. Therefore, the new structure can potentially deeply impact drug design studies, and provides a much improved basis to find efficient nisin analogues.

Moreover, more than 15 years after its discovery, we are eventually very close to obtaining the atomic-scale high-resolution structure of the nisin – Lipid II pore, which will be a substantial achievement and pioneering step for our understanding of lipid II binding drugs. Along the same lines, our approach to isotope-label Lipid II will have a tremendous impact to fully understand other highly promising Lipid II binding drugs such as plectasin that are currently studied in our group, opening exciting avenues for the development of new drugs.

## Materials and Methods

### *Sample preparation*

Nisin and lipid II samples were produced according to the description from Chapter 6. To obtain labelled lipid II samples, labelled rich medium was employed. Lipid II was extracted and purified by anion exchange chromatography (S2).

$^{12}\text{C}/^{13}\text{C}$  mixed-labelled nisin samples were prepared by mixing  $^{12}\text{C}$ -labelled nisin and  $^{13}\text{C}$ -labelled nisin in equal amounts (50/50). The antibiotic solution was then mixed with lipid II-doped DOPC liposomes as described in the previous chapter. The same procedure was applied for the  $^{13}\text{C}/^{15}\text{N}$  mixed-labelled nisin sample.

### *NMR Spectroscopy*

Two-dimensional  $^{13}\text{C}$ - $^{13}\text{C}$  spin diffusion experiments were performed at 280 K with PARIS<sup>3</sup> recoupling, measured in a 950 MHz magnet and 17 kHz MAS frequency. The PARIS recoupling amplitude was 10 kHz with mixing times of 50, 300, 600 and 1000 ms, as described in the Chapter 6. Two-dimensional  $^1\text{H}$ - $^{31}\text{P}$  spin diffusion experiments were performed at 280 K at 800 MHz and 60 kHz MAS frequency. Two dimensional  $^{15}\text{N}$ - $^{13}\text{C}$  polarization transfer experiments to probe nisin – nisin intermolecular contacts were performed at  $\sim 270$  K with PAIN recoupling at 950 MHz and 12 kHz MAS frequency using 5 ms mixing time.

### *Nisin monomer structure calculation*

Distance restraints were derived from the two-dimensional  $^{13}\text{C}$ - $^{13}\text{C}$  spin diffusion and  $^1\text{H}$ - $^{31}\text{P}$ -CP experiments. Dihedral angle restraints were derived for residue M21 using TALOS-N<sup>6</sup>. The distance and dihedral restraints were applied in a simulated annealing protocol using CNS<sup>7</sup> and HADDOCK<sup>8,9</sup>. Structure calculations were carried out in vacuum.



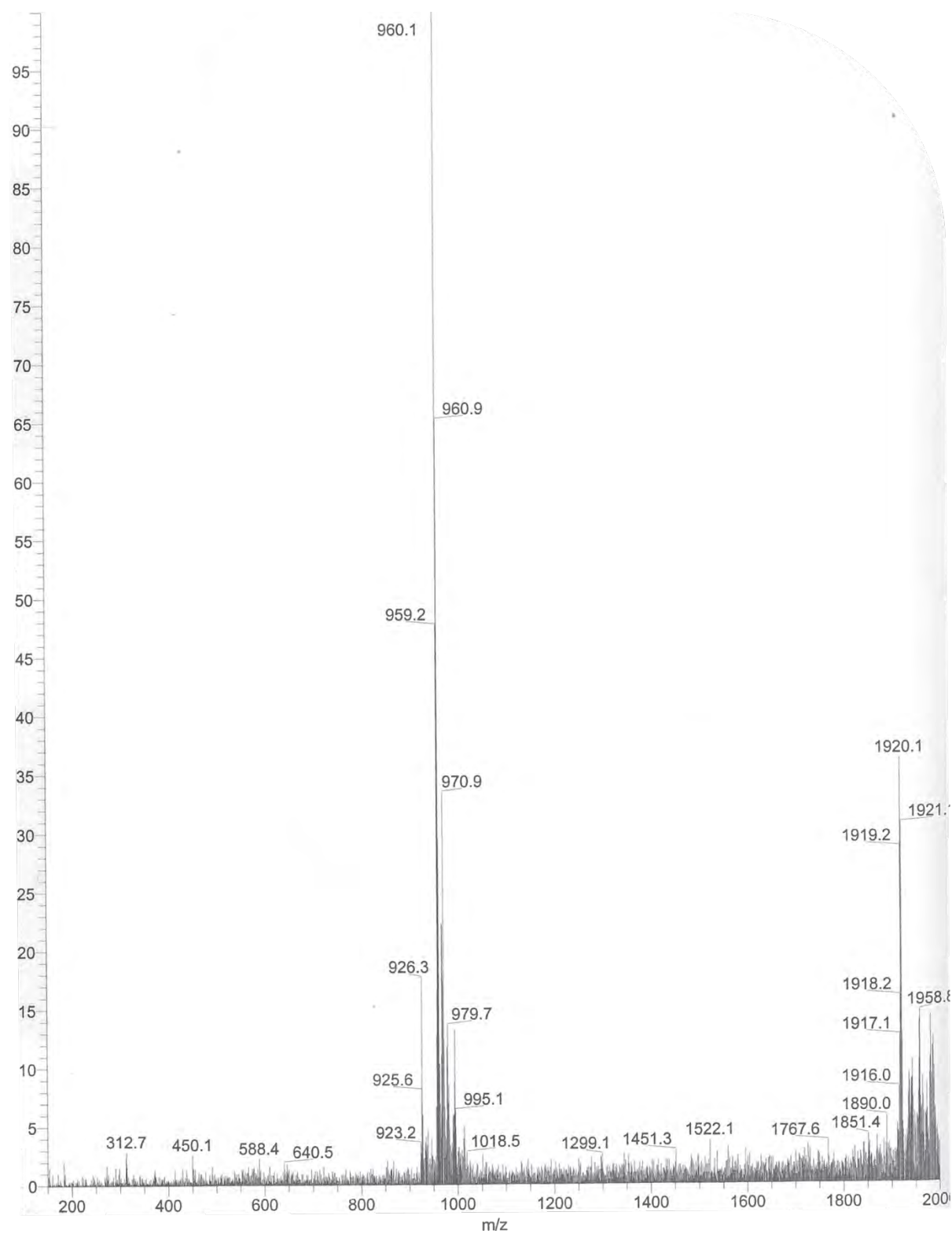


Figure S2. ESI ionization trace of  $^{13}\text{C}$ - $^{15}\text{N}$  labelled lipid II, with isotope-labelled head-group.

## References

- (1) Medeiros-Silva, J.; Jekhmane, S.; Paioni, A. L.; Gawarecka, K.; Baldus, M.; Swiezewska, E.; Breukink, E.; Weingarth, M. High-Resolution NMR Studies of Antibiotics in Cellular Membranes. *Nat. Commun.* **2018**, *9* (1), 3963.
- (2) Lagedroste, M.; Reiners, J.; Smits, S. H. J.; Schmitt, L. Systematic Characterization of Position One Variants within the Lantibiotic Nisin. *Sci. Rep.* **2019**, *9* (1), 935.
- (3) Weingarth, M.; Demco, D. E.; Bodenhausen, G.; Tekely, P. Improved Magnetization Transfer in Solid-State NMR with Fast Magic Angle Spinning. *Chem. Phys. Lett.* **2009**, *469* (4–6), 342–348.
- (4) Lewandowski, J. R.; De Paëpe, G.; Griffin, R. G. Proton Assisted Insensitive Nuclei Cross Polarization. *J. Am. Chem. Soc.* **2007**, *129* (4), 728–729.
- (5) Hasper, H. E.; de Kruijff, B.; Breukink, E. Assembly and Stability of Nisin–Lipid II Pores. *Biochemistry* **2004**, *43* (36), 11567–11575.
- (6) Shen, Y.; Bax, A. Protein Backbone and Sidechain Torsion Angles Predicted from NMR Chemical Shifts Using Artificial Neural Networks. *J. Biomol. NMR* **2013**, *56* (3), 227–241.
- (7) Brünger, A. T.; Adams, P. D.; Clore, G. M.; DeLano, W. L.; Gros, P.; Grosse-Kunstleve, R. W.; Jiang, J. S.; Kuszewski, J.; Nilges, M.; Pannu, N. S.; et al. Crystallography & NMR System: A New Software Suite for Macromolecular Structure Determination. *Acta Crystallogr. Sect. D Biol. Crystallogr.* **1998**, *54* (5), 905–921.
- (8) van Zundert, G. C. P.; Rodrigues, J. P. G. L. M.; Trellet, M.; Schmitz, C.; Kastiris, P. L.; Karaca, E.; Melquiond, A. S. J.; van Dijk, M.; de Vries, S. J.; Bonvin, A. M. J. J. The HADDOCK2.2 Web Server: User-Friendly Integrative Modeling of Biomolecular Complexes. *J. Mol. Biol.* **2016**, *428* (4), 720–725.
- (9) Cyril Dominguez; Rolf Boelens, and; Bonvin\*, A. M. J. J. HADDOCK: A Protein–Protein Docking Approach Based on Biochemical or Biophysical Information. **2003**.



# CHAPTER 8

## Summary and Outlook



## Summary and outlook

Solid state NMR is a powerful technique that enables measuring complex systems such as membrane proteins directly in cellular membranes and at atomic scale. In this thesis I sought to use this technique to characterize biologically important membrane-embedded systems and explore their properties in physiological conditions.

### *High-resolution solid state NMR applications for membrane proteins*

$^1\text{H}$  detected solid state NMR is a powerful approach to study membrane proteins but it hitherto relied on extensive deuteration schemes that severely limit or totally inhibit studies of transmembrane domains and water-inaccessible domains in general. To address this issue, in **Chapter 2** we developed a novel deuteration strategy, dubbed *Inverse Fractional Deuteration (iFD)*<sup>1</sup>, that enables high  $^1\text{H}$ -signal resolution and sensitivity of solvent-inaccessible domains of proteins. This method provided critical insights into the transmembrane region of the archetypical potassium channel KcsA, which included structural elements such as the selectivity filter and the pore helix that have prominent functional roles in the gating cycle of ion channels. The highly favorable resolution and sensitivity in our  $^1\text{H}$ -detected spectra allowed us to perform detailed a analysis of the dynamics and topology of the selectivity filter.

In a proof-of-principle study, the high spectral quality obtained via iFD labelling also enabled, for the first time ever, the use of  $^1\text{H}$  detection to measure a membrane protein directly in native bacterial membranes. Such studies in native cell membranes can be of great importance to understand membrane protein structure and function, as we demonstrated in Chapter 6.

### *Gating-related studies on potassium channels*

The novel methods developed in Chapter 2 paved the way for further studies on ion channels. In **Chapter 3** we performed, for the first time, time-resolved  $^1\text{H}$  detected H/D exchange ssNMR in native-like liposomes<sup>2</sup> to explore the strength of functionally important hydrogen bonds at the water-membrane interface of KcsA. As a result, we identified an unusually strong hydrogen bond network at the turret loop of the  $\text{K}^+$  channel. Accordingly, the aminoacids involved in the network, although fully solvent-exposed, did not fully exchange up to several weeks. A closer structural analysis, supported by MD simulations, suggested that this hydrogen bond network has

functional relevance for the gating mechanisms at the filter. These findings can be applicable to a vast range of other K<sup>+</sup> channels, including mammalian voltage-gated K<sup>+</sup> channels, given that this hydrogen network is highly conserved.

In **Chapter 4** we investigated the molecular determinants for modal gating in K<sup>+</sup> channels on the example of KcsA.<sup>3</sup> Spontaneous activity shifts at constant experimental conditions, known as modal gating, have been observed in many K<sup>+</sup> channels and are regarded as a widespread regulatory mechanism in ion channels. However, the molecular underpinning of modal gating was poorly understood. We combined solid-state NMR with  $\mu$ -second long MD simulations to investigate, in native-like liposomes, three KcsA point-mutants (E71A, E71I, E71Q) that represent different, intrinsically occurring and randomly interchanging gating modes. We showed that dynamical, conformational changes that shift the equilibrium structure of the selectivity filter are the underpinning of modal gating in K<sup>+</sup> channels. We further showed that these conformational changes are triggered by fluctuations in water and hydrogen bonding networks behind the filter.

The supramolecular arrangement of KcsA clusters in native-like membranes was investigated in **Chapter 5** by employing DNP-enhanced ssNMR and MD simulations<sup>4</sup>. Our data demonstrated that opening/closing of the lower gate of KcsA is closely related to channel clustering, thereby establishing a connection between gating and inter-channel communication. We further showed that the clustering effect is mediated through the M0 helices which adhere together upon gate opening.

#### *The nisin – lipid II pore complex*

The alarming rise of drug-resistant bacteria urgently calls for novel antibiotics. Antibiotics that target lipid II, the membrane-embedded precursor of the bacterial peptidoglycan synthesis, are extremely powerful, but the development of new drugs is severely hampered by the absence of a physiologically representative structural basis. Hence, in **Chapters 6 and 7** we presented a pioneering native solid state NMR approach to study Lipid II – antibiotic complexes in the pharmaceutically relevant conformation.<sup>5</sup> Here, we studied the preeminent antibiotic nisin that specifically binds to lipid II forming a pore complex in the bacterial cell membrane. Our results provided the topology of the pore, binding interface, resolved dynamics and complete structure of nisin in the pore complex. The novel nisin structure displayed stark differences to the only structure available so far, which was calculated in rather artificial media and

is regarded as a gold standard for drug design studies.

Strikingly, our studies of the nisin-lipid II pore that were conducted directly in native cellular membranes revealed that nisin displays intrinsic plastic features that adapt to the target bacterial membrane where it inserts. Interestingly these plastic components also correspond to hotspots for drug design. Moreover, we successfully developed an approach to produce  $^{13}\text{C}$ - $^{15}\text{N}$  labelled Lipid II, which will provide the full structure of the pore complex and the structural basis for the development of new antibiotics.

Overall our solid-state NMR approach enables high resolution studies of membrane-active drugs in pharmaceutically relevant conditions. The studies in bacterial membranes will also lead to a rational understanding of how the local cellular environment can modulate antibiotic binding and efficiency.

## Samenvatting en perspectieven

Vaste-stof NMR is een krachtige techniek die het mogelijk maakt om complexe systemen, zoals membraan eiwitten, direct te bestuderen in cellulaire membranen. In deze thesis heb ik deze techniek gebruikt om biologisch belangrijke membraan-gebedde systemen te onderzoeken en bestudeer ik deze eigenschappen onder de meest fysiologische condities.

### *Hoge resolutie vaste-stof NMR applicaties voor membraan eiwitten*

<sup>1</sup>H-gedetecteerde vaste-stof NMR (vsNMR) is een krachtige manier om membraan eiwitten te bestuderen, echter is het afhankelijk van extensieve deutereringsschema's dat het bestuderen van transmembraan domeinen verhinderd. In **Hoofdstuk 2** hebben we een nieuwe deutereringsstrategie ontwikkeld, genaamd *Inverse Fractional Deuteration*, die het mogelijk maakt om hoge <sup>1</sup>H-sigitaal resolutie en sensitiviteit te behalen voor oplossing-ontoegankelijke domeinen of eiwitten. Deze methode bracht inzicht in het transmembraan domain van het kalium kanaal KcsA, inclusief het prominente filter domein. De verbeterde resolution maakte het mogelijk om het filter te karakteriseren en om gedetailleerde analyses uit te voeren van de dynamica en topologie.

De hoge spectrale kwaliteit dat behaald werd middels iFD markering in een principebewijs studie maakt het ook voor de eerste keer mogelijk om <sup>1</sup>H-gedetectie metingen te verrichten op membraan eiwitten direct in de native bacteriële membranen. Dergelijke studies in native celmembranen kunnen van ongekend belang zijn om de structuur en functie van membraan eiwitten te begrijpen, zoals later aangetoond in **Hoofdstuk 6**.

### *Kanaliserings-gerelateerde studies aan kalium kanalen*

De nieuwe methodes die ontwikkeld zijn in Hoofdstuk 2, maakten de weg vrij voor nieuwe studies aan KcsA kanalen. In **Hoofdstuk 3**, hebben we tijdsopgelost <sup>1</sup>H-gedeteceerde vsNMR methoden gebruikt om H/D-uitwisselingskarakteristieken van KcsA in natief-achtige liposomen te onderzoeken. We hebben een ongebruikelijk sterk waterstofbrug netwerk geïdentificeerd bij de turret lus van K<sup>+</sup> kanalen. De aminozuren betrokken in het netwerk, hoewel volledig blootgesteld aan de oplossing, wisselden niet uit over een periode van enkele weken. Een gedetailleerde structurele

analyse, ondersteund door MD simulaties, suggereerde dat dit waterstofbrug netwerk functioneel relevant is voor het kanalisereingsmechanisme bij het filter. Deze resultaten zijn toepasbaar voor een breed scala van andere  $K^+$  kanalen, inclusief voltage-activerende  $K^+$  kanalen van zoogdieren, wanneer gegeven is dat het waterstofbrug netwerk zeer geconserveerd is.

In **Hoofdstuk 4**, hebben we moleculaire determinanten voor modale kanalisering onderzocht in de KcsA, wat wordt gezien als een wijd verspreid mechanisme voor de regulatie van ion kanalen. We hebben vaste-stof NMR gecombineerd met  $\mu$ -seconde lange MD simulaties om drie KcsA punt-mutanten, E71A, E71I en E71Q, die verschillende kanalisereingsmodes repressenteren, in natief-achtige liposomen te onderzoeken. We tonen aan dat conformationele veranderingen bij het selectiviteitsfilter de kanaliseringmodes van het kanaal moduleren. Verder laten we zien dat deze conformationele veranderingen geïnduceerd worden door fluctuaties in water- en waterstofbrug-netwerken achter het filter.

Het supramoleculaire arrangement van KcsA clusters in natief-achtige membranen was onderzocht in **Hoofdstuk 5**, door middel van DNP-ondersteunde vsNMR and MD simulaties. De data toont aan dat het openen/sluiten van de onderste sluis van KcsA nauw gerelateerd is aan kanaal clusters, waarmee een connectie tussen kanalisering en inter-kanaal communicatie ontstaat. Verder laten we zien dat het effect van clusters wordt gemedieerd door de M0 helix domeinen die aan elkaar hechten wanneer de sluis open gaat.

#### *De Nisine – Lipide II porie complex*

De alarmerende toename in medicijn-resistente bacteriën vraagt met spoed voor nieuwe antibiotica. Antibiotica die gericht zijn op lipide II zijn extreem krachtig, echter de ontwikkeling van nieuwe medicijnen is sterk verhinderd door de afwezigheid van een fysiologische representatieve structurele basis. Doordat, in **Hoofdstuk 6 & 7**, presenteren wij een natieve vaste-stof NMR benadering om lipide II – antibiotica complexen in een farmaceutische relevante conformatie te bestuderen. We onderzochten het uitmuntende antibioticum nisine, die specifiek bindt aan lipide II en daarmee een porie complex vormt in de bacteriële membraan. Onze resultaten laten de topologie van de porie, bindingsoppervlak, opgeloste dynamica and een complete structuur van nisine in het porie complex zien. De nieuwe nisine structuur liet grote verschillen zien met de huidige en enige beschikbare structuur, die berekend

was in artificiële media en werd gezien als de gouden standaard voor medicijn-ontwikkelings studies.

Onze studies van de nisine-lipide II porie, die zijn uitgevoerd in natieve cellulaire membranen, laten zien dat nisine intrinsieke plastische karakterstieken vertoont die het mogelijke maken voor nisine om in een bacteriële membraan te gaan. Deze plastische componenten komen ook overeen met hotspots voor medicijn design.

Daarnaast hebben we ook  $^{13}\text{C}$ ,  $^{15}\text{N}$ -verrijkt lipide II succesvol geproduceerd, wat het mogelijk maakte om de volledige structuur van het porie complex op te lossen en daarmee de structurele basis zal vormen voor de ontwikkeling van nieuwe antibiotica.

Samenvattend, onze vaste-stof NMR benadering maakt het mogelijk om hoge-resolutie studies te doen aan membraan-actieve medicijnen onder farmaceutisch relevante condities. Onze studies, direct uitgevoerd op bacteriële membranen, dragen bij aan een begrip hoe de lokale cellulaire omgeving antibiotica binding and efficiëntie kan moduleren.

## References

- (1) Medeiros-Silva, J.; Mance, D.; Daniëls, M.; Jekhmane, S.; Houben, K.; Baldus, M.; Weingarth, M.  $^1\text{H}$ -Detected Solid-State NMR Studies of Water-Inaccessible Proteins In Vitro and In Situ. *Angew. Chemie Int. Ed.* **2016**, 55 (43), 13606–13610.
- (2) Medeiros-Silva, J.; Jekhmane, S.; Baldus, M.; Weingarth, M. Hydrogen Bond Strength in Membrane Proteins Probed by Time-Resolved  $^1\text{H}$ -Detected Solid-State NMR and MD Simulations. **2017**.
- (3) Jekhmane, S.; Medeiros-Silva, J.; Li, J.; Kümmerer, F.; Müller-Hermes, C.; Baldus, M.; Roux, B.; Weingarth, M. Shifts in the Selectivity Filter Dynamics Cause Modal Gating in  $\text{K}^+$  Channels. *Nat. Commun.* **2019**, 10 (1), 123.
- (4) Visscher, K. M.; Medeiros-Silva, J.; Mance, D.; Rodrigues, J. P. G. L. M.; Daniëls, M.; Bonvin, A. M. J. J.; Baldus, M.; Weingarth, M. Supramolecular Organization and Functional Implications of  $\text{K}^+$  Channel Clusters in Membranes. **2017**.
- (5) Medeiros-Silva, J.; Jekhmane, S.; Paioni, A. L.; Gawarecka, K.; Baldus, M.; Swiezewska, E.; Breukink, E.; Weingarth, M. High-Resolution NMR Studies of Antibiotics in Cellular Membranes. *Nat. Commun.* **2018**, 9 (1), 3963.

## Acknowledgments

The author would like to thank the Assessment and Examination Committee members, Prof. Dr. **Antoinette Killian**, Prof. Dr. **Alexandre Bonvin**, Dr. **Eefjan Breukink**, Prof. Dr. **Friedrich Förster**, Prof. Dr. **Henk Haagsman** and Prof. Dr. **Nathaniel Martin**, for their time and consideration of this manuscript.

I can't believe it has been 4 years since I moved to the Netherlands. It has been a spectacular experience in this amazing country. Loved the landscapes, the people, the bikes, and the city. Importantly, *things work* here! The Netherlands and the city of Utrecht took a place in my heart, I will definitely miss this cozy and picturesque city. I could write another book just to thank each and all the people that turned this experience more amazing. Thus, for the sake of the forests, I will swiftly give a word of appreciation.

First and foremost, a big word of gratitude towards my supervisor, **Markus Weingarth**. More than teaching me everything I know about ssNMR, you taught me how to create great science and step up my research. Markus is without a doubt the most pragmatic person I worked with, with clear goals and a sharp mindset. Your training got me a tough skin, and you propelled my achievements. I cannot thank you enough for this opportunity.

I have a lifelong gratitude to **Marleen de Boer**, **Gilbert Cohen** and their family. They welcomed and received me in the Netherlands as they would their own family, and guided me through the whole bureaucratic process. Thus, the success of this thesis started in part with the noble gesture of this family. Coming to the Netherlands was my first experience abroad, and very quickly I learned that no matter where you go there will always be good, kindhearted people everywhere. Thank you very, very much, and wish you all the best that life has to offer. For the record, the best erwtensoep in the Netherlands is made in Lent.

I thank **Marc Baldus** for welcoming me to the solid-state lab, and for all the discussions and feedback during these four years. I enjoyed teaching together with you and our colleagues, it gave me an insight to how things work on the backstage.

A big shout out to **Johan van der Krypton** (because he's a super-man) and **Hans Wienk** for all the outstanding technical support at the NMR machines. And what would we do without the NMR secretariat **Barbara Hendricx** (now at the biology and chemistry department) and **Geeske Badart**, you two are life-saviors. For all the post-docs that prevented me from blowing up the machines, **Klaartje Houben**, **Marie Renault**, **Andrei Gurinov** and **ShengQi Xiang**, thank you for your help. I also want to send a big hug to **Meaghan Ward**, **Chris Skoog** and **'Lil Mookie (Fionn)**.

"*Yo mister white*", I want to thank **Mark Daniëls** for all the help in the lab, especially in the beginning. With much patience, he taught me how to prepare and handle micro-crystalline and membrane-protein preparations. After having called him *Mr. White* for 4 years, he dares to reveal with a straight face that he never watched *Breaking Bad*. "*What, is that a show?*". Just... shame on you Mark. Shame. *You bloody idiot*. I also want to thank **Gert Folkers**, one of the three wise men, who is always ready to help and give his experienced advice for any issue in the biochemistry lab. Doesn't matter what it is, he just knows everything.

Another wise man that knows everything is **Eefjan Breukink**. I'm not kidding, every problem that I had he would reply, "It would be wise to check conditions A and B". I learned from him how to handle lipids, membranes, organisms other than *E. coli*, and how to look at enzymes as tools. It was such an exciting lab to work on! I thank you for your guidance, patience and good mood (plus, finally someone with good taste in music!). I take this chance to thank all the Membrane Biochemistry and Biophysics laboratory, for tolerating my entropy and for giving the feedback and help whenever needed. I specially thank **Antoinette Killian**, **Ruud Cox**, **Martijn Koorengel**, **Xiaoqi Wang**, **Yang Xu**, **Xue Bao**, **Adrian Kopf**. I had a great time with you, and wish you all the best. And you too, **Barend**

**Elenbaas.** Barend and I shared the office for a year, he's awesome and also a highly talented musician. Wish you great success both in music and science.

For the HADDOCK crew. I want to thank their captain **Alexandre Bonvin**. The first time I wanted to come to Utrecht was after a talk from Alex in Lisbon, when I was 19. I was mind-blown. By a twist of fate, several years later, yet after another talk from Alex, **João Rodrigues** pointed me the direction to Utrecht. João if it wasn't for you I wouldn't be here, I thank you for that and for your support on the Nisin project. Alex, thanks for spreading the magic and for the feedback and support, specially in the group meetings. When I started **Gydo van Zundert** and **Mohammed Klapan** were still around for a short period of time. I thank avocado-man for being awesome, and Mohammed for his advice and being super kind. I met so many people from the HADDOCK group: **Anna Vangone**, **Li Xue**, **Jörg Schaarschmidt**, **Mikael Trellet**, **Zeynep Kürkçüoğlu** (congrats for Ozan!) and Mr. Dr. Gang (**Cunliang Geng**). I thank you all for the great time at the lab. **Adrien Melquiond**, I enjoyed teaching with you and witness your passion, wish you the best with your new position. For you too **Irina Moreira** a.k.a. Wonder Woman – it's impossible for common mortals to keep up with you. **Francesco Mille Bornone**, all the best for you, hope you become rich in a big pharmaceutical company so you can pay me a dinner. **Jorge Padel**, primo, wish you good luck to achieve the black belt in coarse grain, shake that MARTINI. **Zuzana Jandova**, thank you for the crazy craziness, you're extremely sharp and funny. **Rodrigo Honorato**, irmão, wish you all the best for your new life in the Netherlands, hope you find even more happiness here. Força aí! **Brian Garcia**, thanks to you I started to listen to more Gojira! \*writes the acknowledgments while listening to Gojira\* **Siri van Keulen** thank you a lot for your help, for taking the time to go over my text and images, it really helped me, and for being always in a good mood. **Frazaneh Parizi**, good luck with your studies and wish great happiness to your new family. **Charlotte van Noort** – Wanda! Thank you for all the help, particularly now with the Dutch translation, and for the fun moments. Wish you the best results for your PhD thesis. We should find another nice series to watch! **Panagiotis Koukos**, you, yes you. Panos is a sharp funny ~~met\*%&#)~~@ guy, he looks tough from the outside, but it's just a facade. If I had to portrait Panos I would paint him with flowers in his head, a pink shirt and birds on his shoulder, like Snow White. I would also paint a lake in the background and replace that canvas region by glass. Jokes aside, I have to thank Panos for far too many things. Particularly for this thesis, I thank him for developing a script to automatically translate the nisin contacts to distance intervals, it saved me quite a lot of time. I also thank Panos for stitching the group together, and for turning me into a proper Englishman. You're badass (not your actual... you know what I mean).

I thank **Rolf Boelens** for his experienced advice, for sharing his views during the group meetings and remarkable stories during the breaks. **Hugo van Ingen**, thanks for your support at the NMR machines and for the feedback during the group meeting. And thank you for bringing your group: **Ulrich le Paige**, thank you for the good times, the (loooong) stories, and for the pastry. Hang in there man! **Heyi Zhang**, what a character, you're one of a kind. I would wish you best of luck, but you'll probably reject it and scream "I make my own luck!". You're awesome. **Velton Horn**, I know you miss our great and long evenings filling the magnets from dawn to dusk, with our productive, philosophical and very intelligent conversations during that period (coffcoff). Wish you all the best with your new job! **Clara van Emmerik**, you're already sorted for life. It was amazing to see how you could get things done effectively yet maintaining a great life/work balance. Best of luck with your new job, and greatest joy for your family. Another extremely effective gentlemen is **Vicenzo Lobbia**, thank you for the good moments and for your suggestions on the lab – you're up for great things.

**Reinier Damman!** I want to thank my office mate from start to end. Thank you for the daily mental support and for all the fun moments, I had a great time. And a big thanks for translating the summary of this thesis. Wish you all the best, for you and **Cátia Frias**. PS: I'm better than you at Krunker. **Yanzhang Luo**, yo Jon, all the best man! Hope all the best for you and Jane here in the Netherlands. **Cecilia Pinto**, I got so happy when I met you! Thank you for all the constant support, and for the help

in the lab too. I truly hope for you to be happy and live your dream life. Another big thanks for the support to **Deni Mance** as well! Thank you for the guidance, for the patience and willingness of explaining us, mortals, NMR. I'm sure we all had a great time. **Alessandra Lucini Paioni**, ale ale ale thank you for all the support at the DNP, for all the fun and for that amazing salami! You're the Italian Rambo! **Helena Ehren**, augen auf you're almost there! I wish you the best of luck with your new projects, I'm happy that you're happy. **Ivan Corbeski**, another crazy hardworking man, with crazy discipline and strong mindset. Dude, thanks all the support and help when I most needed. I still remember, there we were at IAM dragging a couch in the middle of the street, and sweat our way to the third floor just to realize it doesn't fit through the door. "It's ok, now I go back home to sleep." Awesome. Ah, I almost forgot I need to thank **Siddarth Narasimhan** for being the most annoying b@\*#&€ person ever. This devil's spawn exploited and tortured me 365 days per year, sunrise to sunset. Everyday telling me what to do, what to think, what to eat, what to try, what to watch, what to say, what to dress. No one deserves this. Alright, I'm joking. Sid, thanks to you I have now matured; I finally developed into a genuine Leicester man; before I was a slimy caterpillar, now I'm a wonderful butterfly. In the end, I must say that Sid to me is like... an iron lung. I really needed him, but I wished I didn't. Joking man, you're the best, the real MVP.

**Miranda Jekhmane**, partner in crime, sister in arms, thank you a lot for all the support throughout these years, really. And thank you for squashing me against a sofa in the trunk of your car. Many thanks to **Roman Dingjan**, I still remember him climbing the stairs with all the furniture. I wish you two all the happiness for your life together. **Rhythm Shukla** hang on in there, you're very sharp! The torch is on your side now, go set the world on fire! (In a good way you pyromaniac mind!).

I want to thank these hard-working and talented scientists, **Christoph Müller**, **Felix Kümmerer** and **Bram Vermeulen**. These guys were the catalysers and the work-force behind the KcsA projects, they obviously did a fantastic job. **Thorben Maaß** in the shortest time possible, managed set up a lipid purification protocol. With no surprise, all of them already started, or are about to start, their own PhD. Way to go guys! I hope to read your own thesis in a few years. And Bram, go for the Nobel. **Danique Ammerlaan** and **Benjamin Vermeer**, other two talented young scientists, I wish you all the best for your future, you can do it!

**Susana Proença**, thank you for the nice evenings, I was so happy to have a fellow Portuguese around! I wish the best of luck for your projects. I also thank **Nicos Starreveld**, that helped me crack the probabilistic model.

I want to thank my previous mentors. Professor **Eurico Cabrita** thank you for always supporting and promoting your students. You brought us to the world of NMR and inspired us to pursue science. Mestre **Ângelo Figueredo**, thank you for giving me advice, training and discipline in the lab. **Filipa Marcelo** and **Adino Viegas** thank you for the guidance throughout the experiments and results, and how to look at the bigger picture. Professora **Carla Cruz**, you can't imagine how important was the training I had in your laboratory. It help me grow as a researcher, and the chemistry skills I learned were fundamental for the work in Utrecht. I also had a really great time in Covilhã and really miss the time I had there. I wish the best success for my previous colleagues Ana, Helena, Micael, Diogo, Ricardo, Tiago, Inês A., Inês F., Inês R., Sara, Filipa, Elisabete, Sandrina, João, Sérgio and Josué. You people are awesome.

Como diz o outro, agora em bom português. Quero agradecer ao meu pai **Jorge Silva** e à minha mãe **Cristina Silva**, pelo suporte incondicional desde sempre e pela educação que me tornaram a pessoa que sou hoje. Os meus pais são pessoas que trabalham uma vida inteira com muito amor e sacrifício para nos fazer chegar aqui. Um abraço também para os meus irmãos. **Jorge Silva**, espero que sejas muito feliz com o teu trabalho, tenho a certeza que serás o novo veterinário de referência da ilha e arredores. Desejo ao **Pedro Silva** muita força e serenidade para enfrentar esse teu novo desafio. Vais ser um grande engenheiro! Um abraço muito grande à minha avó **Ludovina Silva** que, com muito paciência, sempre me estimulou à curiosidade desde pequenino e guiou-me durante os estudos.

Quero agradecer também a todos os meus tios que me apoiaram quando mais precisei. Em especial, um grande abraço aos meus tios **São** e **Luís** por todo o apoio quando estudei em Lisboa. Nunca me esquecerei quando estive longe e doente, vocês estiveram ao meu lado.

Quero também enviar um abraço ao grande empreendedor **António Camacho**, o meu primeiro *patrão*, por todo o seu grande apoio e gentileza, tanto para comigo e com o seu pessoal. You're the best! Um abraço também ao pessoal do *My Spot*, desejo tudo de bom.

Agradeço imenso também ao **Mário Azevedo**, **Dulce Azevedo** e família pela amizade e todo o apoio quando estudei na Nova de Lisboa. Levo comigo histórias e lições de empreendedores de referencia que ao mesmo tempo são pessoas gentis e humildes.

Finally, I want to thank my everyday support, my beacon, my pillar and my sanity, **Sara Raquel Nascimento Santos Pereira da Silva**. Thank you for always understanding, always caring and always being by my side. Love you <3.

Throughout this journey, more than knowledge, I gained friends for life. I thank you all, deep from my soul, for this wonderful experience.



Now then... which way does the wind blow?

In memory of my grandparents / Em memória dos meus avós

- Américo Oliveira Silva
- José da Silva Medeiros
- Maria da Estrela Botelho Lima

## *In Memoriam*

### **Vasco Botelho Carvalho, 1989 – 2017**



Vasco Carvalho was born in 19<sup>th</sup> July 1989 in Almada, Portugal. In 2012 he received his bachelor's degree in Biochemistry from NOVA Lisbon University. During his studies he obtained an ERASMUS travel grant for his internship in the Tissue Culture Engineering Laboratory (TCEL), under Dr. Krzysztof Wrzesinski and Dr. Stephen J. Frey at the University of Southern Denmark. He then moved to Denmark and obtained a master's degree in Molecular Biosciences at the same institute, with the thesis *Characterization of P450 drug metabolizing enzymes in 3D hepatocyte spheroids grown in a rotational Bioreactor*, also developed at the TCEL group.

He had started his PhD studies in the same field and his work resulted in a paper that he co-authored, with the title *Exponential Growth in Classical 2D and Metabolic Equilibrium in 3D Environments*, published in Plos One.<sup>1</sup> A paper was recently dedicated in his memory.<sup>2</sup>

Vasco was a passionate and dedicated scientist. Personally, he was a gentle, energetic and kindhearted person. Since childhood Vasco was a dedicated scout, he was member of the National Corp of Scouts where he routinely helped the local community and surveilled the forest. It was a lot of fun to have him around, anywhere he passed he would easily make a large number of friends that would hold him dear. He was the lead singer of a metal / rock band, they would mostly do covers with a few originals. I must say that Vasco, with almost absolute certainty, was the biggest Dream Theater fan on the planet.

Vasco put all of his character into what he did. He left the world not before he could give the very best of himself. I strive to do the same!

- (1) Wrzesinski, K.; Rogowska-Wrzesinska, A.; Kanlaya, R.; Borkowski, K.; Schwämmle, V.; Dai, J.; Joensen, K. E.; Wojdyla, K.; Carvalho, V. B.; Fey, S. J. The Cultural Divide: Exponential Growth in Classical 2D and Metabolic Equilibrium in 3D Environments. *PLoS One* **2014**, *9* (9), e106973.
- (2) Wrzesinski, K.; Fey, S. Metabolic Reprogramming and the Recovery of Physiological Functionality in 3D Cultures in Micro-Bioreactors. *Bioengineering* **2018**, *5* (1), 22.

*With the kind contribution from Maria Carvalho, Vasco's sister.*



ORCID

Record

## List of publications

2 × manuscripts in preparation

- (12) Ribeiro, D. O.; Viegas, A.; Pires, V. M.R.; **Medeiros-Silva, J.**; Bule, P; Chai, W.; Marcelo, F; Fontes, C. M.G.A; Cabrita, E.; Palma A. S.; Carvalho A. L.; Molecular basis for the preferential recognition of  $\beta$ 1,3-1,4-Glucans by the Family 11 Carbohydrate-Binding Module from *Clostridium thermocellum*; (2019) *FEBS Letters*, accepted.
- (11) Jekhmane, S; Prachar, M.; Pugliese, R.; Fontana, F.; **Medeiros-Silva, J.**; Gelain, F.; Weingarth, M; Design parameters of tissue engineering scaffolds at atomic scale. (2019) *Angewandte Chemie International Edition*, 58, 2–12
- (10) **Medeiros-Silva, J.**; Jekhmane, S.; Breukink, E.; Weingarth, M.; Towards the native binding modes of Lipid II targeting antibiotics. (2019) *ChemBioChem*, 20, 1-9
- (9) Jekhmane, S.\*, **Medeiros-Silva, J.\***, Li, J., Kümmerer, F., Müller-Hermes, C., Baldus, M., Roux, B., Weingarth., M.; Shifts in the selectivity filter dynamics cause modal gating in K<sup>+</sup> channels. (2019) *Nature Communications*, 10, 12.
- (8) **Medeiros-Silva, J.**; Jekhmane, S.; Lucini Paioni, A.; Gawarecka, K.; Baldus, M.; Swiezewska, E.; Breukink, E.; Weingarth, M.; High-resolution NMR studies of antibiotics in cell membranes. (2018) *Nature Communications*, 9, 3963.
- (7) Tikhonova, E.; Hariharan, P.; **Medeiros-Silva, J.**; Bogdanov, M.V.; Dowhan, W.; Weingarth, M.; Guan, L.; Structural and functional characterization of protein-lipid interactions of the Salmonella typhimurium melibiose transporter MelB 33. (2018) *BMC Biology*, 16, 85.
- (6) Saracino, A.; Fontana, F.; Jekhmane, S.; **Medeiros-Silva, J.**; Weingarth, M.; Gelain, F. Elucidating self-assembling peptide aggregation via Morphoscanner: a new tool for protein-peptide structural characterization. (2018) *Advanced Science*, 5, 1800471.
- (5) Visscher, K.M.; **Medeiros-Silva, J.**; Mance, D.; Rodrigues, J.P.G.L.M.; Daniëls, M.; Bonvin, A.M.J.J.; Baldus, M.; Weingarth, M.; Supramolecular organization and functional implications of K<sup>+</sup> channel clusters in membranes. (2017) *Angewandte Chemie International Edition*, 56, 13222.
- (4) **Medeiros-Silva, J.**; Jekhmane, S.; Baldus, M.; Weingarth, M.; Hydrogen bond strength in membrane proteins probed by time-resolved <sup>1</sup>H-detected solid-state NMR and MD simulations. (2017) *Solid State Nuclear Magnetic Resonance*, 87, 80.
- (3) **Medeiros-Silva, J.**; Mance, D.; Daniels, M.; Jekhmane, S.; Houben, K.; Baldus, M.; Weingarth, M.; <sup>1</sup>H-detected solid-state NMR studies of water-inaccessible proteins in vitro and in situ. (2016) *Angewandte Chemie International Edition*, 55, 13606.
- (2) **Medeiros-Silva, J.**; Guédin, A.; Salgado, G.F.; Mergny, J.L.; Queiroz, J.Q.; Cabrita, E.J.; Cruz, C.; Phenanthroline-bis-oxazole ligands for binding and stabilization of G-quadruplexes. (2016) *Biochimica Biophysica Acta* 1861(5).
- (1) Santos, D.; **Medeiros-Silva, J.**; Cegonho, S.; Alves, E.; Ramilo-Gomes, F.; Santos, A. O.; Silvestre, S.; Cruz, C.; Cell proliferation effects of calix[4]arene derivatives. (2015) *Tetrahedron*, 71, 7593–7599.

## About the author

João Medeiros Silva was born in 1991 in São Miguel, one of the Azores islands in the Atlantic. He grew up and studied in the island in Ribeira Grande before enrolling at the university in the mainland.

He started his Biochemistry studies at NOVA University Lisbon. As an undergraduate student, he did research in sugar-protein interactions by using NMR at the laboratory of Dr. Eurico Cabrita. He received a research fellowship to perform his master's thesis at the laboratory of Dr. Carla Cruz, in the Health Sciences Research Center. There, his studies concerned the synthesis and evaluation of molecules with affinity to G-quadruplex DNA for cancer therapy purposes. His thesis was awarded with the maximum score and his work resulted in two publications. He also received an innovation prize award during his master studies.

In 2015 he moved to Utrecht to start his PhD in the newly formed group of Dr. Markus Weingarth, at the NMR Spectroscopy Group of Utrecht University. His PhD studies mainly involves measuring and characterizing complex biological systems in their native chemical context, by using solid state NMR. So far, his Ph.D. work resulted in 9 research papers, some of which were spread by the international media, 12 scientific talks (6 of which international), 1 poster prize, 2 travel stipend awards and the Bijvoet Center PhD of the year award.